PARSEC SCALE INTRA–DAY VARIABILITY IN RADIO SELECTED BLAZARS: A *MOJAVE* STUDY

A Dissertation

Submitted to the Faculty

of

Purdue University

by

Huthavahana Sarma Kuchibhotla

In Partial Fulfillment of the

Requirements for the Degree

of

Doctor of Philosophy

December 2010

Purdue University

West Lafayette, Indiana

వాచో యత్ర నివర్తంతే, మనో యత్ర విలీయతే
ఏకీ భవంతి యత్రైవా భూతాని భువనాని చా
సమస్తాని చ తత్వానీ సముద్రే సింధవే యథా
కశ్శోకః తత్ర కో మోహః ఏకత్వమనుపశ్యతః

ప్రకాశాత్మికయా శక్త్యా ప్రకాశానాం ప్రభాకరః
ప్రకాశయతి యో విశ్వం ప్రకాశోయం ప్రకాశతాం

------ సురేశ్వర (మానసోల్లాస)

ACKNOWLEDGMENTS

Listing all the people without whose help I coulde not have begun/finished my doctoral work, indvidually by name, would be quite an arduous task. However, I will always remember each and every tiny help, encouragement I received enroute to my PhD. Having said that, I would like to thank my advisor Prof. Matthew Lister, whose guidance and support have been invaluable. I would like to thank Prof. John Finley for introducing me to Astrophysics and for the several conversations we have had over the years on a host of topics. I would like to thank Prof. Maxim Lyutikov for the indelible impression he had over my understanding and approach to Astrophysics, and also for patiently answering all my questions all the time. I would like to thank Prof. Ken Ritchie for agreeing to be a part of my thesis committee. Last but not the least I would like to thank Prof. Alvin Solomon for showing me how enjoyable grad school can be. A big thank you to Sandy for handling all the various grad school paper work over the years with nary a comment or hitch.

Over the years, I was fortunate to have had the pleasure of knowing several wonderful people. I would like to thank my fellow *MOJAVE* group members for their support (especially Tuomas), and particularly members of the Purdue Blazar research group, Preeti Kharb, Talvikki Hovatta, Nathan Cooper, Brandon Hogan and Jignesh Mehta. I would also like to thank the other astrophysics grad students: Suzanne, Kari, Eric, David, Miguel, Jorge, Ben, Daniel, Gabor, Angelo and Qi, for the various discussions we have had. My stay in grad school and Purdue would not have been such fun, if not for Pravin, Vinay, Aman, Avik, Gyan and Srikanth; So thanks a lot guys. I would forever be grateful to Brahma for his guidance and support. Last, but not the least I would like to thank all my teachers, from elementary school to grad. school for showing me the joys of observation, inference, questioning and deduction.

PREFACE

The variability in the radio light curves of Active Galactic Nuclei (AGN), especially on time scales $\leq$ 50 hrs. in the observer's frame, is of immense interest, since it poses severe challenges to the current understanding of the underlying physical mechanisms. In this dissertation, a study of such variability on the pc scales in a sample of highly beamed AGN, which are regularly monitored under the *MOJAVE* program [Lister & Homan, 2005], is presented. *MOJAVE* is a long term survey of a complete sample of the brightest, radio-loud, compact AGN visible in the northern sky. *MOJAVE* builds upon the 2 cm survey program — that was conducted between 1998–2002 [Kellermann et al., 2004] — with improvements over past surveys in terms of angular resolution, sample size, temporal coverage and statistical completeness. Full polarization monitoring of these objects at 2 cm is carried out using the VLBA so-as-to elucidate the properties of their parsec (pc) scale jets, notably kinematics. One of the chief objectives of the *MOJAVE* experiment is to probe the physical mechanisms responsible for the formation and collimation of these highly relativistic jets along with the investigation of the differences – if any – among the various blazar subclasses. The *MOJAVE* database covers epochs from 1994 – 2011, and this vast archive is the chief motivation behind the current endeavor to analyze the IDV characteristics of these AGN.

Extensive background material on AGN structure, classification and the various radiation mechanisms involved is given in § 1 & 2, while the issue of AGN variability is addressed in § 3. A brief introduction to the sample used in the current study, along with some salient results from *MOJAVE*, reported elsewhere, are presented in § 4. Chief results from the current study and a discussion of the IDV properties of some notable sources are discussed in § 6 and 7 respectively. Ideas for future work are given in § 8. All the material up to § 3.1.5 is only introductory, and hence may be skipped by readers familiar with the subject.

TABLE OF CONTENTS

LIST OF TABLES

LIST OF FIGURES

Figure Page

Figure Page

SYMBOLS

$M_\odot$	Mass of Sun $\approx 1.99 \times 10^{33}$ g
G	Universal gravitational constant = 6.673×10^{-11} m^3 kg^{-1} s^{-2}
c	Speed of light in vacuum = 2.998×10^8 m s^{-1}
M_{BH}	Mass of the black hole
R_s	Schwarzschild radius = $2GM/c^2$, where M is the mass of the object.
$\beta_{\rm app}$	Apparent speed
δ	Doppler factor
γ	Lorentz factor
Γ	Bulk Lorentz factor
T_b	Brightness Temperature
T_{eq}	Equipartition Brightness Temperature
$\delta_{\rm var}$	Variability Doppler Factor
$\Gamma_{\rm var}$	Variability Lorentz Factor
$\delta_{\rm eq}$	Equipartition Doppler Factor
$\Gamma_{\rm eq}$	Equipartition Lorentz Factor
D_L	Luminosity Distance
z	Cosmological Redshift
ν	Frequency
α	Spectral index

ABBREVIATIONS

pc	parsec
kpc	kilo–parsec
Mpc	mega–parsec
mas	milli–arcsecond
μas	micro–arcsecond
Jy	Jansky
AGN	Active Galactic Nuclei
QSO	Quasi Stellar Object/Quasar
BLL	BL Lacertae object
FSRQ	Flat Spectrum Radio Quasar
HPRQ	High Polarization Radio Quasar
LPRQ	Low Polarization Radio Quasar
IDV	Intra Day Variability
SMBH	Supermassive Black Hole
VLA	Very Large Array
VLBA	Very Long Baseline Array
MOJAVE	**M**onitoring **O**f **J**ets in **A**GN with **V**LBA **E**xperiments

GLOSSARY

parsec Stands for **par**allax **sec**ond and is the distance to a star whose 'parallax' is one arcsecond. Parallax of a star is half of the angular distance it appears to move on the sky with respect to distant stars during the course of a year. 1 pc $\approx 30.857 \times 10^{15}$ m ≈ 3.2615 light years.

Schwarzschild radius It is a measure of the characteristic length scale associated with an object, and is given by: $R_s = 2GM/c^2$, where M is the mass of the object. Any object with a size/radius smaller than R_s is defined as a black hole, and the imaginary spherical surface at R_s defines its singularity/event horizon. In the case of a stationary black hole, the last stable circular orbit occurs at a distance of $1.5R_s$.

Jansky Named in honor of Karl Jansky, one of the founding fathers of radio astronomy who first discovered radio waves emanating from the Milky Way, Jansky is a non-SI unit of electromagnetic flux density used chiefly in radio astronomy. 1 Jy $= 10^{-26}$ W m^{-2} Hz^{-1}.

Very Large Array The Very Large Array (VLA) is a system of 27 antennas, each 25 m in diameter, arranged in a Y-shaped configuration in New Mexico, USA. VLA has the overall resolution of an antenna 36 km across, with the sensitivity of a dish 130 m in diameter. See `http://www.vla.nrao.edu/`

Very Long Baseline Array The Very Long Baseline Array (VLBA) is the world's highest resolution telescope, with an angular resolution better than 1 mas, which is equivalent to being able to stand in New York and read a newspaper in Los Angeles. The VLBA is a system of ten 25-m antennas located across the continental US. From Mauna Kea, Hawaii to St. Croix, U.S. Virgin Islands, the VLBA's longest baseline spans more than 8000 km, while the shortest baselines are ~ 200 km. See `http://www.vlba.nrao.edu/`

VLA Low–Frequency Sky Survey The VLA Low–Frequency Sky Survey (VLSS), formerly known as 4MASS, is a 74 MHz (4-meter wavelength) continuum survey covering the entire sky north of $-30°$ declination [Cohen et al., 2007a]. Utilizing the VLA, the survey provides images with a resolution of 80", and an average rms noise of 0.1 Jy/beam. See `http://lwa.nrl.navy.mil/VLSS/`

Difmap Standing for *Difference Mapping*, Difmap is a package written by. Martin Shepherd et al. [Shepherd, 1997], and is part of the Caltech VLBI package. It is based on the technique of building a source map, by iteratively subtracting a source model, a collection of delta-functions, from the dirty map via the deconvolution (using CLEAN) of the *residual/difference map*

Luminosity Distance Luminosity Distance (D_L) is defined by the relationship between bolometric luminosity ($L_{\rm bol}$) and flux ($S_{\rm bol}$), and is given by: $D_L = \sqrt{L_{\rm bol}/\left(4\pi S_{\rm bol}\right)}$.

Angular diameter size distance This is another measure of distance, given by: $D_A = l/\theta$ where l, θ are the physical size of the object in question and its angular size in the sky respectively. Hence, in a flat universe $D_L = D_A\left(1+z\right)^2$.

ABSTRACT

Huthavahana, Sarma Kuchibhotla Ph.D., Purdue University, December 2010. Parsec Scale Intra–day Variability in Radio Selected Blazars: A *MOJAVE* Study. Major Professor: Matthew L. Lister.

In this dissertation, the results of a study of the Intra–day Variability (IDV) properties of a sample of blazars, which are regularly monitored under the *MOJAVE* (**M**onitoring **O**f **J**ets in **A**GN with **V**LBA **E**xperiments) program [Lister & Homan, 2005], are presented. A novel 'Gain Transfer' methodology, developed by the *MOJAVE* team, was used to study the parsec (pc) scale IDV properties of blazars using VLBA data, for the first time. Where data were available, brightness temperature and Doppler factors were also estimated.

The present study covers VLBA epochs from 1994 to 2011. Approximately 3800 light curves, from about 390 AGN comprising the full sample, were analyzed for IDV. IDV was detected in $\sim 28\%$ of sources, and $\sim 11\%$ of epochs. When only the 131 AGN from the statistically complete, flux density limited *MOJAVE*_1 sample were considered, IDV was detected in $\sim 61.8\%$ of sources and $\sim 15.2\%$ epochs. Beaming indicators, such as equipartition Doppler factor ($\delta_{\rm eq}$) & apparent speed ($\beta_{\rm app}$), were found to be positively correlated with IDV, while the galactic latitude position of the source was found to be negatively correlated with IDV. No correlation between the source redshift and IDV was found. Also, a correlation between radio flaring & superluminal component ejection and IDV was found. These IDV observations can be qualitatively explained to be arising from the scintillation of compact components dominated by inverse Compton losses.

An important distinction was found between the IDV properties of the various blazar subclasses. As expected, less beamed AGN – viz., galaxies and Compact Steep Spectrum/GigaHertz Peaked Spectrum objects – have been found to be non–IDV sources. Also, almost no genuine BL Lac objects were found to be IDV sources. On the other hand, all intermediate BL Lac/QSO objects (as inferred by the occasional presence of broad lines in their otherwise power-law optical spectra) were found to be IDV sources, with their IDV properties resembling those of quasars. Persistent IDV sources were found to be rare, and with the exception of the high galactic latitude quasar 1156+295, no new rapid IDV source was found.

1. ACTIVE GALACTIC NUCLEI

Approximately 10% of all galaxies have luminosities ranging from 10^{42} erg s^{-1} to 10^{48} erg s^{-1}, about 10^4 times more than that of a typical galaxy. Such unusual actvity in these 'active galaxies' can be traced to its center or nucleus, a region probably $\ll 1pc^3$ in volume (corresponding to an angular size $\ll$ 1mas at their typical redshift). These Active Galactic Nuclei (AGN) outshine the entire host galaxy, often giving it a stellar appearance. AGN are of various types, but display some or all of the following features:

- Continuum emission over a broad range ($\sim$13 orders of magnitude) of frequencies ranging from TeV $\gamma-$ray to radio frequencies. This continuum emission is non-thermal, believed to be due to synchrotron and inverse Compton (IC) processes, and typically has a powerlaw behavior i.e., $S_\nu \propto \nu^\alpha$, with ν being the frequency, α being the spectral index. The Spectral energy distribution (SED) of a typical AGN is as shown in Fig. 1.1.

- Presence of emission lines (and sometimes absorption lines too) in the optical and UV bands. The total line flux is several percent to tens of percent of the continuum flux. These emission lines could be broad (width up to $\sim 10^4$ km s^{-1}) and/or narrow lines.

- Variability in intensity and/or polarization.

- Strong radio emission, accompanied by the presence of relativistic outflows aka 'jets' which extend over kpc to Mpc scales.

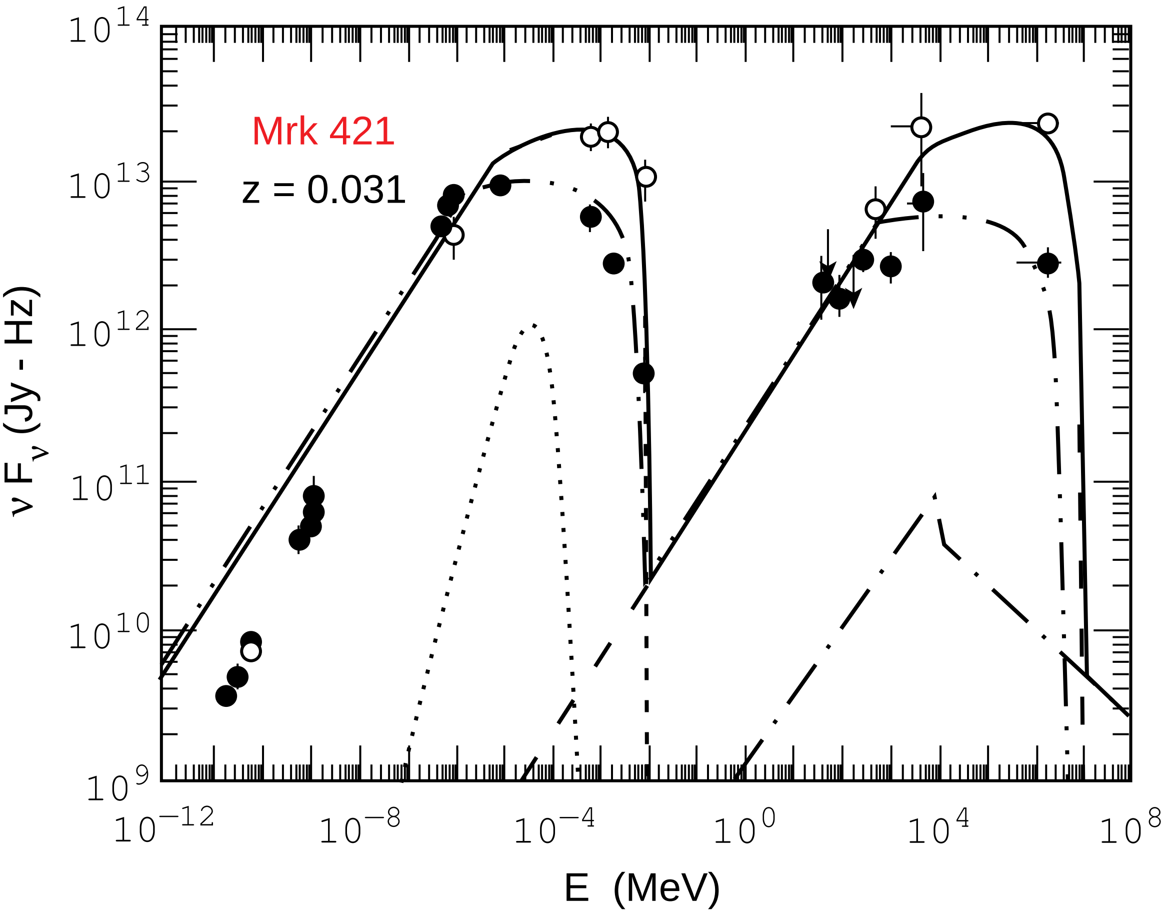

Figure 1.1. Spectral energy distribution (SED) of a blazar. The SED consists of two peaks (humps), the low energy peak is thought to be due to synchrotron emission, while the high energy peak is from Inverse Compton processes. Shown here is the SED of Mrk 421 (1101+384), a 'High Energy' peaked BL Lac object (HBL). Mrk 421, one of the most studied AGN, is a well known TeV source and is characterized by X ray and γ ray flares on an almost daily basis. (Credit: M.A.Catanese, `http://heasarc.gsfc.nasa.gov/docs/cgro/images/epo/gallery/agns/index.html`)

1.1 Structure and Unification

The current model for AGN structure is shown in Fig. 1.2 [Urry & Padovani, 1995]. According to this model, all classes of AGN, despite their apparent differences, host a super massive black hole (SMBH, $10^6 - 10^{10}\ M_\odot$) at their center, whose gravitational potential is the source of AGN luminosity. The characteristic length scale assosciated with these black holes (their Schwarzschild radius) is of the order of 10^{13} cm. Inflowing matter forms an accretion disk around the SMBH, where its angular momentum is dissipated, thus heating up the disk. The accretion disk, which extends out to $\sim 10^{14-15}$ cm from the center, usually has a thermal powerlaw spectrum ($S_\nu \propto \nu^{-1}$) peaking in UV or soft X rays. Electromagnetic energy extracted directly from the spinning black hole [Blandford & Znajek, 1977] or magneto–rotational instabilities (MRI) in the accretion disk [Blandford & Payne, 1982] are thought to power the relativistic jets. Dense clumps of gas in the close vicinity of the SMBH have very high rotational velocities ($\sim 10^4$ km s^{-1}), resulting in a 'leaky absorber' [covering factor of about 0.9, Ferland & Mushotzky, 1982] and hence are responsible for the broad emission lines seen in typical AGN spectra (see Fig. 1.4). These gas clouds, extending $\sim 10^{16}$ cm out, are often referred to as the *Broad Line Region* (BLR). Emission at lower energies (Optical and UV) could be blocked along some lines of sight due to the presence of a warped disk of gas and dust (*torus*) well outside the accretion disk and BLR. Though this obscuring region, extending out to $\sim 10^{17}$ cm, is referred to as a torus, its actual geometric shape is not well known. Beyond this torus lie clumps of gas moving at slower velocities ($< 10^3$ km s^{-1}) and responsible for the narrower emission lines in the spectrum. This region, which can extend out to as far as $\sim 10^{20}$ cm, is referred to as the *Narrow Line Region* (NLR). This is also the region wherein arise the forbidden lines seen in the spectrum [Weedman, 1986]. Polar relativistic outflows aka *jets*, extending out to length scales of $\sim 10^{24}$ cm, complete the picture. These jets are giant radio sources, often when the host galaxy is an elliptical one, but are radio quiet in the case of gas-rich spiral galaxies (as in the case of *Seyferts*). As a result of relativistic beaming, only the jet pointing towards the observer is seen, especially on the pc scales.

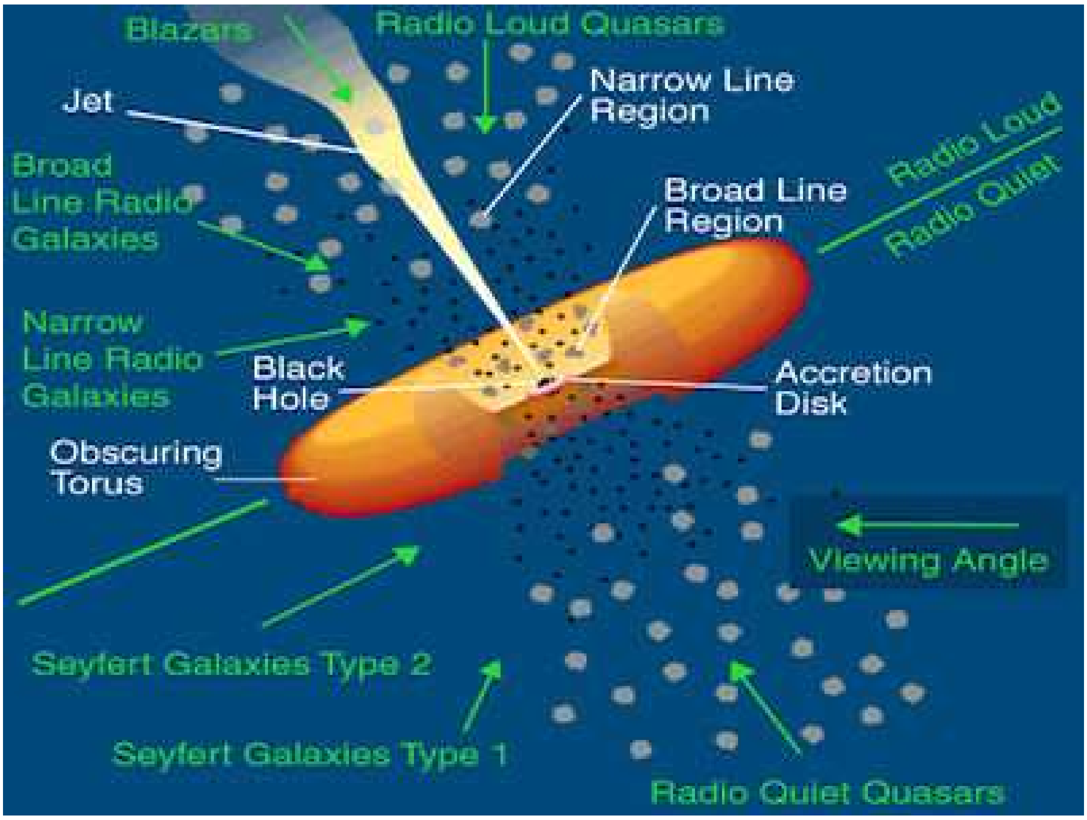

Figure 1.2. A schematic of the current paradigm for AGN structure and its relation to the class of the AGN observed. The various components of the structure of an AGN are shown in white. As per the current 'unification models' [e.g., Urry & Padovani, 1995], the various classes of AGN seen, are purely a result of the anisotropic, doppler boosted AGN emission and due to the differences in the angle between the observer's line of sight (shown in green) & the AGN symmetry/jet axis.

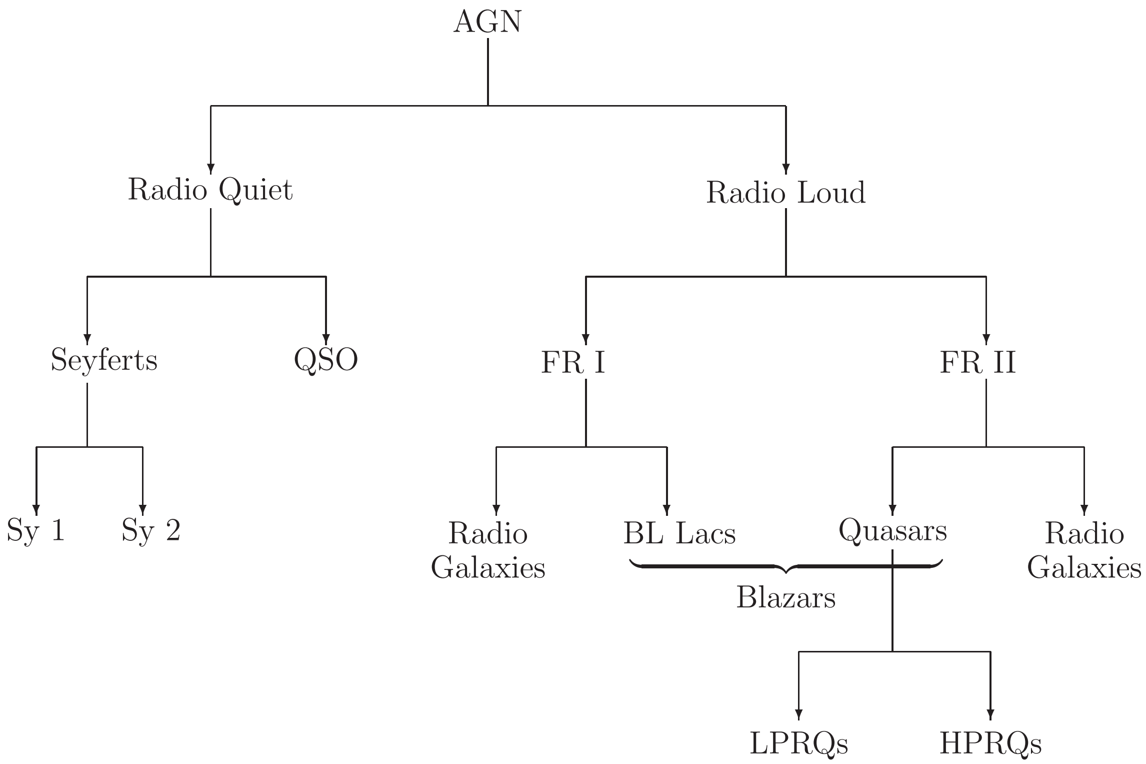

Figure 1.3. Chart showing the broad classification of AGN. QSOs (Quasi Stellar Objects) are often lumped together with Quasars (short for Quasi Stellar Radio Sources) under the category of quasars, though QSOs lack radio emission. The highly beamed class of AGN, called 'blazars', is chiefly comprised of BL Lacs and FR-II quasars.

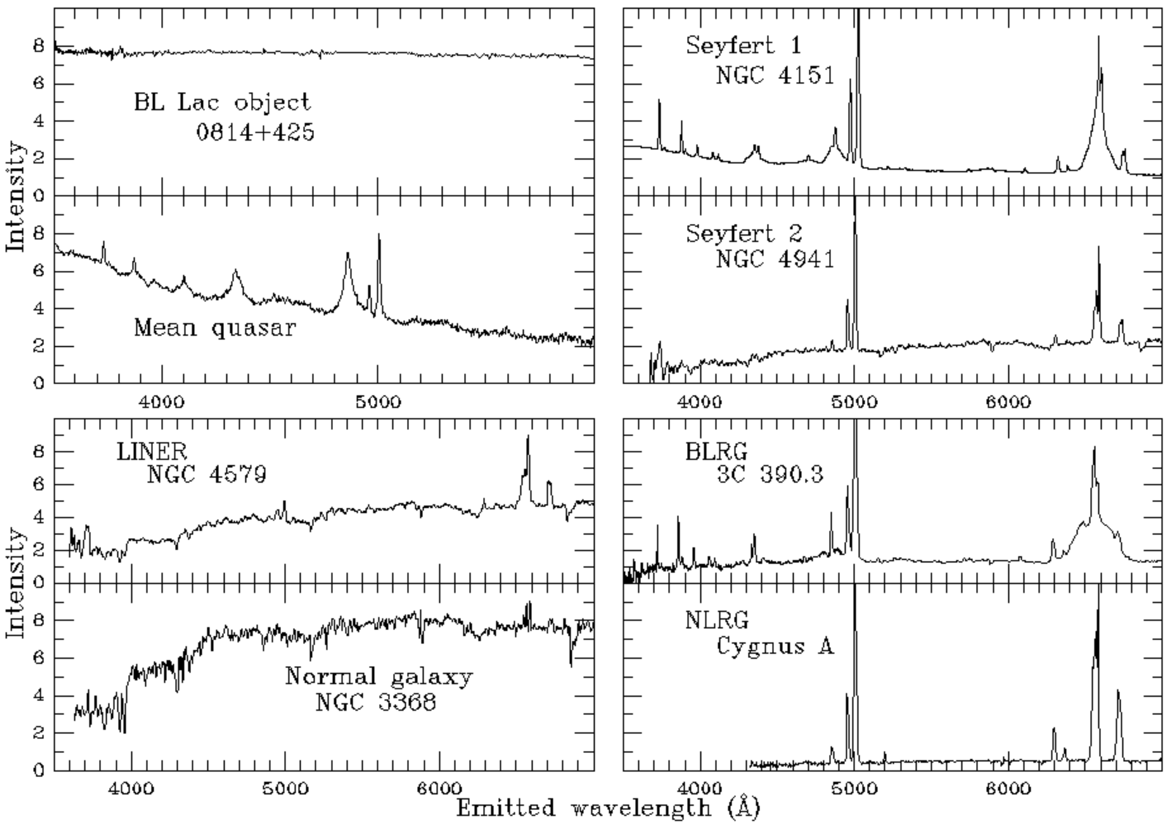

Figure 1.4. Optical spectra for the various types of AGN. NGC 4579 and NGC 4941 spectra are from observations at Mt. Lemmon Observatory [Keel, 1983]. Cygnus A spectrum is from the 4-meter telescope of the Kitt Peak National Observatory [Owen et al., 1990]. The spectra for 0814+425 and 3C 390.3 spectra were obtained with the 5-m Hale telescope at Palomar observatory [Lawrence et al., 1996]. The 'mean quasar' spectrum is from a composite generated by Francis et al. [1991].

1.2 AGN Classification

Due to the varied nature and operating regime of the instruments that were used in the discovery of the different classes of AGN, their taxonomy is very complex, with a zoo of different names, detection criteria (often arbitrary/instrument specific and with no obvious physics reason), spectral, polarization and variability features. A broad classification of AGN is presented in Fig. 1.3.

One obvious way of AGN classification would be on the basis of their spectra. Sample spectra depicting the differences between the various classes of AGN are shown in Fig. 1.4. Quasars, Seyfert 1 galaxies & Broad Line Radio Galaxies [BLRGs] have spectra consisting of a featureless continuum and broad, narrow emission lines and are classified as Type I. The line of sight to these objects is thought to be nearer to the axis of the dusty torus. Seyfert 2 galaxies & Narrow Line Radio Galaxies [NLRGs] do not have broad emission lines in their spectra and are classified as Type II. These objects are thought to be viewed edge-on and hence the BLR is hidden. Detection of broad emission lines in polarized (reflected) light lends credence to this hypothesis [Antonucci & Miller, 1985]. Objects with unusual spectra viz., no lines [BL Lacs], flat spectra (Flat Spectrum Radio Quasars [FSRQs], $S_\nu \propto \nu^{-\alpha}$, $\alpha \sim 0.5$), and the presence of Broad Absorption Lines [BAL QSOs], etc., are classified as Type 0 AGN. A cartoon illustrating the relation between viewing angle and AGN classification in the current unification paradigm is presented in Fig. 1.2. Though this simple geometric model nicely explains the differences in the optical properties of the various classes of AGN, it does not provide a rationale for the radio loudness/quietness of certain classes compared to others.

Kellermann et al. [1989] define AGN to be radio loud, if the ratio of their radio (5 GHz) to optical (B–band) flux exceeds a fiduciary value of 10 viz., $F_{5\ \mathrm{GHz}}/F_B \geq 10$. By this definition, about 10% of all AGN qualify as being radio loud. Radio quiet AGN are in actuality not radio silent, but radio weak. There exists a sharp distinction between the two classes, with the radio quiet sources being two to three orders of magnitude weaker in radio power, compared to their radio loud counterparts. Strong evidence for the radio emission in the radio quiet AGN being due to very weak jets has also been reported [Blundell & Beasley, 1998]. Seyferts (of types both 1 & 2) are the most prominent among the radio quiet AGN. But radio quiet quasars are more optically luminous than Seyferts. It should be noted that there exist no radio quiet AGN with significant variability.

1.2.1 Fanaroff–Riley (FR) Classification

Radio loud objects are typically divided into two FR classes depending on their luminosity. It was first noticed by Fanaroff & Riley [1974] that the relative positions of regions of high and low surface brightness in the lobes of extragalactic radio sources are correlated with their radio luminosity. This conclusion was based on a set of 57 radio galaxies and quasars, from the complete 3CR catalogue, which were clearly resolved at either 1.4 GHz or 5 GHz into two or more components. Fanaroff and Riley divided this sample into two classes using the ratio of the distance between the regions of highest surface brightness on opposite sides of the central galaxy or quasar, to the total extent of the source up to the lowest brightness contour in the map (R_{FR}). Sources with $R_{FR} <$ 0.5 were classified to be of type I and others type II. It was found that nearly all sources with luminosity $L_{178\,\mathrm{MHz}} \leq 2 \times 10^{32}$ h_{100}^{-2} ergs $\mathrm{Hz}^{-1}\mathrm{str}^{-1}$ were of type I while the brighter sources were nearly all of type II. This luminosity boundary is not very sharp, and there is some overlap in the luminosities of sources classified as FR-I or FR-II solely based on their morphology. For a spectral index of $\alpha \simeq 1$, the dividing luminosity at 5 GHz is $L_{5\,\mathrm{GHz}} \leq 7 \times 10^{30}$ h_{100}^{-2} ergs $\mathrm{Hz}^{-1}\mathrm{str}^{-1}$, with the approximate dividing line being given by: $L_R \propto L_{op}^2$. The seperation between the two classes is the most distinct in a 2 dimensional optical–radio luminosity plane, where each class follows a different, approximately linear correlation [Fig. 1.5, Owen & Ledlow, 1994].

FR-I: Fig. 1.6 & 1.7 show radio maps of FR-I galaxies. As can be seen from the images, the low brightness regions are farther from the central source than the high brightness regions. The lobes have steeper spectra, indicating synchrotron aging losses to be the highest there. Jets, typically two sided on kpc scales, have been detected in $\sim 80\%$ of FR-I galaxies, which are often distorted and plume-like. The emission from the jets is highly polarized, the average polarization over the jets being $\sim 30\%$, and the projected magnetic field is perpendicular to the jet axis. FR-I sources are associated with bright, large galaxies (D or cD) that have a flatter light distribution than an average elliptical galaxy and are often located in rich clusters with X-ray emitting gas [Owen & Laing, 1989, Prestage & Peacock, 1988]. As the galaxy moves through the cluster the gas can sweep back and distort the radio structure through ram pressure, which explains why narrow-angle-tail or wide-angle-tail sources appear to be derived from the FR-I class of objects [Kembhavi & Narlikar, 1999].

FR-II: Fig. 1.8 shows a Very Large Array (VLA) image of the nearby narrow line FR-II galaxy Cygnus A. As can be seen from the image, a typical FR-II source consists of a bright compact core, with two extended lobes on either side. At the edge of these lobes are regions of enhanced luminosity, called *hot spots*, which often appear connected to the compact core via the jets. These sources were thought to be 'edge-darkened' prior to the improvements in telescope dynamic range and angular resolution allowed for the detection of these hotspots as distinct structures. In keeping with the overall high luminosity of this type of sources, their cores and jets are also brighter than those in FR-I galaxies in absolute terms; but relative to the lobes these features are much fainter in FR-II galaxies. FR-II galaxies usually are giant ellipticals, but not first-ranked cluster galaxies, and but for their nuclear emission, are normal in every other aspect. Jets are detected in $< 10\%$ of luminous radio galaxies, but in nearly all FR-II quasars and are typically one sided even on kpc scales. FR-II jets are generally smooth and narrower than their FR-I counterparts, with magnetic fields oriented predominantly parallel to the jet axis.

The smooth nature of FR-II jets is thought to be indicative of highly supersonic flows, while FR-I jets are thought to be subsonic, making them amenable to distortions via interaction with the ambient medium. There are two possibilities for this difference in jet speeds.

1. Jets in all radio galaxies and quasars are produced in similar central engines, always emerge with supersonic speeds from the engine and are slowed down to subsonic speeds when there is sufficient interaction: The fact that FR-Is seem to inhabit richer environments supports this idea.

2. Engines powering FR-I and FR-II sources are different in nature, producing subsonic and supersonic jets respectively: Recent findings of a difference in the spin parameters of the SMBH at the centers of these two kinds of sources, with FR-II galaxies all hosting SMBH with spin parameters higher than a threshold value [Daly, 2008], lends credence to this hypothesis.

As can be seen from Fig. 1.5, for a given radio luminosity, there exists an optical luminosity limit separating the two types of source, with the FR-II sources being fainter than this limit and FR-Is being brighter. Since the transition occurs at a fixed radio luminosity, De Young [1993] concludes that there is no major difference in the central engine for the two kinds of sources, and the difference in large scale morphology must be an environmental effect. De Young [1993] also suggests that jets in FR-I galaxies are decelerated a short distance outside their production region. Thus, in the short distance before significant deceleration begins, these jets interact very little with the matter, and have low luminosity, which explains the gap often found between the nucleus and the base of jets in FR-I sources (e.g., see Fig. 1.7). The dense ambient medium can be produced by the inflow of gas into the central region, owing to stellar mass loss, flows set up by interactions, cooling flows, etc. It is to be noted that cooling flows are expected and to an extent observed in clusters of galaxies, whose central galaxies very often happen to be FR-Is. It is expected that active star formation will take place owing to the enhanced density of the central region, and also the action of the jet on it. This should make the central regions of FR-I galaxies bluer than those in FR-II galaxies. Testing such a prediction requires good S/N images of a number of radio galaxies in two or more colours, but a detailed study along these lines is yet to be made [Kembhavi & Narlikar, 1999].

The second possibility, that the differences between the FR-I and FR-II galaxies are due to qualitative differences in the properties of the central engine, has been considered by Baum et al. [1995]. They base their conjecture on a detailed study of the correlations between radio luminosity, emission line luminosity and host galaxy magnitude of a large sample of FR-I and FR-II galaxies, spanning 10 orders of magnitude in luminosity and containing a number of galaxies of the two types that overlap in luminosity. The principal differences they found in the two types are as follows:

1. FR-II galaxies produce about an order of magnitude more optical line emission than the FR-I galaxies at the same host galaxy absolute magnitude or radio luminosity. FR-II galaxies are orders of magnitude brighter in line emission than radio-quiet galaxies of the same optical magnitude, while FR-I and radio-quiet galaxies of the same magnitude have comparable line emission.

2. Emission line luminosities of FR-I galaxies are correlated with their absolute magnitude, while no such correlation exists for FR-II galaxies.

3. Emission line luminosity in both types of galaxy is correlated with total and core radio luminosities, but the regression line for each type has a different slope and intercept.

4. There is a strong correlation between core and total radio luminosities for both galaxy types. The distribution of the two galaxy types in the $\log(\mathrm{L_{rc}} / \mathrm{L_{r,ext}})$,

$\log L_R$ – plane, where L_{rc} and $L_{r,ext}$ are the 408 MHz core & extended radio luminosities respectively, and $L_R = L_{rc} + L_{r,ext}$, is continuous and the regression lines fitted separately to FR-I and FR-II galaxies in this plane are not significantly different.

Baum et al. [1995] conclude that the line emission in FR-Is could be produced by processes in the host galaxy. In contrast to this, available evidence suggests that in FR-IIs the lines are produced as a result of an ionizing continuum from the nucleus. This points to a possible important difference between the central engines of FR-I and FR-IIs: the engines in the FR-Is produce far less ionizing radiation and funnel a higher fraction of their total energy output into the kinetic energy of the jets than FR-IIs. They furthermore suggest that FR-I sources are produced when the accretion rate onto the central black hole is low while FR-II sources arise when the accretion rate is high. This might explain the perceived difference in black hole spins of the two kinds of sources. This leads to a difference in the nature of the jets produced, producing subsonic jets when the spin is low and supersonic jets when it is high. These different jet properties in turn can result in different levels of interaction with the ambient medium, creating the different radio morphologies. It has also been suggested that the accretion rate could decline with time, causing an FR-II galaxy to evolve into an FR-I. Though the observed differences in the ambient environments of these two types of sources seem to argue against them having an evolutionary connection, it is possible that at least some of the FR-Is began as FR-IIs, and in the dense environments of rich clusters, relatively quickly evolved to their current FR-I state [Hill & Lilly, 1991].

As can be seen from Fig. 1.3, the highly beamed class of AGN, called 'blazars', is chiefly comprised of BL Lacs and FR-II quasars. BL Lacs (whose prototype is BL Lacertae and hence the name) are characterized by rapid flux variability, highly polarized optical emission, with optical spectra (see Fig. 1.4) consisting of mostly weak emission lines, i.e., emission lines whose width is $< 5\,\text{Å}$ [Stickel et al., 1991]. Having lower surface brightness than quasars, hence seen at lower redshifts, BL Lacs are usually

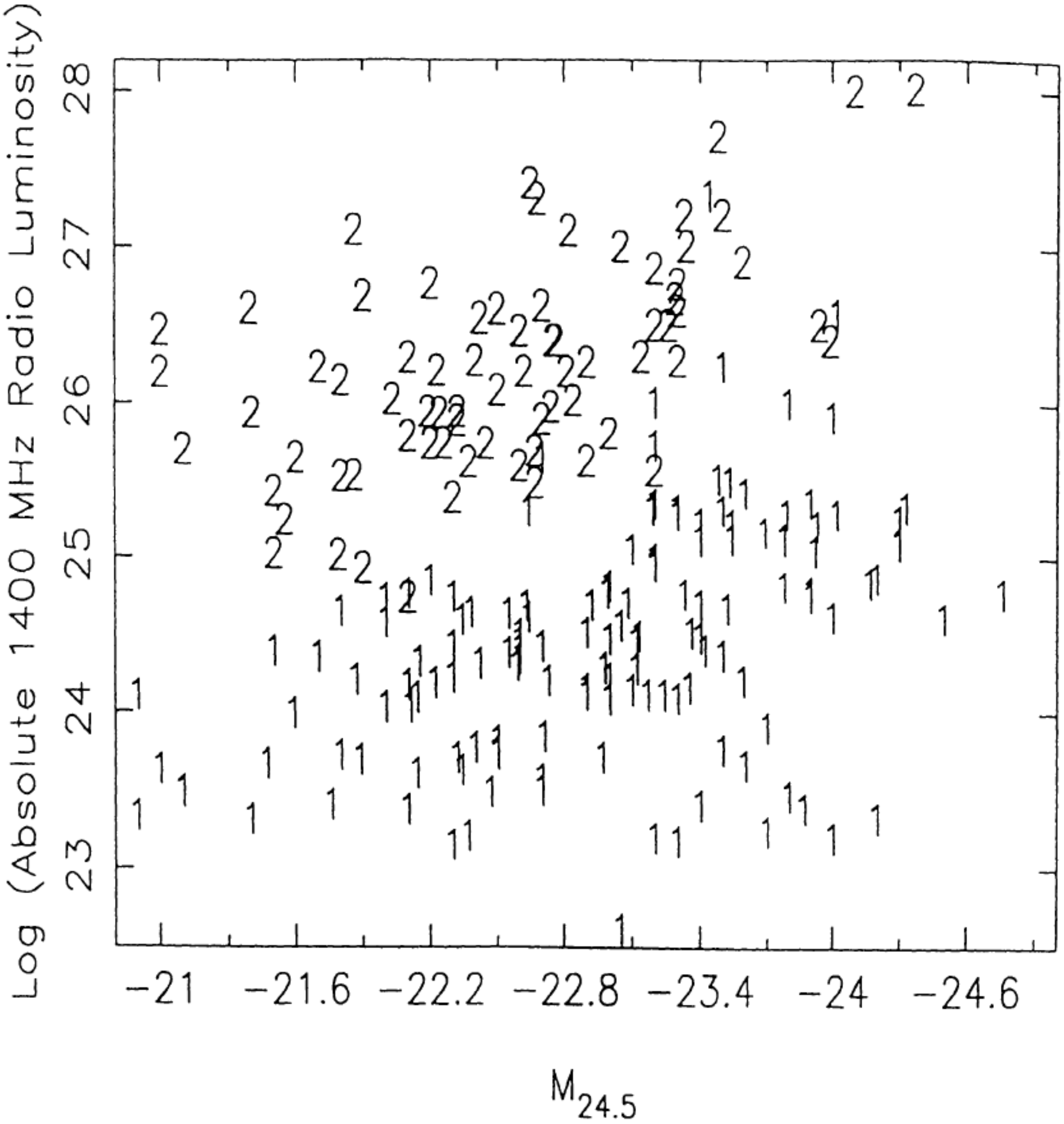

Figure 1.5. Distribution of FR-I (denoted by '1') and FR-II radio galaxies (denoted by '2') as a function of their 1.4 GHz radio luminosity and absolute B magnitude, reproduced from Owen & Ledlow [1994]. The approximate diagonal boundary is given by $L_R \propto L_{op}^2$.

thought to be beamed FR-Is, but recently some evidence to the contrary has been reported [Landt & Bignall, 2008, Cara & Lister, 2008]. QSOs (Quasi Stellar Objects) are often lumped together with Quasars (short for Quasi Stellar Radio Sources) under

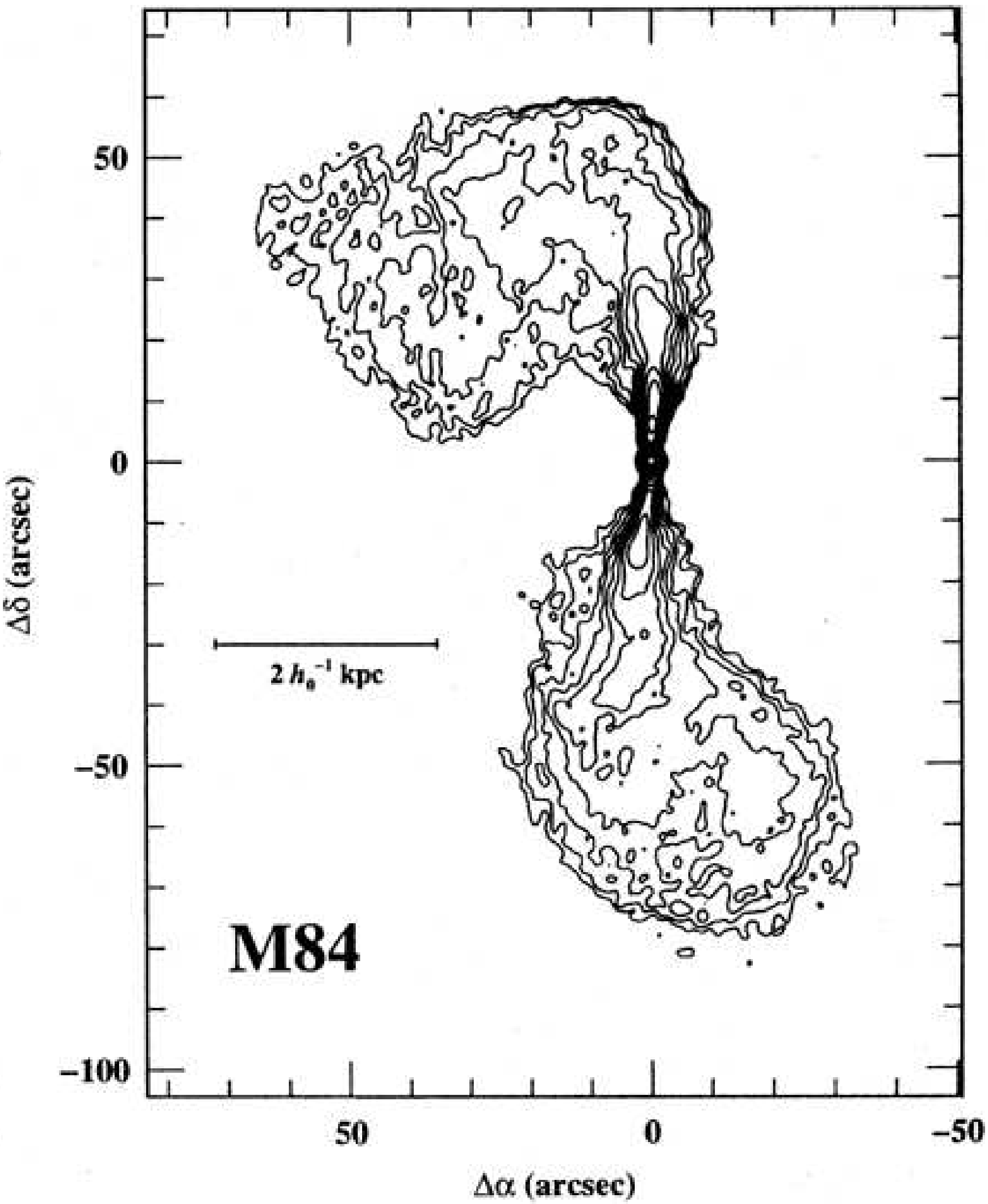

Figure 1.6. Example of a Fanaroff-Riley type I (FR-I) galaxy. This is a radio map of the Virgo cluster elliptical galaxy M84 (3C 272.1 = NGC 4373), based on 4.9 GHz VLA data [Laing & Bridle, 1987].

the category of quasars, though QSOs lack radio emission. Quasars, with their high optical luminosities ($\sim 10^{12} L_\odot$) usually have a 'star-like' appearance (and hence the term stellar) with spectra consisting of narrow as well as broad emission lines. FR-II quasars are often subdivided into High Polarization Radio Quasars (HPRQs) and Low Polarization Radio Quasars (LPRQs) based on their optical polarization, with the division at 3% [Wills et al., 1992]. Broad Absorption Line (BAL) quasars are another subclass that show broad absorption lines, indicative of rapid ejection of absorbing material from the central nucleus. Based on optical variability, some quasars have also been labelled Optically Violent Variable (OVV) quasars. But for a handful of sources, the *MOJAVE* sample of $\sim$ 200 AGN consists exclusively of blazars (see section 4.2).

1.3 Anatomy of AGN: On kpc scales

The large scale structure of AGNs can be categorized into a small number of components, which fall into a few basic types. At the simplest level, the kpc scale structure consists of two lobes which straddle the central AGN (see Fig. 1.8). In a few cases, the AGN is surrounded by a halo which cannot be sensibly divided into a pair of lobes, but at least some of these must be ordinary twin-lobed objects seen end-on, so the lobes are superposed. Even more rarely, objects with a single lobe clearly separated from the AGN are detected. However, AGN with more than two associated lobes are seldom detected. The lobes often contain bright compact substructure in the form of jets or hotspots. Operational definitions for some of the aforementioned anatomical features are described below. These definitions are fairly ad-hoc attempts to reflect the features which seem obvious to the eye.

Jets: Bridle [1986] defines a kpc jet to be a feature that is "(a) at-least four times as long as it is wide; (b) distinguishable from other extended structure (if any) either spatially or by brightness contrast, and (c) is aligned with the centre of activity it is closest to." The centre of activity can generally be identified with the location of the compact core. If no core is detected, the centre is identified with the brightest AGN that lies within the radio structure, or the centre of the brightest galaxy (if there is no obvious AGN). There is very strong, albeit indirect evidence that radio jets trace the path of collimated outflows from the core and the rest of the radio structure is believed to be a by-product of these jets.

In AGN with one-sided kpc jets, or twin jets in which one is distinctly brighter than the other, the lobe containing the (brighter) jet is almost always less depolarized than the lobe on the other ("counter-jet") side. Unified schemes explain the effect neatly, as follows. The asymmetry between the two jets is caused by relativistic beaming, so the brighter jet is coming towards us and hence on the nearer side. The two lobes are embedded in the interstellar medium (ISM) or halo of the host galaxy. Hence, the optical depth towards the farther lobe is higher than that towards the nearer lobe. Therefore, the farther lobe (on the counter-jet side) is more depolarized, due to Faraday rotation. This is the '*Laing-Garrington Effect*' [Laing, 1988, Garrington et al., 1988]. Jets on the kpc scale are sometimes classified as "strong-flavour" jets or "weak-flavour" jets. Strong-flavour jets have smaller opening angles, projected magnetic fields parallel to the jet, with signs of edge brightening in the transverse profile. Weak-flavour jets on the other hand, have larger opening angles, a projected magnetic field perpendicular to the jet (at least near the jet axis), center-brightened transverse profiles and are exclusively seen in FR-Is. It is hypothesized that the weak-flavour jets are low Mach number, turbulent flows [Bicknell et al., 1990].

Lobes: The collimated relativistic jets seen on kpc scales usually terminate in giant radio–emitting plumes called lobes. Hence, these lobes serve as huge reservoirs of energy ($\sim 10^{61}$ ergs). Leahy [1993] defines a lobe to be "an extended region of emission which is not a jet, showing billowy or filamentary substructure, whose perimeter is mostly well-defined in the sense that the projected magnetic field is parallel to the edge, the intrinsic polarization is $> 40\%$, and the intensity tends to zero as the perimeter is approached". Hotspot complexes are simply the brightest regions of these lobes, whereas jets are not parts of lobes. Lobe emission excluding the hotspot complex, is called the *diffuse lobe*. Diffuse lobes are believed to be "cavities" where the normal interstellar or intergalactic medium has been displaced by very hot, low-density material from the jets. Diffuse lobes can usually be subclassified into *Bridges* (center of the lobe closer to the compact core than to the hotspot complex) and *Plumes* (also known as *Tails* in some cases). A lobe is classified as being 'relaxed' if the brightest peak at high resolution is not part of a hotspot or jet. Thus, relaxed lobes may contain very weak hotspots or jets, although in most cases neither is visible. Because of this, the bridge/plume distinction cannot be reliably made for relaxed lobes. A few lobes show faint extensions known as *wings*. In AGN oriented close to the line of sight, the centroid of the lobes could be coincident with the core, giving rise to the appearance of a ring like emission encircling the core, on kpc scales. Such a morphology is aptly named the *halo*. An example of a *halo* can be seen in the quasar 1156+295 (Fig. 7.7). Haloes are almost inevitably relaxed because the presence of any compact structure could be used as a basis for dividing the *halo* into a pair of lobes.

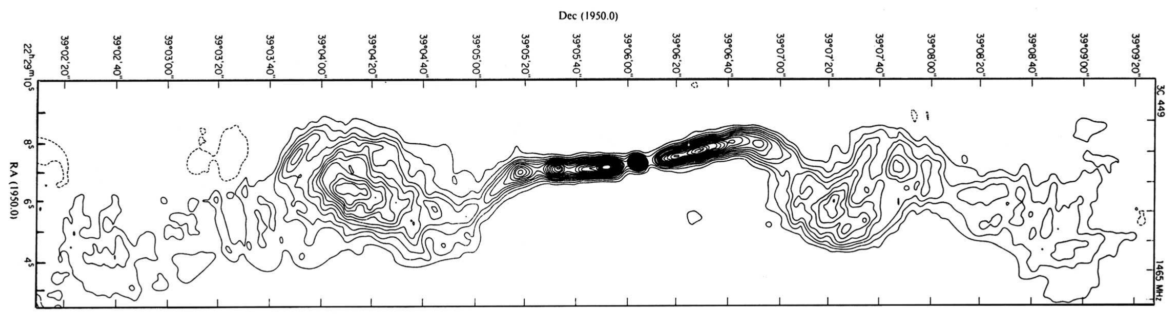

Figure 1.7. VLA map of the FR-I galaxy 3C 449 (z = 0.0181, type: cDE4) at 1.465 GHz [Perley et al., 1979]. The jets are generally smooth in appearance, but higher resolution observations show knots on a smooth ridge of emission, the southern jet being more knotty than the northern one.

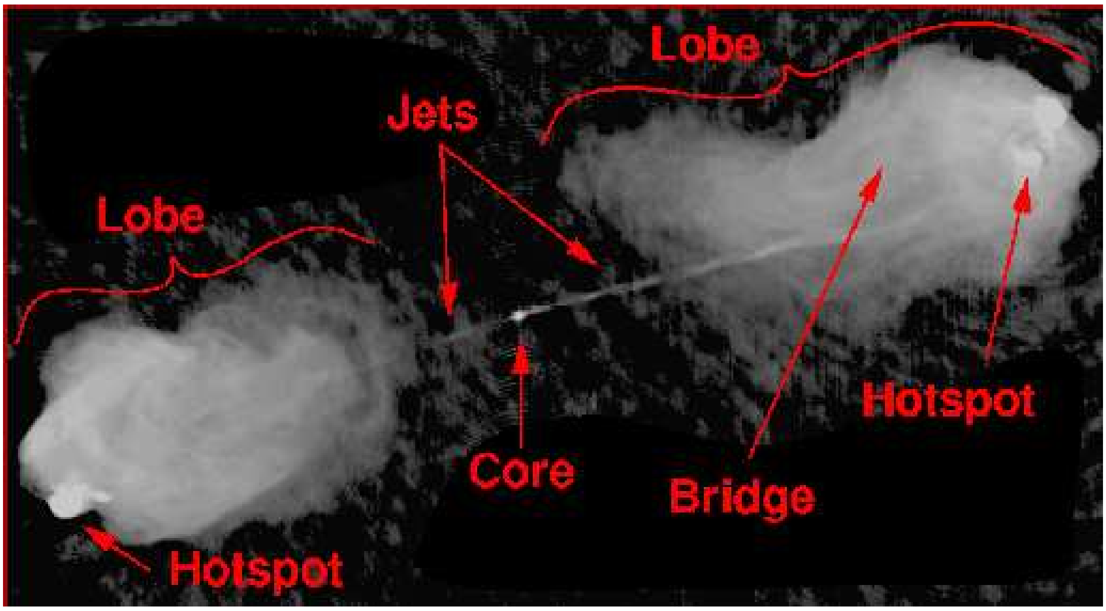

Figure 1.8. Cygnus A (1957+405, z = 0.0561) is an excellent example of a narrow line Fanaroff-Riley (FR) type II radio galaxy, characterized by faint, extended, very narrow (well collimated) jets, distinct lobes, and clear hot spots at the outer edges of the lobes, often where the jets intersect the outer edges [Leahy, 1997]. These are in general more powerful radio sources than the FR-I objects, with the difference being frequently attributed to higher Lorentz factors of the FR-II jets. The image highlights the extent of the radio source beyond the central galaxy, extending ∼140 kpc if seen sideways.

1.4 Anatomy of AGN: The VLBI picture

But for the absence of extended lobes and hot spots in FR-Is, the two classes of radio loud AGN share several common observed structural features - at least on the pc scales - the chief being a compact **core** and **jets**.

Core: The core is the high surface brightness, unresolved feature (down to the sub–mas scale) observed at the center of an AGN. Hence, the linear size of these cores is a few pc at most. It is believed to be the base of the pc scale jets seen, containing the 'nozzle' that accelerates & collimates these jets to supersonic, super Alfvén speeds [Meier et al., 2001], along with the central SMBH and its accretion disk. Most of the bright AGN have 'flat spectrum' cores ($|\alpha| < 0.7$, where α is the spectral index). This flatness of the radio spectrum is believed to be the result of synchrotron self-absorption among a sequence of regions along the expanding jet with progressively larger sizes and turnovers at progressively lower frequencies. A population of relativistic particles with spectral index $p = 2$ would give rise to a synchrotron spectrum with spectral index $\alpha = -0.5$ in the optically thin regime (see section 2.1 for a discussion on synchrotron radiation and its spectrum). A few bright AGN however, have an inverted spectrum or show a turnover in their spectrum. A brief discussion about these steep spectrum sources is included in section 6.2. In a very few objects (usually FR-Is) the core shows twin jets. The jet in the core is usually in the same direction as the brighter large-scale jet, if there is one, and in some cases the jet can be traced directly from the core to kpc scales.

The accurate identification of the position of the compact core can often be tricky. The most straightforward way would be to image the source using VLBI techniques and identify the brightest compact, flat spectrum component with the core, which is accurate more often than not. However, sometimes the core could be self-absorbed (see section 2.1) and hence obscured from view. For example, in the radio galaxy $0238-084$ (NGC 1052; $z = 0.005037$, $\beta_{\rm app} \sim 0.3$)[1], there exists a gap in emission in the middle of two features thought to be the jet and counterjet, since several features moving outward along these features are seen. Using multifrequency VLBA observations, Kadler et al. [2004] have hypothesized that the core feature is indeed obscured by strong free–free absorption associated with a circumnuclear torus. In other cases, no flat spectrum component may be seen, mostly due to spectral confusion, i.e., some jet component with its steep spectrum being the brightest one by virtue of its favorable alignment with line of sight of the observer. In such cases, using

[1]See: `http://www.physics.purdue.edu/MOJAVE/sourcepages/0238-084.shtml`

multi-epoch images of the source, stationary features from which components seem to emanate and/or recede could be identified. Such stationary components could either be associated with features in the jet [e.g., recollimation shock in the jet; see Fig. 1.11, Marscher et al., 2008] or the core itself. Typically the core is the brightest and/or the most variable of these stationary features. However, in some extremely rare cases, the core might not be the brightest feature. In such a case, multi-frequency images can be used, with the position of an optically thin feature being used as a reference point to align the images. The core would then be the feature whose size seems to decrease with increasing frequency. The size of the core $\propto \nu^{-1}$, if energy equi-partition is assumed (see section 2.3.2). For instance in the LPRQ 0923+392 (4C $+39.25$; $z = 0.695$, $\beta_{\rm app} \sim 4.3$)[2], the core is not the brightest feature; instead it is the fainter feature to the West of it (see Fig. 1.9, 1.10). This was inferred using multi-frequency images precisely in the aforementioned fashion [Lister & Smith, 2000]. In several other sources, especially compact, steep spectrum sources, often neither flat spectrum features nor ejected components are evident. In such cases, locating the position of the core is next to impossible [e.g., Radio galaxy 2021+614 (OW 637; $z = 0.227$, $\beta_{\rm app} \sim 0.4$),[3] Mellott & Lister, 2004].

Jets: In the Very Long Baseline Interferometry (VLBI) images of AGN jets, the observed optically thick cores represent the self-absorbed part of the conical jet. Usually this VLBI core is assumed to be stationary. Mostly one-sided jets are seen on the pc scales, as a result of Doppler beaming. For instance, of the 135 sources in *MOJAVE*– I sample, only 5 seem to have 2-sided jets on the pc scale [Lister et al., 2009a]. Regions of enhanced emission called components/knots are observed along these jets. They are thought to be a result of relativistic shocks propagating down the jet according to the shock–in–jet models [e.g., see Fig. 1.11; Marscher, 2005, Marscher et al., 2008]. Despite their successful application to a lot of sources, these models cannot explain

[2] See: `http://www.physics.purdue.edu/MOJAVE/sourcepages/0923+392.shtml`

[3] See: `http://www.physics.purdue.edu/MOJAVE/sourcepages/2021+614.shtml`

all the observed features like intrinsic accelerations or long-lived components. Alternate models involving interactions with ambient plasma, such as the two-fluid models [e.g., Pelletier & Sol, 1992] have also been proposed. The jet components have been observed to exhibit both ballistic as well as non-ballistic (bent jet) trajectories [Kellermann et al., 2004]. Models involving helical motions coupled with Kelvin–HelmHoltz instabilities have been invoked to explain the bent jets in some sources [e.g., Lobanov & Zensus, 2001, for 3C 273]. Bent jets can also be explained using models involving the precession of the *nozzle* in the nucleus. This precession may be due to a SMBH binary, which has been invoked in the case of a few sources, most notably OJ 287 [Valtaoja et al., 2000] and PKS 0420−014 [Britzen et al., 2001]. Apparent superluminal speeds, again a consequence of Doppler boosting (see section 4.1), are often observed in these components. Ejection of superluminal components has been assosciated with flaring, e.g., radio flares in PKS 0420−014 [Britzen et al., 2000], $\gamma-$ray flares [Jorstad et al., 2001] and also with heightened IntraDay Variabiility [Sarma & Lister, 2009, see section 6.7].

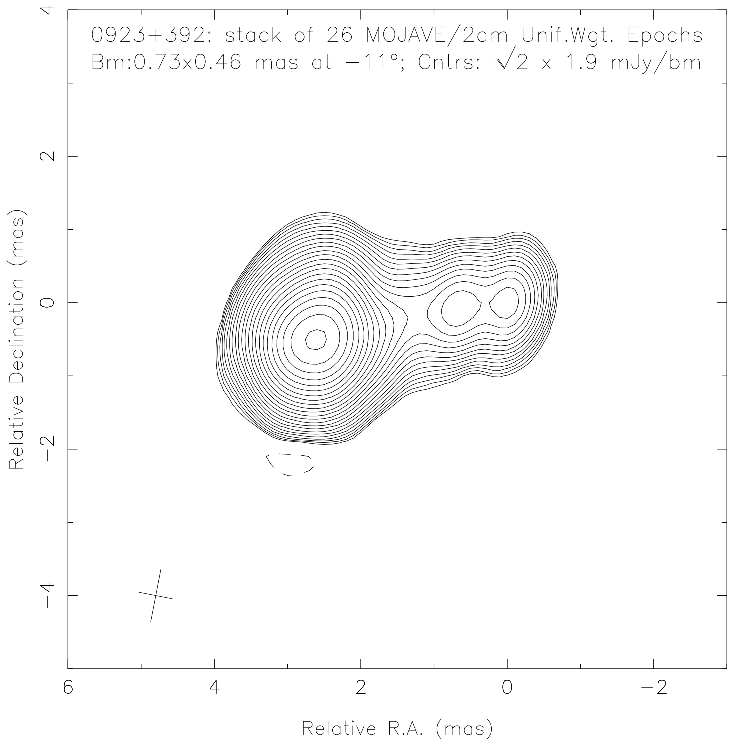

Figure 1.9. Stacked, uniformly weighted, 2 cm VLBA images of 0923+392 from the *MOJAVE* project [Lister et al., 2009a].

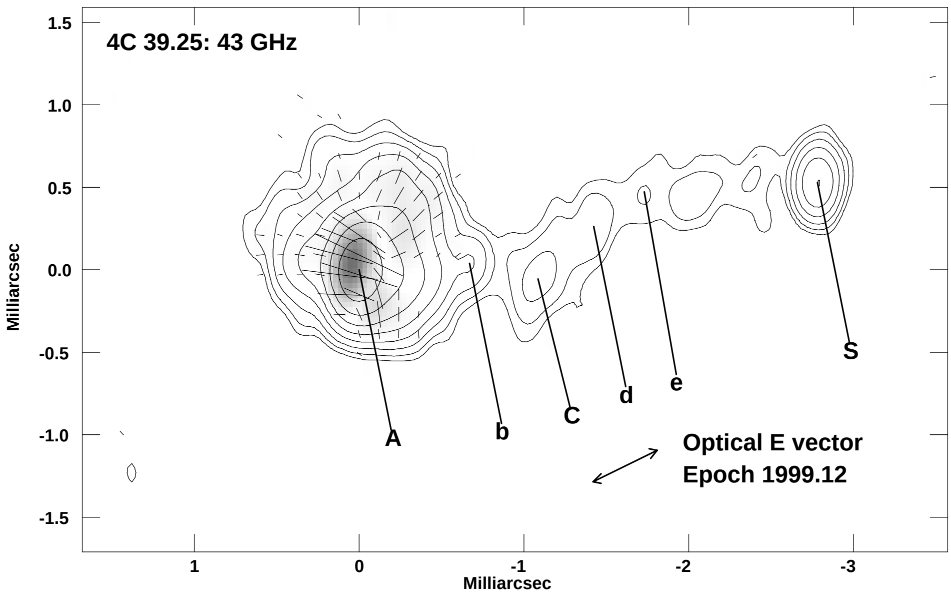

Figure 1.10. 7 mm VLBA image of the LPRQ 0923+392 [Lister & Smith, 2000]. Comparing this image with Fig. 1.9, the feature marked 'S' may be identified as the core.

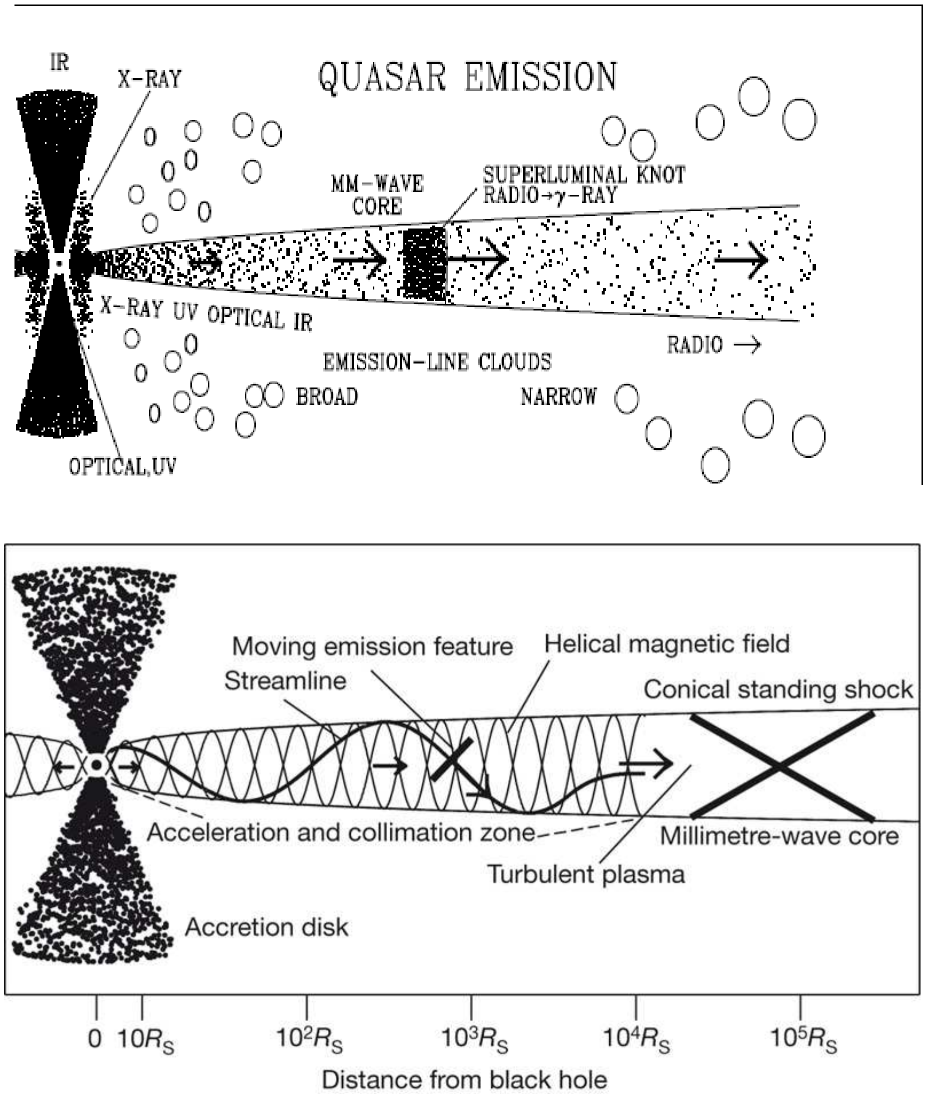

Figure 1.11. Cartoon of the physical structure and emission regions of the pc scale jet of a radio-loud AGN. Shown are the various emitting regions along with their respective spectral regimes (top panel) and the structure (bottom panel) of the inner jet [Marscher, 2005, Marscher et al., 2008].

2. RADIATION MECHANISMS

The most distinguishing feature of radio loud AGN is the presence of jets, whose radio emission is primarily of synchrotron origin. The content of these jets is highly debated. It is unclear whether the jet content is mostly electron–positron pairs (leptonic jets) or electron–proton pairs (hadronic jets) or if the jets are particle starved and B–field (Poynting flux) dominated instead.

2.1 Synchrotron radiation

The radio emission of jets is chiefly of synchrotron origin. Synchrotron photons are emitted when relativistic particles gyrate in a magnetic field. Charged particles spiraling in a magnetic field experience a Lorentz force which is perpendicular to the direction of propagation. Acceleration due to this force is given by:

$$\mathbf{a}_\perp = \frac{q}{\gamma mc}\,\mathbf{v}_\perp \;\times\; \mathbf{B} \tag{2.1}$$

where the Lorentz factor $\gamma = \left(\sqrt{1-\beta^2}\right)^{-1}$ and $\beta = v/c$.
Since the power radiated by an accelerating charged particle $P \propto q^2 a^2$ [Jackson, 1999], the power emitted by the gyrating charge is:

$$P_{\rm sync} = \frac{2}{3}\left(\frac{q^2}{mc^2}\right)^2 \gamma^2 \beta_\perp^2 B^2 \tag{2.2}$$

For an isotropic distribution of velocities, averaging over all angles at a given β:

$$\langle \beta_\perp^2 \rangle = \frac{2}{3}\beta^2 \quad \text{and hence,}$$

$$P_{\rm sync} = \left(\frac{2}{3}\,\frac{q^2}{mc^2}\right)^2 \gamma^2\beta^2 B^2 = \frac{4}{3} c\,\sigma_T \left(\gamma^2 - 1\right) U_B \tag{2.3}$$

where $\sigma_T = \frac{8\pi}{3}\left(\frac{q^2}{mc^2}\right)^2$ is the Thomson cross section and $U_B = \frac{B^2}{8\pi}$ is the magnetic energy density [Rybicki & Lightman, 1979]. Since the mass of a proton is ~ 2000 times the mass of an electron, the contribution of protons towards the observed synchrotron radiation can be neglected. Also, since in all astrophysical cases of interest $\gamma \gg 1$, equation (2.3) may be written numerically as:

$$P_{\rm sync} \approx 2.659 \times 10^{-14} \gamma^2 U_B \text{ ergs s}^{-1} \tag{2.4}$$

Emission of synchrotron photons leads to a *cooling* of the emitting electrons. Typical synchrotron cooling time scale is defined as:

$$\tau_{syn} = \frac{\gamma m_e c^2}{P_{\rm sync}} \approx \frac{25}{\gamma B^2} \text{ yrs, where B is measured in Gauss} \tag{2.5}$$

Though the aforementioned radiation field is that of a dipole in the rest frame of the emitting particles, in the observer's frame, it would be beamed into a narrow cone with opening angle $\sim 1/\gamma$. This *Doppler boosting* plays a key role in all high energy astrophysical phenomena. Also, in the non-relativistic case, the single particle spectrum of this field would only have one component, at the *gyro-frequency* ($\omega_B = eB/m_e c$). In the relativistic case however, this spectrum would extend to something of the order of a critical frequency ($\omega_c = \gamma^2 \omega_B = \gamma^2 (eB/m_e c)$). Also, in this case the spectrum is a function of ω/ω_c only. The spectral emissivity of a single ultra relativistic particle due to synchrotron radiation is shown in Fig. 2.1. As can be seen from that figure, it peaks at $\omega = 0.29\ \omega_c$.

Similar results can be derived for an ensemble of particles. Often the number density of particles with energies between E and $E + dE$ (or γ and $\gamma + d\gamma$) obeys a power law distribution i.e.,

$$N(\gamma)\, d\gamma \propto \gamma^{-p} d\gamma \quad \gamma_1 < \gamma < \gamma_2$$

For $\gamma_1 \approx 0$ & $\gamma_2 \approx \infty$, $P_{\rm tot} \propto \omega^{-(p-1)/2} \Rightarrow$ Spectral index: $\alpha = -\left(\frac{p-1}{2}\right)$

Also, Intensity: $I(\nu) \propto B^{(1-\alpha)} \nu^{\alpha}$

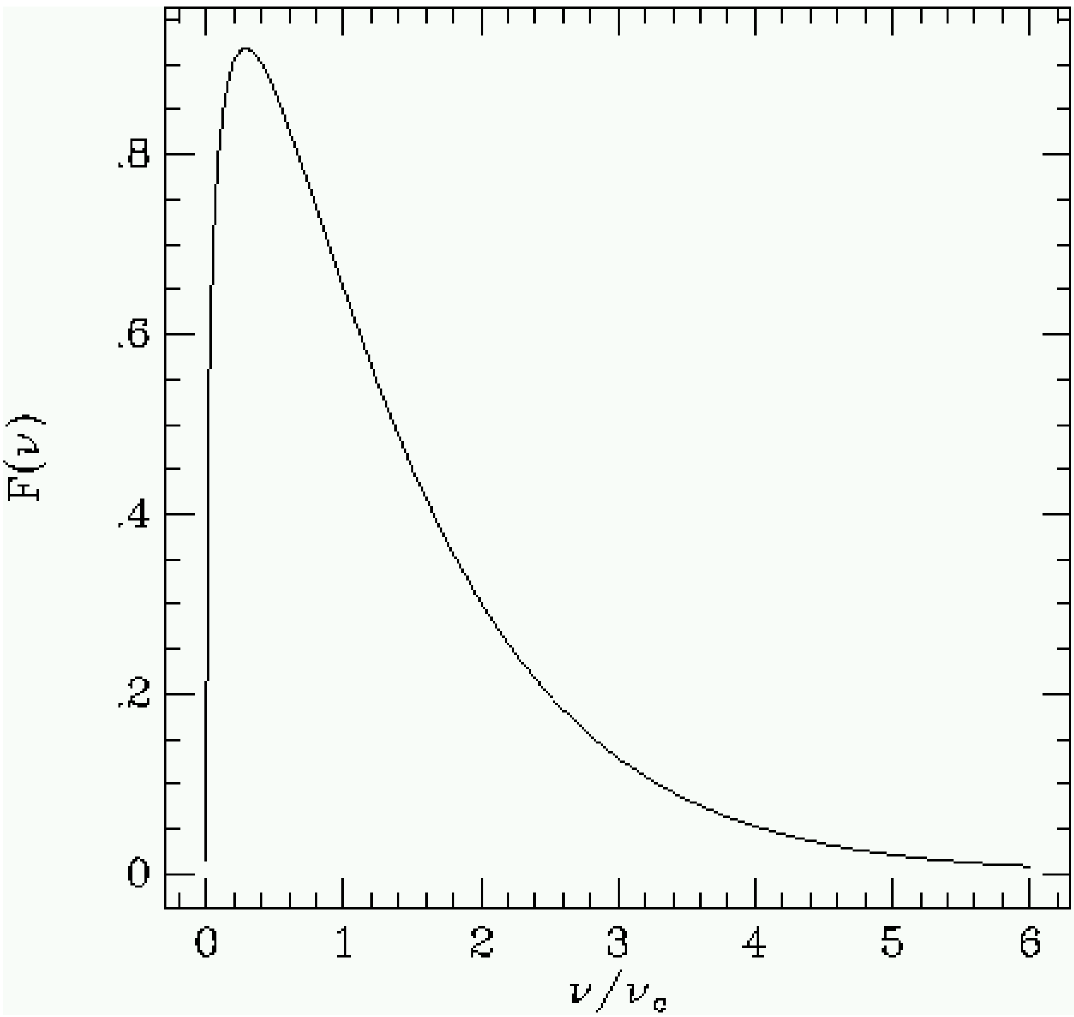

Figure 2.1. The spectral emissivity of an ultra relativistic charged particle due to synchrotron radiation [Rybicki & Lightman, 1979]. The maximum of the emission spectrum is at $\omega = 0.29\ \omega_c$, where the *critical frequency* $(\omega_c) = \gamma^2 \omega_B$.

Though the energy spectrum of the emitting particles is not a thermal equilibrium spectrum (and hence a concept of 'temperature' is not strictly valid), a characteristic temperature can be derived. Since the radiation spectrum peaks around ω_c (see Fig. 2.1) and the particles in question are ultra-relativistic ($\gamma \gg 1$), the emission and absorption processes of radiation are roughly associated with a single energy ($E \approx \gamma mc^2$). Since the typical relaxation time required for the particle spectrum to relax to its equilibrium state is large, a temperature may be associated with this energy, i.e.,

$$T = \gamma \frac{mc^2}{3k_B} = \left(\frac{\omega}{\omega_B}\right)^{1/2} \frac{mc^2}{3k_B} \tag{2.6}$$

When the brightness temperature of the radiation field ($\propto I_\omega/\omega^2$ in the Rayleigh–Jean's limit) becomes comparable to the kinetic temperature of the emitting particles, absorption of the emitted photons by the emitting particles (aka *Self Absorption*) becomes important. Hence, in the case of a Synchrotron Self Absorption spectrum,

$$I_\omega/\omega^2 \propto \left(\frac{\omega}{\omega_B}\right)^{1/2} \frac{mc^2}{3k_B} \quad \text{Or} \quad I(\omega) \propto \omega^{5/2} \tag{2.7}$$

Hence, for a self-absorbed synchrotron source, the photon spectral index $(\alpha) = 5/2$, independent of the particle spectrum, as can be seen from Fig. 2.2. The spectrum from Synchrotron self-absorption is responsible for the turnover seen in many AGN spectra, notably those of the 'Gigahertz Peaked Spectrum' (GPS) sources and the turnover frequency marks the transition from the optically-thick to the optically-thin regime. Presence of multiple unresolved components with slightly different turnover frequencies could result in a flat overall spectrum. The flat overall spectral nature of AGN cores is hypothesized to be the result of such a phenomenon, the so called *'cosmic conspiracy'* [Cotton et al., 1980].

2.2 Inverse Compton radiation

The population of relativistic particles responsible for synchrotron emission can also upscatter (Inverse Compton scatter) photons to higher energies, thus giving rise to 'Inverse Compton' (IC) radiation. The second peak in the blazar SED (Fig. 1.1) is thought to be the result of such a process. The IC seed photons could either be the synchrotron photons emitted by the very same population of relativistic particles – in the Synchrotron Self Compton (SSC) scenario – or 'external' photons like those from the accretion disk or ambient starlight (EIC models) or the Cosmic Microwave Back-

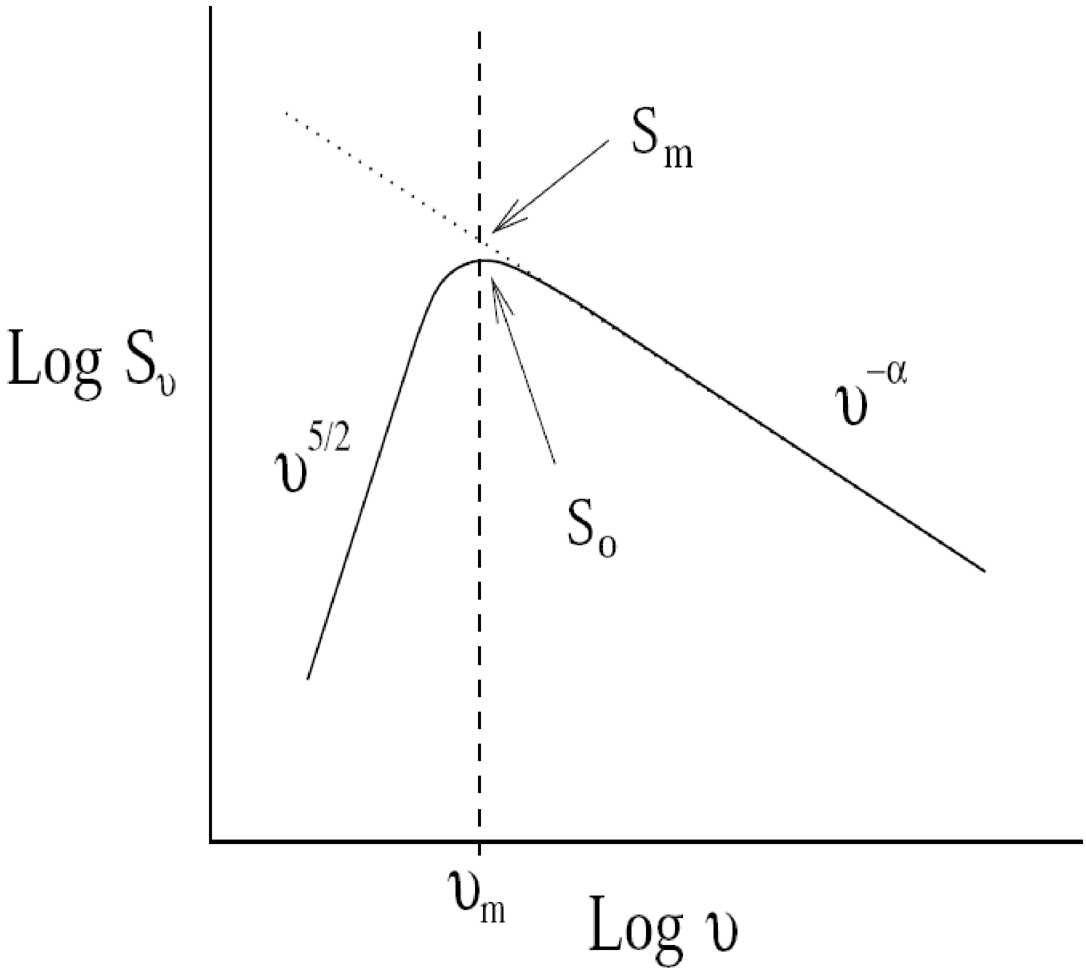

Figure 2.2. Cartoon depicting the synchrotron spectrum from a homogeneous source [Rybicki & Lightman, 1979]. ν_m is the turnover frequency, while S_0, S_m denote the observed and extrapolated peak flux densities at the frequency. The source is optically thick (thin) for frequencies lesser (greater) than ν_m.

ground (CMB) photons (IC/CMB models). The energies of the seed photon (prior to scattering), in the rest frame of the scattering particle and the IC photon (in the aftermath of scattering) are roughly in the ratio $1 : \gamma : \gamma^2$ [Rybicki & Lightman, 1979]. Hence, for a suitable value of γ radio and infrared photons could be upscattered to X-ray and TeV γ-ray energies.

The expression for the IC power for a single scattering ($P_{\rm IC}$) is very similar to that for synchrotron power (equation 2.3).

$$P_{\rm IC} = \frac{4}{3} c\, \sigma_T \left(\gamma^2 - 1\right) U_{\rm rad} \tag{2.8}$$

where $U_{\rm rad}$ is the energy density of the seed photon field. Hence the ratio of IC luminosity to synchrotron luminosity is simply:

$$\frac{L_{\rm IC}}{L_{\rm sync}} = \frac{U_{\rm rad}}{U_B} \tag{2.9}$$

2.3 Brightness Temperature

Radio observations are at sufficiently long wavelengths for observed thermal continuum sources to be far beyond the black-body maximum. Hence, using Rayleigh – Jean's law, the specific intensity of the source $F_\nu \approx 2k_B T \lambda^{-2}$ or $F_\nu \propto T$. Hence, a 'Brightness Temperature' (T_b), which is equivalent to the temperature of a black body radiating the same flux density as the source, may be defined:

$$T_b^{obs} = \frac{c^2}{2k_B \nu^2}\, I_\nu = \frac{c^2}{2k_B \nu^2}\, \frac{S_\nu}{\Omega} \quad , \tag{2.10}$$

where $k_B,\ c$ are the Boltzmann constant & speed of light respectively, ν is the observing frequency and I_ν is the intensity. The final expressions for T_b would then be [Ghisellini et al., 1993, Tingay et al., 2001]:

$$\begin{aligned} \text{For a homogeneous optically–thick disk: } T_b^{obs} &= 1.762 \times 10^{12}\ \mathrm{K}\ \left[\frac{S_{\rm Jy}}{\nu^2_{\rm GHz}} \left(\theta^{\rm maj}_{\rm mas}\ \ \theta^{\rm min}_{\rm mas}\right)^{-1}\right] \\ \text{When using Gaussians: } T_b^{obs} &= 1.221 \times 10^{12}\ \mathrm{K}\ \left[\frac{S_{\rm Jy}}{\nu^2_{\rm GHz}} \left(\theta^{\rm FWHM,maj}_{\rm mas}\ \ \theta^{\rm FWHM,min}_{\rm mas}\right)^{-1}\right] \end{aligned} \tag{2.11}$$

where $\theta^{\rm FWHM,maj},\ \ \theta^{\rm FWHM,min}$ are the angular sizes of the major & minor axes in units of mas

The brightness temperature in the comoving frame of the source is then simply:

$$\begin{aligned} T_b^{co} &= T_b^{obs}\,(1+z)^{3-\alpha} \ \text{ where } \alpha \text{ is the spectral index viz., } S_\nu \propto \nu^\alpha \\ &= T_b^{obs}\,(1+z)^{0.5} \ \text{ for the optically thick case, since } \alpha = \tfrac{5}{2} \end{aligned} \tag{2.12}$$

For calculating the values of quantities like brightness temperature in the observer's frame, i.e., their beamed values, the following Lorentz invariants [Rybicki & Lightman, 1979] are useful:

$$
\begin{aligned}
\text{Specific Intensity } (I_\nu): \ \frac{I_\nu}{\nu^3} &= \text{Lorentz Invariant} \\
\text{Flux Density } (S_\nu): \ \frac{S_\nu}{\nu^3} &= \text{Lorentz Invariant} \\
\text{Optical Depth } (\tau) = \frac{l}{\sin\theta}\,\alpha_\nu &= \text{Lorentz Invariant}\ , \\
\text{where } \frac{l}{\sin\theta} - \text{ thickness of medium along the propagation direction} & \\
\text{and } \alpha_\nu - \text{Absorption coefficient} \Rightarrow \nu\alpha_\nu &= \text{Lorentz Invariant} \\
\text{Emission coefficient } (j_\nu) = \alpha_\nu S_\nu \Rightarrow \frac{j_\nu}{\nu^2} &= \text{Lorentz Invariant}
\end{aligned}
\tag{2.13}
$$

Similarly, the rules for transforming the frequency of radiation are:

$$
\begin{aligned}
\nu_{\rm co} &= \delta\,\nu_{\rm em} \\
\Rightarrow \nu &= \frac{\delta}{1+z}\,\nu_{\rm em}
\end{aligned}
\tag{2.14}
$$

where $\nu_{\rm em}$, ν, $\nu_{\rm co}$ are the emission frequency, observed frequency & frequency in the comoving frame respectively, while δ, z are the Doppler factor and cosmological redshift.

2.3.1 Inverse Compton Catastrophe

The ratio of IC luminosity to synchrotron luminosity (equation 2.9) can be written in terms of the brightness temperature [Kellermann & Pauliny-Toth, 1969]

$$
\frac{L_{\rm IC}}{L_{\rm sync}} \sim \left(\frac{T_b}{10^{12}\ \rm K}\right)^5 \left[1 + \left(\frac{T_b}{10^{12}\ \rm K}\right)^5\right] \left(\frac{\nu_m}{100\ \rm GHz}\right) \tag{2.15}
$$

where ν_m is the peak/turnover frequency. As can be seen from the above formula, below 10^{12} K, synchrotron emission dominates. However, above this threshold temperature, Compton losses start to dominate and second order inverse Compton scattering

(IC of already upscattered photons) becomes important $\left[(L_{\rm IC}/L_{\rm sync}) \sim (T_b/10^{12})^{10}\right]$. This leads to rapid cooling of the relativistic particles and their T_b quickly drops below 10^{12} K. This phenomenon is called 'Inverse Compton catastrophe'. Hence, the T_b of any AGN cannot remain higher than 10^{12} K for significant periods of time [Kellermann & Pauliny-Toth, 1969]. Non-standard particle spectra have been proposed to raise the threshold intrinsic brightness temperature for the onset of catastrophic cooling beyond the limit of 10^{12} K [e.g., threshold $T_b \sim 10^{14}$ K, Tsang & Kirk, 2007]. In summary, T_b peaks at $\nu \approx \nu_m$, with

$$\begin{aligned} T_b &\propto \nu^{1/2} \qquad && \nu < \nu_m \\ T_b &\propto \nu^{-(p+3)/2} \qquad && \nu > \nu_m \end{aligned} \tag{2.16}$$

2.3.2 Equipartition Brightness Temperature

For a moving source, the observed flux density (S_{ob}) can be related to the comoving flux density (S) via the following expressions [Blandford & Königl, 1979]

$$\text{For a narrow cylindrical/continuous jet: } S_{ob}(\nu) = \left(\frac{\delta}{1+z}\right)^{2-\alpha} S\left(\frac{\nu}{\delta/(1+z)}\right)$$

$$\text{For a blobby jet: } S_{ob}(\nu) = \left(\frac{\delta}{1+z}\right)^{3-\alpha} S\left(\frac{\nu}{\delta/(1+z)}\right) \tag{2.17}$$

where α is as usual the spectral index. So, for a source at $z = 1$ and $\alpha = -0.5$, even for a modest Doppler factor of 5, the observed intensity would be boosted by a factor of 10. Another consequence of relativistic beaming would be the contrast in fluxes of the approaching jet vs. the receding jet, given by:

$$\frac{S_j}{S_{cj}} = \left(\frac{1+\beta\cos\theta}{1-\beta\cos\theta}\right)^{2-\alpha} \tag{2.18}$$

Moreover, the variability timescale of any flux changes would appear shortened by a factor of $[\delta/(1+z)]$. If a jet has components moving at different speeds, a distant observer would predominantly see the components moving with $\beta \sim \cos\theta$ (since δ is maximized).

Equipartition assumes that the particle energy density and the magnetic field energy density are equal i.e.,

$$\eta = \frac{U_p}{U_B} = \frac{8\pi}{B^2}\,\gamma\mu_m c^2 \sim 1 \tag{2.19}$$

where B, μ_m & γ are the magnetic field, mean mass per particle and Lorentz factor respectively. For a power-law distribution of particles with spectral index $(p) = 2.5$ $(\Rightarrow\ \alpha = 0.75)$, the intrinsic brightness temperature $\left(T_b^{\rm int}\right)$ is given by:

$$T_b^{\rm int} = \eta^{2/17}\,T_b^{\rm eq} \tag{2.20}$$

where $T_b^{\rm eq}$ is the equipartition brightness temperature, given by $T_b^{\rm eq} \approx T_{eq}$ [Readhead, 1994]. As can be seen from the above equation, for $T_b^{\rm int} \sim 10^{12}$ K, $\quad \eta \sim 20^{8.5} \sim 10^{11}$ i.e., the particle distribution is very far from equipartition, which requires fine-tuning and hence is physically unexpected. Hence, AGN cores are typically assumed to be near equipartition, meaning their intrinsic brightness temperature is known and the observed brightness temperature is related to this value via the doppler factor.

$$T_b^{\rm obs} = \delta_{\rm eq}\,T_b^{\rm eq} \tag{2.21}$$

This gives another independent way (besides spectral modelling, variability modelling, jet vs. counter-jet flux ratios + apparent jet speed information, etc.) of estimating the Doppler factor.

3. AGN VARIABILITY

Variability over time scales ranging from a few minutes to a few years and across the entire electromagnetic spectrum has been observed in AGN, with the fastest variations ($\sim 10^2$ s) being detected in the X–ray and $\gamma-$ray regimes. Variability studies yield crucial information regarding source structure beyond the imaging resolutions currently achievable. From causality arguments, the size of the emitting region (R) must be:

$$R \leq 2\,\gamma^2 c \Delta t \tag{3.1}$$

where Δt is the variability time scale in the source frame and γ is the Lorentz factor [Rybicki & Lightman, 1979]. Since different emission mechanisms (and hence different characteristic spectral & temporal regimes) dominate in different parts of the AGN (see Fig. 1.11), a multi-wavelength study of the correlations between variability at various wavelengths would help understand the physical processes involved. For instance, time delays between the optical continuum and optical emission-line variations are used to deduce the size of the line emitting region and hence the distance between the central engine and the BLR. This *Reverberation mapping* technique is frequently used in estimating the mass of the SMBH [Peterson et al., 2004].

There are different ways of defining the observed variability time-scale. However, Wagner et al. [1996] cite that the most commonly used one is the logarithmic variability time-scale defined as:

$$t_{\rm var} = \left|\frac{d\ln S}{dt}\right|^{-1} = \frac{\langle S\rangle}{\Delta S}\,\Delta t \tag{3.2}$$

$$\text{And } t_{\rm co} = \frac{t_{\rm var}}{1+z}$$

where $\langle S \rangle$ and ΔS are the mean flux density & its standard deviation respectively, and $t_{\rm co}$ is the variability time in the source comoving frame. Using the aforementioned causality arguments, the source size can then be written as:

$$\theta = 3.56 \times 10^{-4} \mathrm{Gpc}^{-1} t_{\rm var} \left(\frac{1+z}{D_L} \right) \mathrm{mas} \tag{3.3}$$

where D_L is the luminosity distance. Combining Eqns. 2.12 & 3.3, the apparent/comoving brightness temperature can be estimated, which may then be used to calculate the variability Doppler factor ($\delta_{\rm var}$) from:

$$\delta^3_{\rm var} = \frac{T^{co}_b}{T^{int}_b} \tag{3.4}$$

where T^{int}_b is the intrinsic or unbeamed brightness temperature [Lähteenmäki et al., 1999, Hovatta et al., 2009]. Typical choices for T^{int}_b are either the equipartition value ($\sim 10^{11}$ K, see section 2.3.2) or Inverse Compton threshold value ($\sim 10^{12}$ K, see section 2.3.1).

The terminology used to characterize variability at radio frequencies is as follows [Wagner & Witzel, 1995]:

- **Low frequency variability (LFV):** Variability at $\nu < 1$ GHz with typical time-scales of months to years and amplitudes ranging from $3 - 30\%$.
- **Flickering:** A stochastic variation on time-scales of days to weeks and amplitudes of a few percent.
- **Extreme Scattering Events (ESE):** High amplitude (up to 100%) radio variability and a characteristic frequency dependence; Typical light curve consists of a minimum bracketed by maxima on either side [e.g., Fiedler et al., 1994, Senkbeil et al., 2008].
- **Intra–day Variability (IDV):** Variability on an 'observed' time-scales typically ≤ 50 hrs., with amplitudes of a few 10s of percent at GHz frequencies, but could be as high as $> 100\%$ in extreme cases (see section 3.1).

3.1 Intra–day Variability

Flux density variations at centimeter wavelengths on time scales of hours to days – in both total intensity and polarization – known as IDV, is often observed in blazars. Type II IDV sources have variability timescales of a few min./hrs., while the type I sources have time scales $>$ 2 days [Heeschen et al., 1987]. IDV surveys, like the recently concluded *MASIV* survey, have shown that $\sim$ 50% of compact FSRQs are IDV sources, while IDV is seldom seen in steep spectrum sources or sources with an extended jet structure (jet dominated sources) [Lovell et al., 2003b, 2008]. Changes in the characteristic variability time-scales, viz., slowing down or sudden appearance of a more pronounced variability state or even a complete cessation of IDV, are commonly observed. In fact, a majority of IDV sources are only intermittent/episodic, i.e., they show IDV only in a few epochs [Lovell et al., 2003a]. IDV is usually more prominent at lower frequencies i.e., 2 GHz – 5 GHz. However, IDV has been detected even in the mm regime [Kraus et al., 2003]. Polarized flux density variability amplitudes are usually higher than those in total flux density, as expected on theoretical grounds [Medvedev, 2000]. Rapid swings in the polarization angle, accompanied by very little variability in both total as-well-as polarized flux density amplitudes have also been reported [e.g., Gabuzda et al., 2000a].

The physical origin of such IDV remains unclear. Correlations and/or anti-correlations between lightcurves in various frequency bands have been observed in some sources [Wagner & Witzel, 1995], which bolsters the speculation that some intrinsic phenomena (see section 3.1.1) are responsible for IDV in these sources. However, in a majority of cases the observed variability time-scales (eqn. 3.2) imply brightness temperatures (eqn. 3.3, 2.12) $\sim 10^{20}$ K, far in excess of the theoretical Compton limit of 10^{12} K for incoherent synchrotron sources [Kellermann & Pauliny-Toth, 1969], which is a major challenge for source intrinsic IDV models. Doppler boosting can alleviate this problem, but the inferred $\delta_{\rm var}$ (eqn. 3.4) $\geq 10^2$. Low radiative efficiency of synchrotron mechanisms would then imply very large values for the particle and magnetic energies of the jet, thus constraining the maximum bulk Lorentz factors attainable [Begelman et al., 1994]. Moreover, only $\Gamma \sim 10 - 25$ have been measured by the various VLBI monitoring surveys [e.g., Cohen et al., 2007] prior to the *MOJAVE* program. Several source-extrinsic IDV mechanisms have also been proposed (see section 3.1.2). Their chief drawback however, is the difficulty in explaining why $\sim 60\%$ of IDV sources exhibit only intermittent IDV [Lovell et al., 2007, 2008].

3.1.1 Intrinsic Mechanisms

Variability over timescales ranging from a few minutes to a few years is ubiquitous among AGN. For instance in the BL Lac object PKS 2155−304, rapid variability over time scales as short as 5 minutes to a few hours have been reported, in TeV $\gamma-$rays [Aharonian et al., 2007], in X-rays [Zhang et al., 1999] and at optical wavelengths [Paltani et al., 1997]. In most of such cases, intrinsic models have proved successful. Hence, looking for an intrinsic explanation for IDV at cm wavelengths is logical. Correlation between the optical and radio lightcurves in the BL Lac object 0716+714 ($z = 0.31$, $\beta_{\rm app} \sim 10.1$),[1] is often cited as a strong evidence in favor of intrinsic IDV mechanisms [Wagner et al., 1996]. Biggs et al. [2001] have reported indubitable evidence for intrinsic IDV in the gravitationally lensed system 0218+357. Also, Tingay et al. [2001] have reported a correlation between the IDV type of the source and the measured brightness temperature, with type I sources having lower T_b values than type II sources. Lovell et al. [2008] have reported a similar trend after analysis of their extensive sample from the *MASIV* survey. Though all these observations strongly favor an intrinsic explanation for IDV, the inexplicably large $T_b/\delta_{\rm var}$ problem persists. Coherent radiation mechanisms, though free of the IC catastrophe problem — the theoretical limit of 10^{12} K is applicable for the incoherent synchrotron mechanism

[1]See: `http://www.physics.purdue.edu/MOJAVE/sourcepages/0716+714.shtml`

only; See section 2.3.1 — have a hard time accounting for the broadband nature of IDV phenomena, and hence are seldom favored.

Though some intrinsic variability models argue against the occurrence of the IC catastrophe by proposing alternating radiation processes, thus obviating the high T_b problem, most models make use of special geometrical considerations or modified shock-in-jet models for the emitting source to produce the required high Γ values. Relativistic shock models (Fig. 1.11) have successfully explained the multi-frequency flares and the correlations/anti-correlations seen among them, notably the simultaneous swings in the radio and optical polarization angle [e.g., Marscher et al., 2008].

The observed variability time-scales are then modelled by modifications to these generic shock models. For instance, propagation of a shock front, illuminating the inhomogeneous structure of the underlying jet could be thought to determine the temporal scale. Thus, the size calculated from causality arguments does not correspond to the physical size of the AGN, but instead is a function of the jet cross-section and shock thickness [e.g., Qian et al., 1991, 2002] and hence the size restrictions imposed by high T_b values do not arise. A variation of this idea is the model proposed by Spada et al. [1999]. In their scheme, a slab of e^- traversing along the steady jet radiates only upon crossing a conical shock. The radiation from successive slices of this slab will be temporally separated and their superposition is responsible for the variability in the light curve, with observed $T_b \leq 3 \times 10^{17}$ K being possible. Observation of a correlation between superluminal component ejection and IDV (see section 6.7) certainly favors this scenario.

Models involving jet components traversing helical trajectories, giving rise to varying beaming factors (*light-house effect*), with the presence of multiple such knots giving rise to rapid flux variability, have also been proposed [Camenzind & Krockenberger, 1992]. Indeed, the presence of such helical trajectories has been observed in some sources [e.g., Kellermann et al., 2004]. Another variation of this idea is the *swinging jet* model proposed by Gopal-Krishna & Wiita [1992], which was able to quanititavely explain the various correlations between total flux and polarized flux variability seen in several sources.

3.1.2 Extrinsic Mechanisms

Source extrinsic models, as the name implies, aim to overcome the problem of high $T_b/\delta_{\rm var}$ by attributing IDV to propagation effects. Though some unconventional theories, for example involving gravitational microlensing [Gopal-Krishna & Subramanian, 1991], have been proposed, they generally have not been supported. Scintillation effects seen in radio light curves of pulsars are a natural choice, with refractive interstellar scintillation [Rickett et al., 1995] being at the forefront. These models have had considerable success in explaing the IDV of several sources. Hence, scintillation models along with their implications and success are discussed in the ensuing section.

3.1.3 Inter-Stellar Scintillation

In the optical, point sources (as seen by the eye, like stars) twinkle – while planets, due to their large angular size, do not – due to atmospheric turbulence. Similarly, small scale inhomogeneities in the ionized component of the local interstellar medium (ISM) can lead to scintillation at radio frequencies. Several effects of this Inter Stellar Scintillation (ISS), like angular broadening, variability in intensity, broadening of pulse profiles, etc., have been observed in pulsars. Low frequency variability (LFV) in extragalactic sources has also been confirmed to be due to ISS [e.g., Spangler et al., 1993]. ISS is also expected to modulate the radio flux from compact extragalactic sources like AGN and gamma ray bursts (GRBs). Prior to the discussion on detection/confirmation of ISS in IDV sources, a consideration of the various scattering regimes involved is crucial.

Primarily based on dispersion measure observations of pulsars, a simple ISM model has been developed by Taylor & Cordes [1993]. This model can be used to estimate ISS effects for any line of sight. Since, there are no more free parameters to be considered in this model, unique predictions for the scattering of extragalactic sources are possible.

When the wavefront from a distant source is perturbed by fluctuations in the refractive index of the intervening medium, spatial variations in the received flux (the 'scintillation pattern') is seen in the observer's plane. The transverse relative velocity of the observer–source line of sight with respect to the scattering medium leads to temporal flux variations [Narayan, 1992]. Two basic length scales play a major role in describing the various scattering regimes. Firstly, the Fresnel scale, given by

$$\begin{aligned} r_F = \sqrt{\frac{\lambda D}{2\pi}} \;\Rightarrow\; \theta_F = \frac{r_F}{D} = \frac{8}{\sqrt{D\nu}}\ \mu\text{as} \\ t_F = \frac{r_F}{v} = 1.2 \ \times \ 10^6 \ v^{-1} \sqrt{\frac{D}{\nu}} \quad , \end{aligned} \tag{3.5}$$

where D is the distance between the scattering screen and the observer, λ is the wavelength, and $\theta_F,\ v$ denote the angular size of the Fresnel scale and the transverse speed (in km s^{-1}) respectively [typically $v = 50;$ Walker, 1998]. The other length scale is the 'diffractive' scale $r_{\rm diff}$, defined as the transverse seperation over which the phase fluctuation is coherent to within a specified limit (1 rad in radio astronomy and $\sqrt{6.88}$ rad in optical astronomy, corresponding to the 'Fried length'). Since all astrophysical scintillation phenomena involve ionized media, cold plasma, the dispersion relation can be combined with the Kolmogorov turbulence spectrum (power-law spectrum with index 11/3) to yield:

$$r_{\rm diff} \propto \left(\lambda^2 D\right)^{-\frac{3}{5}} \quad \Rightarrow \quad \frac{r_{\rm diff}}{r_F} \propto \nu^{\frac{17}{10}}\, D^{-\frac{11}{10}} \quad . \tag{3.6}$$

Thus, the strength of scattering increases with wavelength as well as distance [Narayan, 1992]. The aforementioned ratio can then be used to distinguish between the various sacttering regimes. Since the spectrum of inhomogeneities is a Kolmogorov distribution, with the normalization being determined by the structure constant C_n, an integrated measure can be used to model the physics involved [Gabányi, 2006], namely

$$\text{Scattering Measure (SM)} = \int_0^D C_n^2 \, dx \quad . \tag{3.7}$$

There are several ways to characterize scattering. The scattering measure can then be used to calculate a parameter called the 'scattering strength' (ξ) given by

$$\xi = 2.6 \ \times \ 10^3 \ \text{SM}^{0.6} \ D^{0.5} \ \nu^{-1.7} \quad , \tag{3.8}$$

where ν is in GHz, D is in kpc and SM is in kpc m$^{-20/3}$ [Walker, 1998]. The physical interpretation of this parameter is that when $\xi = 1$, scattering introduces substantial phase fluctuations over half a radian (i.e., across the Fresnel zone). Hence, $\xi = 1$ marks the transition between the 'weak' ($\xi \ll 1$) and 'strong' ($\xi \gg 1$) scattering regimes, with the frequency dependence of this scattering strength being:

$$\xi = \left(\frac{\nu}{\nu_0}\right)^{\frac{17}{10}} \tag{3.9}$$

where ν_0 is the transition frequency which is usually between $5-15$ GHz (see Fig. 3.1). As can be seen from Fig. 3.1, sources close to the galactic plane should be able to scintillate up to higher frequencies. However, the angular size of the first Fresnel zone at the transition frequency (θ_{F0}) increases with galactic latitude (see Fig. 3.2). Thus, even sources/components with larger sizes located near the galactic poles can scintillate. The scintillation time-scale at the transition frequency may then be written as (combining Eqns. 3.5, 3.8):

$$t_{F0} = 2.4 \ \times \ 10^3 \left(\frac{D^2}{\text{SM}}\right)^{3/17} \left(\frac{50\,\text{km s}^{-1}}{v}\right) \text{s} \ \sim 1 - 3\,\text{h} \quad . \tag{3.10}$$

Away from the galactic plane, $D \propto$ SM and hence $t_{F0} \sim$ constant, i.e., independent of the actual line of sight [Walker, 1998].

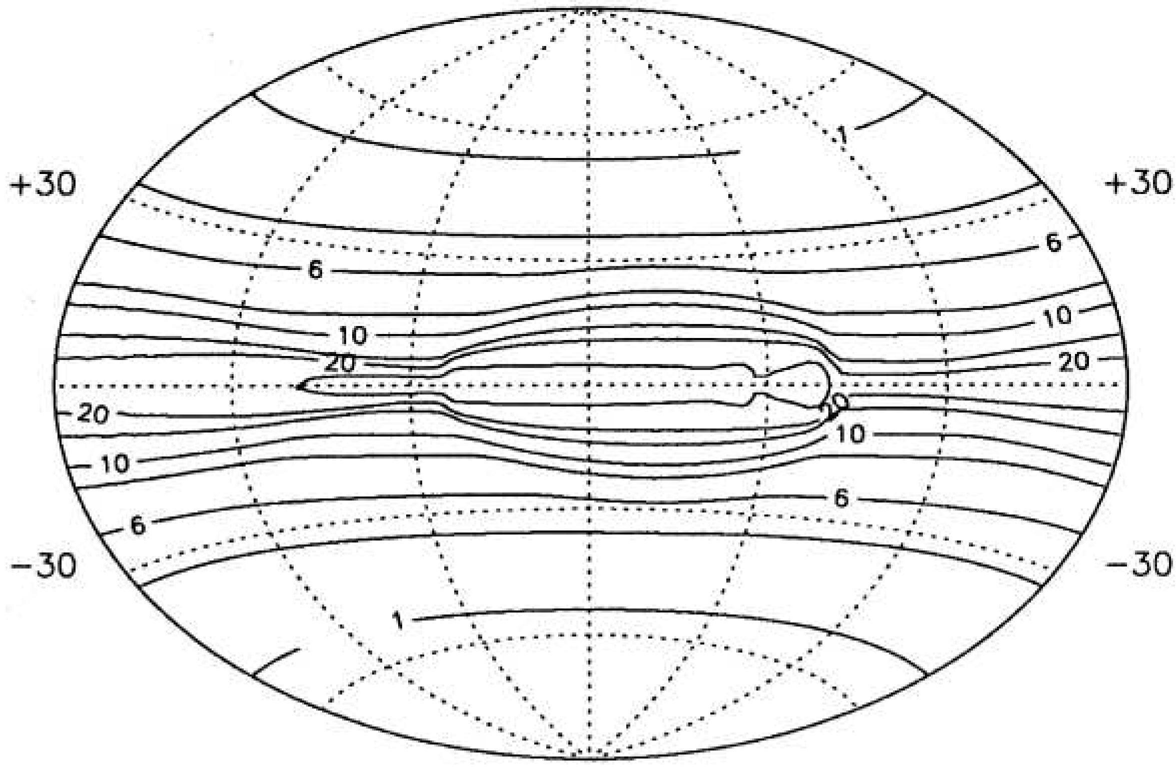

Figure 3.1. Transition frequency (ν_0) – defined as the frequency at which the scattering strength is unity – plotted in galactic coordinates [Credit: Walker, 1998]. The dashed lines mark intervals of 30°/60° in latitude/longitude, while the solid lines show constant ν_0 contours, with levels 4, 5, 6, 8, 10, 15, 20 & 40 GHz. As is evident from the plot, for most of the sky, ν_0 falls in the range $5 - 15$ GHz.

Weak scattering: This is the regime where $r_{\text{diff}} \gg r_F$, meaning the phase fluctuations within the first Fresnel zone remain coherent. Therefore,

$$\text{Modulation Index } (m) = \frac{\text{RMS}}{\text{Mean}} \approx \left(\frac{r_F}{r_{\text{diff}}}\right)^{\frac{5}{6}} < 1 \quad ,$$

and hence, the name 'Weak scattering'. Weak scattering is a wide bandwidth phenomenon. Expressions for the remaining parameters (for a point source) are:

$$m_{\text{point source}} = \xi^{5/6} = \left(\frac{\nu_0}{\nu}\right)^{17/12} \quad ,$$
$$\theta_F = \theta_{F0}\sqrt{\frac{\nu_0}{\nu}} \quad \& \quad t_F \sim 2\sqrt{\frac{\nu_0}{\nu}} \quad . \tag{3.11}$$

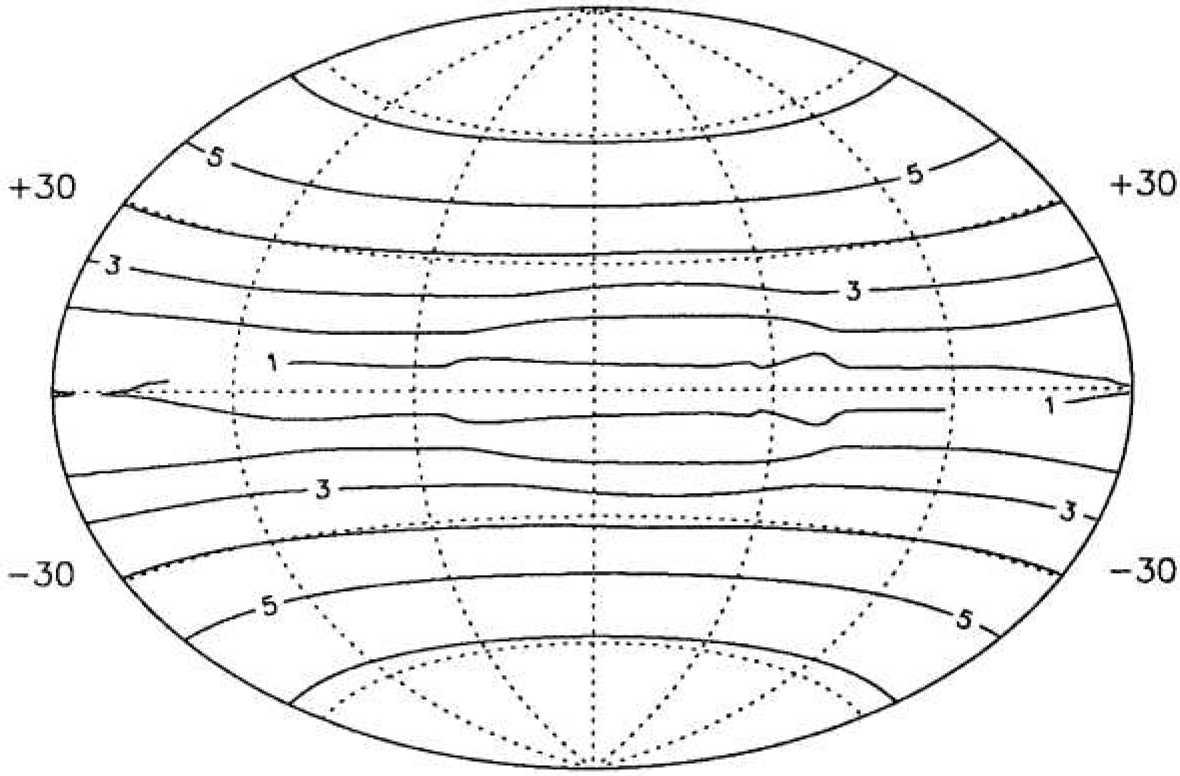

Figure 3.2. Plot of the angular size of the first Fresnel zone (θ_{F0}) at the transition frequency (ν_0) plotted in galactic coordinates, with 1 μas contours [Credit: Walker, 1998]. Sources/components smaller than the appropriate θ_{F0} would be able to scintillate.

Since radiation from extragalactic sources emanates from a logarithmically broad range of length-scales (see Fig. 1.11), they cannot be considered to be point sources. Hence, their modulation indices are expected to be smaller and their variability timescales longer. Accordingly, for a source of size θ_s ($> \theta_F$):

$$m = m_{\text{point source}} \left(\frac{\theta_s}{\theta_F}\right)^{-7/6} \quad \& \quad t_s = t_F \left(\frac{\theta_s}{\theta_F}\right) \tag{3.12}$$

Strong scattering: This regime is characterized by $r_{\text{diff}} \ll r_F$ and hence r_F becomes irrelevant. In such a regime, two kinds of variability are expected:

1. **Diffractive scintillation** involving fast, narrow band variations: These are a result of intereference among the multiple paths from source to observer.

The scattering screen can be considered to be a sum of a large number of coherent patches (of size $r_{\rm diff}$) and hence the image of a point source is 'scatter broadened' to size $\theta_{\rm scat} \sim \lambda/r_{\rm diff}$. Since the interfering rays at any point need to be coherent, diffractive scintillation is quenched when the source size or the observation bandwidth is too large.

Diffractive scintillation leads to a Rayleigh distribution of flux, with the mean and fluctuations being equal [Goodman, 1997] i.e.,

$$\langle S^2 \rangle = 2\langle S \rangle^2 \quad \Rightarrow m_{\text{point source}} = \frac{\text{RMS}}{\text{Mean}} = \frac{\langle S^2 \rangle}{\langle S \rangle^2} - 1 = 1 \tag{3.13}$$

Thus, the characteristic of diffractive scintillation is that a point source should exhibit large modulations of the order of 100%. But this manifests only over a bandwidth

$$\frac{\Delta\nu}{\nu} = \xi^{-2} = \left(\frac{\nu}{\nu_0}\right)^{17/5} \quad . \tag{3.14}$$

For a source of size θ_s,

$$m = \left(\frac{\theta_d}{\theta_s}\right), \qquad \text{where } \theta_d = \theta_F\ \xi^{-1} = \theta_{F0}\left(\frac{\nu}{\nu_0}\right)^{6/5} \quad ,$$

$$t_d = \left(\frac{\theta_s}{\theta_d}\right)\ t_F\ \xi^{-1} \sim 2\left(\frac{\theta_s}{\theta_d}\right)\ \left(\frac{\nu}{\nu_0}\right)^{6/5}\ \text{h} \quad . \tag{3.15}$$

Diffractive scintillation is not expected to play a prominent role in IDV, due to the very small scintillation source sizes required and the fact that the observed modulation index is usually < 1 supports this. However, in J1819+3845, the most rapid IDV quasar known, it is thought that diffractive scintillation plays the key role [Dennett-Thorpe & de Bruyn, 2002].

2. **Refractive InterStellar Scintillation (RISS)** involving slow, broad band variability: This is due to refraction by inhomogeneities (of the size of the scatter broadened source) in the ISM and hence the name. In this regime, the dominant length scale is:

$$r_{\rm ref} = \frac{r_F^2}{r_{\rm diff}} \quad . \tag{3.16}$$

Expressions for the modulation index and other quantities, for a source of size (θ_s) are as follows [Narayan, 1992, Goodman, 1997, Walker, 1998]:

$$m_{\text{point source}} = \xi^{-1/3} = \left(\frac{\nu}{\nu_0}\right)^{17/30} \quad ,$$

$$\theta_r = \theta_F \; \xi^{-1} = \theta_{F0} \left(\frac{\nu_0}{\nu}\right)^{11/5} \quad ,$$

$$m = m_{\text{point source}} \left(\frac{\theta_r}{\theta_s}^{7/6}\right) \quad \text{and} \quad t_r \sim 2 \left(\frac{\theta_s}{\theta_r}\right) \left(\frac{\nu}{\nu_0}\right)^{11/5} \text{h} \quad . \tag{3.17}$$

The aforementioned formulae may be used to judge if the IDV seen at a given frequency could indeed be of ISS origin.

3.1.4 Annual Modulation

As can be seen from the formulae for scintillation time-scales from the previous section, the transverse velocity of the screen with respect to the line of sight to the source plays a key role in determining the IDV time-scale. Hence, a natural consequence would be a seasonal variation in the same during the course of an year due to the Earth's annual motion around the Sun. This phenomenon called 'Annual Modualtion' is illustrated in Fig. 3.3. Indeed, such a pattern (Fig. 3.5) has been observed in 5 IDV sources to date, namely J1128+5925 [Gabányi et al., 2007], J1819+3845 [Dennett-Thorpe & de Bruyn, 2002], 1257−326 [Bignall et al., 2003], 1519−273 [Jauncey et al., 2003] and 1622−253 [Carter, et al., 2009]. Claims have also been made for the presence of the same in a couple of other sources too [e.g., Savolainen & Kovalev, 2008, see section. 7.3]. Apart from being a tell-tale sign of ISS origin for IDV, Annual modulation could also be used to probe the properties of the ISM [e.g., Rickett et al., 1995]. For instance, if the scattering screen is assumed to be stationary with respect to its local inertial reference frame, a significant slowing down of IDV during the latter half of the year (around September) is expected and is indeed observed in a few sources (Fig. 3.4). However, the recently concluded *MASIV* survey results indicate no evidence for such slowing down, which leads to the inefernce that the scattering clouds have significant transverse velocities in their local inertial reference frames [Lovell et al., 2003a, 2008].

The other prominent signature of ISS is the delay in variability pattern arrival times at two widely-spaced telescopes. This is a tricky experiment, since the sky position of the source must be such that there indeed are two telescopes/arrays which can see it simultaneously, and the variability must be rapid enough for the delay to be detectable. Such measurements have been made in a couple of sources, notably 0405−085, where a delay of $\sim$ 140s has been measured between the ATCA (Australia) and the VLA [Bignall et al., 2003].

Yet another signature of ISS is a frequency-dependent delay in the light curve variability pattern, which has been seen in a few sources [e.g., Bignall et al., 2003, ; see Fig. 3.4]. Also, in case of ISS, a galactic latitude dependence of IDV sources is to be expected, since the probability of the line of sight passing through a scattering screen is higher near the galactic plane than near the poles. However, only weak dependence of this nature has been observed [Lovell et al., 2007, Lazio et al., 2008].

3.1.5 Summary

In summary, the underlying mechanism for IDV is still open for debate, with several models involving both source-intrinsic as well as source-extrinsic mechanisms, in vogue. Variations of the shock-in-jet model lead the source-intrinsic class, while scintillation models dominate the source-extrinsic scenario. All in all, the current understanding is that observed IDV is due to superposition of some intrinsic mechanism(s), and refractive scintillation in the ISM (RISS), to varying degrees. Confirmation of ISS as the prominent IDV mechanism would imply the presence of μas sized components [Goodman, 1997] – much smaller than currently possible imaging resolution – thus allowing for the indirect study of source structure at very high resolutions. If IDV is primarily source intrinsic, a comparitive study of IDV vs. non-IDV sources would help understand the underlying acceleration processes. Either way, study of IDV sources could provide novel insights into AGN jet physics.

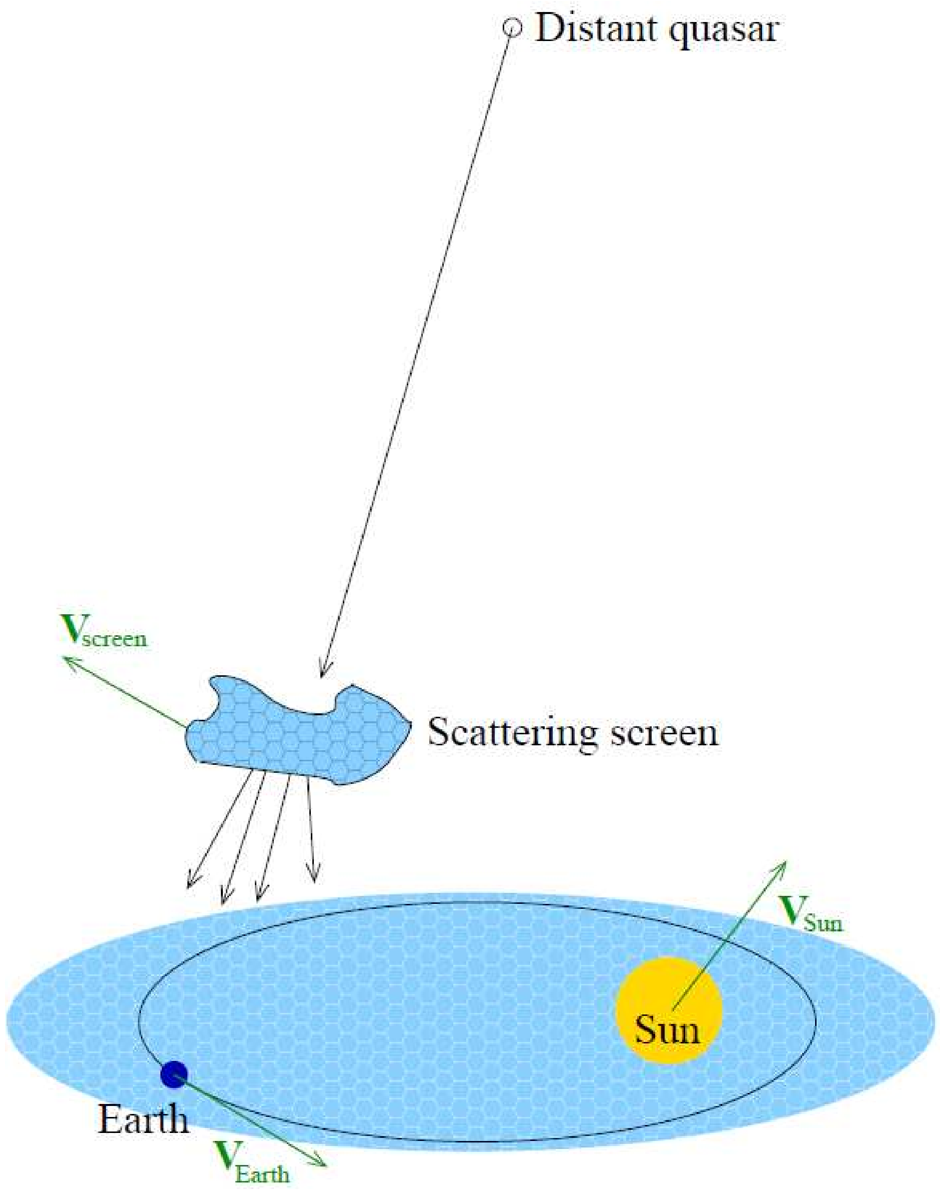

Figure 3.3. A cartoon illustrating the 'Annual Modulation' phenomenon [Credit: Gabányi, 2006]. The ISM constituting the scattering screen, creates a scintillation pattern via refractive scattering i.e., focusing and defocusing of the distant quasar light. As the Earth moves through the projection of this spatial pattern (shown in light blue), flux density variations are observed. The observed variability time scales depend on the relative velocity between the screen, observer and hence the vector sum of the three velocity vectors (shown in green).

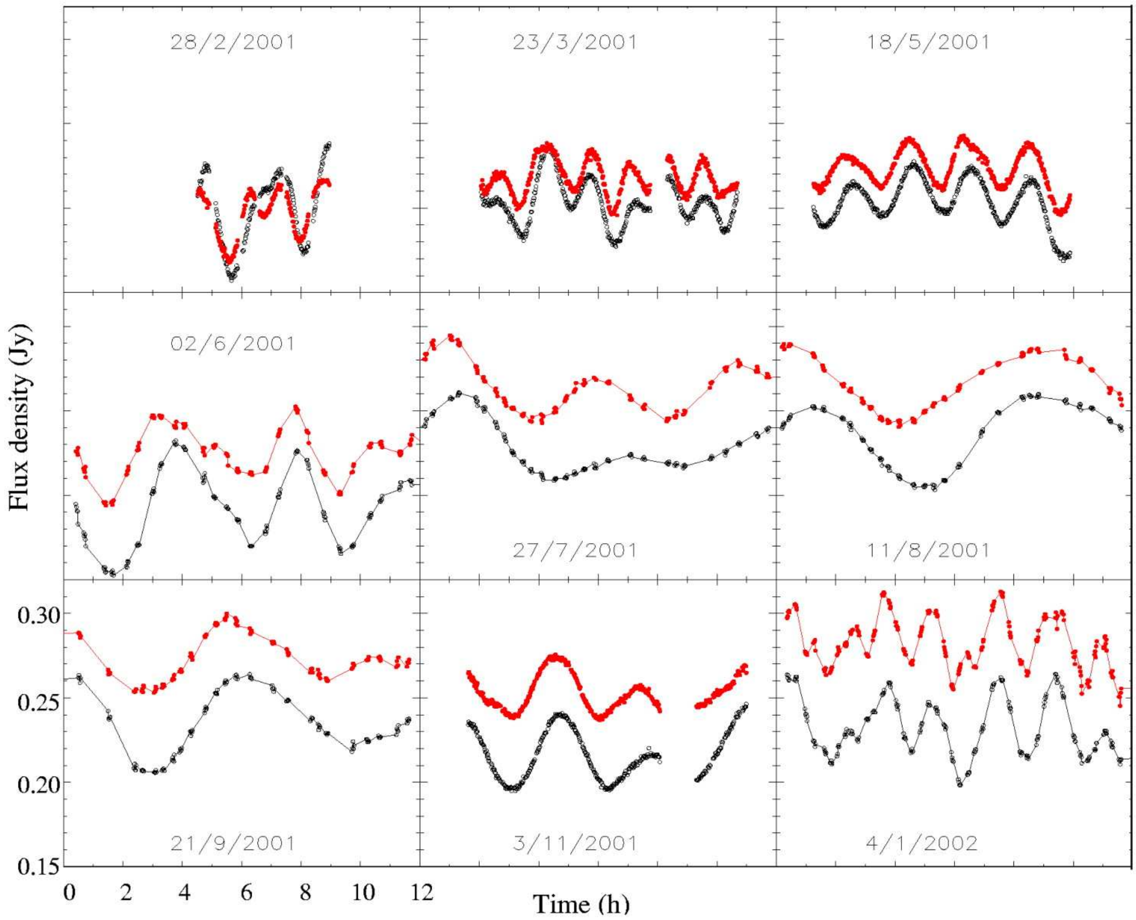

Figure 3.4. Simultaneous multi-epoch 4.8 GHz (black) and 8.6 GHz (red) light curves for the rapid IDV source 1257−326 [Bignall et al., 2003]. *Annual Modulation* is clearly evident.

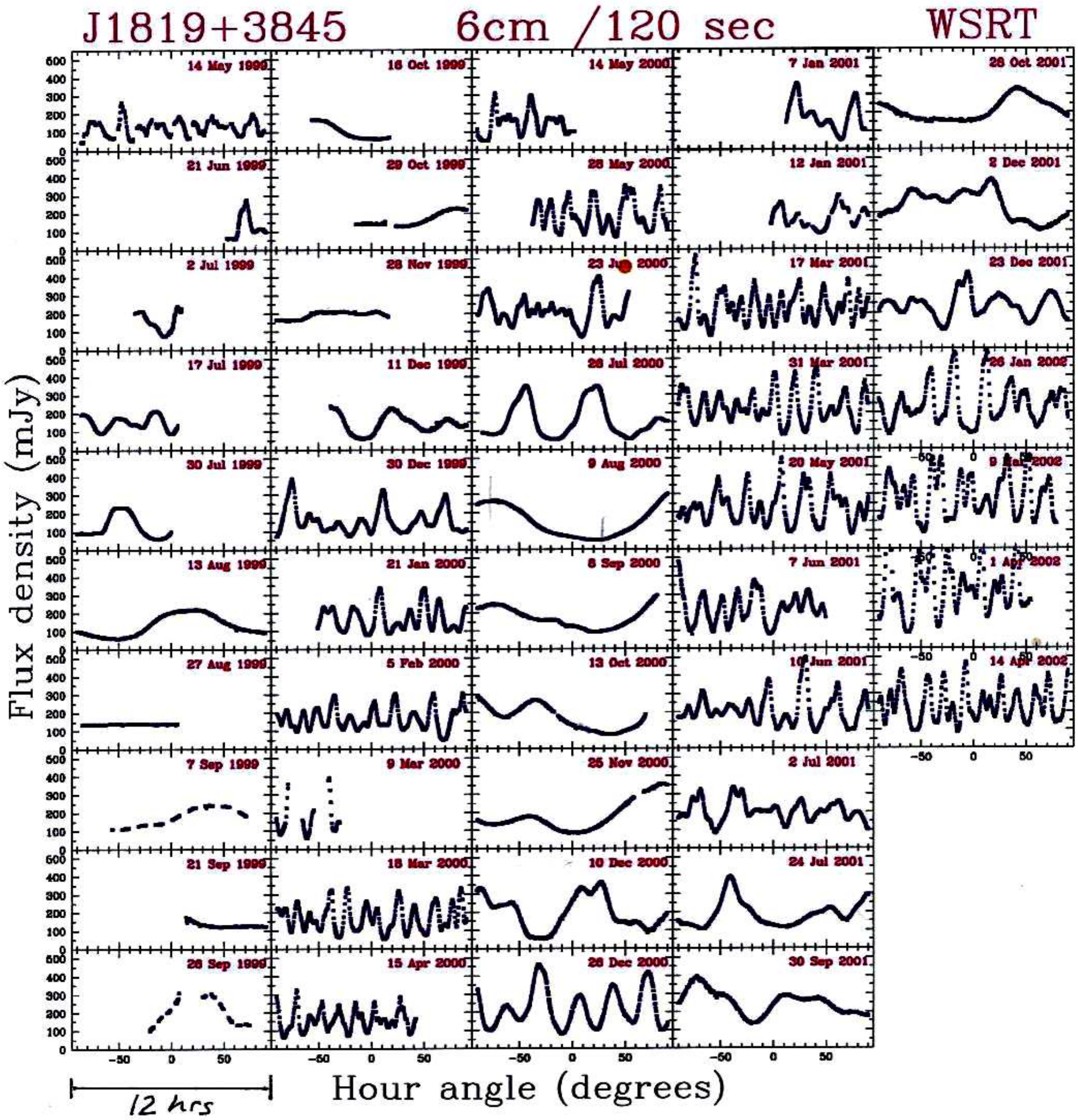

Figure 3.5. 6 cm light curves for the rapid IDV quasar J1819+3845 [Dennett-Thorpe & de Bruyn, 2002] obtained with Westerbork Radio Synthesis Telescope (WSRT). The light curves are from observations spanning the epochs May 1999 to April 2002. Seasonal changes in variability timescale are evident, with the fastest variability around February – March and the slowest variability around August – September. Such an *Annual Modulation* in IDV timescales is a signature of InterStellar Scinitillation (ISS) and arises due to change in the relative velocity of the scattering ISM cloud with respect to the observer on Earth (see Fig. 3.3).

4. *MOJAVE*

The work in this thesis focuses on radio loud AGN, particularly blazars. Rapid variability and frequent ejection of components/blobs are some of the hallmarks of this class of AGN. Apparent speeds of these components are often measured to be greater than the speed of light. This phenomenon known as 'superluminal motion' is a consequence of bulk relativistic motion of the ejected components, and is briefly discussed in § 4.1. The *MOJAVE*[1] sample selection criteria and some salient results from this campaign, are discussed in § 4.2 and 4.3 respectively.

4.1 Superluminal Motion and Beaming

Superluminal motion is an illusion caused by the bulk relativistic motion of luminous material at a very small viewing angle (close to 0°). It was first proposed by Rees [1966] and detected in the quasar 3C 279 (1253−055) by Whitney et al. [1971] and Cohen et al. [1971] using long baseline interferometric techniques. Fig. 4.1 shows an illustration of such a system. Consider a jet component ejected at an angle θ to the line of sight, at a speed v. It emits a photon at point A, and at a time interval Δt later, another photon at point B, received by an observer at point O. Since the observer is located very far from the source, OA —— OB. But in the meantime, the component travels a distance $v\Delta t\cos\theta$ towards the observer and hence the second photon has to travel a slightly smaller distance than the first photon to reach the observer. So, the apparent speed as perceived by the observer is:

$$v_{\rm app} = \frac{v\sin\theta}{c - v\cos\theta} \quad \Rightarrow \quad \beta_{\rm app} = \frac{\beta\sin\theta}{1-\beta\cos\theta} \tag{4.1}$$

[1] `http://www.physics.purdue.edu/~mlister/MOJAVE/`

Since, by definition, apparent speed (β_{app}), Doppler factor (δ) and bulk Lorentz factor (Γ) are given by:

$$\beta_{\text{app}} = \frac{\beta\sin\theta}{1-\beta\cos\theta}; \quad \delta = \frac{\sqrt{1-\beta^2}}{1-\beta\cos\theta}; \quad \Gamma = \frac{1}{\sqrt{1-\beta^2}}$$

$$\therefore\ \beta_{\text{app}} = \frac{\sin\theta}{\frac{1}{\sqrt{1-\Gamma^{-2}}} - \cos\theta} \quad \& \quad \delta = \frac{1}{\Gamma - \sqrt{\Gamma^2-1}\,\cos\theta} \tag{4.2}$$

$$\text{Now} \quad \frac{\beta\sin\theta}{\beta_{\text{app}}} = 1-\beta\cos\theta = \frac{\sqrt{1-\beta^2}}{\delta} \quad = x \text{ (say)}$$

$$\Rightarrow\ x = \frac{2}{1+\delta^2+\beta_{\text{app}}^2}; \quad \Gamma = \frac{1}{x\delta} = \frac{2\delta}{1+\delta^2+\beta_{\text{app}}^2}$$

$$\theta = \arctan\left(\frac{x\beta_{\text{app}}}{1-x}\right) = \arctan\left(\frac{2\beta_{\text{app}}}{\beta_{\text{app}}^2+\delta^2-1}\right) \tag{4.3}$$

Thus, a knowledge of β_{app} and δ would allow for the estimation of jet properties like the viewing angle and bulk Lorentz factor.

For a given value of β, the maximum value of β_{app} occurs at $\theta_m = \arccos\beta$ i.e.,

$$\beta_{\text{app}}^{\max} = \cot\theta_m = \sqrt{\Gamma^2-1}$$

$$\text{Hence, for superluminal motion: } \beta_{\text{app}}^{\max} \geq 1 \ \Rightarrow \Gamma \geq \sqrt{2} \tag{4.4}$$

$$\text{Also, the maximum Doppler factor value is } (\delta_m) = \frac{1}{\Gamma - \sqrt{\Gamma^2-1}}$$

$$\therefore \text{ For large } \Gamma \text{ i.e., } \beta \approx 1,\ \delta_m \approx 2\Gamma \tag{4.5}$$

The other important quantity is the observed luminosity L_{obs}, given by:

$$L_{\text{obs}} = \delta^p\, L_{\text{int}} \tag{4.6}$$

where $L_{\rm int}$, δ are the intrinsic luminosity and Doppler factor respectively. The index $p = 2 - |\alpha|$ for a continuous jet, and $p = 3 - |\alpha|$ in the case of a spherical blob. Here α denotes the spectral index. In above expression for luminosity, it has been assumed that the radiation mechanism is synchrotron emission. Since the pc–scale AGN jets are continuous, and the radio spectral index for 'flat' sources is zero (i.e., $|\alpha| \sim 0$ for the *MOJAVE* sample), the above expression for observed luminosity may simply be written as:

$$L_{\rm 2\,cm\,VLBA} = \delta^2\, L_{\rm int} = \frac{L_{\rm int}}{\left[\Gamma - \sqrt{\Gamma^2 - 1}\,\cos\theta\right]^2} \tag{4.7}$$

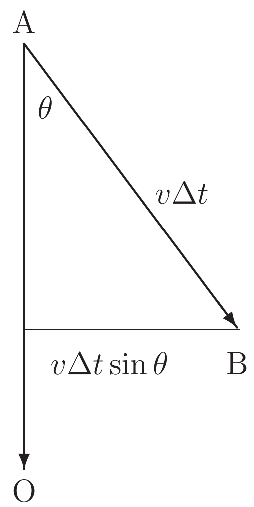

Figure 4.1. Illustration of the phenomenon of apparent 'Superluminal Motion'. The observer located at **O** notices a jet component originating at **A** and moving with an intrinsic relativistic velocity v towards **B**. Hence, the apparent transverse speed measured by the observer is: $v_{\rm app} = (v\sin\theta)\,/\,(c - v\cos\theta)$, where θ is the angle between the line of sight and the jet velocity vector.

4.2 The Sample

Blazars are an extreme class of radio source that represent only a small percentage of active galactic nuclei (AGN), and are characterized by highly relativistic jets oriented close to the line of sight. Doppler beaming tends to make a jet emission flux density–limited sample consist entirely of blazars only. Hence, though a sample of highly beamed AGN lends itself very well to a comprehensive study of kinematics, variability and other physical phenomena, care must be taken to quantify the biases introduced by beaming. Lister & Marscher [1997] have shown that such biases can be properly accounted for, if a large sample ($\geq$ 100 jets) with rigorous jet emission based selection criteria, is employed.

The erstwhile 2 cm survey [Kellermann et al., 2004] was one of the first experiments to make a systematic study of bright AGN using the NRAO's[2] VLBA, regularly imaging over 150 AGN jets from 1994.0 to 2002.0. The finding that the observed superluminal pattern speeds are indeed related to the underlying flow is one of its important discoveries. However, since the experiment collected only total intensity (Stokes I) data, magnetic fields in these jets could not be studied. Moreover, the sample was not a statistically complete one for beamed jets, by virtue of being drawn from a low-frequency catalog. Hence, a complementary campaign to conduct full polarimetric observations of a complete sample chosen on the basis of 15 GHz VLBA data only, was begun in 2002. This project, named **M**onitoring **O**f **J**ets in **A**GN with **V**LBA **E**xperiments (*MOJAVE*) aims to make statistical statements regarding the properties of the various blazar subclasses. The sample currently contains $\sim$ 200 sources. There are 135 sources satisfying the following criteria:

- J2000.0 Declination $> -20°$
- Galactic latitude $|b| > 2.5°$
- VLBA 2 cm correlated flux density exceeding 1.5 Jy (2 Jy for sources below the celestial equator) at any epoch between 1994.0 and 2004.0.

which were part of the original (*MOJAVE_1*) sample [Lister & Homan, 2005, Lister et al., 2009a]. Subsequently, in the *Fermi/GLAST* era, the sample was extended to

[2] The National Radio Astronomy Observatory is a facility of the National Science Foundation operated under cooperative agreement by the Associated Universities, Inc.

include sources of particular interest based on their $\gamma-$ray properties, and satisfying the following criteria:

- The brightest *Fermi* LAT–detected AGN from the first 11 month LAT catalog [$\sim$ 100 sources Abdo et al., 2009, 2010], which satisfy the following criteria:
  - J2000.0 Declination $> -30°$
  - Estimated 2 cm VLBA flux density $>$ 200 mJy, based on prior VLBA Calibrator Survey (VCS) observations at 2 and 8 GHz [Petrov et al., 2008]

The *MOJAVE* sample (see Table A.1 for a complete list of sources) and especially the *MOJAVE*_1 sample, is dominated by quasars, with the weak-lined BL Lacs and radio galaxies making up $\sim$ 13.6% and $\sim$ 9.2% of the sample, respectively. By selecting on the basis of compact flux density at a short wavelength, the sample favors highly beamed relativistic jets (i.e., blazars), making it well suited for quantifying the strong selection effects associated with blazar samples [Lister & Marscher, 1997]. Kpc–scale 20 cm radio imaging observations of hitherto unstudied *MOJAVE* sources using the VLA are also currently in progress [Cooper et al., 2007, Kharb et al., 2010].

An overview of the properties of the full sample viz., source types, optical polarization and GeV detection is presented in Table 6.2. In all, there were 373 sources (Fig. 4.2) in the full sample, of which 246 were QSOs, 54 were BL Lac objects, 37 were galaxies (Gal) and 11 were intermediate BLL/QSO sources, as inferred from the presence of some broad lines in their otherwise power–law optical spectra. The remaining sources did not have a known optical classification. Among these objects with known optical identification and measured optical polarization values, 88 sources – comprising 52 QSOs, 24 BL Lac objects, 1 Gal and all the intermediate BLL/QSOs – are known to have high optical polarization[3]. Also, 210 of the sources, comprising 137 QSOs, 42

[3]High Polarization: Optical polarization $>$ 3% [Wills et al., 1992]

BL Lac objects, 8 Gal, 12 of unknown type, and all the intermediate BLL/QSOs have a published GeV detection[4].

4.3 Some Salient Results

MOJAVE is a long term program that seeks to better understand the physics of AGN on the pc-scale via regularly-spaced, full polarimetric, high resolution VLBA observations [Kellermann et al., 1998, 2004, Lister & Homan, 2005, Lister et al., 2009a]. Fig. 4.3 (top panel) shows the measured $\beta_{\rm app}$ values for all the sources in the *MOJAVE* sample as a function of their 2 cm VLBA luminosity. Also plotted is a curve depicting the $\beta_{\rm app}$ and observed luminosity that would be measured for a source with given Lorentz factor and intrinsic luminosity values, when being viewed at various angles. The observed luminosity for such a source is given by equation 4.7, while $\beta_{\rm app}$ is given by equation 4.2. The values chosen for the curve are: $\log L_{\rm int} = 25,\ \Gamma = 45$. The viewing angle increases from 0° to 90° towards the left. This curve is for illustrative purposes only and is not a fit to the data. The presence of such an envelope to the measured $\beta_{\rm app}$ is indicative of the existence of a maximum Γ (about ≤ 50). As expected, radio galaxies, which are usually oriented close to the plane of sky, have low $\beta_{\rm app}$. The highest $\beta_{\rm app}$ measured [(currently ~ 59.1) Lister et al., 2009b] corresponds to the high redshift GeV quasar 0805−077 ($z = 1.837$, $\beta_{\rm app} \sim 59.1$)[5], the high-valued outlier in the above plots.

Fig. 4.3 (bottom panel) is identical to the top panel in that figure, but with only sources with a *Fermi* GeV detection being shown. As is evident from the above discussion, in the $\beta_{\rm app}$ vs. VLBA luminosity plot, sources with higher intrinsic luminosity and/or higher beaming are expected to lie closer to the illustrative envelope. Such sources should be among the first ones detected by the *Fermi* LAT instrument, if

[4]Only sources in the *Fermi* LAT 1–year catalog (LAT 1FGL, covering the time period August, 2008 to July, 2009: `http://fermi.gsfc.nasa.gov/ssc/data/access/lat/1yr_catalog/`) were defined to be GeV detected, as discussed in § 6.1.

[5]See: `http://www.physics.purdue.edu/MOJAVE/sourcepages/0805-077.shtml`

GeV emission is also beamed. Hence, it is expected that GeV non–detected sources lie towards the center of the envelope, which indeed appears to be the case.

Fig. 4.4 (top panel) shows the observed 74 MHz luminosity [from the VLSS program Cohen et al., 2007a] vs. 2 cm VLBA luminosity data for the *MOJAVE* sources, where available, while the same data for the GeV sources alone is shown in the bottom panel. A strong correlation between the two luminosity values is evident for the blazars, while galaxies show no such correlation. This correlation may be interpreted to indicate that the intrinsic jet power and Lorentz factor (which in turn is a measure of the jet speed) are indeed connected. Unbeamed/extended emission is a chief contributor towards the low frequency VLA luminosity, while the VLBA luminosity is beamed. Therefore, the VLSS 74 MHz luminosity values have a weaker dependence on the viewing angle compared to the 2 cm VLBA data. Galaxies, being oriented close to the plane of the sky, are less beamed than blazars. Hence, their measured VLBA luminosities are much lower than the intrinsic values, and hence Galaxies area located towards the left in this plot. If a given galaxy were to be viewed close to the observer's line of sight (viz., become a blazar), then the corresponding data point is expected to shift horizontally to the right. Another way of stating the same is that, the *MOJAVE* sample being primarily a flux density limited sample, the galaxies in the sample happen to be present due to them being at low shift, while the rest of the sample is selected due to their beaming properties.

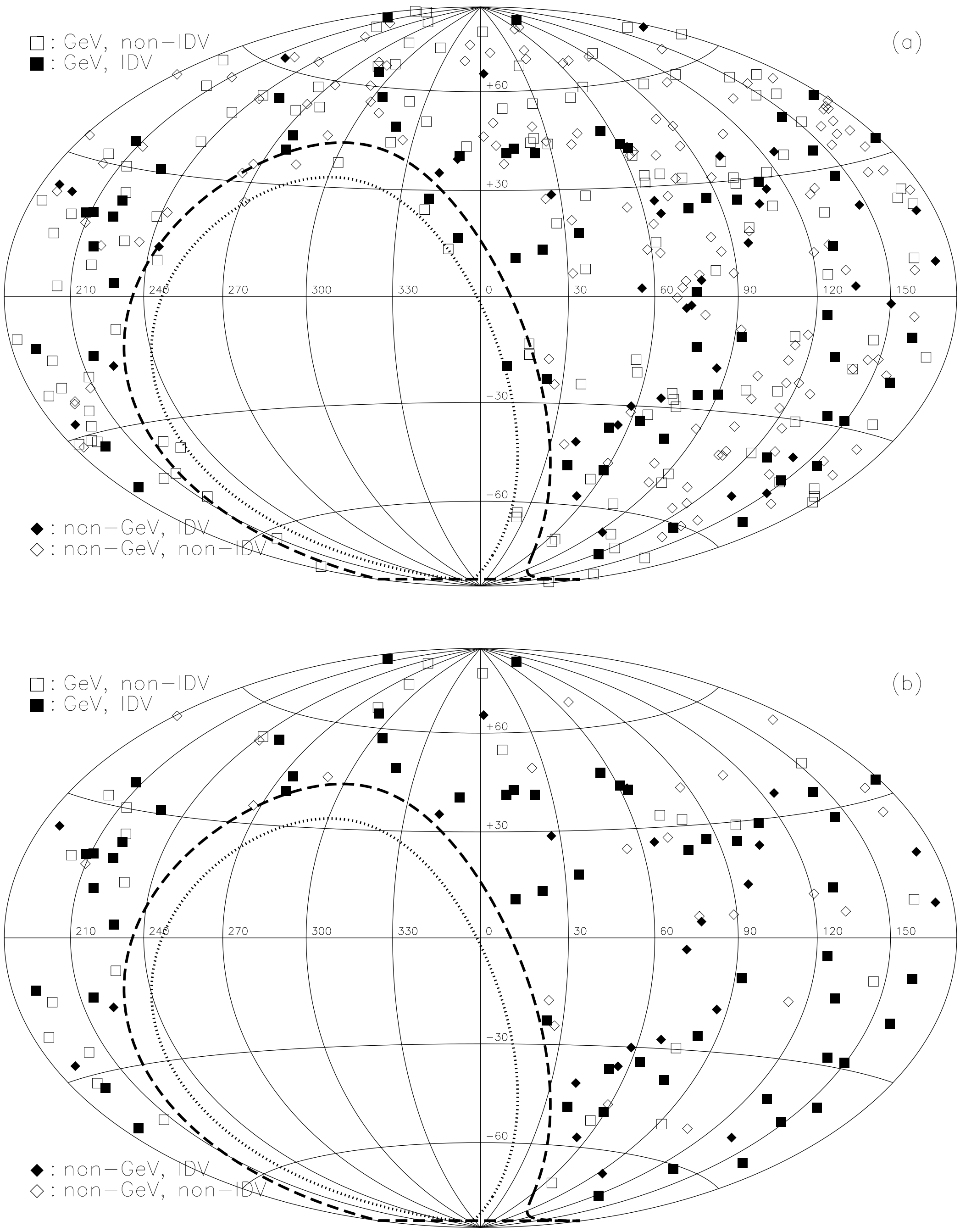

Figure 4.2. (a): Galactic coordinate Aitoff map showing the location of all the sources in the full sample. Of the 373 sources in the full sample, 269 show no IDV, with 129 of them having a GeV detection. Of the 104 IDV sources, 37 have no GeV detection. (b): Galactic coordinate Aitoff map showing the location of the sources in the flux-limited *MOJAVE_1* sample only. Of the 131 sources from this sample considered in this IDV study, 50 show no IDV, with 27 of them having a GeV detection. Of the 81 IDV sources in this sample, 22 have no GeV detection. Also shown, are the declination $= -30°$ cutoff for the full sample (dotted line) and declination $= -20°$ cutoff for the *MOJAVE_1* sample (dashed line).

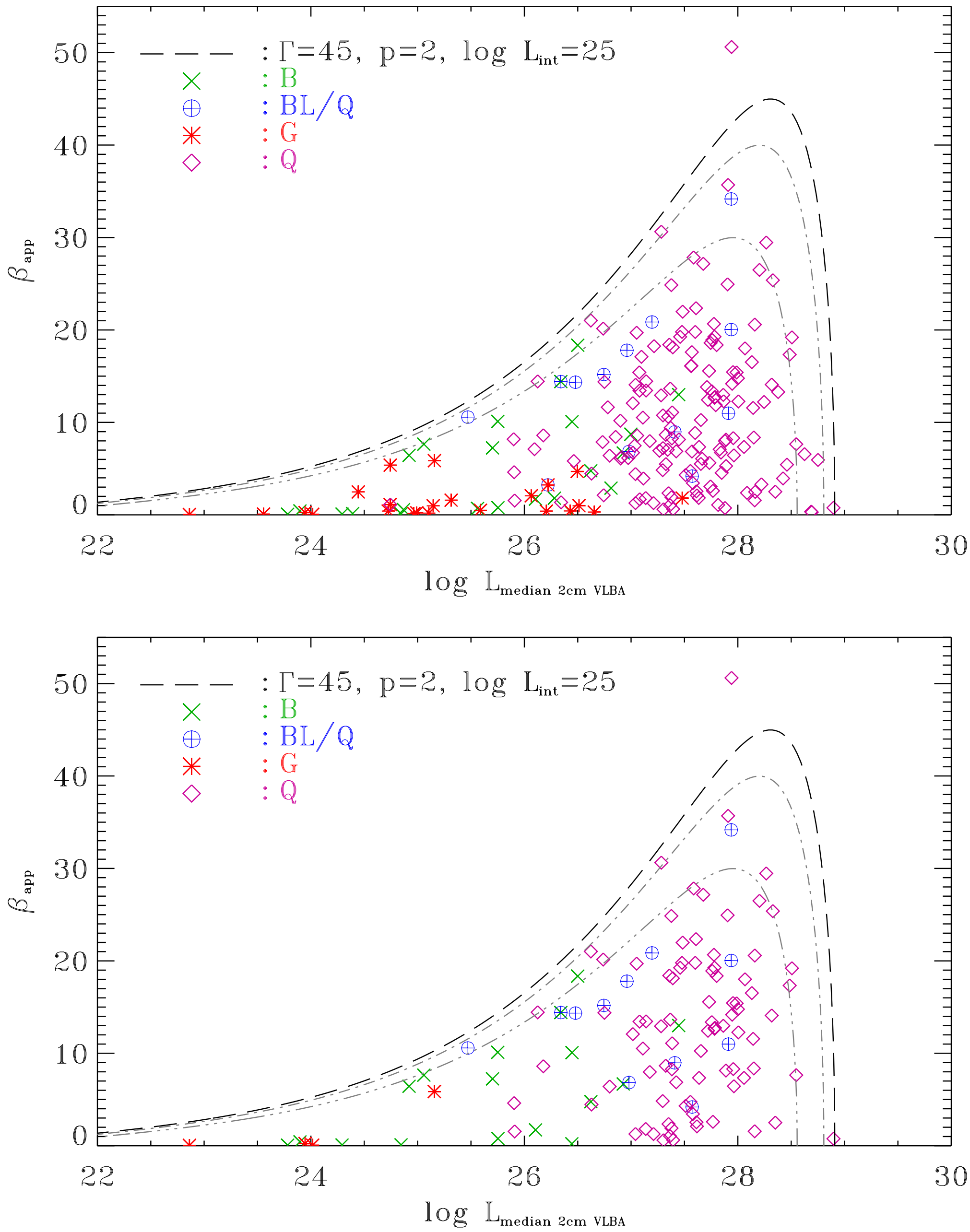

Figure 4.3. *Top*: Plot showing the $\beta_{\rm app}$ vs. 2 cm VLBA luminosity for sources in the full *MOJAVE* sample. *Bottom*: Plot identical to the top panel, but showing only the sources with a *Fermi* GeV detection. The various symbols correspond to the different source classes: B – BLLs, G – Galaxies, Q – QSOs, BL/Q – Intermediate BLL/QSO sources. Also plotted is a dashed curve depicting the $\beta_{\rm app}$ and observed luminsoity that would be measured for a source with given Lorentz factor and intrinsic luminosity values, when being viewed at various angles. The values chosen for the curve are: $\log L_{\rm int} = 25,\ \Gamma = 45$. The viewing angle increases from 0° to 90° towards the left. This curve is for illustrative purposes only and is not a fit to the data.

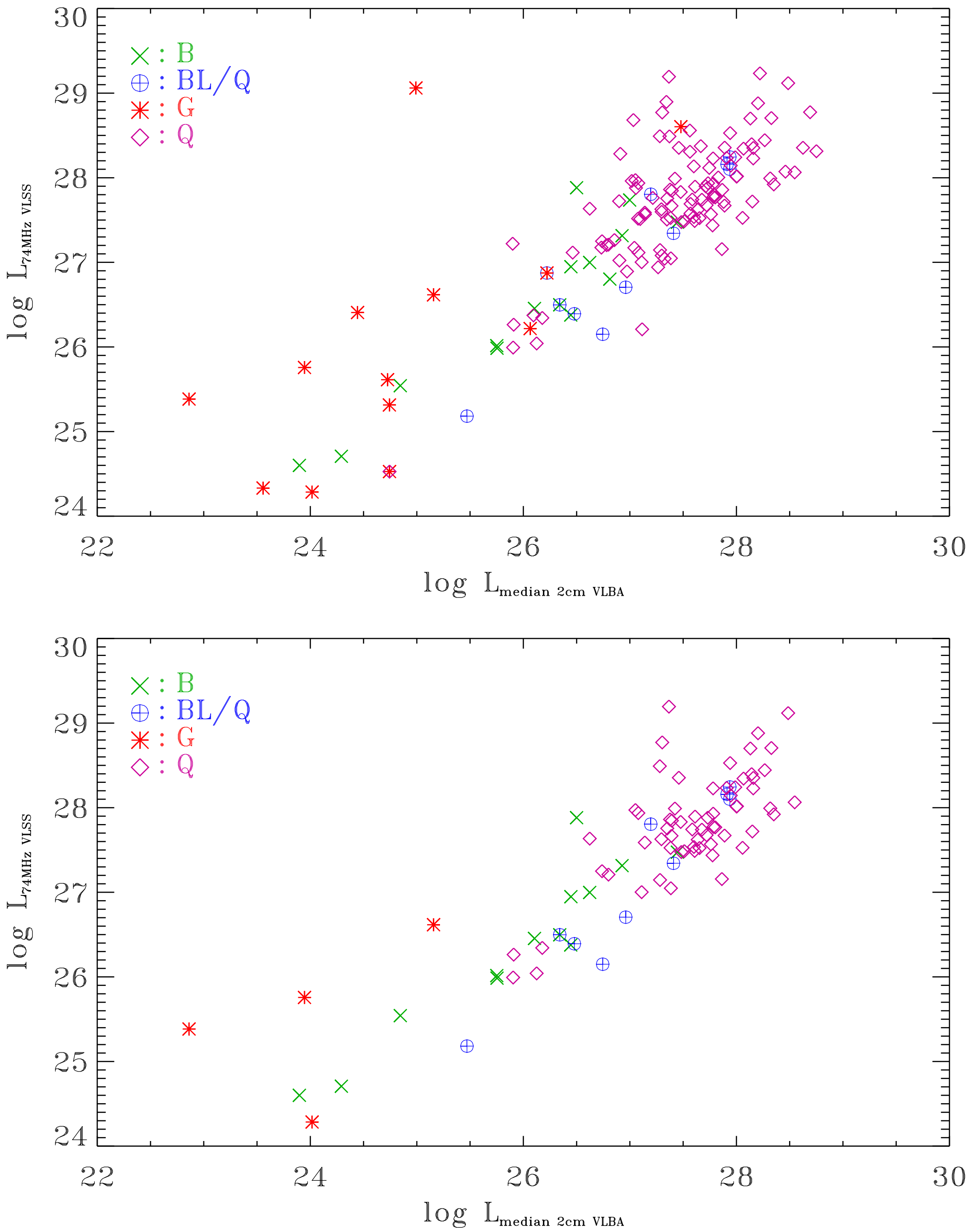

Figure 4.4. *Top*: Plot showing the observed 74 MHz luminosity (from the VLSS program) vs. 2 cm VLBA luminosity for the same sources. The data point at the top left corner corresponds to the nearby narrow line FR-II galaxy Cygnus A. *Bottom*: plot identical to the top panel, but showing only the sources with a *Fermi* GeV detection.

5. IDV: OBSERVATIONS & DATA ANALYSIS

5.1 Interferometry Basics

Radio interferometry allows for the achievement of resolutions hitherto impossible with single aperture telescopes. An interferometer setup consists of 2 or more elements (or *stations* or *antennas*), giving rise to $N(N-1)/2$ baselines, where N is the number of antennas. The goal is to map the sky brightness distribution with the best possible resolution. The basic steps involved in generating images using radio interferometry are as follows:

1. Complex wavefronts from the source arriving at each telescope are measured with radio receivers. Artificial delays are inserted in the signal paths of each telescope so as to make them to be at the same effective distance from the source. Signals from each baseline (a pair of telescopes) are interfered (correlated) and the resulting complex fringe visibilities are recorded as a function of time.

2. The visibilities from a given pair of telescopes sample spatial frequencies on the sky in proportion to the projected separation of the telescopes i.e., the nominal resolution of the baseline is 1/D, where D is the projected length (in wavelength units) of the baseline in the sky. The structure orthogonal to this projected baseline remains unresolved. Since the baseline separation and orientation relative to the source change as the Earth turns, each baseline samples a locus of spatial frequencies as a function of time. This is called Earth rotation synthesis. Hence, in order to generate the best possible image, every observation of a source is broken down into short scans spread out over the duration of the experiment, with the final data-set being a collation of these individual scans.

3. Since the radio antennas are ground-based, atmospheric fluctuations along with instrumentation effects, introduce a large variability in the measured visibilities. Hence observations of a source are interspersed with observations of a calibrator, which usually is a nearby bright point source. The measured complex visibilities are then interpolated onto a 2D spatial-frequency plane called the (u,v) plane.

4. The simplest method of image reconstruction is by using the *CLEAN* algorithm and self calibration. This technique involves finding the best-fitting model to the visibility data. Delta functions, representative of point sources, are placed within a given region around the image location of the source (clean window) and convolved with the point spread function (beam). The Fourier transform of this map yields the visibility model, which is then compared to the actual data to find the best-fitting model. This process is carried out iteratively, until the expected rms noise levels are attained. The final such model is called the clean model and can be used to generate the clean map or image of the source. The clean model is unphysical since it consists of only Delta functions; Instead it is merely a mathematical description of the visibility data.

5.2 Data Reduction

With the exception of the recent *MASIV* survey, IDV experiments to date have been only carried out with single dish radio telescopes or compact arrays like the ATCA. A typical IDV experiment consists of short scans ($\sim$ 1 min) alternating between the source and a nearby calibrator. This mode – referred to as the *snapshot mode* – allows for the estimation of atmosphere–induced variability and systematic/instrument variability (aka calculation of gain factors) for the calibrator, which by definition is assumed to have constant flux density. These gain factors can then be applied to the source data – this is valid, since the source as well as the calibrator are chosen to be in the same part of the sky – so that any remaining variability must be source specific. This technique, however, does not work for the VLBA, since at the angular resolutions of VLBA there are no true calibrators i.e., bright unresolved point sources. IDV is believed to be exclusively limited to the compact flat spectrum AGN core, which is usually resolved only at the angular resolutions of the VLBA. Hence, though the VLBA could potentially be a very valuable tool for studying IDV, since its angular resolution allows for modelling of only the core neglecting any extended emission even on the pc scale – a problem for bright sources – lack of good calibrators is a huge drawback.

In the current study, a novel gain correction technique developed by the *MOJAVE* team was used, allowing for a detailed study of IDV using the VLBA for the first time. A basic description of this technique is presented in Fig. 5.1. Each *MOJAVE* observation involves monitoring 25–30 sources distributed evenly over the sky, in a 24 hour span, with approximately eight 5 minute scans per source, so as to maximize its (u,v) coverage. In the preliminary step, the data for each source are reduced independently using AIPS[1] following the standard VLBA procedures. The editing/flagging of bad data, time-averaging and imaging (generation of clean maps and models) are carried out in Difmap. Details of this process have been reported elsewhere [Lister & Homan, 2005]. These edited (u,v) files (henceforth referred to as uvf_raw_edt files) along with the relevant clean map and clean model files are stored in the *MOJAVE* archive.

In the first step of the IDV analysis, using AIPS, the uncalibrated, time–averaged (u,v) fits-format file and clean map for each source in an experiment are read from the *MOJAVE* archive. Using standard VLBA data reduction procedures from the AIPS cookbook [2], the solution tables (*SN tables*, containing the gain correction factors) for each individual source are produced in AIPS. Subsequently, the solution tables from all the sources in the experiment are collated together and smoothed – for each antenna, IF and polarization channel separately – using a median box $\pm$ 3hrs.

[1] **A**stronomical **I**mage **P**rocessing **S**ystem; `http://www.aips.nrao.edu/`

[2] `http://www.aips.nrao.edu/CookHTML/CookBook.html`

in width (see Fig. 5.1). The smoothed solution table is then applied to each source to produce the *Gain Transferred* or GAINT file, while the original (raw) solution table is applied to produce the *Self Calibrated* or SELFC file for that source. The raw gain correction factors were calculated under the assumption that any flux density variability in a source is entirely due to atmospheric and instrumental effects i.e., the variability is not source specific. Hence, the basic idea behind the smoothing step is that the majority of sources in an experiment are non-IDV, implying that the gain corrections calculated for an IDV source must be anomalously different from those of its neighboring sources. So, using the gain correction factors extrapolated from neighboring sources would allow for the estimation of variability induced by the atmospheric and instrumental corrections, i.e., variability not specific to the source in question, and any remaining variability must be due to IDV. Thus, the paucity of calibrators can be overcome, as has been demonstrated in the past via a similar technique [e.g. Homan & Lister, 2006, Savolainen & Kovalev, 2008]. All the subsequent steps are carried out in Difmap.

In the second step, the delta functions representing the core (usually the brightest feature) components in the clean model are replaced by a variable, elliptical Gaussian, which is then used to modelfit the data. Subsequently, the Gaussian is allowed to vary only in flux–density viz., its position, size and shape are fixed at their best-fitting values, to generate the template model. The psf/clean beam, in conjunction with the brightest contour, was used as a guide to decide which delta functions are to be considered part of the core. The source file is then broken down into individual scans, and each scan is fit using the template model to calculate the flux density. These flux densities are then used to plot the light curve. This process is repeated for both the GAINT as well as the SELFC files of each source in every experiment. The procedure used for the calculation of errors in flux density is described in the ensuing section. Finally, *low-elevation scans*[3] were excluded from the light curve. Furthermore, any scans with anomalously–high best fit reduced χ^2 values and/or low number of visibilities compared to the rest of the scans were also eliminated from the light curve, since these scans created an artificial sudden dip (and hence perceived variability) in the light curve. Sample GAINT and SELFC light curves are shown in Fig. 5.2. All the aforementioned steps were (mostly) automated using Perl scripts. A sample script containing all the relevant analysis steps is presented in Appendix B. Besides the VLBA data obtained specifically during the current campaign, under the aegis of the *MOJAVE* program, all available/suitable 15 GHz archival VLBA data was re-analyzed [see Lister et al., 2009a, for details] and used in this IDV study.

5.3 Estimation of Equipartition Doppler Factors

Complementary to the IDV study, equipartition doppler factors (δ_{eq}) were calculated. As has been discussed in section 2.3.2, the assumption that VLBA core of the jet is at/near equipartition, at least during its non flaring phase, is valid on physical grounds. Moreover, several authors have inferred the same from VLBA observations [e.g., Lobanov et al., 2000, Lee et al., 2008, O'Sullivan & Gabuzda, 2009]. Hence, it was assumed that the median of the bottom half of the VLBA flux densities for a given source (so called 25% median) corresponds to the equipartition value and so the intrinsic T_b at this epoch must be equal to T_{eq} [Readhead, 1994]. But the ratio of observed and intrinsic T_b values is δ_{eq} by definition (Eq. 2.21). This is analogous to the analysis reported by Homan et al. [2006], but on a larger sample. The calculated δ_{eq} values can then be combined with β_{app} information from *MOJAVE* kinematics analysis [Lister et al., 2009b] to calculate the Lorentz factor and orientation angle for each source.

[3]A *low-elevation* scan was arbitrarily defined as a scan that does not meet the following criteria: (1) Less than 3 (out of 10) antennas are at an elevation $< 15°$; (2) At least 2 antennas are at an elevation $\geq 30°$.

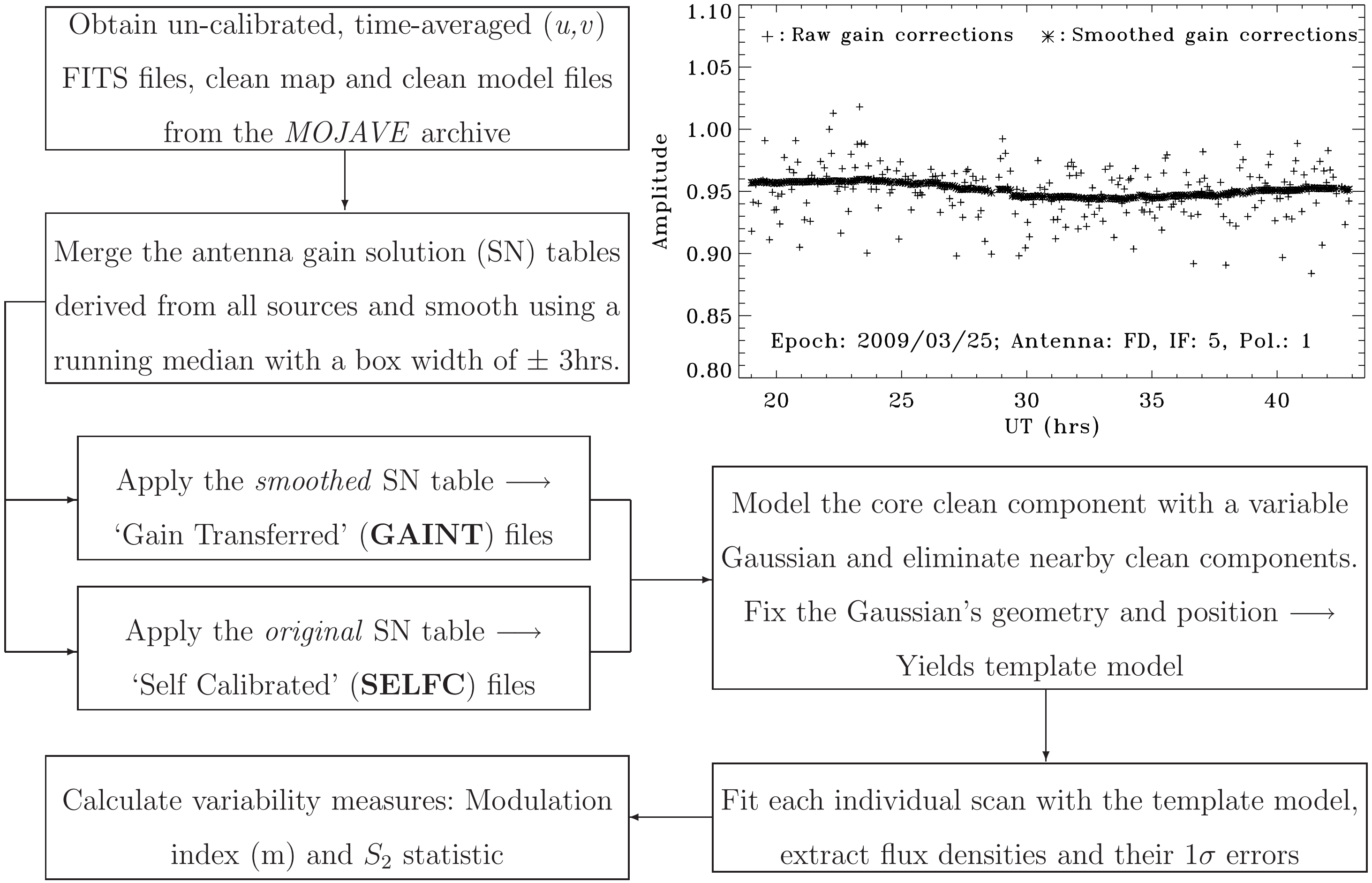

Figure 5.1. Flowchart showing the data reduction methodology used in the current IDV analysis. Also shown is a sample plot of the original ('*raw*') gain correction factors along with their smoothed values for the Fort Davis (FD) antenna, Left hand circular polarization, IF channel 5 from the VLBA epoch 2009 March 25.

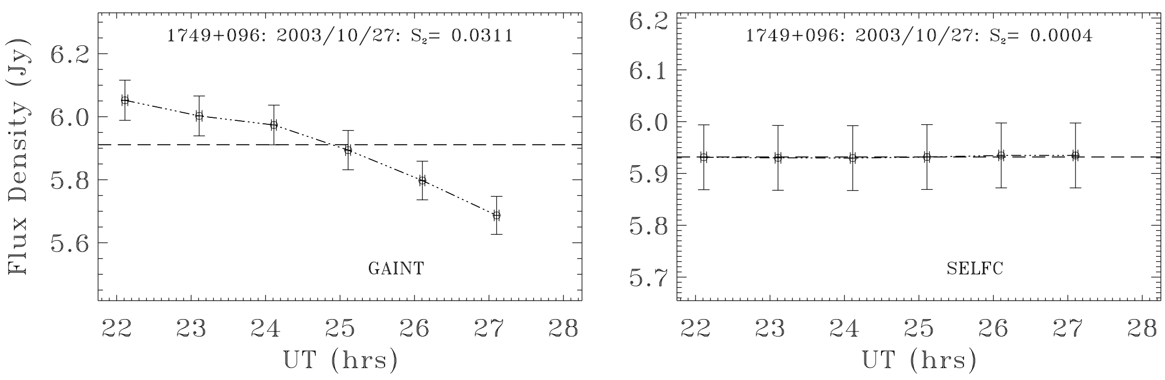

Figure 5.2. *Left:* GAINT light curve for the intermediate BL Lac/QSO 1749+096 (OT 081). This light curve was produced by using the gain correction factors from neighboring sources to eliminate atmospheric and instrumental variability, allowing for the detection of source specific variability. *Right:* SELFC light curve for the same source from the same epoch. The underlying assumption behind self calibration is that all the variability is atmospheric or instrumental. However, this might lead to a suppression of IDV detection, as demonstrated above.

5.4 Error Analysis

An accurate estimate of the 1σ errors of the individual scan flux density measurements would be very useful in determining whether a light curve shows IDV or not. Uncertainties in model-fitting parameters may be estimated by varying the parameter of interest until the reduced χ^2 — defined as $\bar{\chi}^2 = \chi^2/\mathrm{N}$, N being the number of degrees of freedom — is increased by unity, which would give a 1σ estimate. The number of degrees of freedom (N) is usually defined as the number of independent data points (the number of visibilities in this case) minus the number of model parameters. Difmap has an inbuilt function *uvstat*, which returns various *(u,v)* plane visibility statistics such as the number of unflagged visibilities (*nvis*) and the reduced χ^2 (*chisq*). Hence, the uncertainties in flux density of each data point in a light curve (corresponding to one individual scan) may be estimated by calculating the best-fitting χ^2_{red} using the *uvstat* (*chisq*) command and varying the flux density until this value increases by unity. This is the 1σ error of the model only, and does not take into account the errors that may have been introduced earlier in the data reduction path, such as systematic uncertainties in the absolute flux density scale. The uncertainties in the derived mean flux, modulation index and S_2 statistic may then be estimated using standard error propagation formulae [Wall & Jenkins, 2003], as given below.

The mean flux density $\left(\bar{S}\right)$ and its uncertainty (σ) are given by:

$$\bar{S} = \sum_{i=1}^{N} \sigma^2 \, \frac{S_i}{\sigma_i^2} \qquad\qquad \frac{1}{\sigma^2} = \sum_{i=1}^{N} \frac{1}{\sigma_i^2} \tag{5.1}$$

where $S_i,\ \sigma_i$ denote each individual scan's flux density and its uncertainty respectively, while N is the total number of scans in the light curve.

The variability of each scan (V_i) and its uncertainty $(\sigma_{\mathrm{v_i}})$ are given by:

$$V_i = \frac{S_i}{\bar{S}} - 1 \qquad\qquad \sigma_{\mathrm{v_i}} = \left(\frac{\sigma}{\bar{S}}\right) \sqrt{\left(\frac{\sigma_i}{\sigma}\right)^2 + V_i^2 - 1} \tag{5.2}$$

The rms and its uncertainty (σ_{RMS}) are given by:

$$\mathrm{RMS} = \sqrt{\frac{1}{N} \sum_{i=1}^{N} \left(S_i - \bar{S}\right)^2} \qquad \sigma_{\mathrm{RMS}} = \left(\frac{\sigma}{N}\right) \left(\frac{\bar{S}}{\mathrm{RMS}}\right) \sqrt{\frac{1}{\sigma^2} \sum_{i=1}^{N} (V_i \sigma_i)^2 - \left(\sum_{i=1}^{N} V_i\right)^2} \tag{5.3}$$

The modulation index (m) and its uncertainty (σ_m) are given by:

$$m = \frac{\mathrm{RMS}}{\bar{S}} = \sqrt{\frac{1}{N}\sum_{i=1}^{N}\left(\frac{S_i}{\bar{S}} - 1\right)^2} = \sqrt{\frac{1}{N}\sum_{i=1}^{N} V_i^2}$$

$$\sigma_m = \left(\frac{\sigma}{Nm\bar{S}}\right) \sqrt{\frac{1}{\sigma^2}\sum_{i=1}^{N}(V_i\sigma_i)^2 + \left(\sum_{i=1}^{N} V_i^2 + \sum_{i=1}^{N} V_i\right)\left(\sum_{i=1}^{N} V_i^2 - \sum_{i=1}^{N} V_i\right)} \quad (5.4)$$

$$\Rightarrow \sigma_m = \sqrt{\left(\frac{\sigma_{\mathrm{RMS}}}{\bar{S}}\right)^2 + \left(\frac{\sigma}{Nm\bar{S}}\right)^2 \left(\sum_{i=1}^{N} V_i^2\right)^2}$$

Another measure of variability is the S_2 statistic. The S_2 statistic and its uncertainty (σ_{S_2}) are given by:

$$S_2 = \frac{S_{\max} - S_{\min}}{S_{\max} + S_{\min}} \qquad \sigma_{\mathrm{S}_2} = \left(\frac{2}{S_{\max} + S_{\min}}\right)^2 \sqrt{\left(\frac{S_{\max}\sigma_{\min}}{2}\right)^2 + \left(\frac{S_{\min}\sigma_{\max}}{2}\right)^2} \quad (5.5)$$

where $S_{\max}$, $S_{\min}$ denote the maximum and minimum flux densities in the light curve respectively, with $\sigma_{\max}$ and $\sigma_{\min}$ being their corresponding uncertainties.

However, in the case of radio interferometric data, the aforementioned approach is quite controversial. Unfortunately, uncertainties in the VLBI model-fit parameters are notoriously difficult to determine due to poorly known number of degrees of freedom in the self-calibrated VLBI data, non-linear response to interferometric array coverage, and interdependencies between different model parameters [Savolainen et al., 2006]. Therefore, a technique similar to the one followed by Lovell et al. [2003b] was adopted, and the overall distribution of measured variability statistics was used to estimate the instrumental noise level. To the first order, the uncertainties in the flux density measurements are comprised of two independent components: (1) a multiplicative part p that is proportional to flux density, which is due to uncertainties in antenna gains as well as errors due to dynamic range, and (2) an additive part s that is independent of source flux density. Consequently, the flux density variance due to instrumental effects can be expressed as:

$$\sigma_{\mathrm{S}}^2 = (p\bar{S})^2 + s^2 \tag{5.6}$$

A criterion for IDV classification can then be that:

$$\sigma_{\mathrm{S}}^2 > C^2 \cdot \left[\left(p\bar{S}\right)^2 + s^2\right] \quad , \tag{5.7}$$

where C is the critical value from the χ^2_{N-1} distribution for the required confidence limit and $N-1$ degrees of freedom. As is evident from Eqn. 5.6, at low flux density values, the additive term is the dominant source of error, while for the high flux density sources, the multiplicative term dominates. Hence, the values of s, p may be estimated from observations of known non–IDV sources in the low and high flux density limits, as discussed in § 6.2.

The current analysis involves modeling the VLBA core of the source using a single Gaussian. If the core has an unusually complex structure/polarization, this step may lead to artificial variability in the light curve, which was found to be the case for the radio galaxy 0316+413 (3C 84), as inferred from the light curves having a similar profile in almost every epoch. The pc scale VLBA structure of the superluminal HPRQ 2251+158[4] (3C 454.3) is also highly polarized and complex, with the core containing less than $\sim 50\%$ of the total 2 cm VLBA flux density. Modeling such a source with a single Gaussian *may* lead to artificial light curve variability. Also, these two sources have been reported to be non-IDV sources from VLA measurements [Lovell et al., 2008]. Hence, they have been excluded from the current analysis. As a result of beaming, the core of 0923+392[5] is not the brightest feature in the jet [Lister & Smith, 2000]. Since IDV is thought to arise primarily in the flat spectrum core, this source was excluded as well. The 2 cm core of the galaxy 0238−084 (NGC 1052) is completely self-absorbed at 15 GHz [Kadler et al., 2004] and hence this source was

[4] `http://www.physics.purdue.edu/MOJAVE/sourcepages/2251+158.shtml`
[5] `http://www.physics.purdue.edu/MOJAVE/sourcepages/0923+392.shtml`

also excluded. Furthermore, any light curve with less than 4 scans was deemed unreliable and was excluded. This left approximately 3800 light curves spanning about 350 epochs (from 1994 – 2011), corresponding to about 375 sources, in the current analysis.

Several authors have remarked on the difficulty in assigning variability to light curves via automated algorithms [e.g., Lovell et al., 2003b] and hence, manual inspection of light curves is often used to classify a source to be IDV/non–IDV. However, the large size of the *MOJAVE* database makes this unfeasible. In § 6.2, the non–IDV nature of compact sources with steep or peaked spectra is confirmed. Hence, the light curves of such sources may be used to develop a criterion to distinguish IDV sources from the non–IDV ones among the flat spectrum sources.

6. RESULTS & DISCUSSION

In this chapter the results from the IDV analysis, as well as other complementary studies carried out as part of this dissertation, are presented. At the end of this chapter, a qualitative model explaining all the IDV results (§ 6.8), is proposed.

6.1 Equipartition Doppler Factors

Prior to discussing the results from the IDV analysis, a discussion of the results from the brightness temperature analysis is provided here. The assumptions and methodology behind this analysis was described in § 5.3. As expected, less beamed AGN (like radio galaxies, CSS/GPS sources) have low δ_{eq}. Also, the equipartition doppler factors calculated are in good agreement (for several sources) with those inferred via other techniques like SED modelling [e.g., Madau et al., 1987] and modeling of long term light curves [e.g., Singal & Gopal-Krishna, 1985, Ghisellini et al., 1993, Hovatta et al., 2009, see Fig. 6.1]. These δ_{eq} values, in conjunction with the β_{app} values from the *MOJAVE* program, were subsequently used to calculate the bulk Lorentz factors (Γ).

Of the 207 sources for which the T_b values were calculated, only 7 sources have $T_b \geq 5 \times 10^{12}$ K, and in almost all these cases, these anomalously high values may be attributed to a sparse number of observing epochs and/or modeling difficulties. The lowest T_b value in the sample was $\sim 1.5 \times 10^{8}$ K, and as expected, the lowest T_b values corresponded to the galaxies in the sample. Also, 76 of the sources have variability Doppler factors (δ_{var}) reported in literature [Hovatta et al., 2009] along with well established apparent speeds [Lister et al., 2009a]. There is a fair agreement between the Lorentz factors derived from the equipartition T_b values and those inferred from these δ_{var} values (Spearman rank correlation coefficient of 0.63 at a significance level of $\sim 98.5\%$). Some of the reported δ_{var} values, however, may be systematically underestimated due to the frequency of scheduled mm–wave observations and difficulties in the modeling of very rapid flares [Hovatta et al., 2009, and references therein]. As expected, almost all the sources with high T_b values were found to have a GeV detection (see § 6.6).

Fig. 6.2 shows a plot of the estimated δ_{eq} against the apparent speeds inferred from the *MOJAVE* program, for the various source types. As expected, radio galaxies and BL Lac objects have smaller δ_{eq} values compared to QSOs. The intermediate BL Lac/QSO objects, so classified due to the presence of broad lines in their optical spectra, have δ_{eq} values closer to the highly beamed QSOs than BL Lacs. This is in agreement with the IDV results from the current analysis and the initial results from the *Fermi* team [e.g., Abdo et al., 2009, 2010]. Also shown in the aforementioned plot, are δ_{eq} vs. β_{app} profiles expected from a source with a given intrinsic bulk Lorentz factor viewed at different angles. It is evident once again that the observed data seems to be enveloped by a constant Γ curve. The presence of such an envelope is not unexpected in light of Fig. 4.3, and given the fact that the observed VLBA radio luminosity depends on the Doppler factor. It is also to be noted that all the outliers to the bottom left of the plot are from the 2 cm survey sources which are currently not being monitored by the *MOJAVE* program, and hence the β_{app}, δ_{eq} data might be less accurate due to paucity of epochs. All the sources with a *Fermi* GeV detection are indicated in black.

Fig. 6.3 shows the δ_{eq} values plotted against the hard X-Ray (10 – 50 keV) luminosity for the *MOJAVE* sources with available data. The X-ray data are from the BAT instrument aboard the *Swift* mission. The jet beaming factors indeed appear to be correlated to X-ray luminosity (Kendall's tau coefficient of 0.35 at a significance of

$\sim 99.6\%$).

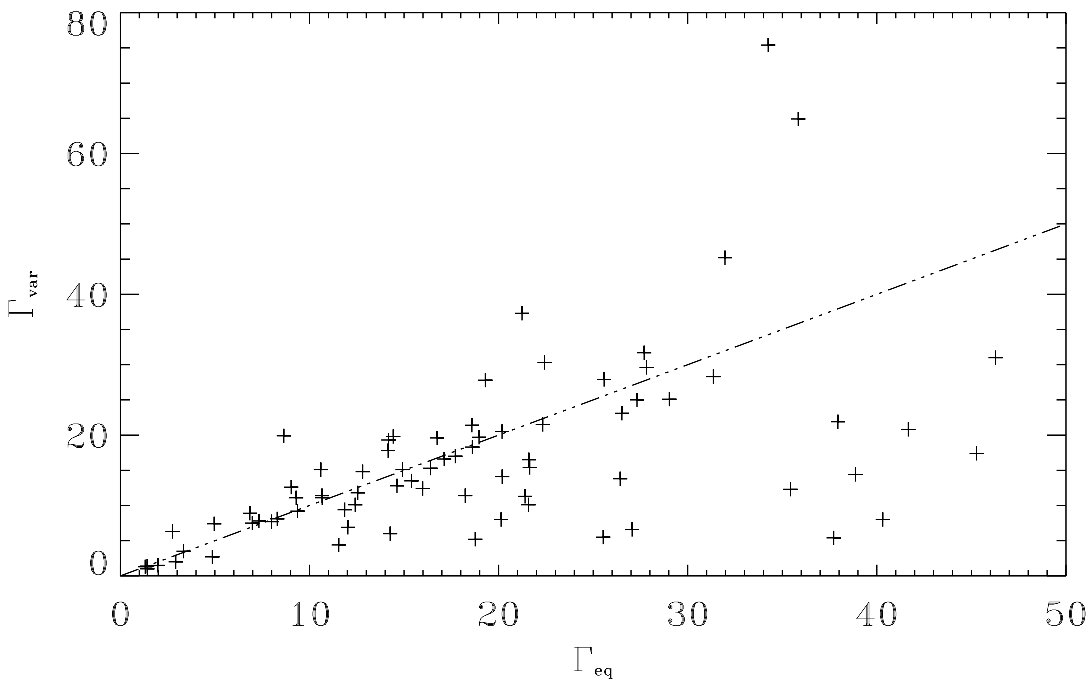

Figure 6.1. Plot of the variability Lorentz factors (Γ_{var}) vs. the equipartition Lorentz factors (Γ_{eq}) for *MOJAVE* sources with available data. The Γ_{var} values are from Hovatta et al. [2009], who have used the Doppler factors calculated from their 37 GHz light curves in conjunction with the β_{app} values from *MOJAVE* to calculate Γ_{var}.

6.2 GPS/CSS sources

Giga-Hertz Peaked Spectrum (GPS) and Compact Steep Spectrum (CSS) radio sources are compact ($\leq$ 1 kpc & $\leq$ 15 kpc respectively) with convex shaped radio spectra, and well defined peaks [near 1 GHz and 0.1 GHz respectively; O'Dea, 1998]. They make up a significant fraction of the bright radio sources at cm wavelengths. One of the chief characteristic features of these objects is lack of any significant radio variability, and mostly no evidence of Doppler boosting [O'Dea, 1998]. However, their milliarcsecond radio morphology is strikingly similar to those of normal radio galax-

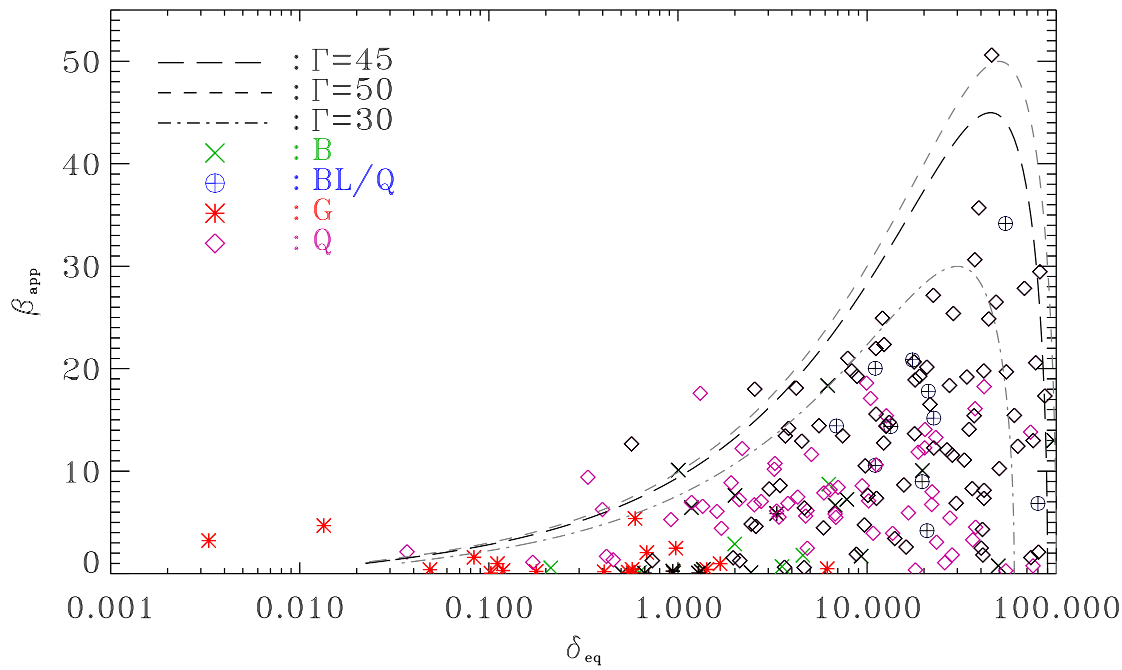

Figure 6.2. Plot showing the $\beta_{\rm app}$ vs. $\delta_{\rm eq}$ factors from the current analysis. The various symbols correspond to the different source classes: B – BLLs, G – Galaxies, Q – QSOs, BL/Q – Intermediate BLL/QSO sources. Also plotted are curves depicting the $\beta_{\rm app}$ and Doppler factors that would be measured for a source with given intrinsic Γ, when being viewed at various angles. The values chosen for the curves are: $\Gamma = 45$, 50 & 30 respectively. The viewing angle increases from $0°$ to $90°$ towards the left. The presence of such an envelope is to be expected in light of Fig. 4.3. Indicated in black are all the sources with a *Fermi* GeV detection.

ies (classical doubles). Because of this similarity and the observed high radio power, these sources are thought to be no different from other galaxies. The reason for their compactness could then be either:

1. They reside in a dense ambient environment and hence the absence of large scale structure [*frustrated jet* scenario, van Breugel, et al., 1984]; However, recent X-ray data suggests that the column densities towards GPS/CSS sources are no different from those of normal galaxies.

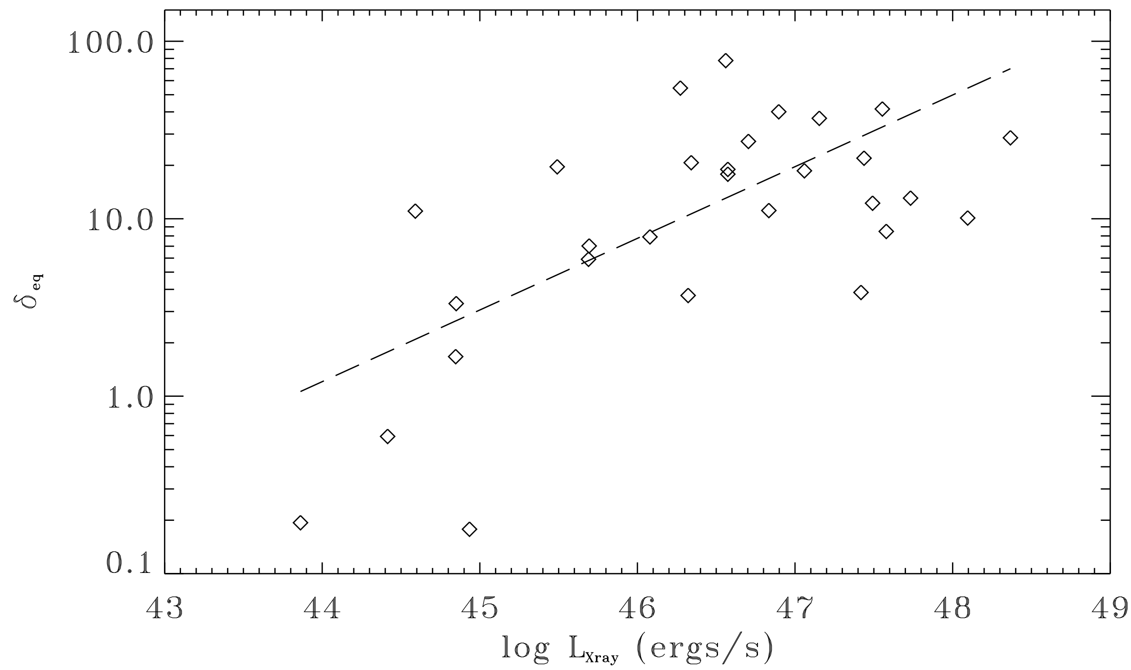

Figure 6.3. Plot of the hard X-ray ($10-50$ keV) luminosity vs. δ_{eq}. The X-ray data are from the BAT instrument aboard the *Swift* mission. The jet beaming factors indeed appear to be correlated to X-ray luminosity (Kendall's tau coefficient of 0.35 at a significance of $\sim$ 99.6%).

2. They are merely young and hence haven't had the chance to develop large scale structures [e.g., Fanti, et al., 1995]; This is the widely accepted scenario; but there are far too many 'young objects' compared to the 'old ones' assuming normal duty cycles of $\sim 10^8$ yrs. Also, some authors have pointed out that some of these GPS/CSS sources are short–lived radio objects, and will never evolve into large scale objects [e.g., Gugliucci et al., 2005, Kunert-Bajraszewska et al., 2006]. Recently it has been speculated that radiation pressure instabilities in the accretion disk limiting the duty cycle to $< 10^3 - 10^4$ yrs, and hence confining the ejecta to within their host galaxies can circumvent this problem [Czerny et al., 2009].

The *MOJAVE* sample, due to its selection bias, contains only a few CSS/GPS sources. Fig. 6.4 shows a plot of the mean flux density vs. the modulation index for various CSS/GPS/Steep spectrum sources in the *MOJAVE* sample. The superluminal BLRG 3C 111 (0415+379) has been plotted separately, since IDV has been detected in this source in an epoch (during an intense flare), despite it being a steep spectrum source. However, the IDV characteristics of the CSS/GPS sources seem to be markedly different from other sources. For instance, as can be seen from Fig. 6.4, almost all the CSS/GPS sources seem to have very low modulation indices (statistically not different from zero) and low core flux densities.

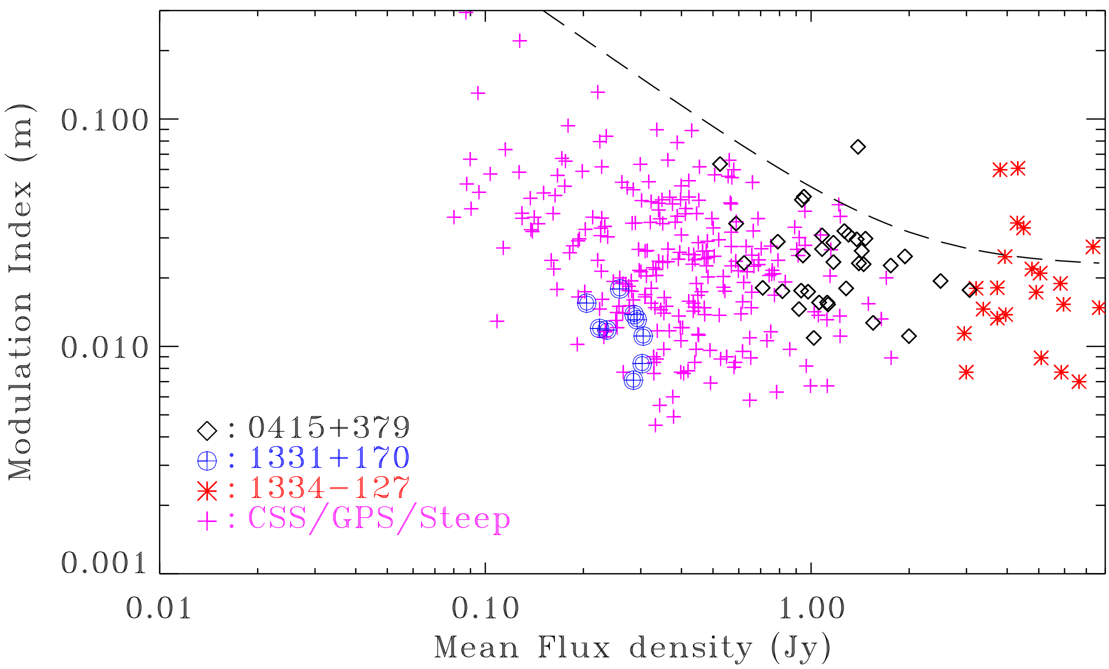

Figure 6.4. Plot showing the Modulation index (m) at various epochs for various CSS/GPS/Steep sources in the *MOJAVE* sample. The values for the superluminal BLRG 3C 111 (0415+379), which shows IDV in an epoch despite being a Steep spectrum source, are shown separately. The dashed line marks the threshold between IDV and non–IDV sources. Also, shown are the m values for a source classified as 'FSRQ' in literature (1331+170), and for a 'candidate GPS' source (1334−127).

In Fig. 6.5 sample GAINT light curves for a few selected CSS/GPS sources are shown. CSS/GPS sources have lower flux densities compared to the blazars in the current sample. The observed flux density is a function of the intrinsic luminosity of the source, its redshift and the Doppler factor (Eqn. 4.7). The low T_b values[1] for these sources indicate the absence of a Doppler boosted core, and hence the low observed fluxes. Their IDV light curves appear remarkably flat (compare Fig. 6.5, 6.6).

IDV light curves can thus potentially serve as another diagnostic tool [besides, e.g., polarization in the core, Peck & Taylor, 2000] in discriminating between bonafide CSS/GPS sources and 'masquerading' ones. The latter are actually beamed blazars with flat cores, but with significant extended emission, thus resulting in single dish radio spectra similar to CSS/GPS sources. As an example, consider the case of 1331+170[2], a EGRET detected source, (but interestingly absent from the LAT 1FGL catalog), which has been classified a FSRQ in the literature. But current analysis indicates otherwise (Fig. 6.7). Subsequently, its spectrum was collected as part of the RATAN program, and was indeed found to be peaked around 5 GHz, but steep below 1 GHz (Fig. 6.8). Though the spectrum is clearly convex shaped, the GPS classification is only tentative due to the paucity of long term spectral data, since several sources are known to show a temporarily inverted spectrum during flares, but otherwise have a flat or highly variable spectrum [Torniainen et al., 2005].

On the otherhand, 1334−127[3] has been classified a 'candidate GPS', but IDV data appears to be contradictory (Fig. 6.9). The same is borne out by its spectrum (Fig. 6.10). In fact, Kedziora-Chudczer [1998] has also reported IDV activity in this source. The high measured β_{app} value [10.26 Lister et al., 2009b] and high δ_{eq} value also argue

[1]The T_b values being discussed are the comoving values, i.e., the source redshift has been accounted for while calculating them.

[2]See `http://www.physics.purdue.edu/MOJAVE/sourcepages/1331+170.shtml`

[3]See `http://www.physics.purdue.edu/MOJAVE/sourcepages/1334-127.shtml`

against 1334−127 being a GPS source.

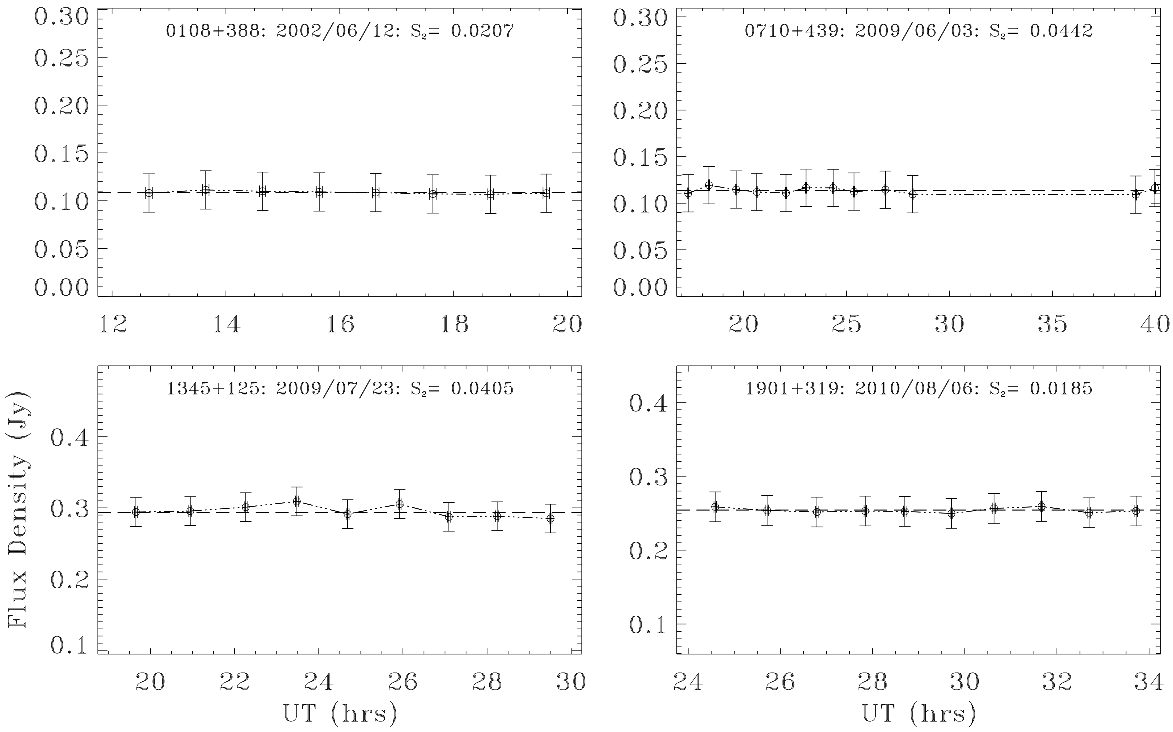

Figure 6.5. Sample 2 cm VLBA light curves of some CSS/GPS sources. As expected, the light curves are very flat, and hence the modulation indices for CSS and GPS sources may be used to discriminate between IDV and non-IDV sources. For comparison, sample 2 cm VLBA light curves of some IDV sources are shown in Fig. 6.6.

6.3 IDV Results

CSS/GPS sources have very stable long term radio light curves, and hence are often used as VLBA flux calibrators, since some are point sources even at VLBA resolutions. These sources, along with other steep spectrum radio sources, have been reported to be non-IDV sources. The *MOJAVE* sample due to its selection bias, contains only 18 CSS/GPS and 10 steep spectrum sources. Plots of the various variability indices

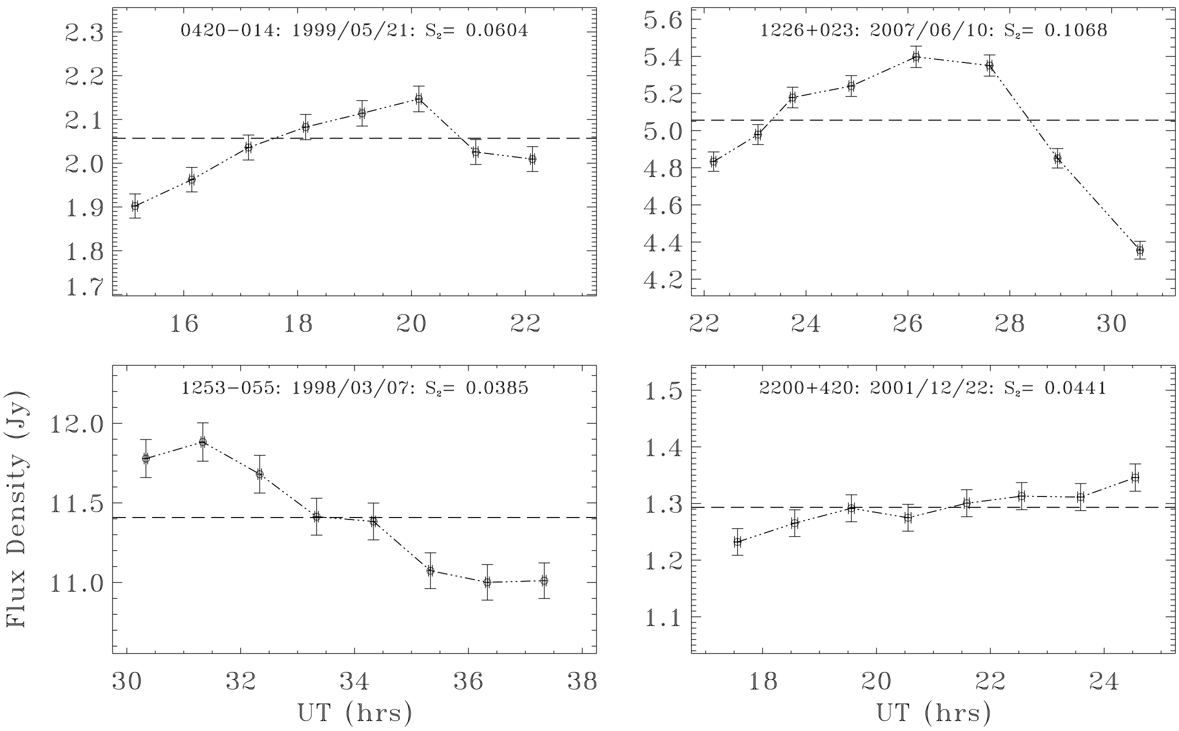

Figure 6.6. Sample VLBA 2 cm light curves for selected IDV sources. These light curves are markedly different from the IDV light curves of GPS/CSS sources (Fig. 6.5).

plotted against the average GAINT flux density for sources with steep or peaked spectra are shown in Fig. 6.11. The plots of variability indices calculated from the GAINT light curves of these sources are indistinguishable from their counterparts calculated from the SELFC light curves, which lends credence to the assumption that these sources indeed show no IDV. Hence, these sources may then be used to establish a suitable criterion to distinguish between the IDV and non–IDV light curves among the rest of the sample. As can be seen from Fig. 6.12, the flux density RMS values for these sources are all $\leq$ 50 mJy. Steep spectrum sources also typically exhibit no IDV (see Fig. 6.12). Henceforth CSS/GPS and steep spectrum sources will be grouped into one category. It was also find that, with the exception of the CSS LPRQ 1828+487[4] (size > 20 kpc; $z = 0.692$, $\beta_{\rm app} = 13.7$), these sources have low T_b values $\left(\lesssim 10^{11}\ \mathrm{K}\right)$.

[4]http://www.physics.purdue.edu/MOJAVE/sourcepages/1828+487.shtml

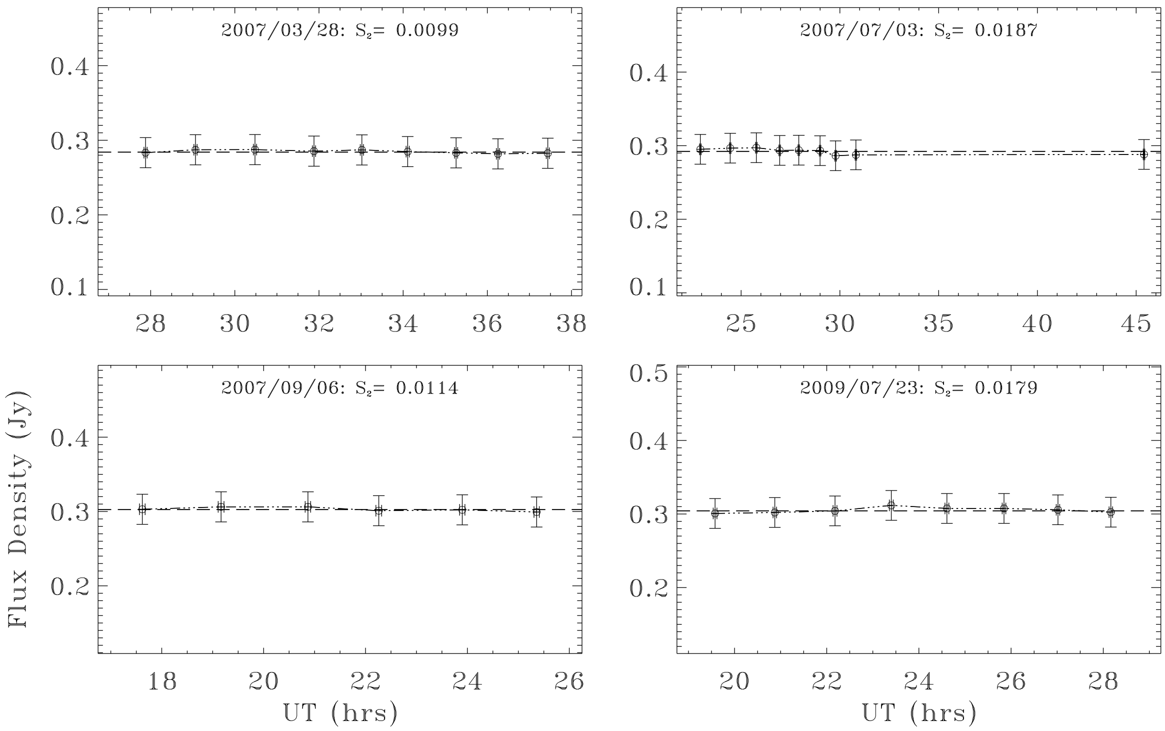

Figure 6.7. 2 cm VLBA light curves for the QSO 1331+170. Though classified as FSRQ, the light curves appear similar to those of known CSS/GPS sources (Fig. 6.5), and its spectrum is also peaked (Fig. 6.8).

From its high $\beta_{\rm app}$, strong extended emission on kpc scales [log $\rm R_{kpc} = -0.42$; Lister et al., 2001] – both uncharacteristic of CSS/GPS sources – and pc scale jet structure, 1828+487 may be considered a mis-classified CSS source.

Fig. 6.13 shows the RMS values plotted against the average flux density and the histogram of RMS distribution for all the sources included in the current study. The RMS distributions for the CSS/GPS/Steep spectrum sources and flat spectrum sources are clearly quite different, with the RMS distribution of the flat spectrum sources having a long tail. Fig. 6.14 shows the variability indices plotted against the average flux density for the full sample. Using the plots in Figs. 6.11, 6.13, the values of the parameters p, s were found to be 0.015 and 20 mJy respectively for 99.9% confidence

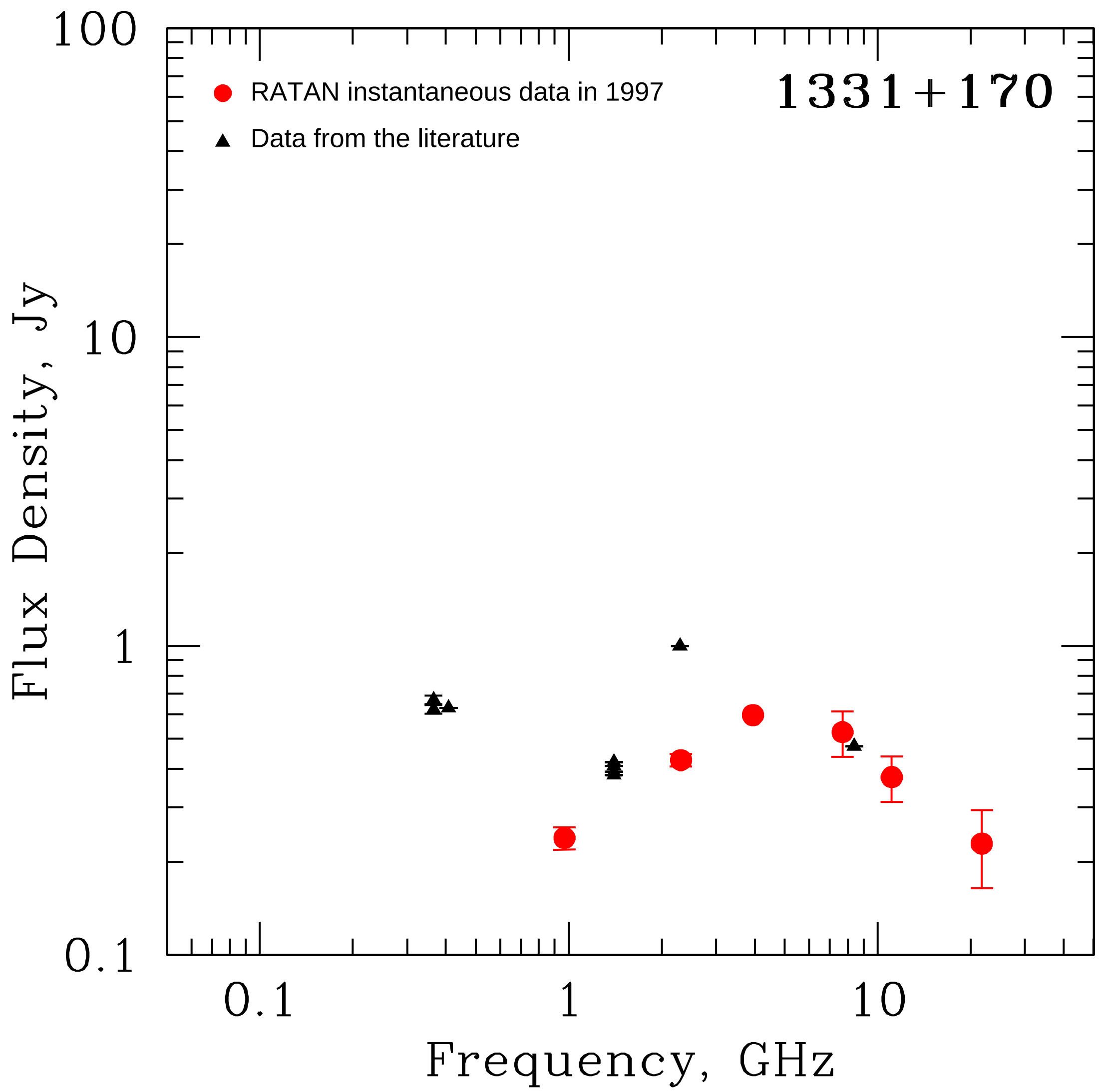

Figure 6.8. The radio spectrum of the EGRET detected QSO 1331+170 (OP 151; z = 2.084). This source has been previously classified as a FSRQ; But current IDV analysis indicates it to be a GPS source. A spectral peak around 5 GHz is clearly evident.

level, which can then be used to determine the IDV criterion for each light curve via Eqn 5.7. In summary, any light curve satisfying the following criteria: $RMS \gtrsim 40$ mJy and modulation index (m) $\gtrsim 3\%$, was classified to be exhibiting IDV. Fig. 6.12 shows

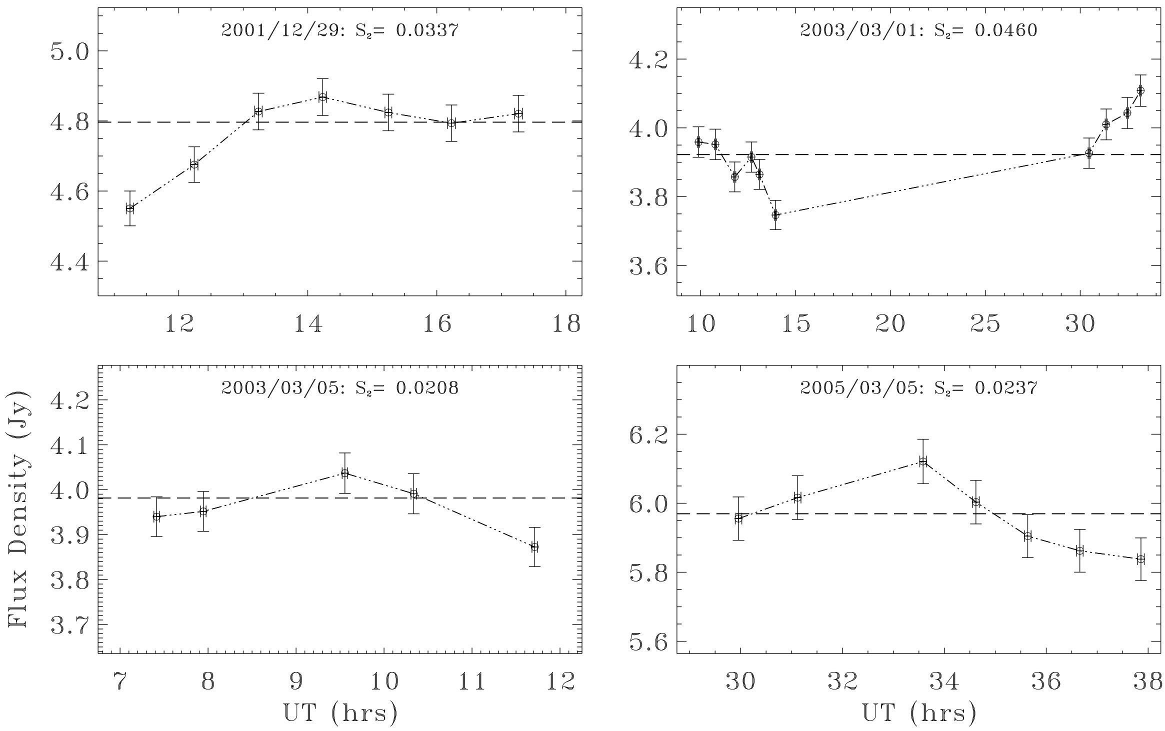

Figure 6.9. Sample 2 cm VLBA IDV light curves for the HPRQ 1334−127. Though classified as a 'candidate GPS' source, this source shows IDV. Its spectrum is also variable, and does not show any clear peak (Fig. 6.10).

the RMS values plotted against the average flux density and the histogram of RMS distribution for the CSS/GPS/Steep spectrum sources only. The RMS values in excess of 40 mJy are due to the superluminal BLRG 0415+379 (3C 120)[5].

Both the modulation index as well as the S_2 statistic are highly correlated and exhibit similar behavior (Fig. 6.14), with a Kendalls's rank (Tau) correlation coefficient of $\sim$ 1.0 at a significance level of $>$ 99.9%. This is to be expected, since both these quantities are measures of variability.

[5] See `http://www.physics.purdue.edu/astro/MOJAVE/sourcepages/0415+379.shtml`

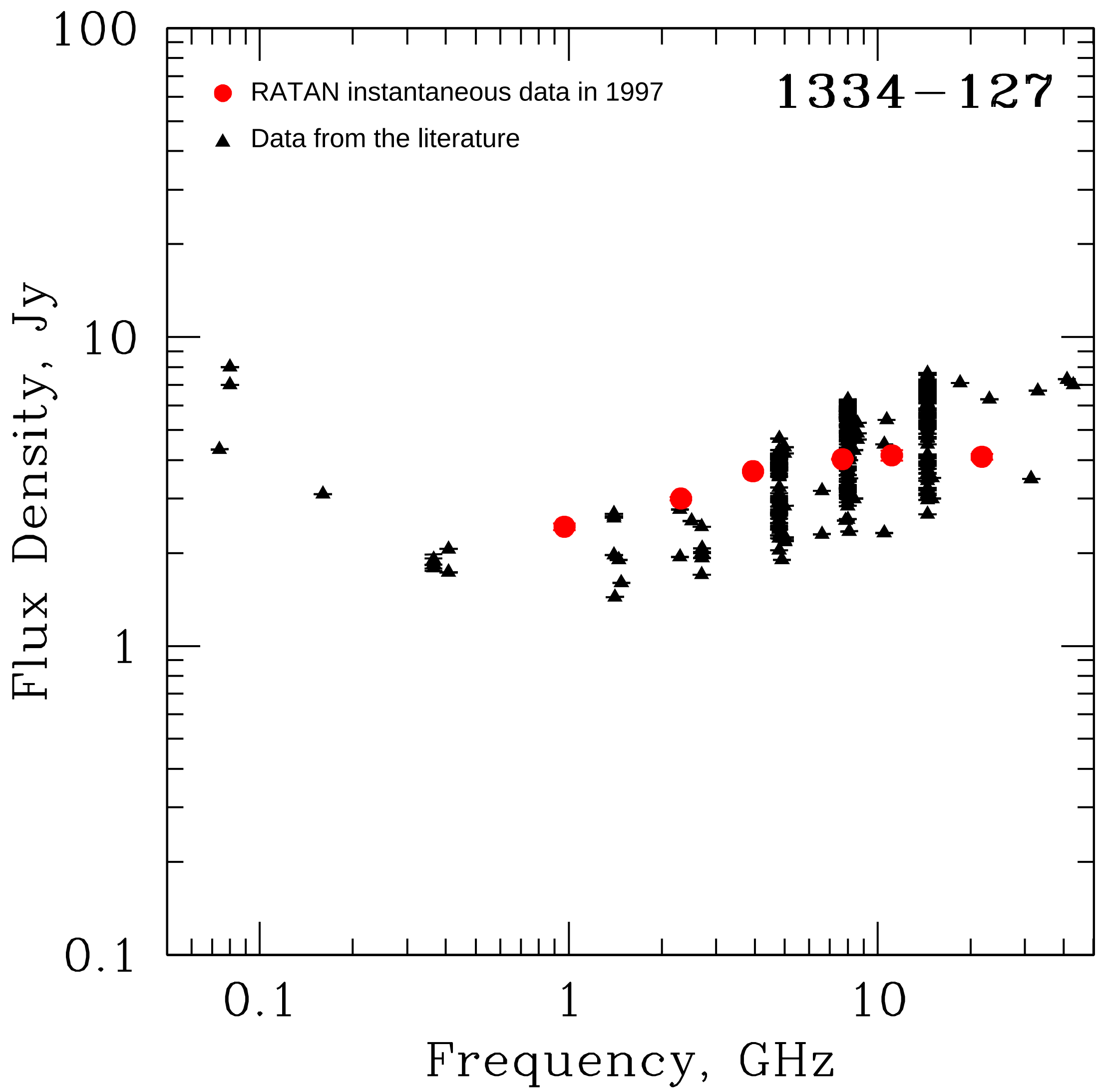

Figure 6.10. The radio spectrum of the 'candidate GPS' GeV HPRQ 1334−127 ($z = 0.539; \beta_{\rm app} \sim 10.26$). The spectrum is highly variable, with no evidence of any clear peak. IDV in this source was detected using the current analysis.

6.4 IDV Modulation Index: Some Trends

The modulation index (m) appears to be anti-correlated with $\delta_{\rm eq}$ and $\beta_{\rm app}$, as can be seen from Fig. 6.15, 6.16. In these plots, the values of the various variability indices viz., modulation index (m) and the S_2 statistic, are plotted against $\beta_{\rm app}$ and $\delta_{\rm eq}$. In general the correlation between the modulation indices and $\delta_{\rm eq}$ is much stronger (see Table 6.1). The negative correlation between m and $\delta_{\rm eq}$ implies that IDV is hard to detect in highly beamed (viz., very bright) sources, especially with single dish or compact array observations, since the IDV core cannot be resolved from the surrounding emission. Higher resolution VLBI observations would greatly increase the value of IDV studies, like the current one using the VLBA.

The reason for the negative correlation between m and $\delta_{\rm eq}$ is most probably due to the very strong positive correlation between flux density and beaming (Fig. 6.17). The rms values are also positively correlated with $\delta_{\rm eq}$ (see Fig. 6.18 & Table 6.1), but the strength of this correlation is smaller. Hence, the modulation index, which is rms/mean, would be expected to be negatively correlated, albeit weakly, with $\delta_{\rm eq}$.

6.5 Statistical properties of IDV in radio-selected AGN

6.5.1 Relative frequency of the IDV phenomenon

A brief summary of IDV results from the current study is presented in Table 6.2. Of the 373 sources analyzed, 269 never exhibited IDV, while 67 exhibited IDV in multiple epochs. The total number of epochs analyzed per source ranged from 1 to 72 (Fig. 6.19), with the median values being 16 and 3 for the IDV and non-IDV sources respectively. For sources showing IDV in more than one epoch, the median number of IDV epochs is 4.

6.5.2 Dependence of IDV on the optical AGN class

A clear distinction among the IDV characteristics of QSO and BL Lac objects was found. IDV is more common among the QSOs (with variability detected in $\sim 25.7\%$

Table 6.1. Correlation properties of the various variability indices

Correlating Quantities	Spearman's Rank		Kendall's (tau) Rank	
	rank	significance	rank	significance
(1)	(2)	(3)	(4)	(5)
$\beta_{\rm app}$ vs. Mean flux density	0.4109	> 0.9999	0.4563	1
$\beta_{\rm app}$ vs. rms	0.2937	> 0.9999	0.1928	> 0.9999
$\beta_{\rm app}$ vs. Modulation index	-0.1933	0.9955	-0.1324	0.9960
$\beta_{\rm app}$ vs. S_2 statistic	-0.2004	0.9968	-0.1370	0.9971
$\delta_{\rm eq}$ vs. Mean flux density	0.6307	> 0.9999	0.4563	1
$\delta_{\rm eq}$ vs. rms	0.4596	> 0.9999	0.3153	1
$\delta_{\rm eq}$ vs. Modulation index	-0.3036	> 0.9999	-0.2044	> 0.9999
$\delta_{\rm eq}$ vs. S_2 statistic	-0.3124	> 0.9999	-0.2099	> 0.9999

Note. — Columns are as follows: (1) Quantities being correlated; (2) Spearman's rank correlation coefficient; (3) two sided significance of the correlation; (4) Kendall's (tau) rank correlation coefficient; (5) two sided significance of the correlation.

of QSOs and 19.8% of all QSO light curves) than in BL Lacs or Galaxies ($\sim$ 1.7% and 2.2% of light curves respectively). On the other hand, objects classified as intermediate BL Lac/QSO – with $\sim$ 20.4% of the light curves being IDV – appear to be as variable as QSOs. Also, all these intermediate objects have high optical polarization and a GeV detection. The source 0003−066 (NRAO 005) is listed to be an unconfirmed BL Lac object by Véron-Cetty & Véron [2001], but also has been classified a galaxy by others [e.g., Vijayanarasimha et al., 1985, Kedziora-Chudczer, 1998]. However, it has one of the highest values of fractional linear polarization in cm VLBA images of the *MOJAVE_1* sample [Lister & Homan, 2005] and its VLBA map reveals a one-sided structure, with superluminal apparent speed [Lister et al., 2009a]. Thus, the only confirmed BL Lac in the current sample with persistent IDV (Table 6.3) is 0716+714, a well known IDV source with rapid, correlated variability at cm, mm and optical wavelengths and therefore thought to be intrinsic in origin [e.g., Wagner et al., 1996, Fuhrmann et al., 2008]. 0716+714[6] has one of the highest values of measured $\beta_{\rm app}$ for a BL Lac object, and has been frequently ejecting radio components of late. It may also be noted that quasi–periodic oscillations (on the time scale of $\sim$ 15 min) in its optical light curve, from December 2008, of 0716+714 have also been reported [Bindu et al., 2010].

Another noteworthy finding is that, compared to genuine BL Lacs, not only do a larger fraction of light curves from intermediate BL Lac/QSOs show IDV, but also every one of these objects exhibits IDV. A serendipitous discovery of IDV in 2131−021, via VLBI studies at 6 cm, has been reported [Gabuzda et al., 2000b].

[6]See: `http://www.physics.purdue.edu/astro/MOJAVE/sourcepages/0716+714.shtml`

Table 6.2. IDV properties of the various source types in the full AGN sample

Type	Sample Size		High Opt.Pol.		GeV		Epochs	IDV Incidences	
	N	% IDV	N	% IDV	N	% IDV	N	N_IDV	% IDV
(1)	(2)	(3)	(4)	(5)	(6)	(7)	(8)	(9)	(10)
QSO	246	31.7%	52	67.3%	137	37.3%	2250	320	14.2%
BL/Q	11	100%	11	100%	11	100%	379	49	12.9%
BLL	54	14.8%	24	29.2%	42	14.3%	510	16	3.1%
Gal.	37	10.8%	1	0%	8	13%	318	11	3.5%
U	25	12%	⋯	⋯	12	8.3%	69	3	4.4%
Total:	373	27.9%	88	60.2%	210	31.9%	3526	399	11.3%

Note. — Columns are as follows: (1) Source type, where QSO = quasar, BLL = BL Lac object, Gal. = active galaxy, BL/Q = intermediate BL Lac/quasar as inferred from the presence of broad lines in their optical spectra (but usually listed as BLL), and U = optically unidentified; (2) total number of objects in the sample; (3) fraction of objects with IDV detection; (4) number of objects with known optical polarization $> 3\%$; (5) fraction of high optical polarization objects showing IDV; (6) number of objects with GeV detection; (7) fraction of GeV detected sources showing IDV; (8) total number of epochs analyzed; (9) number of epochs showing IDV; (10) fractional number of epochs showing IDV.

Table 6.3. IDV properties of genuine BL Lacs with IDV detection in at least one epoch

Source (1)	Epochs (2)	IDV (3)	incidences (4)
0003−066[a]	22	4	18.2%
0048−097	15	2	13.3%
0109+224	17	1	5.9%
0716+714	37	5	13.5%
0808+019[b]	13	1	7.7%
0814+425	18	1	5.6%
1413+135	14	1	7.1%
1514−241	13	1	7.7%
All:	149	16	10.8%

[a]Sometimes classified as Gal. in literature, e.g., Vijayanarasimha et al. [1985]

[b]High z (1.148); Sbarufatti et al. [2005] report MG II line width of 5.1Å, close to that of QSOs.

Note. — Columns are as follows: (1) IAU Name (B1950.0); (2) total number of epochs in the sample; (3) number of IDV epochs; (4) fraction of epochs showing IDV.

Table 6.4. IDV properties of intermediate BL Lac/Quasars

Source (1)	Epochs (2)	IDV (3)	Incidences (4)
0215+015	12	2	16.7%
0235+164	24	2	8.3%
0754+100	23	4	17.4%
0823+033	25	2	8.0%
0851+202	67	14	20.9%
0954+658	26	1	3.8%
1749+096	45	5	10.9%
1803+784	27	4	14.8%
1823+568	39	2	5.1%
2131−021	19	3	15.8%
2200+420	71	10	14.1%
All:	379	49	12.9%

Note. — Columns are as follows: (1) IAU Name (B1950.0); (2) total number of epochs in the sample; (3) number of IDV epochs; (4) fraction of epochs showing IDV.

6.5.3 Apparent speed and Brightness Temperature dependence of IDV

Lister et al. [2009b], Kellermann et al. [2004] and Ros et al. (in prep.) have measured apparent speeds ($\beta_{\rm app}$) for 207 sources in the *MOJAVE* sample. Fig. 6.20 shows the distribution of this quantity for the full sample as well as that for only the IDV sources, in which a positive correlation between $\beta_{\rm app}$ and fractional number of sources showing IDV is evident. Excluding the lone outlier 0805−077 ($z = 1.837$, $\beta_{\rm app} = 50.6$) – a non-IDV source – a Kendall's tau correlation coefficient of 0.81 with a significance level of 98.9% was inferred. The exclusion of 0805−077 is justified, since the $\beta_{\rm app}$ bins above $\beta_{\rm app} = 40$ have no sources (and hence the fractional number of sources showing IDV is undefined), which would lead to spurious estimates of the correlation coefficient. Also estimated, were the T_b values for 200 sources in the sample as described in § 5.3. Of these, 74 show IDV. The distribution of T_b values in the full *MOJAVE* sample, along with that of the IDV sources alone is presented in Fig. 6.21. A positive correlation between T_b and fractional number of sources showing IDV was found with, the correlation coefficient being 0.5 at a significance level of 94%. This correlation could have been stronger, but for the sources with T_b values in the bin $(3 - 3.5) \times 10^{12}$ K. Of the 3 sources in this bin, 2 are non-IDV. This could be attributed to the fact that these sources have fewer total VLBA epochs compared to most of the other sources. The 2 non-IDV sources (1417+385 and $1243-072$) have only 6 and 7 epochs of data respectively – they are among the latest additions to the *MOJAVE* sample and hence span a smaller time range – while the lone IDV source has a slightly higher number of epochs (10). It is also noteworthy that all 3 of these high T_b sources have a GeV-detection, thus providing additional data in support of their high beaming factors. If this bin is excluded, the correlation indeed is stronger (0.69 at 98.3% significance).

In determining the fractional number of sources showing IDV as a function of $\beta_{\rm app}$ or T_b, no distinction between whether a source exhibited IDV in only one (or few) epochs or in most of the epochs analyzed i.e., is a persistent IDV source, was made. However, it is of interest to see if any correlations exist between any of the aforementioned source properties and persistence of IDV. Hence, the total number of epochs analyzed and the number of epochs that showed IDV for all the sources in a given $\beta_{\rm app}$ or T_b bin were plotted (Figs. 6.20 panel b and 6.21 panel b). Also plotted were the distribution of fractional number of epochs showing IDV in Figs. 6.20 panel d and 6.21 panel d. It is evident from these plots that AGN with high beaming factors are much more likely to exhibit IDV at any given epoch, i.e., there is a positive correlation between the fractional number of epochs showing IDV and $\beta_{\rm app}$ (95.7% significance level), and T_b (significance level of 94.1%). However, the correlation becomes stronger (99.7% significance level) if the bin $25 \leq \beta_{\rm app} \leq 30$ is excluded. Similarly, upon the exclusion of the bin $3 \times 10^{12} \leq T_b < 3.5 \times 10^{12}$ K – due to the low number of observations – the correlation becomes more significant (97.8%).

6.5.4 Galactic latitude and Redshift dependence of IDV

Fig. 6.22 shows the galactic latitude distribution of all the sources in the current sample (unshaded) along with that of the IDV sources (shaded). Also shown is the galactic latitude dependence of the fractional number of IDV sources from the sample. A negative correlation (correlation coefficient = -0.79; $>$ 99.9% significance level) between the galactic latitude and fractional number of IDV sources was found, indicating a higher fraction of IDV sources among those closer to the galactic plane, where a higher number of scattering screens and larger scattering probability is to be expected. This is consistent with results from the *MASIV* survey [Lovell et al., 2008]. However, from Fig. 6.22 panel d it is evident that no correlation exists between the fractional number of epochs showing IDV and the galactic latitude. There are 342 AGN in the full sample of 373 sources, which have a known redshift (z). Fig. 6.23 presents the z distribution for all these sources along with the ones with

IDV detection. No correlation between IDV detection and source redshift was inferred.

6.5.5 Seasonal dependence of IDV

A recognized signature of ISS is *annual modulation* viz., a change in variability time-scales due to changes in the relative velocity of the scattering clouds as a result of Earth's annual motion, when combined with that of the Sun with respect to the Local Standard Rest-frame (see § 3.1.4). If the scattering clouds are indeed stationary in the LSR (as is usually assumed), a slowing down of IDV is to be expected in the latter half of the year, due to the relative velocity of the scattering screen with respect to an observer on the Earth being lower at that time. The relatively high fractional errors in the VLBA light curves, sombined with the *MOJAVE* observing mode (see § 6.8) make the current analysis less sensitive to slow and low amplitude IDV. Hence, in the IDV/non-IDV classification scheme adopted here, a smaller fraction of IDV incidences in the latter half of the year is to be expected. Fig. 6.24 shows the distribution of IDV incidences as a function of calendar year day number. As can be seen from the panel 'b' of this figure, the distribution is flat and the correlation coefficient has very low significance level. A similar result was reported by Lovell et al. [2007]. This result may be construed to support the hypothesis that intrinsic variability is the dominant mechanism for IDV, at least in a highly beamed sample like *MOJAVE*. However, the expected slowing down in IDV is very sensitive to the assumptions regarding the scattering screen velocities, and others have proposed this non-slowing to be indicative of non-stationary scattering clouds [e.g., Lovell et al., 2008].

6.6 The *MOJAVE_1* Sample

Not all the objects in the full sample have multiple epochs of data in the *MOJAVE* archive (as they were not part of the flux-density limited *MOJAVE_1* sample and hence have not been observed regularly). Since IDV is an episodic phenomenon, the number of epochs a source has been observed in plays a crucial role in determining whether it is classified as an IDV source or not. Hence, in this section only the 135 objects in the original *MOJAVE_1* sample of Lister & Homan [2005] have been analyzed. After excluding 4 sources (as discussed in § 6), the current analysis consists of 131 sources, of which, IDV was detected in 81 ($\sim 61.8\%$), with 61 sources exhibiting IDV in multiple epochs. This is slightly higher than the fractions reported in other surveys [e.g., Quirrenbach et al., 1992, Lovell et al., 2008], which is to be expected since the *MOJAVE_1* sample spans a larger number of epochs per source compared to the aforementioned observations and also, only the highly beamed (and hence highly variable) sources are being considered.

Fig. 4.2 panel b shows the sky positions of all the sources in this sample. Table 6.5 gives the details of IDV detection among the various source types. IDV was detected in $\sim 15\%$ of epochs. The number of epochs for each source ranges from 4 to 72, with the median number being 15 (18 for the IDV sources and 12 for the non-IDV sources only). The IDV detection rate among the QSOs and the intermediate BLL/QSO sources is very similar ($\sim$ 18% & 13.6% of epochs respectively) while the genuine BL Lacs and radio galaxies appear to be predominantly non-IDV (IDV detection rate of only $\sim 6.1\%$ and 6.5% respectively).

6.6.1 Brightness Temperature vs. *Fermi* GeV Detection

Of the 135 sources in the *MOJAVE_1* sample, 87 have a GeV detection, viz., are part of the *Fermi* LAT 1–year catalog. Of these 87 sources, 53 sources have no EGRET detection. Of the 48 sources classified to be non–GeV, 4 sources have no LAT 1–year detection, but have a *probable* EGRET identification [Mattox et al., 2001, Sowards-Emmerd et al., 2003, 2004]. Fig. 6.25 shows the T_b distribution for the 121 members of the *MOJAVE_1* sample with well defined T_b values. Of the 3 non–GeV sources in the *MOJAVE_1* sample with a high T_b value, 2 have a 'probable' EGRET detection, but no LAT detection as yet. The remaining source – 2037+511 ($z = 1.686$, $\beta_{\rm app} = 3.3$) – has a high redshift, which probably is responsible for its non-detection as of date. Two more sources (making a total of 4) have only a EGRET 'probable' identification, but no LAT 1–year detection and hence classified by us to be non-GeV sources. All 4 of these sources also are high redshift sources. Also, as expected, most of the GeV detected sources with $T_b \lesssim 10^{11}$ K are low redshift sources. The only exception to this is the high $\beta_{\rm app}$ GeV source: 1127$-$145 ($z = 1.184$, $\beta_{\rm app} = 14.2$), which is consistent with the fact that powerful (i.e., high Γ) sources are indeed very rare. Tingay et al. [2001] have reported a similar correlation between EGRET detection and brightness temperature values measured from space VLBI, in a much smaller sample. A strong positive correlation between $\beta_{\rm app}$ and GeV detection has also been observed [Lister et al., 2009c], which is to be expected from Fig. 6.25. This is in agreement with the recently reported correlation between $\delta_{\rm var}$ and GeV detection [Savolainen et al., 2010]. These results further corroborate recent findings that GeV $\gamma-$ ray emission is beamed. All the sources with high T_b values are also among the sources with high T_b at 86 GHz [Lee et al., 2008]. It was also noticed that among the top 20 *MOJAVE_1* sources with the highest GeV variability index values (as tabulated in the LAT–1yr catalog), 17 show IDV. This is in accordance with previous observations that both IDV activity as well as GeV emission correlate strongly with beaming.

The same IDV analysis as in § 6.5 was repeated, but this time for only the 131 sources in the *MOJAVE_1* sample. The results qualitatively remain the same, in that, once again a strong negative correlation between IDV detection and galactic latitude (correlation coefficient of -0.6 at 99.7% significance level) and a strong positive correlation between IDV detection and $\beta_{\rm app}$, T_b (significance levels of 99.6% and 98.6% respectively) were inferred. Yet again, no correlation between IDV detection and redshift

Table 6.5. IDV properties of the various source types in the flux density–limited *MOJAVE_1* sample

Source Type	Total Number		High Opt.Pol.		GeV		Epochs	IDV Incidences	
	N	IDV	N	IDV	N	IDV	N	N_IDV	% IDV
(1)	(2)	(3)	(4)	(5)	(6)	(7)	(8)	(9)	(10)
QSO	98	61.2%	40	77.5%	65	66.2%	1620	291	18.0%
BL/Q	10	100%	10	100%	10	100%	353	48	13.6%
BLL	13	53.8%	12	50.0%	10	50.0%	245	15	6.1%
Gal.	7	42.9%	···	···	3	33.3%	154	10	6.5%
U	3	33.3%	···	···	1	0.0%	28	1	3.6%
Total:	131	61.8%	62	75.8%	89	66.3%	2400	365	15.2%

Note. — Columns are as follows: (1) Source type, where QSO = quasar, BLL = BL Lac object, Gal. = active galaxy, BL/Q = intermediate BL Lac/quasar as inferred from the presence of broad lines in their optical spectra (but usually listed as BLL), and U = optically unidentified; (2) total number of objects in the sample; (3) fraction of objects with IDV detection; (4) number of objects with optical polarization > 3%; (5) fraction of high optical polarization objects showing IDV; (6) number of objects with GeV detection; (7) fraction of GeV detected sources showing IDV; (8) total number of epochs analyzed; (9) number of epochs showing IDV; (10) fractional number of epochs showing IDV.

was found.

6.7 3C 279: A Correlation between IDV and flaring?

3C 279 ($1253-055$; $z = 0.536$, $\beta_{\rm app} \sim 20.6$)[7] is a luminous HPRQ with frequent flares across the electromagnetic spectrum, and is currently the only known TeV quasar [Albert et al., 2008]. Intra-night variability in the optical light curves for this source was reported by Oke [1967]. Correlations between ejection of VLBI components in 3C 279, and flaring in the cm & mm wavebands has also been observed [Wehrle et

[7]See: `http://www.physics.purdue.edu/MOJAVE/sourcepages/1253-055.shtml`

al., 2001, Savolainen et al., 2002]. 3C 279 shows IDV in almost all the epochs in the current analysis, as is evident from Fig. 6.27, which shows the modulation index and S_2 for all the epochs included in the analysis. A sudden, sharp increase in variability around 1999.74 may be noted. During 1999–2000 a giant flare (brightest to date) in optical, X-Ray as well as $\gamma-$rays was observed along with variability on the time-scale of a day [Hartman et al., 2001]. A superluminal component ejection around the same time has also been inferred [Fig. 6.28 Lister et al., 2009b]. An association between superluminal component ejection events at radio frequencies and γ–ray flaring episodes in this source, has also been observed [Jorstad et al., 2001, Lindfors et al., 2006].

Fig. 6.29 shows the long term VLBA light curve for 3C 279 from the 2 cm *MOJAVE* monitoring data. Also shown is the light curve for the component modeled as the 'IDV core' in the current analysis. The two light curves for the most part follow the exact same trend, reflecting the highly core dominant morphology of the parsec-scale jet. Around the second half of 1999, a rapid variability in the flux densities can be seen. The same is reflected in the single dish multi-frequency UMRAO data (Fig. 6.30; courtesy: M.Aller[8]). The instantaneous slopes of these light curves at each epoch, taken to be the slope of the linear fit to the flux density values at that epoch and the epochs immediately preceding and succeeding it, has also been estimated. Fig. 6.29 shows these values along with the the modulation index values from the IDV analysis. The modulation index clearly shows sharp spikes at the end of 1999, coincident with precipitous changes in the slopes of the two light curves. This trend has been observed in some other sources as well (see § 7).

[8] `http://www.astro.lsa.umich.edu/obs/radiotel/gif/1253_055.gif`

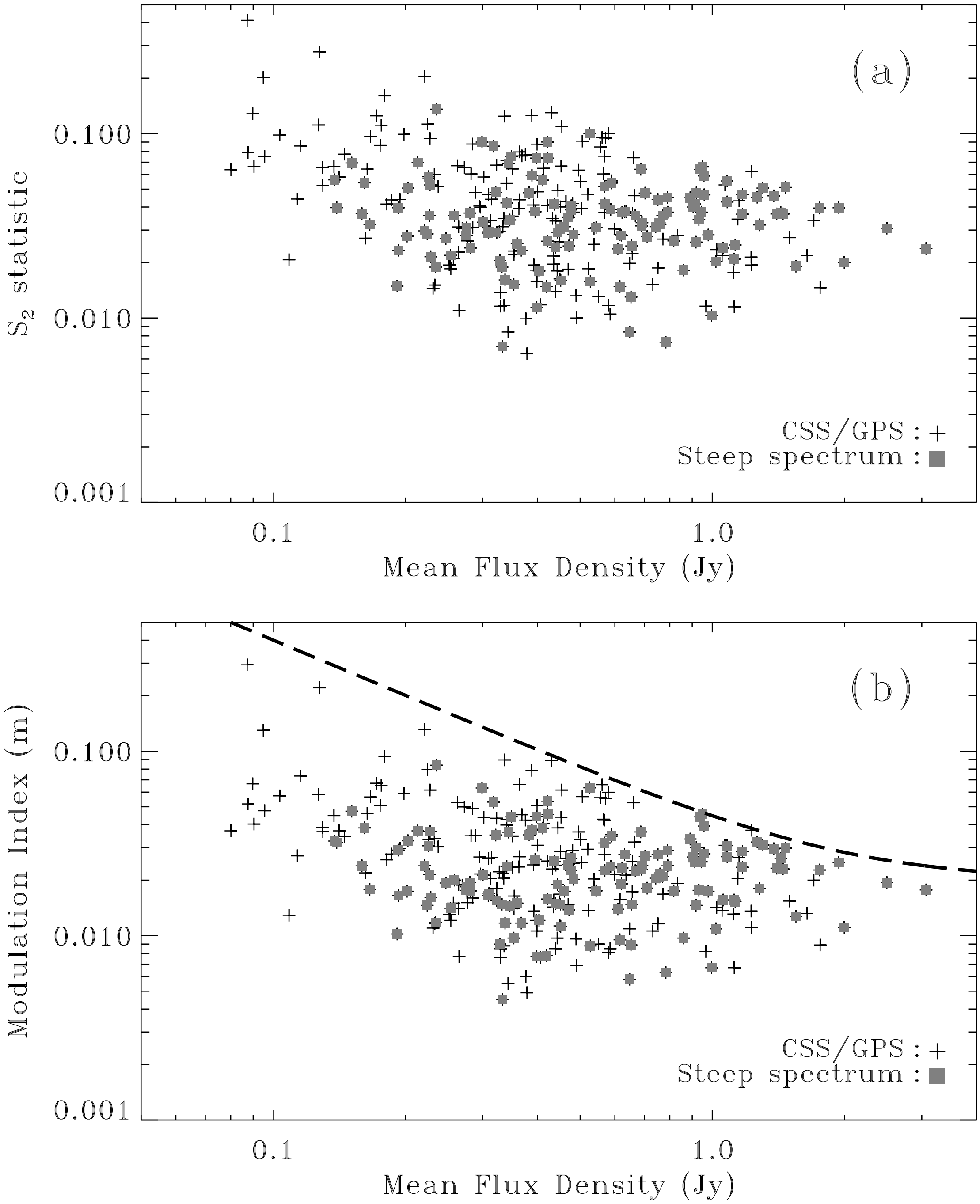

Figure 6.11. (a): Plot of the S_2 variability statistic vs. S_{mean} for CSS/GPS and steep spectrum sources only. (b): Plot of the modulation index (m) vs. the GAINT average flux density (S_{mean}) for CSS/GPS and steep spectrum sources, with the dashed line marking the threshold adopted for distinguishing IDV sources/epochs from the non–IDV ones (see § 5.4). As expected all these sources have very low variability indices, and hence have been used to determine the threshold for variability classification. The variability indices for the steep spectrum sources are similar to those of the CSS/GPS sources alone, indicating that the steep spectrum sources are also generally non–IDV.

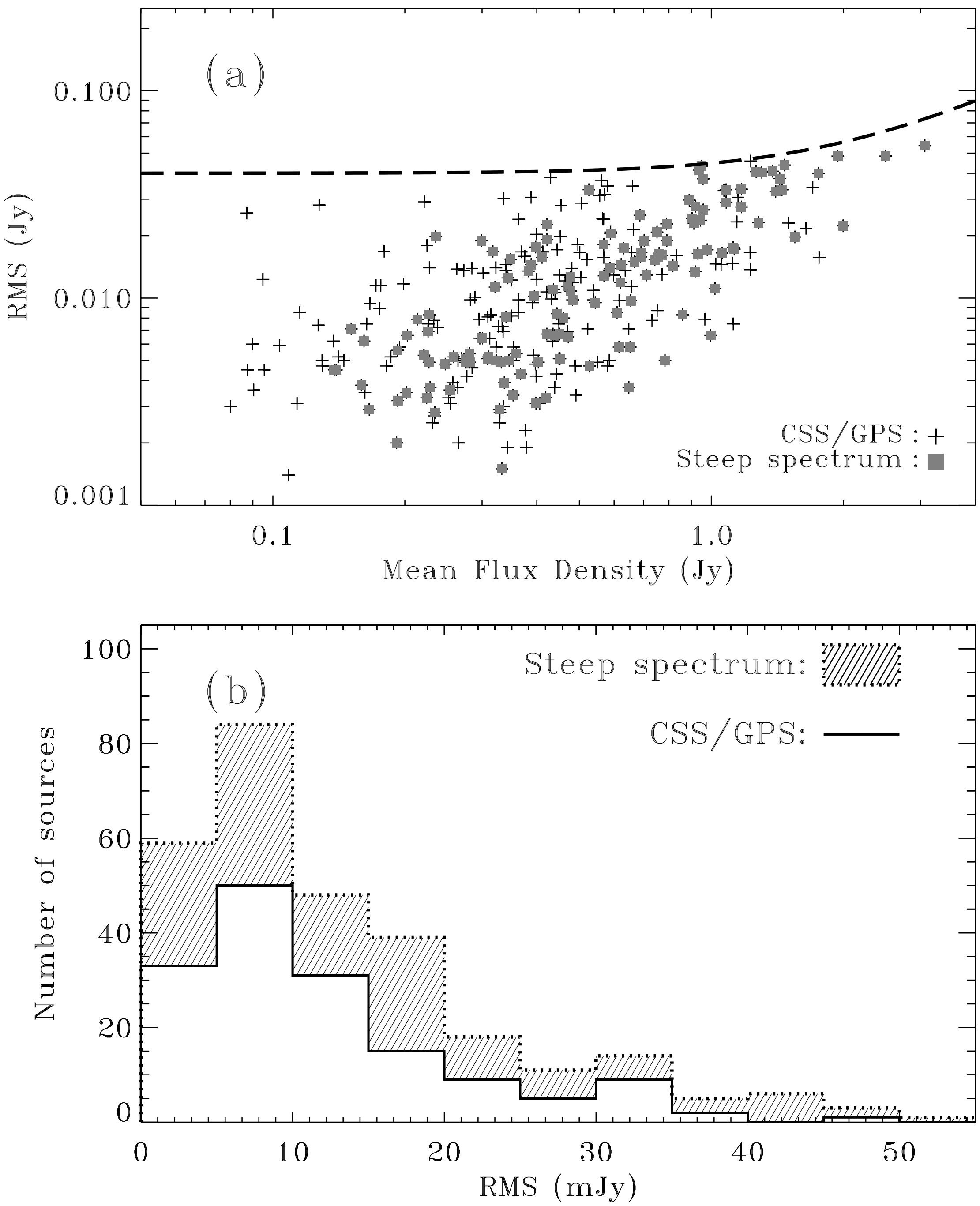

Figure 6.12. (a): Plot of RMS vs. the GAINT average flux density (S_{mean}) for the CSS/GPS/Steep spectrum sources included in the current study. The dashed line marks the threshold adopted for distinguishing IDV sources/epochs from the non–IDV ones. (b): Distribution of RMS for these sources. The RMS values in excess of 40 mJy are from the superluminal steep spectrum source 0415+379 (3C 120).

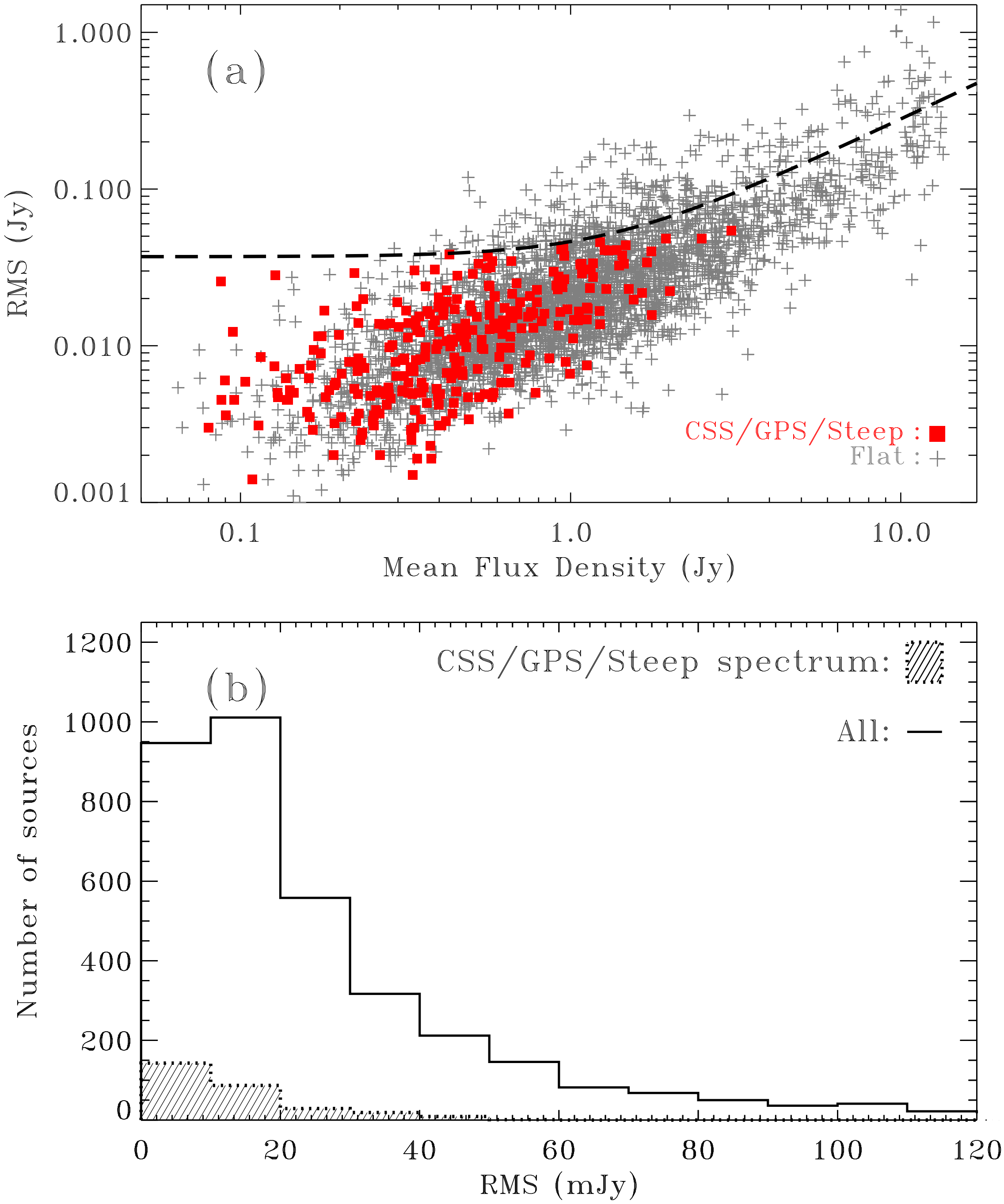

Figure 6.13. (a): Plot of RMS vs. the GAINT average flux density (S_{mean}) for all the sources in the *MOJAVE* sample. The dashed line marks the threshold adopted for distinguishing IDV sources/epochs from the non–IDV ones. (b): Distribution of RMS for these sources. The tail of the distribution for the full sample has not been shown completely, for ease of plotting.

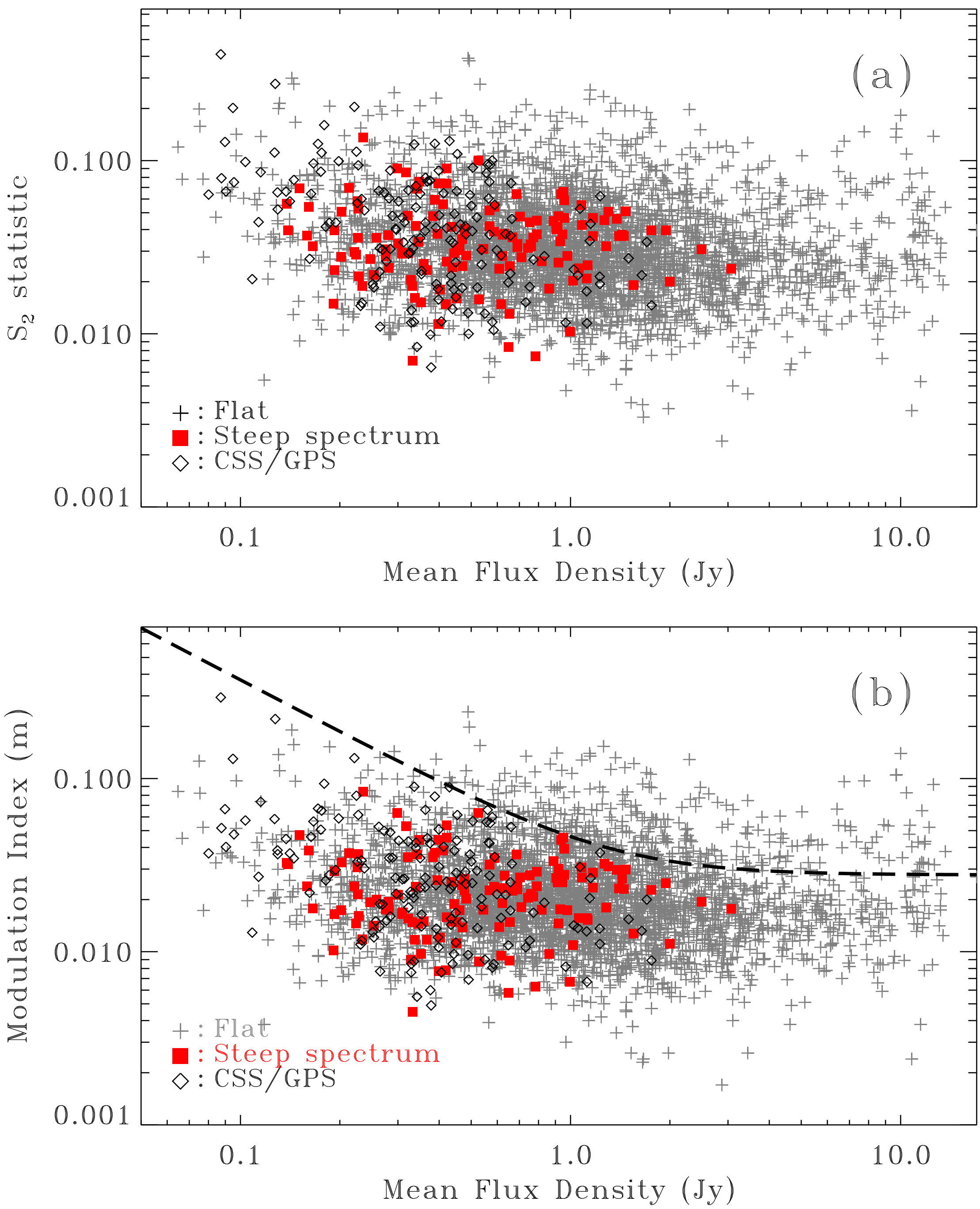

Figure 6.14. (a): Plot of the S_2 statistic vs. the mean flux density for all the sources in the current sample. (b): Plot of the modulation index (m) vs. the mean flux density for the same sources. The dashed line marks the threshold adopted for distinguishing IDV sources/epochs from the non–IDV ones.

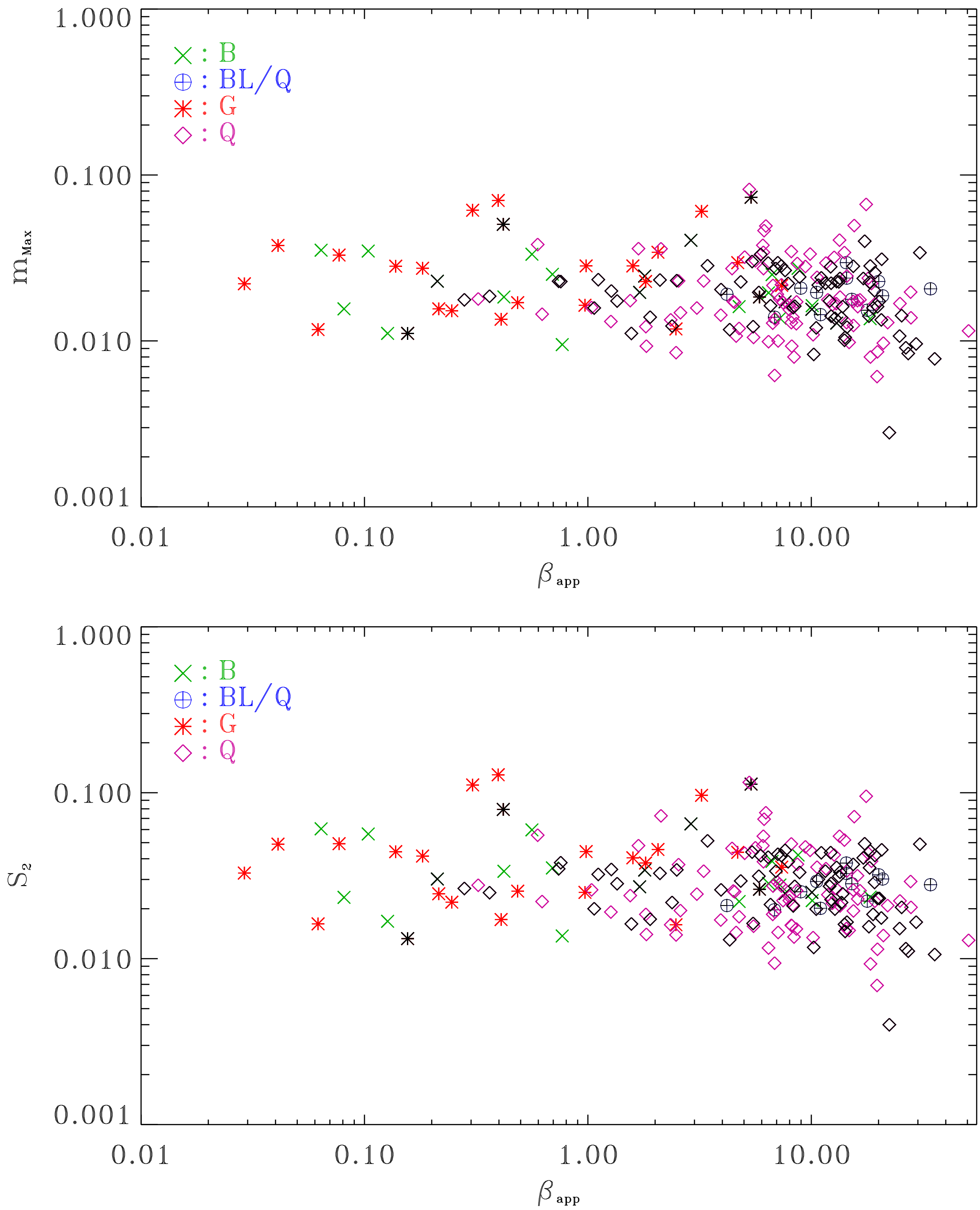

Figure 6.15. Plots of the variability indices viz., modulation index (m) & S_2, vs. $\beta_{\rm app}$, for the various source types: *Top*: m vs. $\beta_{\rm app}$; *Bottom* : S_2 vs. $\beta_{\rm app}$; Symbols in black indicate the values for IDV sources. The m & S_2 plotted represent the first quartile (top 25%) values for each source.

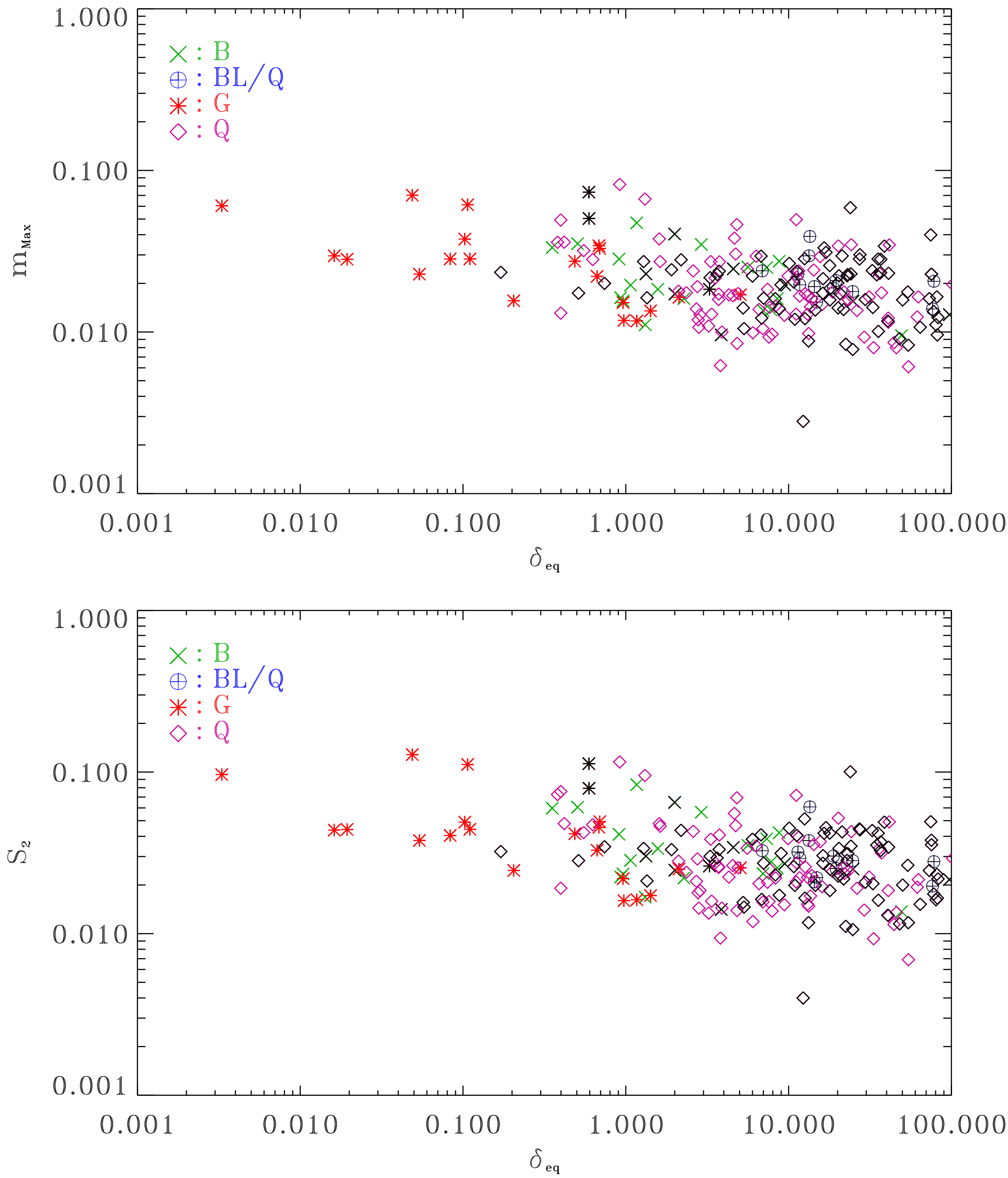

Figure 6.16. Plots of the variability indices viz., modulation index (m) & S_2, vs. δ_{eq}, for the various source types: *Top*: m vs. δ_{eq}; *Bottom*: S_2 vs. δ_{eq}. Symbols in black indicate the values for IDV sources. The m & S_2 plotted represent the first quartile (top 25%) values for each source.

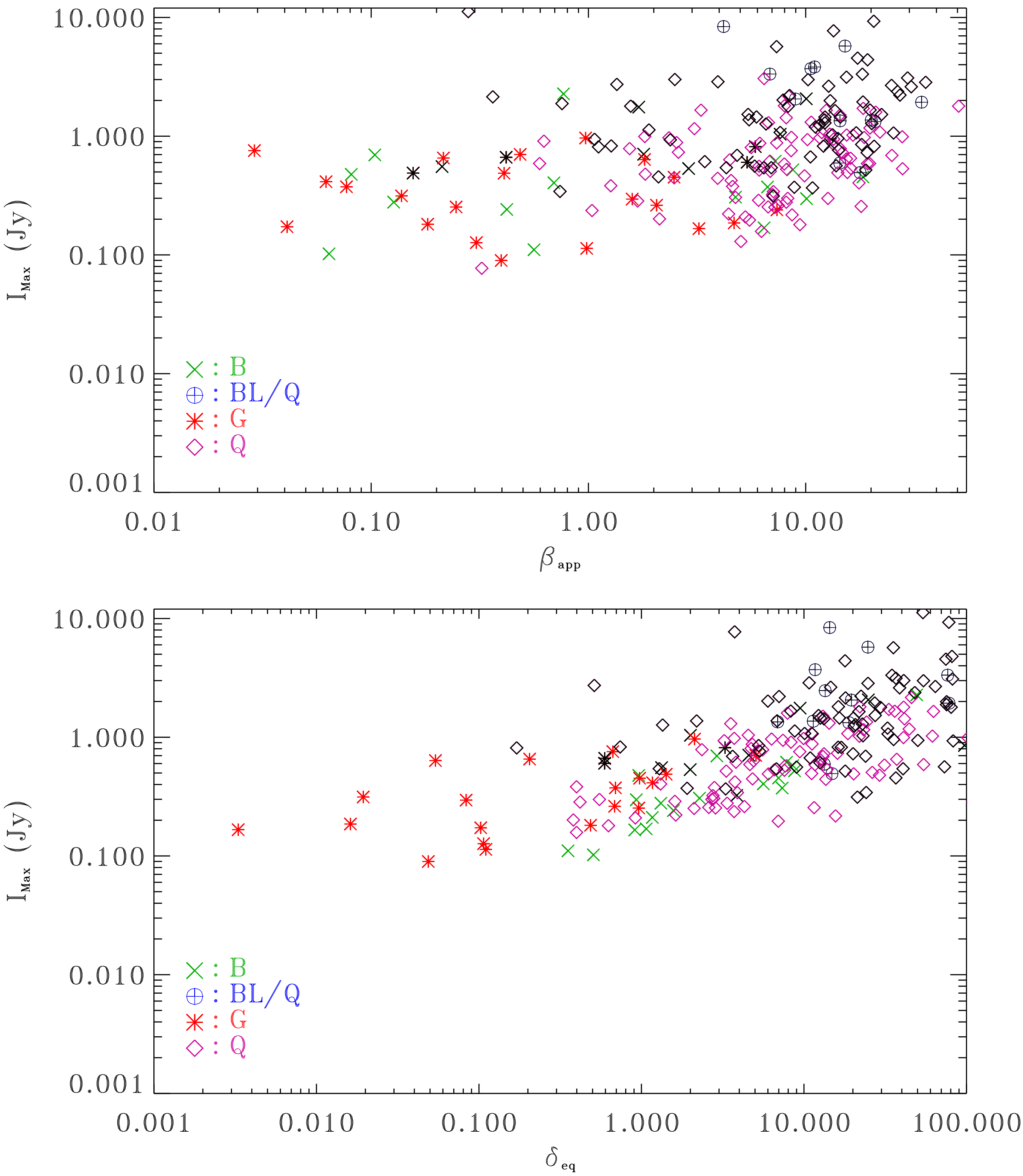

Figure 6.17. Plots of the IDV core flux density vs. beaming indicators, for the various source types: *Top*: Flux density vs. β_{app}; *Bottom*: Flux density vs. δ_{eq}. Symbols in black indicate the values for IDV sources. The flux density values plotted represent the first quartile (top 25%) values for each source. A very strong positive correlation between beaming indicators and flux density is evident.

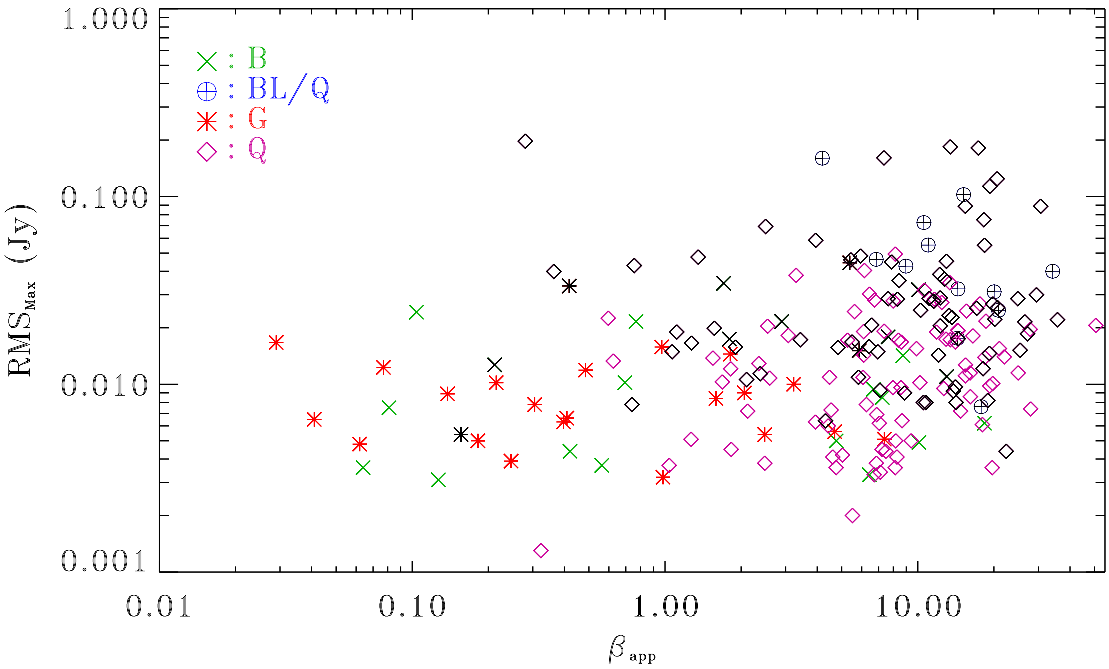

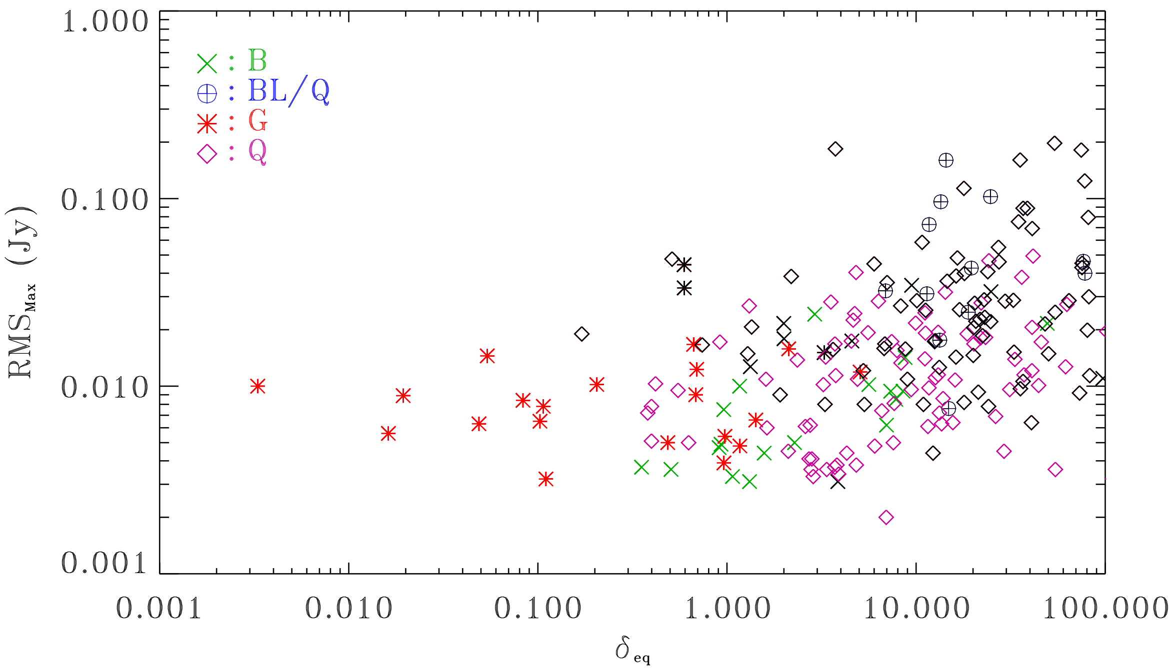

Figure 6.18. Plots of IDV RMS vs. beaming indicators, for the various source types: *Top*: RMS vs. $\beta_{\rm app}$; *Bottom*: RMS vs. $\delta_{\rm eq}$. Symbols in black indicate the values for IDV sources. The RMS value plotted represents the first quartile (top 25%) values for each source.

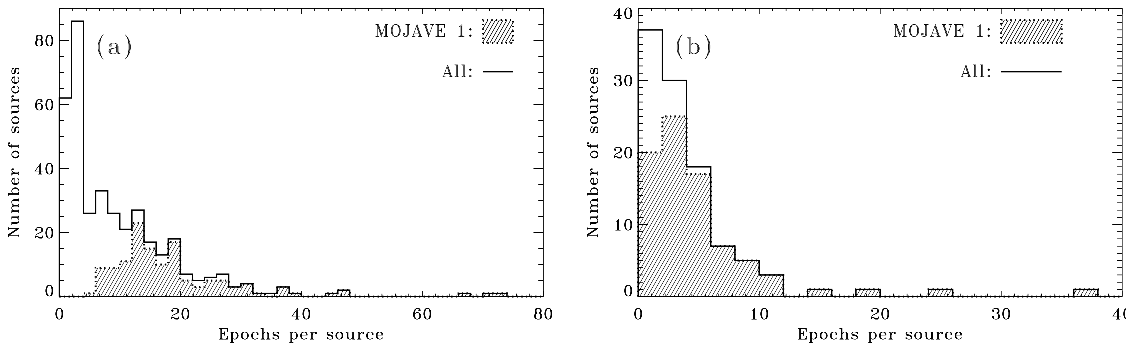

Figure 6.19. (a): Distribution of the number of VLBA epochs analyzed per source in the full sample (unshaded), and the flux-limited *MOJAVE_1* sample (shaded), consisting of 373 and 131 sources respectively. (b): Distribution of the number of epochs analyzed per source for only the objects showing IDV in both the samples. In the full sample, there were 269 non-IDV sources, while 67 showed IDV in multiple epochs. In the *MOJAVE_1* sample, the number of non-IDV sources was 50, while 61 sources had multiple IDV episodes.

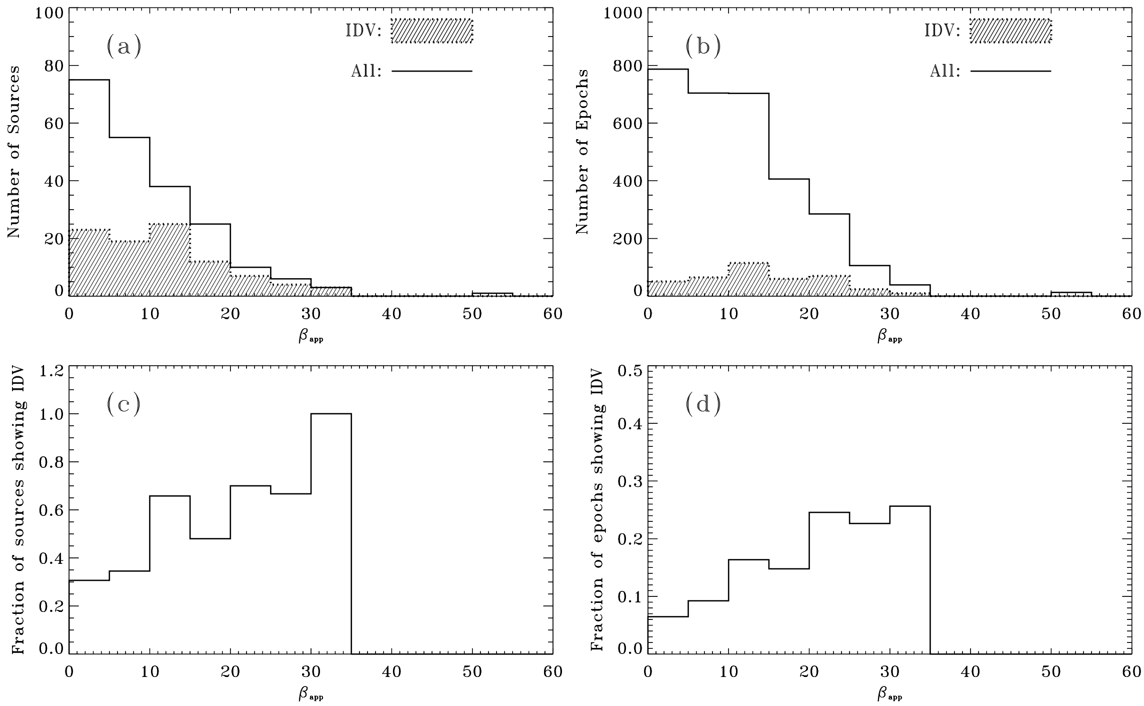

Figure 6.20. (a): Apparent speed (β_{app}) distribution of IDV sources (shaded), and that for all the sources in the *MOJAVE* sample (unshaded). (b): Distribution of the total number of VLBA epochs analyzed (unshaded) and IDV epochs (shaded) as a function of the β_{app} of the corresponding sources. (c): Fractional number of IDV sources from the sample (ratio of the shaded to the unshaded line histograms from panel 'a') as a function of their β_{app}. (d): Distribution of the fractional number of epochs showing IDV as a function of the source β_{app}. AGN with faster jets show a much higher tendency to have exhibited IDV on at least one occasion, as is evident from panel 'c'.

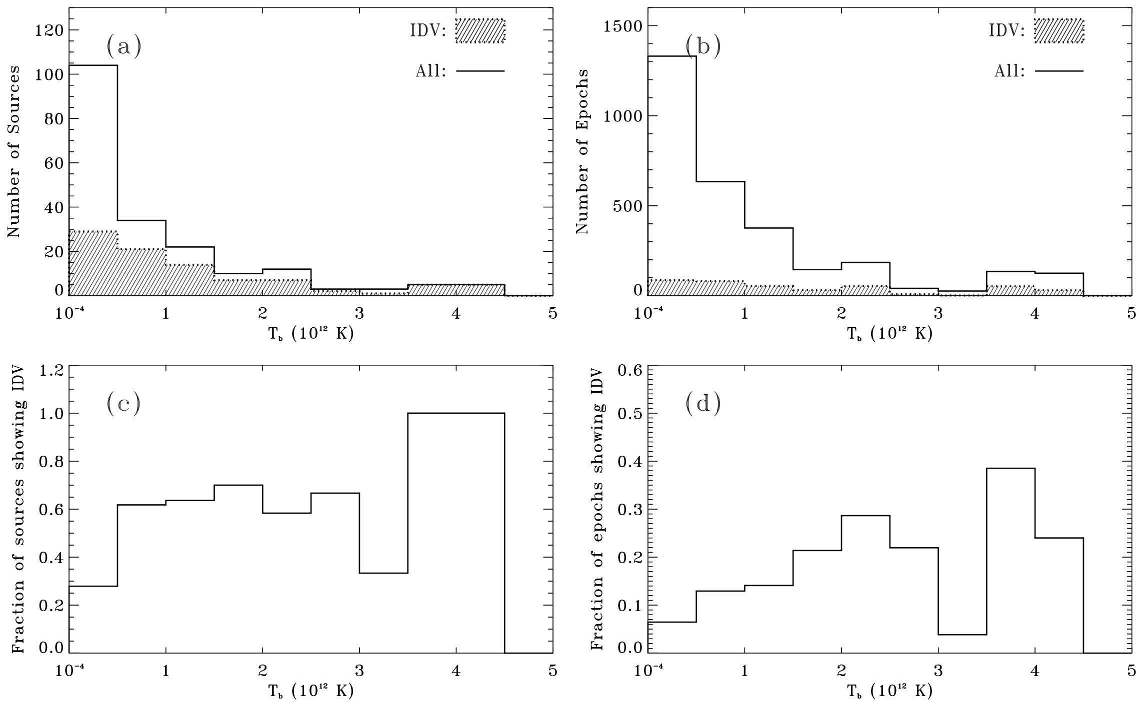

Figure 6.21. (a): Distribution of T_b for IDV sources (shaded), and for all the sources in the *MOJAVE* sample (unshaded). (b): Distribution of the total number of VLBA epochs analyzed (unshaded), and IDV epochs (shaded) as a function of the T_b of the corresponding sources. (c): Fractional number of IDV sources from the sample (ratio of the hatched to the solid line histograms from panel 'a') as a function of their T_b. (d): Distribution of the fractional number of epochs showing IDV as a function of the source T_b. A strong positive correlation between T_b and fractional number of IDV sources, as well as between T_b and fractional number of epochs showing IDV is present.

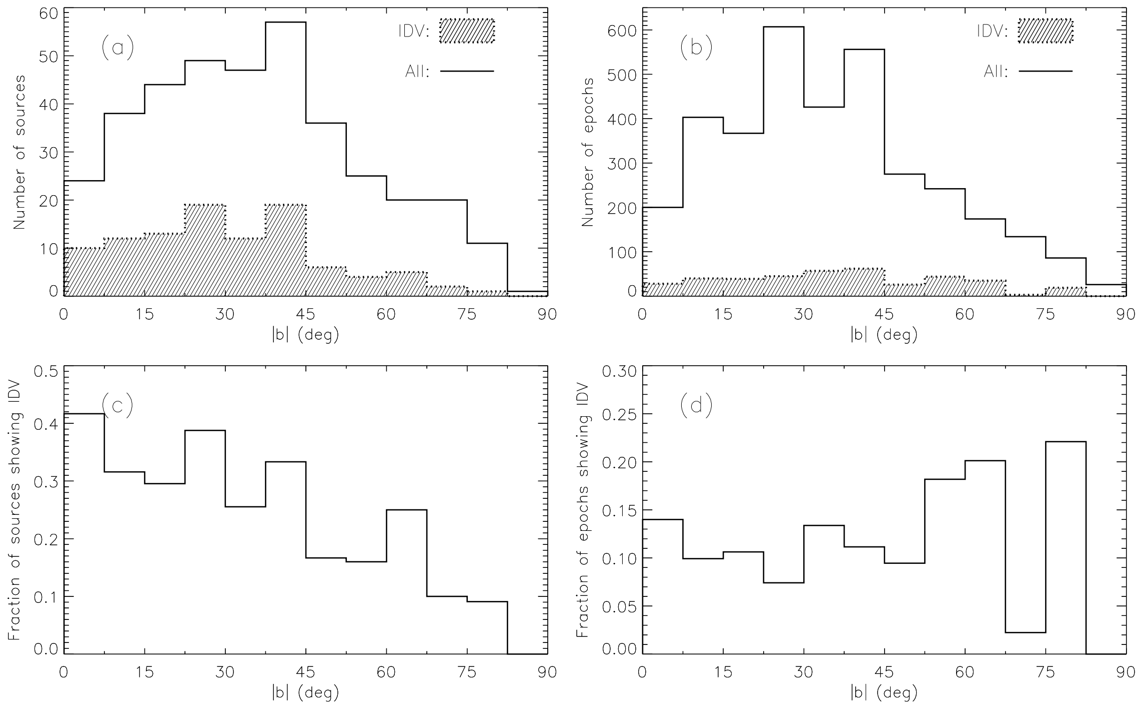

Figure 6.22. (a): Galactic latitude ($|b|$) distribution of IDV sources (shaded), and that for all the sources (unshaded) in the current sample. (b): Distribution of the total number of light curves analyzed (unshaded), and the number of IDV light curves (shaded) found as a function of $|b|$. (c): Fractional number of IDV sources (ratio of the shaded to the unshaded line histograms from panel 'a') from the sample as a function of their galactic latitude. (d): Galactic latitude dependence of the fractional number of IDV light curves found (ratio of the shaded to the unshaded line histograms from panel 'b'). A strong negative correlation ($> 99.9\%$ significance level) between galactic latitude and fractional number of IDV sources is present.

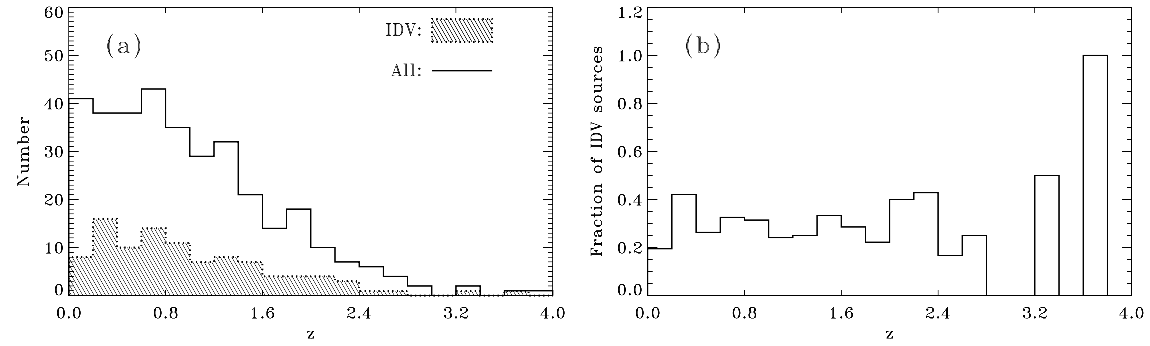

Figure 6.23. (a): Redshift (z) distribution for IDV sources (shaded), and for the full sample (unshaded). (b): Fractional number of IDV sources from the sample (ratio of the shaded to the unshaded line histograms from panel 'a') binned by redshift. No significant correlation between z and fractional number of IDV sources was found.

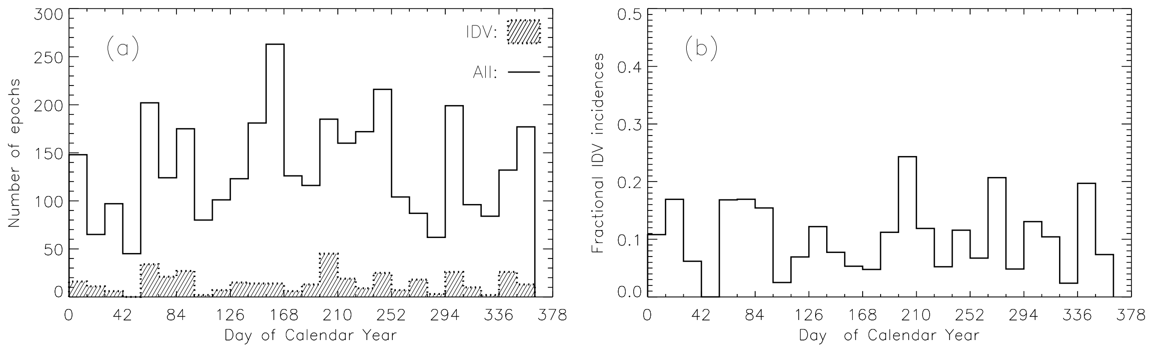

Figure 6.24. (a): Distribution of IDV detection in the current sample as a function of calendar year day number for the full sample (unshaded) and for the IDV sources (shaded). (b): Fractional number of IDV incidences (ratio of the shaded to the unshaded line histograms from panel 'a') as a function of the calendar year day number. No significant correlation between IDV incidence and the day number of the observing epoch was found.

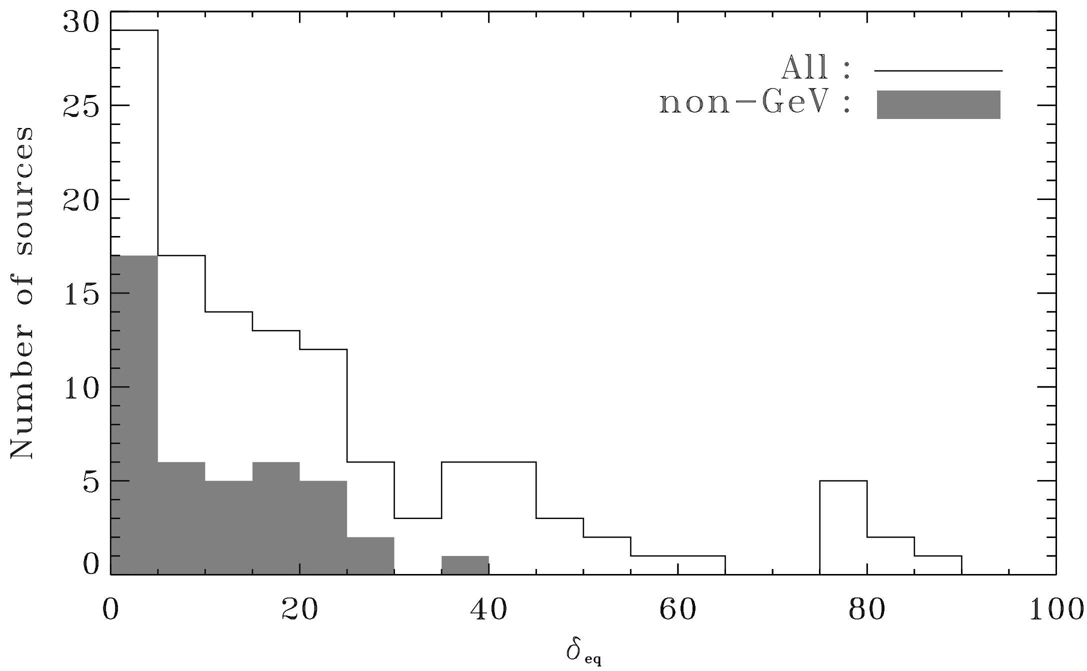

Figure 6.25. Distribution of the brightness temperatures (T_b) for all sources (unshaded) and only the non-GeV sources (shaded) in the original flux density–limited *MOJAVE*_1 sample. Of the 121 sources with well-determined T_b values included in this analysis, 78 sources are part of the *Fermi* LAT 1–year catalog. Of these 78 sources, 45 sources have no EGRET detection. Of the 43 non–GeV sources, 4 sources have no LAT 1–year detection, but have a *probable* EGRET identification [Mattox et al., 2001, Sowards-Emmerd et al., 2003, 2004].

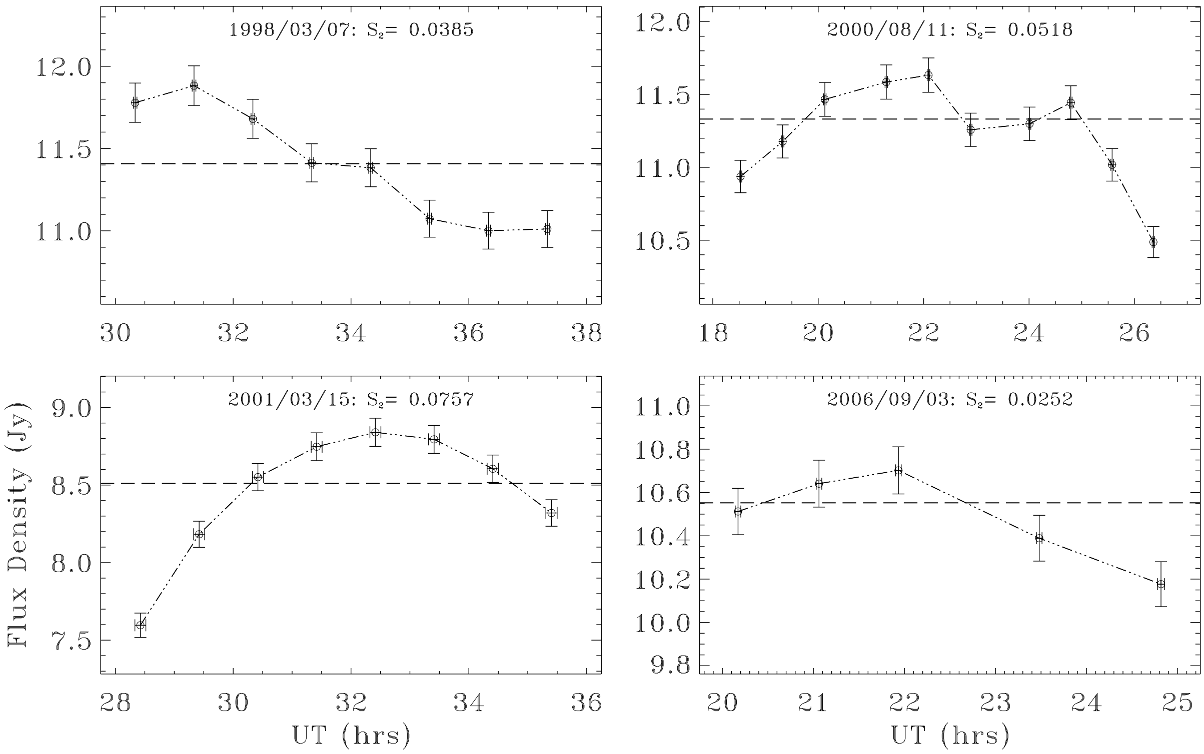

Figure 6.26. Sample multi-epoch VLBA 2 cm light curves for 3C 279, one of the few persistent IDV sources in the current study.

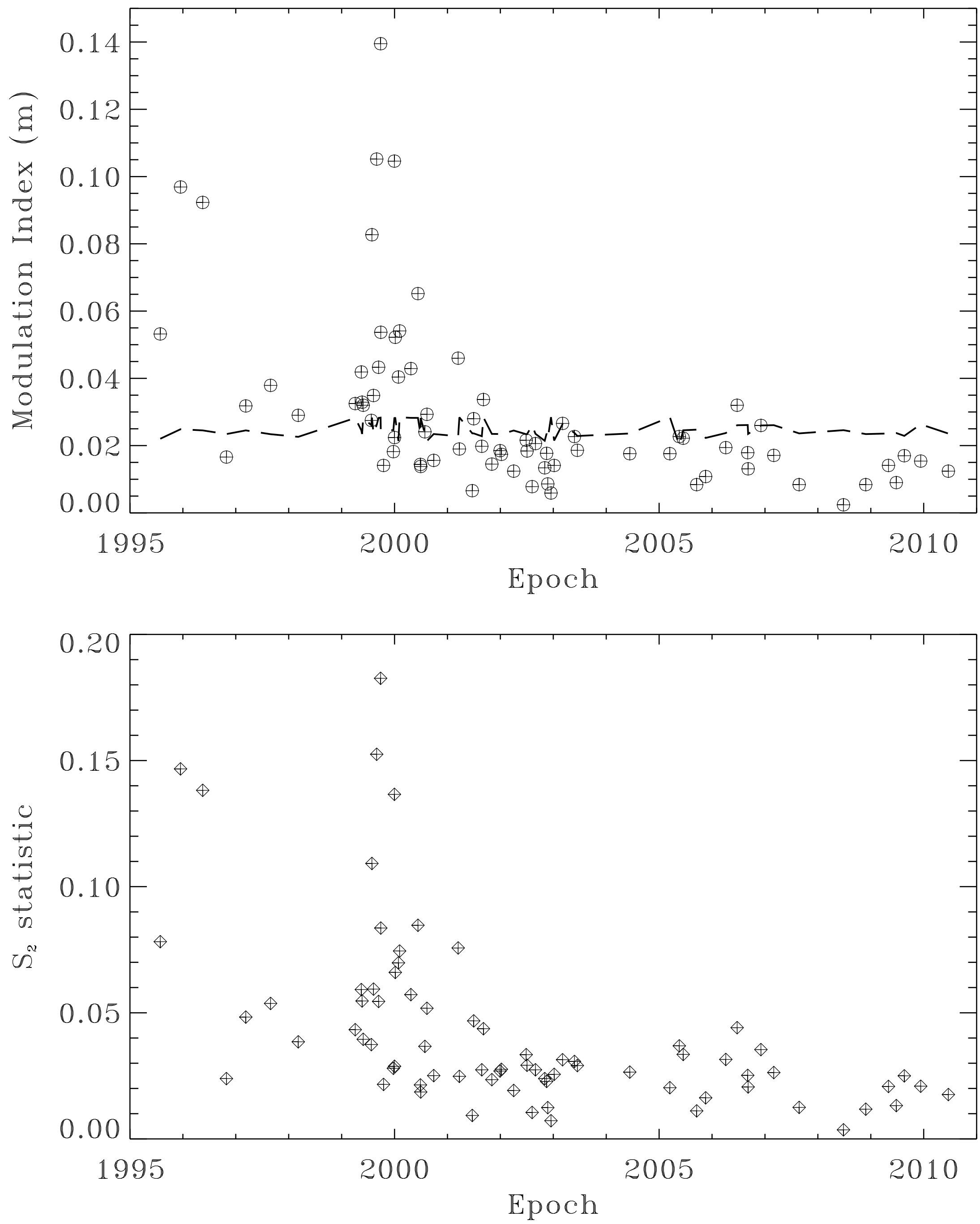

Figure 6.27. *Top*: Plot of the S_2 statistic at various epochs for the HPRQ 3C 279 (1253−055). *Bottom*: Plot of the modulation index (m) at various epochs for 3C 279, with the dashed line marking the cut off m value used viz., any epoch with m value below the line is deemed to be non–IDV. A sharp rise in IDV activity around the third quarter of 1999 is evident and this episode coincides with a giant flare observed at multiple frequencies, and a superluminal radio component ejection.

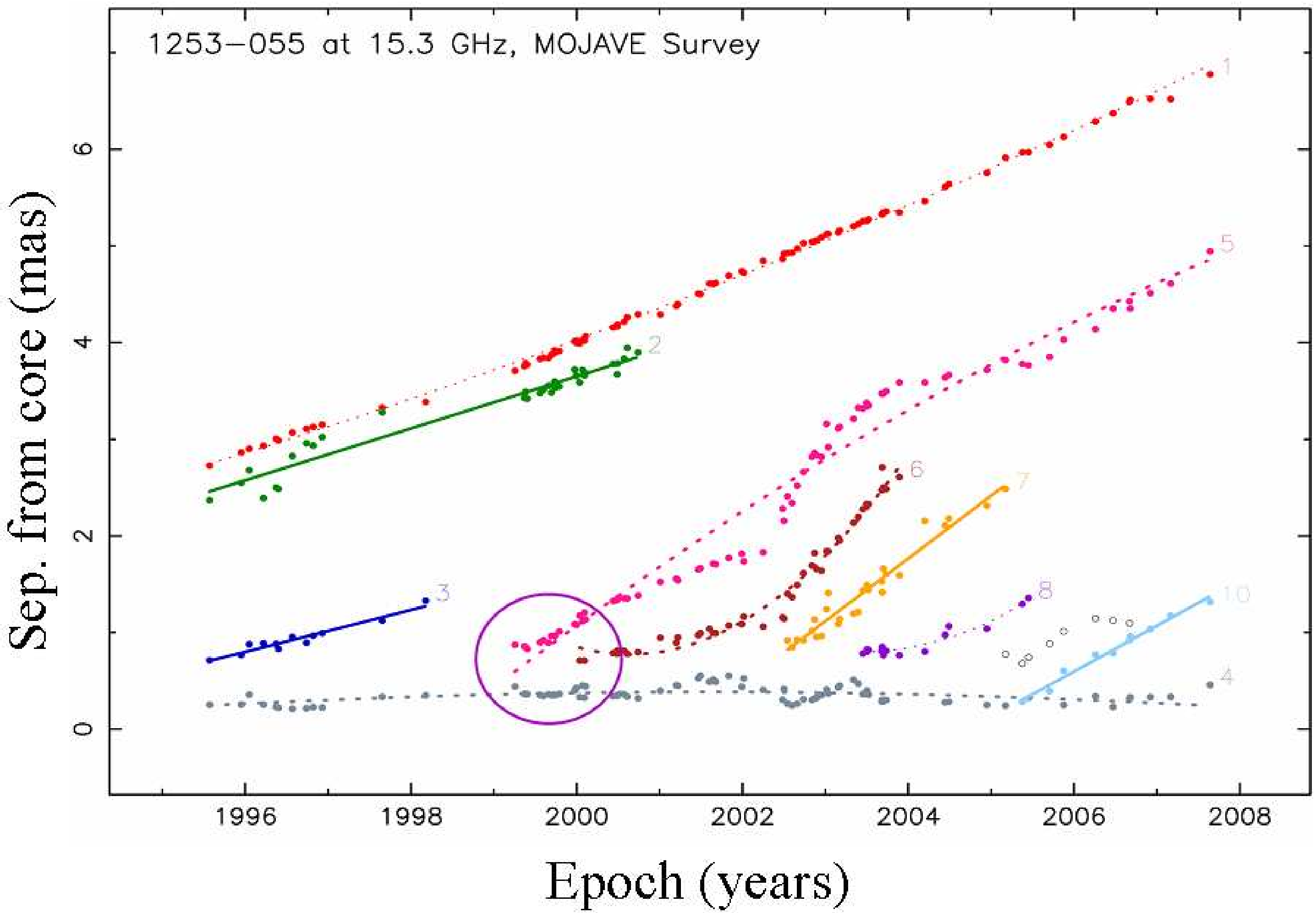

Figure 6.28. Plot showing separation vs. time for the various jet components of the HPRQ 1253−055. The plot is from Lister et al. [2009b].

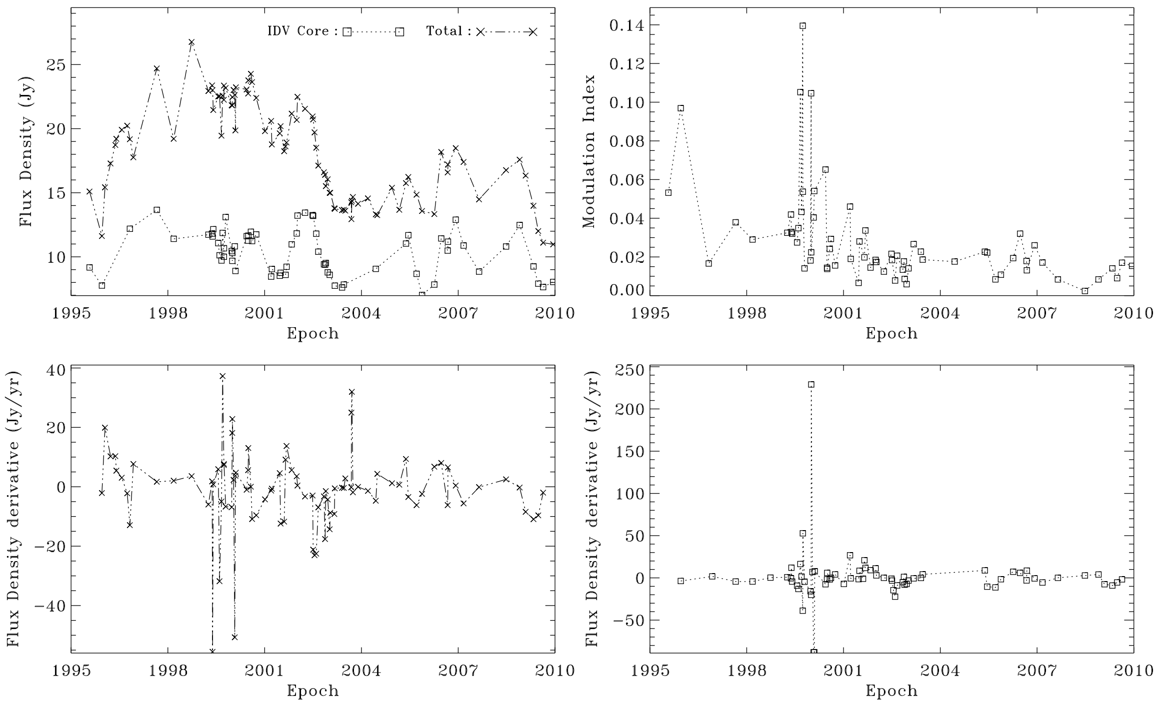

Figure 6.29. Long term 2 cm VLBA light curves for the HPRQ 3C 279. *Top left*: Plot of the total integrated VLBA flux density and the flux density of the 'IDV core' modeled in the current IDV analysis. The two light curves for the most part follow the exact same trend. Around the second half of 1999, a rapid variability in the flux densities occurred. *Top right*: Plot showing the IDV modulation index at various epochs for this source. *Bottom left*: Slope of the VLBA 2 cm total flux density light curve. *Bottom right*: Slope of the flux density light curve of the IDV core.

6.7.1 Other IDV trends

Though a trend towards increasing compactness during episodes of IDV activity was noticed, no statistical statement in this regard could be made, since most of the sources in the sample are very compact. The median compactness index on milliarcsecond scales (S_{VLBA}/S_{tot}) for the *MOJAVE* sample is 0.93 [Kovalev et al., 2005]. Here, S_{VLBA}, S_{tot} denote the VLBA flux density and single dish flux density respec-

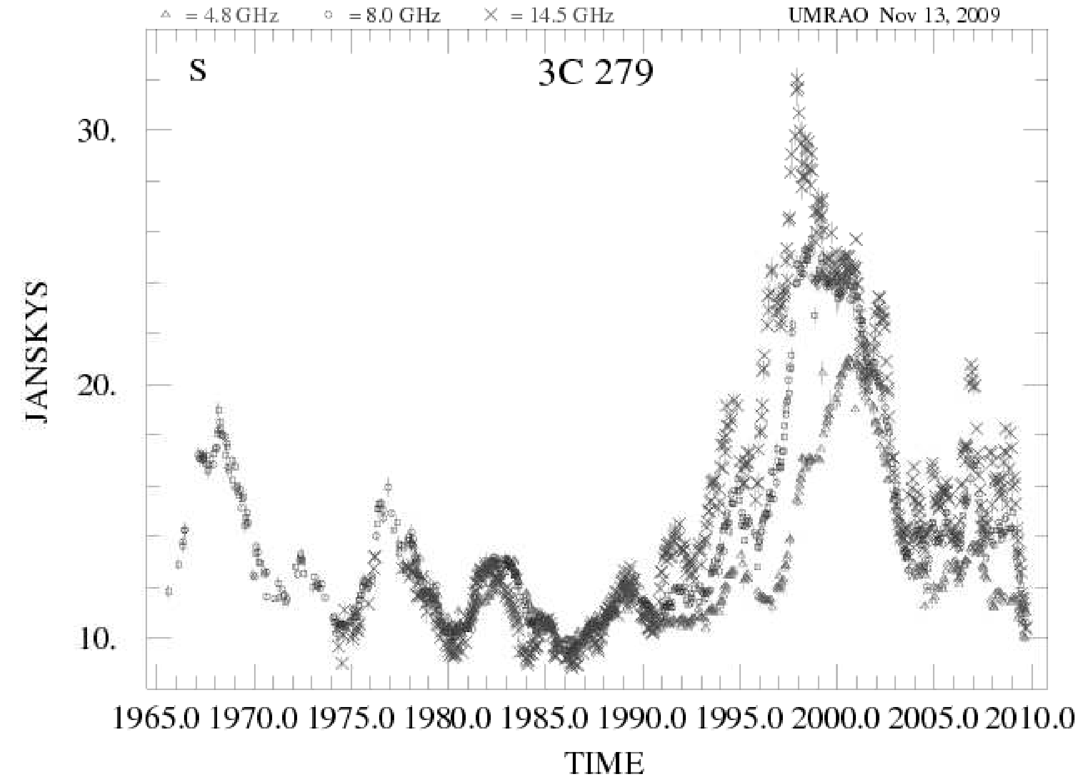

Figure 6.30. The long-term lightcurve of the quasar 1253−055. A rapid flare near the end of 1999 is evident at all frequencies. Data were obtained at the University of Michigan Radio Astronomy Observatory (UMRAO), which is supported by funds from the University of Michigan. (Data courtesy: M.Aller)

tively.

No IDV was detected in the extremely X-ray and γ-ray active blazars Mrk 421 and Mrk 501 (see Fig. 6.32), which also happen to be the two BL Lacs with the lowest redshifts in the sample. This absence of IDV is consistent with the lack of large variability in their long term radio light curves [Teräsranta et al., 2005] and sub-luminal apparent speeds [Piner & Edwards, 2005, Edwards & Piner, 2002]. Similarly, with the exception of 0716+714, no persistent IDV activity was detected in any other genuine BL Lac objects, consistent with the fact that these objects generally have lower apparent speeds than quasars [Lister et al., 2009a]. Also, the IDV activity among

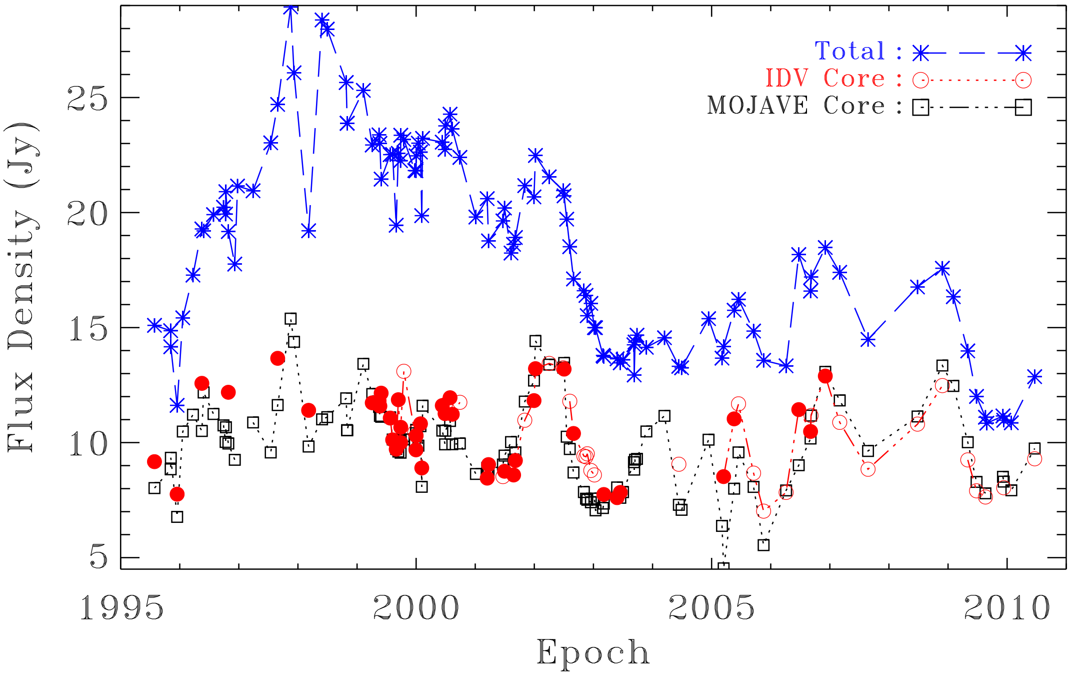

Figure 6.31. VLBA 2 cm light curves for the TeV quasar 1253−055. Shown are the total 2 cm VLBA flux density, flux density of the IDV core, as well as the flux density of the 'core' (as modelled in the kinematic analysis) for this source. Epochs with pronounced IDV activity (e.g., Fig. 6.26) are indicated by filled symbols.

BL Lacs and intermediate BL Lac/QSO sources appears to be slower and of lower amplitude, compared to that in quasars.

Persistent IDV was detected in only a few sources, indicating the rarity of such a phenomenon. Fig. 6.33 shows the VLBA 2 cm light curves for one such persistent rapid IDV source, 0420−014. Rapid multiwavelength variability in polarization in this source has already been reported by others [e.g., D'Arcangelo et al., 2007]. IDV also has been detected in a few compact sources, having an inverted spectrum, and hence previously thought to be CSS/GPS sources. One such source has been discussed in § 6.2 (Fig. 6.9, 6.4), while the light curves for another such source – 0552+398 – are shown in Fig. 6.34. Besides the long term radio variability of such sources and their polarization features, this IDV detection is a further evidence that they are merely misclassified CSS/GPS sources.

6.8 A Qualitative Model for IDV

The IDV properties of QSOs and BL Lacs appear to be quite distinct. Of the 54 BL Lacs in the sample, IDV has been detected only in 8 sources (Table 6.3), and with the exception of 0716+714, none of them are persistent IDV sources. It has also been observed that the IDV in these sources has lower amplitude and longer timescale compared to the other IDV sources, with most of the IDV BL Lacs showing only marginal IDV. On the other hand, the intermediate BL Lac/QSOs resemble QSOs in their IDV characteristics. Almost all of these sources in the sample (10 out of 11) exhibit IDV in multiple epochs (Table 6.4). It is interesting to note that the preliminary results from the spectral analysis of *Fermi* LAT data seem to indicate a similar phenomenon, in that the low energy-peaked BL Lacs (LBLs, to which most of these intermediate sources belong) resemble QSOs in their $\gamma-$ray properties [Abdo et al., 2010]. IDV was also detected in a higher fraction of sources with known high optical polarization. In the blazar unification paradigm, high optical polarization sources are more beamed than the low polarization sources, since their synchrotron jet emission makes a significant contribution to their optical flux. As T_b (and hence IDV activity) is strongly correlated with beaming, sources with high polarization are more likely to exhibit IDV. Similarly, a higher fraction of IDV sources have a GeV detection compared to the non-IDV sources ($\sim 2/3$ & $1/3$ of IDV and non-IDV sources in the full sample respectively). This is to be expected, since GeV emission is highly beamed and IDV detection also correlates with beaming indicators. The disparity is slightly smaller when only the *MOJAVE_1* sample of highly beamed blazars is considered ($\sim 3/4$ & $1/2$ respectively). Similar trends are to be expected between polarization and GeV detection as well, which indeed was found to be the case (Table 6.5).

It is not surprising that the majority of non-IDV sources have very few epochs per source. This is in good agreement with past results that IDV is a highly episodic phenomenon and hence can be confirmed in an object only via multi-epoch observations. Observed IDV is likely due to a combination of rapid, source-intrinsic variability and other extrinsic mechanisms such as inter-stellar scintillation (ISS; especially in the refractive scattering regime). But it is still under debate as to which of these two mechanisms plays the dominant role. There are several indications that at least in the case of bright radio sources (as in the current sample), intrinsic jet properties play a vital role. The supporting observations are as follows:

(a) A correlation between variability RMS and the T_b values, and a negative correlation between modulation index and source flux density was observed. IDV detections among the various blazar subclasses are different, with the IDV sources being mostly QSOs and intermediate BLL/QSO sources. There was almost no IDV in genuine BL Lac objects. This is perhaps due to lesser beaming, as is evident from their generally lower T_b, δ and $\beta_{\rm app}$ values [Hovatta et al., 2009, Lister et al., 2009a], and lower flare amplitudes in their long term radio light curves compared to quasars [Hovatta et al., 2008, Nieppola et al., 2009]. This is consistent with common unification models [e.g., Urry & Padovani, 1995] according to which the radio selected BL Lacs are (slower) FR-I jets seen close to the line of sight, X-ray selected BL Lacs are FR-I jets seen at slightly larger viewing angles, while HPQs (core dominated QSOs), LPQs (lobe dominated QSOs) and Radio galaxies are FR-IIs seen at increasingly larger viewing angles [Ghisellini et al., 1993]. A strong positive correlation between IDV detection and $\beta_{\rm app}$, T_b (Fig. 6.20 and 6.21) was also observed.

(b) From Tables 6.2 and 6.5, it is evident that IDV is more prevalent among the flux-density limited *MOJAVE_1* sample sources compared to the full sample, in that both the fractional number of sources showing IDV as well as the fractional number of epochs exhibiting IDV are higher for the *MOJAVE_1* sample. in fact $\sim$ 80% of all the IDV sources detected in the current study are part of the *MOJAVE_1* sample, while the non *MOJAVE_1* sources showing IDV in more than one epoch comprise only $\sim$ 5% of all IDV sources. This may partly be due to this subset of sources having higher number of epochs analyzed (and spanning a larger time-range) per source on an average, compared to the rest of the sample. However, in light of the correlations found between beaming indicators and IDV, it is conceivable that the chief reason for this increased prevalence of IDV is the fact that the *MOJAVE_1* sources have higher beaming factors compared to the rest of the sample (and hence their inclusion in the flux-density limited sample in the first place).

(c) Most of the prominent IDV sources appear to have highly variable radio spectra, with an increasing spectral index/inverted spectrum at $\nu > 10$ GHz, once again indicative of an intrinsic IDV mechanism at work. Other authors have arrived at a similar conclusion regarding spectral indices, from IDV studies based on smaller samples [Kedziora-Chudczer, 1998]. Also, the IDV episodes in most of the sources seem to be coincident with flaring and/or component ejection events (see § 6.7). There are also preliminary indications that the variability amplitude is correlated with the strength and rapidity of the flare.

(d) The lack of strong VLBA flux calibrators, coupled with intrinsic errors associated with the *gain transfer* methodology leads to relatively large fractional errors in the flux density measurements. This limitation, coupled with the fixed *MOJAVE* observing strategy of $\sim$ 8 scans per source at roughly 1hr. intervals, renders the current analysis sensitive only to rapid, large amplitude variability. But the observing frequency (15.3 GHz) is well beyond the 'transition frequency' of $\sim$ 5 GHz, where rapid large amplitude variability is expected from standard ISS models. Moreover, most of the confirmed ISS sources are very faint (hence none were part of the current study) and the amplitude and prevalence of IDV has been observed to decrease with increasing source flux density [Lovell et al., 2008].

(e) If ISS were indeed the dominant IDV mechanism in the current sample, one would expect a negative correlation between redshift and IDV detection. This is due to *scatter broadening* of high z sources in the intervening inter-galactic medium (IGM). Moreover, the expected (1+z) dilation in variability timescales should make us less sensitive (as discussed above) to IDV sources at high redshifts. Hence, a negative correlation between redshift and fractional number of IDV sources is to be expected. However, no such correlation was observed. One explanation for this could be the selection bias of the flux limited sample towards increasingly beamed/more intrinsically luminous objects at higher redshifts, which might offset any increased *scatter broadening*, thus destroying the expected negative correlation. No slowing down of IDV (and hence decreased frequency in IDV incidences) was observed during the latter half of the calendar year, as is to be expected from ISS models involving scattering clouds stationary with respect to the LSR [e.g., Lovell et al., 2007]. This favors intrinsic variability being the dominant IDV mechanism in the present sample. However, the expected slowing down is very sensitive to assumptions regarding the velocities of the scattering screens and Lovell et al. [2008] explain a similar result from the *MASIV* experiment to mean that the scattering clouds have significant velocities with respect to the local reference frame.

(f) Several of the IDV detections in the sample come from sources with well known intra-night variability in the optical. This is in contrast to some confirmed interstellar scintillators such as J1128+592 [Gabányi et al., 2007] which show almost no optical variability on intra-night time scales [Wu et al., 2008, 2009]. Also, no radio IDV activity in classical BL Lac objects such as 0735+178, which are unusually optically quiescent on intra-night time scales [Goyal et al., 2009], was detected.

However, ISS does appear to play some role in IDV as evidenced by the fact that a significant negative correlation between galactic latitude and IDV detection was detected, an observation also reported by other authors [e.g., Lovell et al., 2008]. Further evidence can be found in the broader angular sizes among non-scintillating sources as compared to those in scintillating sources [Ojha et al., 2004].

To reconcile all of these observations, the following qualitative model may be invoked: The blazar core produces bright, compact components/blobs, whose radio emission is beamed towards the observer. The high brightness temperatures of these blobs would result in their rapid flux decay (on the order of $\sim$ days) due to Inverse Compton (IC) losses ['Inverse Compton Catastrophe'; Hoyle et al., 1966, Kellermann & Pauliny-Toth, 1969]. This would lead to rapid variability/flaring at high frequencies (optical and higher energies). The compactness of these blobs would allow for their scintillation at cm wavelengths, resulting in radio IDV. This model would account for the association between flaring, component ejection and IDV episodes (e.g., in 3C 279) and the fact that most of the IDV sources detected in the current study are well known for their rapid optical activity. Also, correlations between IDV and source-intrinsic properties such as source type, spectral shape, beaming ($\beta_{\rm app}$, T_b) along with observer dependent properties such as the galactic latitude of the source, can be explained. Sources at higher redshifts would have to have higher beaming factors in order to be members of a flux density limited sample. This higher beaming would compensate for scatter broadening due to the IGM and destroy the expected negative correlation between the fractional number of sources showing IDV and redshift. This would explain the observed lack of correlation between IDV detections and redshift (Fig. 6.23). However, IC losses set an upper limit on the brightness temperature ($\sim 10^{12}$K), which would lead to a lower limit on the size of these compact features ($T_b \propto S\theta^{-2}$). Therefore, higher flux densities result in larger sizes and hence lesser scintillation, which would account for the decreasing number of IDV detections with increasing source flux density observed [e.g., Lovell et al., 2008]. Moreover, sources with higher beaming factors would be more likely to be persistent IDV sources by virtue of their flaring activity and hence, the strong observed correlation between fractional number of epochs showing IDV and $\beta_{\rm app}$, T_b. One caveat to this simple model is that not all flaring episodes would lead to the observance of IDV, since a bending of the jet away from the observer's line of sight during the flare, would lead to debeaming. Such an inference regarding debeaming was indeed made from the long term monitoring of the evolution of the cm – mm spectrum of the persistent IDV HPQ 1641+399 [3C 345; Stevens et al., 1996].

Due to the higher space density of scattering clouds closer to the galactic equator, even sources with moderate δ factors in that part of the sky are likely to scintillate. This is due to the fact that, in the strong scattering, RISS regime, for a source to scintillate and exhibit IDV, the following criterion needs to be satisfied: $\theta \lesssim \theta_F$, where $\theta,\ \theta_F$ denote the angular size of the source and the angular Fresnel size respectively. But

$$\theta \sim \frac{1}{\Gamma}\left(\frac{R_{em}}{D_{AGN}}\right) \tag{6.1}$$

where R_{em} and D_{AGN} are the size of the emitting region and distance to the AGN respectively, while Γ is the bulk Lorentz factor. Also,

$$\theta_F \sim \sqrt{\frac{\lambda}{D_{screen}}} \tag{6.2}$$

where λ and D_{screen} are the observing wavelength and the scattering screen distance respectively. To the first order, in equation 6.1, Γ may be replaced by the Doppler factor (δ). Combining equations 6.1 and 6.2, a lower limit for the δ required for the source to scintillate may be determined. That limit is given by:

$$\delta \gtrsim \left(\frac{R_{em}}{D_{AGN}}\right)\sqrt{\frac{D_{screen}}{\lambda}} \tag{6.3}$$

In otherwords, $\delta_{threshold} \propto \sqrt{D_{screen}}$. The ISM local bubble is modeled to be elongated, with D_{screen} values ranging from ~ 30 pc in the galactic plane to as much as

200 pc within 20° of the north galactic pole [Cox & Reynolds, 1987]. Smaller D_{screen} values would imply smaller $\delta_{threshold}$ values, leading to scintillations even in weakly beamed sources, and hence the higher observed fraction of IDV sources closer to the galactic plane (Fig. 6.22 panel c) and the strong negative correlation between galactic latitude and fractional number of IDV sources. However, these low beaming factors would also result in diminished source-intrinsic variability and hence most of these sources would not show persistent IDV. The combination of these two effects could then explain the absence of any correlation between galactic latitude and the fractional number of epochs showing IDV, as can be inferred from Figure 6.22 panel d. Also, since $\delta_{threshold} \propto \sqrt{\nu}$, at higher observing frequencies only the highly beamed sources scintillate and hence the paucity of IDV sources at these frequencies. It also implies that the sources showing IDV up to (or at) higher frequencies have higher beaming factors than those that show IDV only at lower frequencies. This would also explain the lack of IDV sources among genuine BL Lacs (in the present study at 15.3 GHz), since under the unification paradigm, BL Lacs are thought to be the low power FR Is (and hence have smaller Γ values) with their jets aligned close to the observer's line of sight. Radio galaxies and CSS/GPS sources also would not exhibit IDV by virtue of their being mostly in the plane of the sky, and hence small δ values.

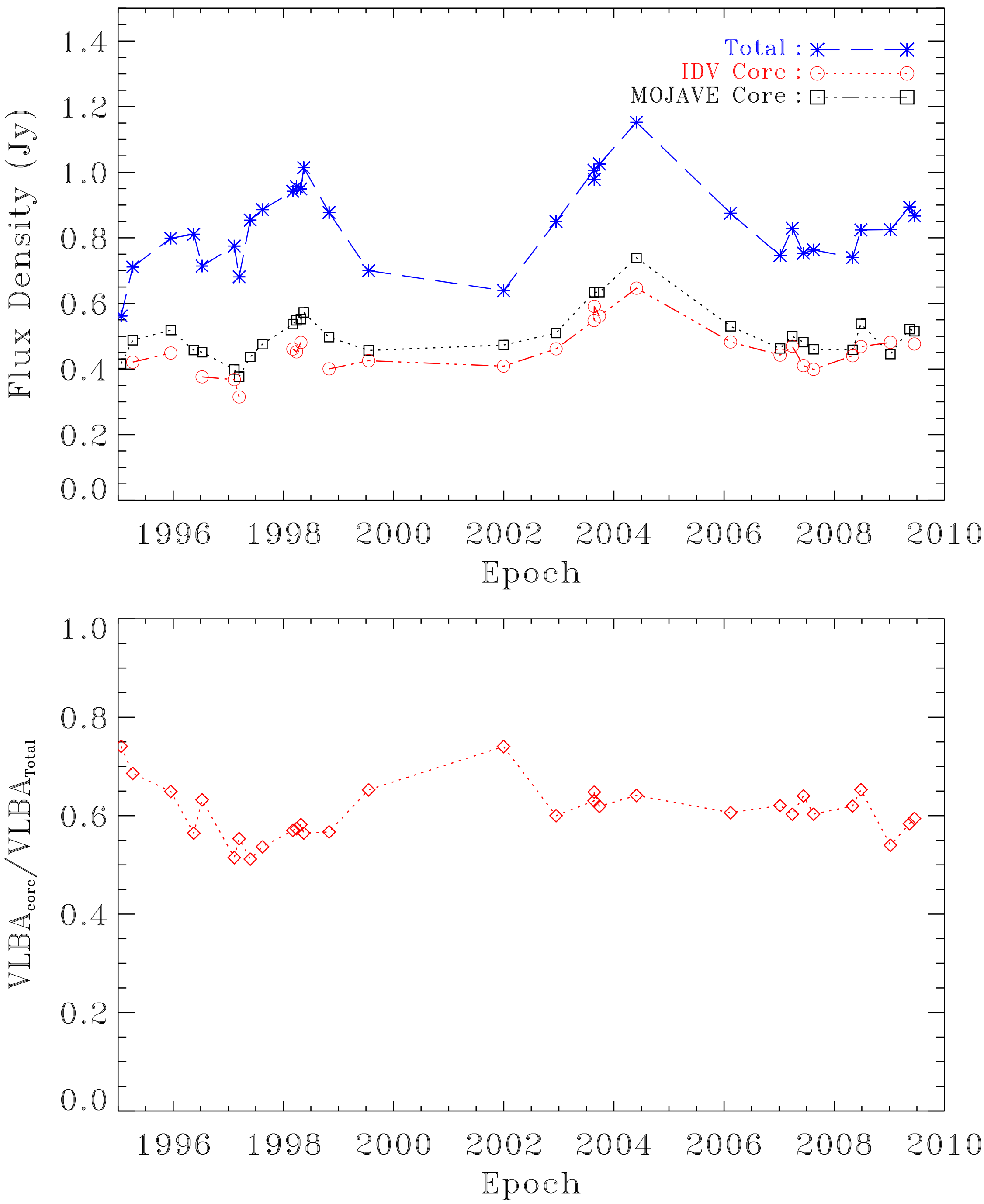

Figure 6.32. VLBA 2 cm light curves for the extremely X–ray active BL Lac object 1652+398 (Mrk 501). *Top*: Shown are the total 2 cm VLBA flux density, flux density of the IDV core, as well as the flux density of the 'core' (as modelled in the kinematic analysis) for 1652+398. *Bottom*: Plot of the 'compactness', defined as the ratio of the VLBA 15 GHz core flux density to the VLBA total flux density for this source. No IDV has been detected in this source in the current study.

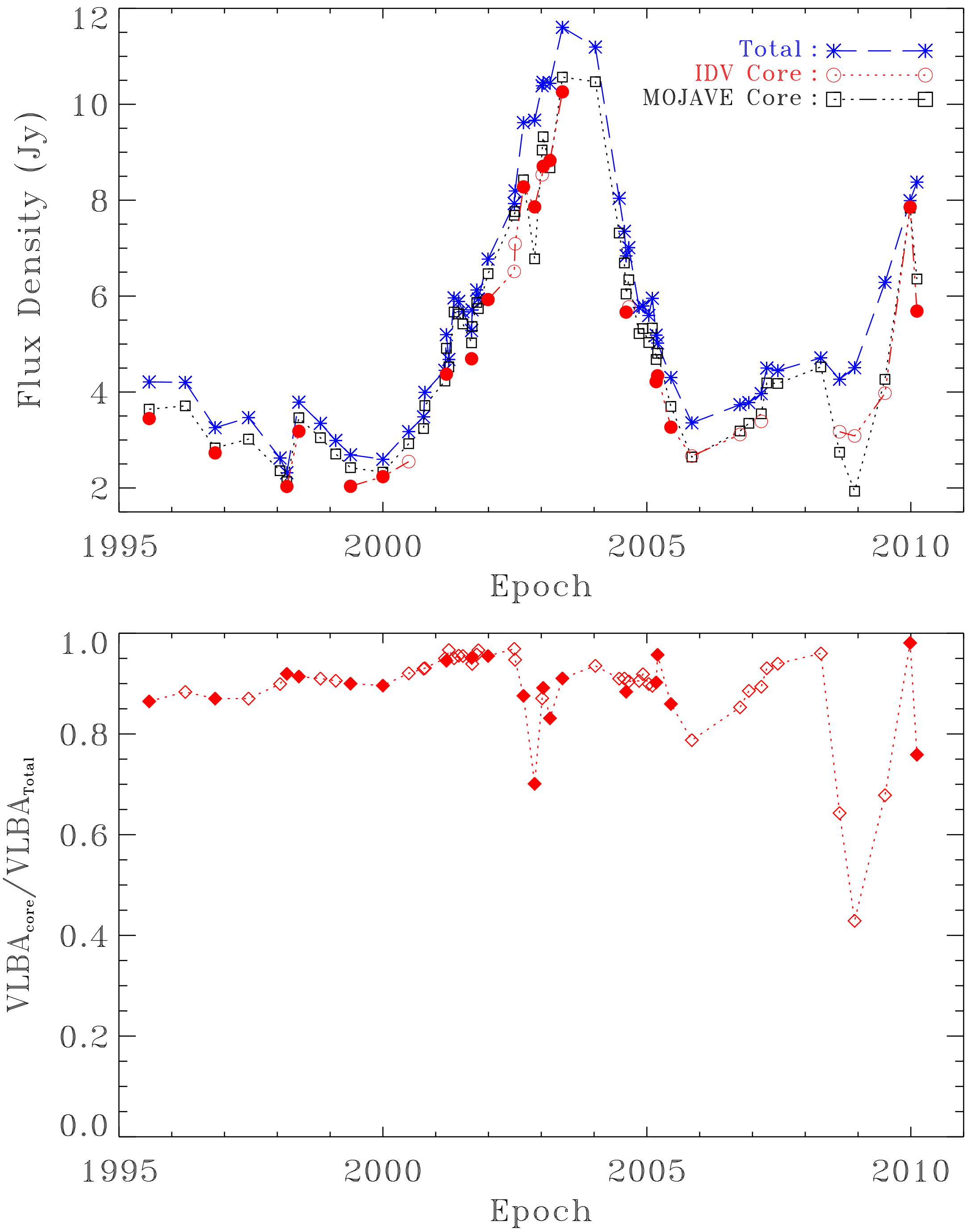

Figure 6.33. VLBA 2 cm light curves for the HPRQ 0420−014, one of the extremeley rare persistent IDV sources in the *MOJAVE* sample. *Top*: Shown are the total 2 cm VLBA flux density, flux density of the IDV core, as well as the flux density of the 'core' (as modelled in the kinematic analysis) for this source. *Bottom*: Plot of the 'compactness' for this source. A rapid variability in polarization at multiple wavelengths has been reported in this source [D'Arcangelo et al., 2007, D'Arcangelo, 2010].

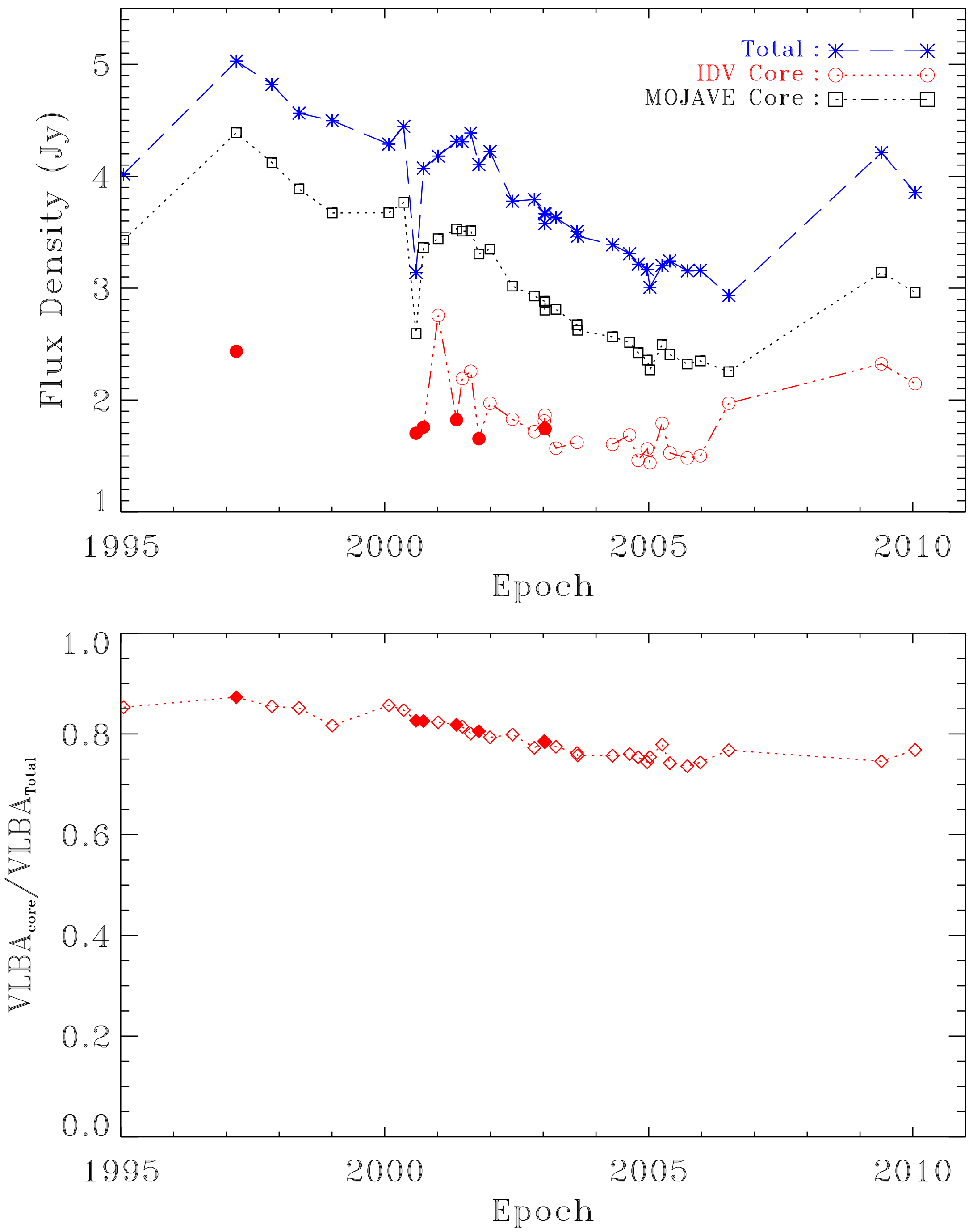

Figure 6.34. VLBA 2 cm light curves for the 'candidate GPS' source 0552+398. *Top*: Shown are the total 2 cm VLBA flux density, flux density of the IDV core, as well as the flux density of the 'core' for this source. *Bottom*: Plot of the 'compactness' for this source. 0552+398 is currently classified as 'non–GPS' based on radio polarization and variability. A sudden dimming of the core accompanied by episodes of IDV activity is evident around the middle of 2000.

7. IDV PROPERTIES OF SELECTED INDIVIDUAL SOURCES

7.1 0607−157

The quasar 0607−157 ($z = 0.324$, $\beta_{\rm app} \sim 3.9$)[1] has been classified as a radio IDV source [Kedziora-Chudczer, 1998]. A giant flare, with a very rapid decline in the VLBA flux density ($\sim$ 3.7 Jy in 19 days) was observed at the beginning of 2000 (Fig. 7.2). The same was confirmed by the multi-frequency single-dish light curves (Fig. 7.4). Episodes of pronounced IDV activity also seem to be coincident with this flare. Usually superluminal component ejection is seen in assosciation with such giant flares. But no such component has been observed following this flare [Lister et al., 2009b].

These two observed phenomena viz., rapid flaring and decay in flux density, accompanied by a detection of IDV, and non–appearance of new radio components, may be explained as follows: The core might have produced small, bright components, which, due to IC losses, cool rapidly [on the timescale of few days; Hoyle et al., 1966, Kellermann & Pauliny-Toth, 1969]. This would account for both the sharp decline in flux density, and the lack of new radio component ejection. But, for IC losses to dominate, from T_b arguments, a case can be made that these bright, short-lived components must be small in size, and hence able to scintillate. This could explain the appearance of pronounced IDV at the time of flaring. If the scintillating components do not cool rapidly enough, one could observe the ejection of new components accompanying this flaring/IDV activity in radio VLBI maps, as was the case with 3C 279 (see § 6.7). A less pronounced version of this phenomenon was noticed in a few other objects. For

[1] See: `http://www.physics.purdue.edu/MOJAVE/sourcepages/0607-157.shtml`

example, the case for the intermediate BLL/QSO source BL Lac is presented in § 7.2.

7.2 BL Lac

Episodes of IDV activity seem to be correlated with the declining phase of flaring activity in some sources, most notably 2200+420 (BL Lac; $z = 0.0686$, $\beta_{\mathrm{app}} \sim 10.6$)[2]. In Fig. 7.5 the multi-epoch, 2 cm VLBA light curve for this source is shown, while the light curves from some of the epochs exhibiting IDV activity are shown in Fig. 7.6. As can be seen from these two figures, there appears to be a higher probability of observing IDV in the source during phases of sharp change in its long-term light curve. Also, a superluminal component ejection was observed near the end of 2001 [Lister et al., 2009b] and an episode of IDV activity was also noticed around the same time, akin to the case of 3C 279. A somewhat similar trend is also evident in the QSO 0607−157 (see § 7.1).

7.3 1156+295: Brightest rapid IDV source?

Of special interest is the HPRQ 1156+295 (4C + 29.45; $z = 0.729$, $\beta_{\mathrm{app}} \sim 24.9$)[3]. 1156+295 has a 2-sided halo morphology (Fig. 7.7) with a bent jet (Fig. 7.8) on kpc scales. The pc scale image of this source is shown in Fig. 7.10. 1156+295 is a bright $\gamma-$ray source and has been detected by EGRET [Mattox et al., 2001] as well as *Fermi* (above 10σ). This is the only new source with rapid, large amplitude variability discovered in the *MOJAVE* program [Savolainen & Kovalev, 2008]. At a galactic latitude of 78.37°, 1156+295 is the highest galactic latitude IDV source in the current sample. As can be seen from the spectrum (Fig. 7.9), 1156+295 exhibits a large variability at frequencies above 10 GHz, thus suggesting an intrinsic explanation for its IDV. Fig. 7.12 shows the long term VLBA light curves for this source. However, as can be

[2]See: `http://www.physics.purdue.edu/MOJAVE/sourcepages/2200+420.shtml`

[3]See: `http://www.physics.purdue.edu/MOJAVE/sourcepages/1156+295.shtml`

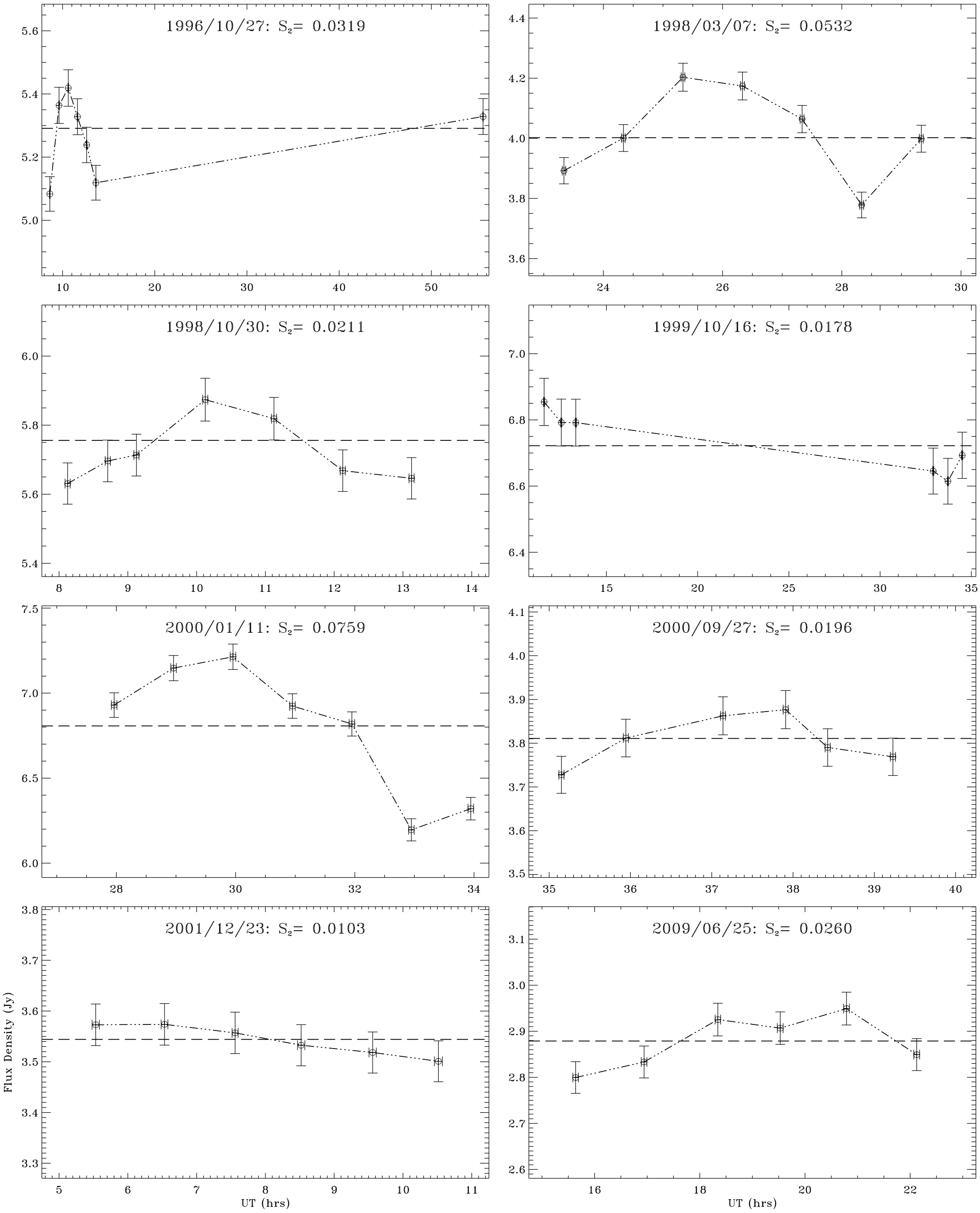

Figure 7.1. Multi-epoch VLBA 2 cm light curves for 0607−157, one of the few persistent IDV sources in the current study.

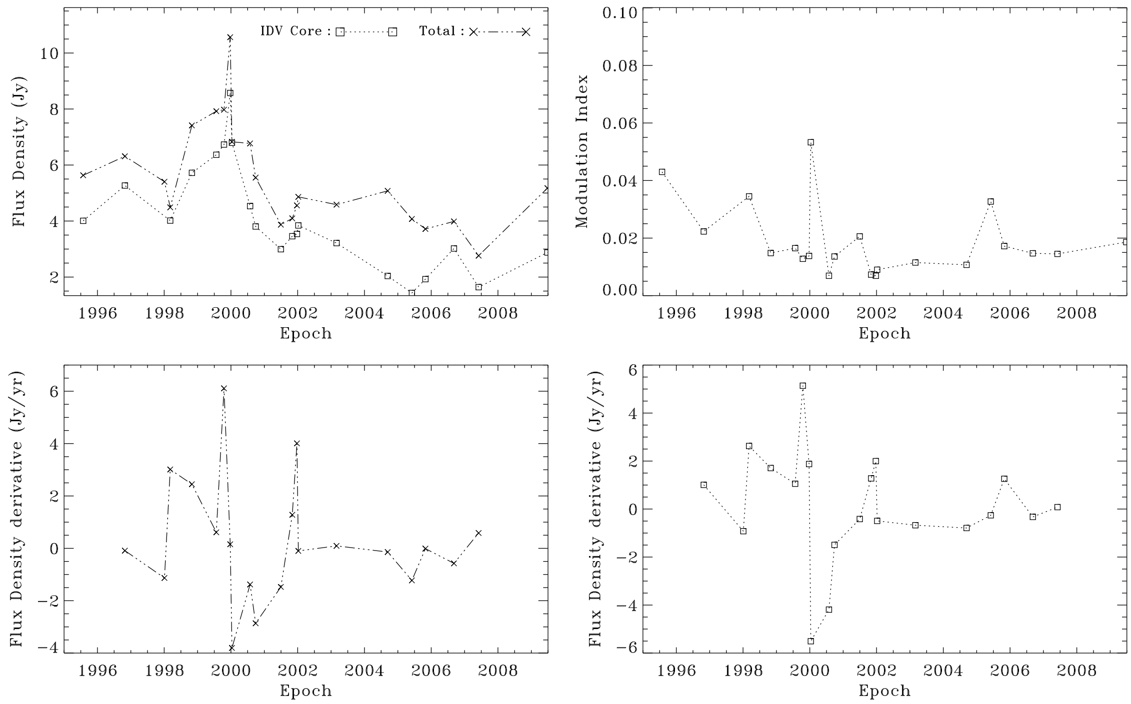

Figure 7.2. Long term 2 cm VLBA light curves for the QSO 0607−157. *Top left*: Plot of the total integrated VLBA flux density and the flux density of the 'IDV core' modeled in the present analysis. The two light curves for the most part follow the exact same trend. Around the beginning of 2000, an extremely rapid variability in the flux densities occurred. *Top right*: Plot showing the IDV modulation index at various epochs for this source. *Bottom left*: Slope of the VLBA 2 cm total flux density light curve. *Bottom right*: Slope of the flux density light curve of the IDV core. The modulation index clearly shows a sharp rise around the beginning of 2000, coincident with rapid changes in the flux densities and slopes of the two light curves.

seen from Fig. 7.13, this source shows some signs of *annual modulation*, with shorter variability time-scales at the beginning of the year. If confirmed with further data, this source would be the brightest among the half a dozen IDV sources with confirmed seasonal modulation. But the peculiarity of this source is the fact that the modulation index at 15 GHz is larger than that at 5 GHz [Lovell et al., 2007], which is hard to

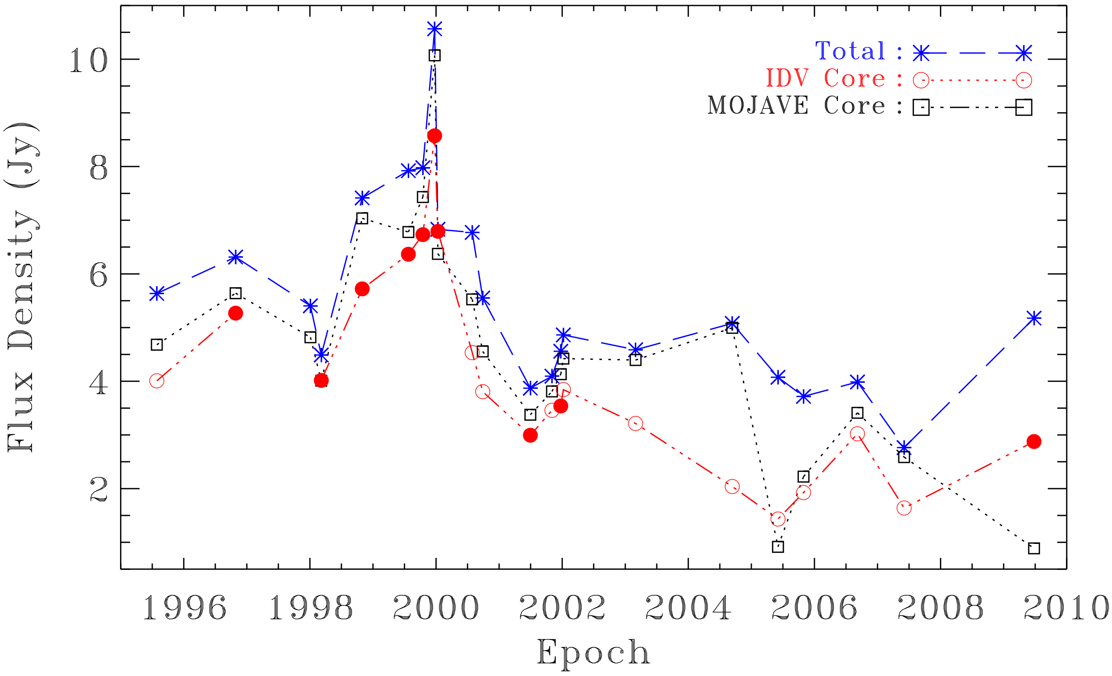

Figure 7.3. VLBA 2 cm light curves for the quasar 0607−157. Shown are the total 2 cm VLBA flux density, flux density of the IDV core, as well as the flux density of the 'core' (as modelled in the kinematic analysis) for this source. Epochs with pronounced IDV activity (e.g., Fig. 7.1) are indicated by filled symbols.

reconcile within the scope of standard RISS models. Also, its high galactic latitude is unfavorable for any strong scattering event. Moreover, recent (June 2008) multi-frequency single dish observations have yielded light-curves which do not show the characteristic correlations between the various frequency bands (L.Fuhrmann, priv. comm.). Also, similar observations in November 2008 did not show any IDV activity (B.Peng, priv. comm.), making this source all the more peculiar and warranting further study.

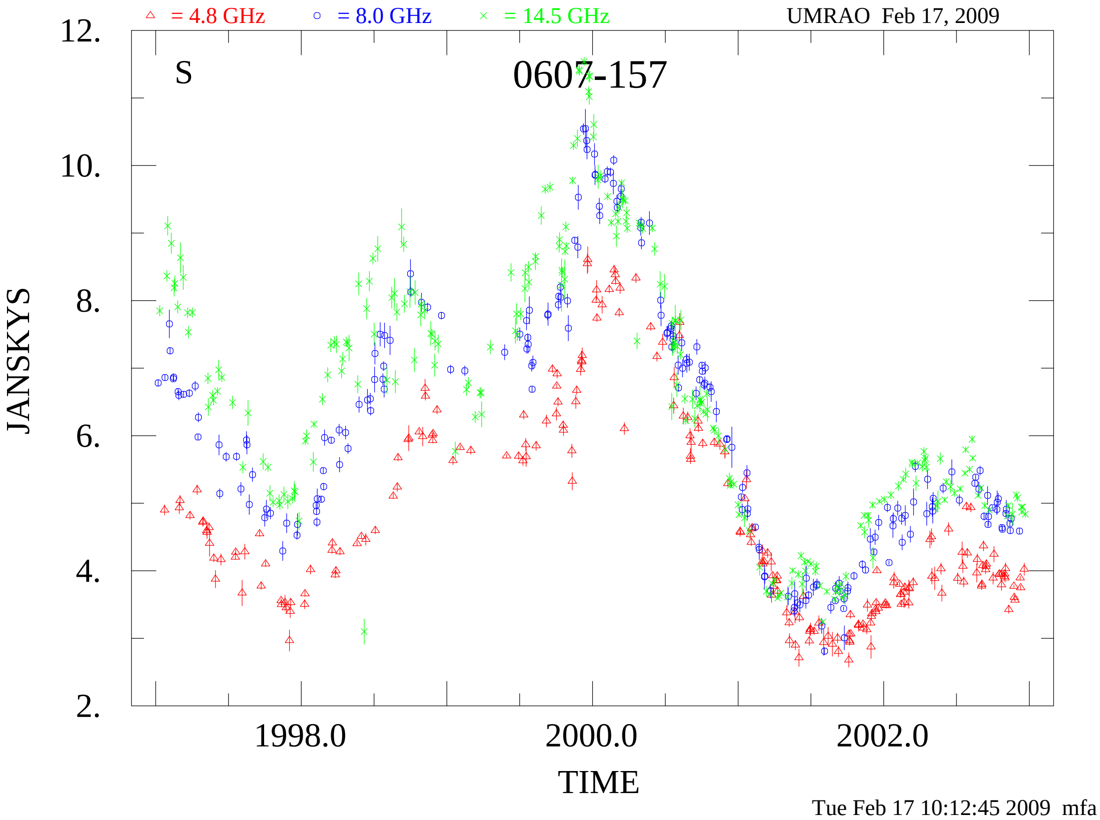

Figure 7.4. The long-term lightcurve of the quasar 0607−157. A rapid flare at the end of 1999 is evident at all frequencies. Data were obtained at the University of Michigan Radio Astronomy Observatory (UMRAO), which is supported by funds from the University of Michigan. (Data courtesy: M.Aller)

7.4 1749+096

The intermediate BLL/QSO source 1749+096 (4C + 09.57, OT081; $z = 0.322$, $\beta_{\rm app} \sim 6.8$)[4] is one of the few persistent 'slow' (Type-I) IDV sources detected in the current study. The cm and mm waveband images of 1749+096 (Fig. 7.14, 7.15) appear to be very similar to those of the rapid IDV source 1156+295 (Fig. 7.10, 7.11), in that both the objects are very compact, with a bent pc–scale jet. Sample IDV light curves and the long term VLBA light curves for this source are shown in Fig. 7.16

[4]See: `http://www.physics.purdue.edu/MOJAVE/sourcepages/1749+096.shtml`

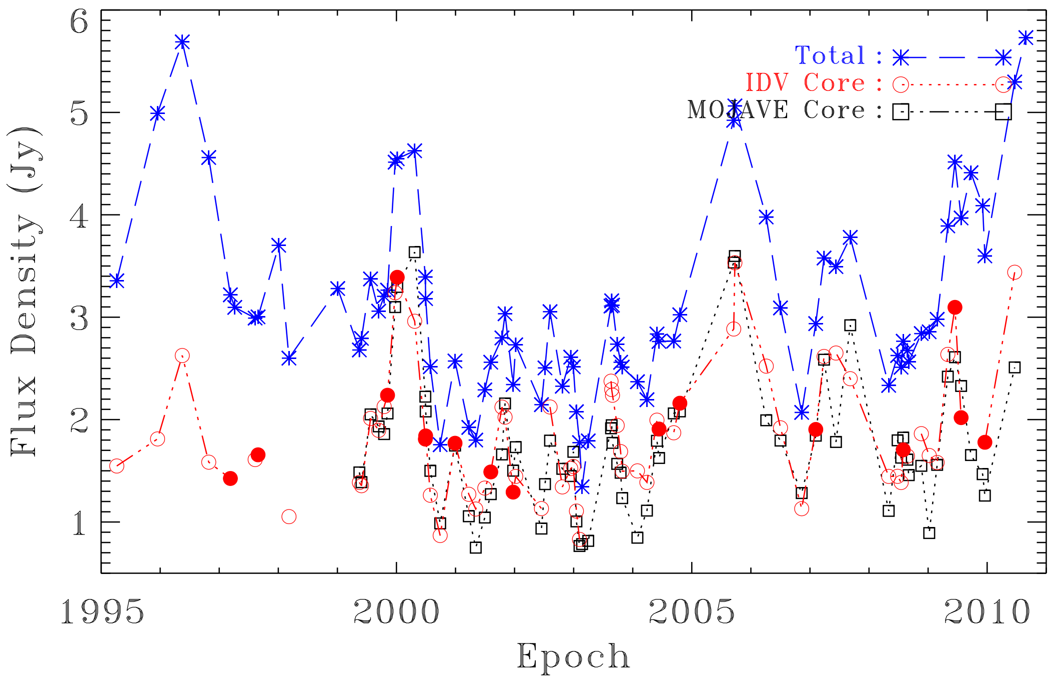

Figure 7.5. VLBA 2 cm light curve for BL Lac (2200+420). Shown is the total flux density for this source, which exhibits a lot of variability. Epochs with pronounced IDV activity (Fig. 7.6) are indicated by filled circles.

and 7.17 respectively. These results are in line with the results from the *MASIV* survey which indicate that the scintillating (IDV) sources are more compact than the non-scintillating sources [Ojha et al., 2004].

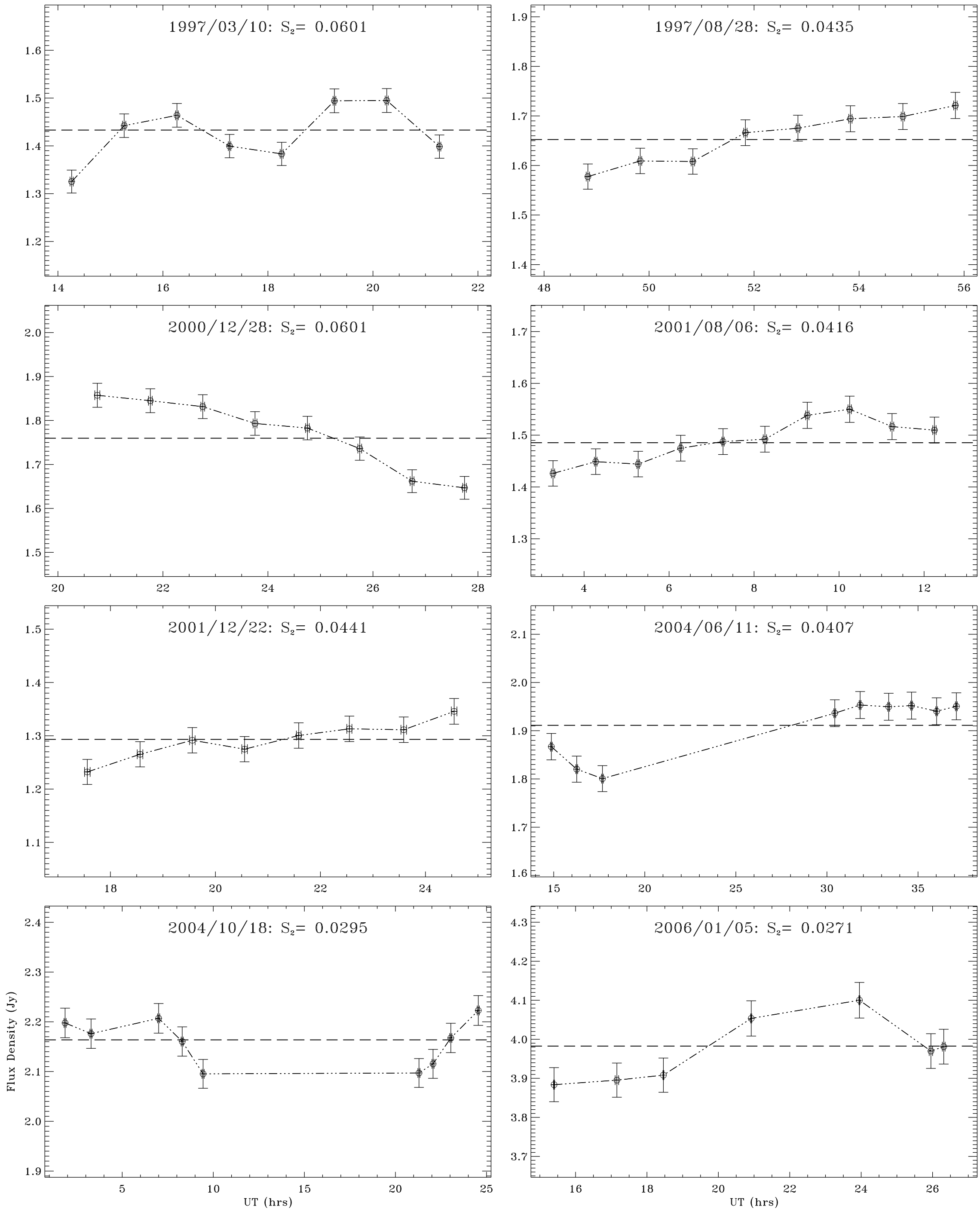

Figure 7.6. Multi-epoch VLBA 2 cm light curves for the intermediate BLL/QSO source 2200+420 (BL Lac). As with other intermediate BLL/QSO sources, the IDV activity in this source seems to be slower than that seen in a few QSOs. As can be seen from Fig. 7.5, episodes of pronounced IDV activity seem to correlate with the declining phase of major flares.

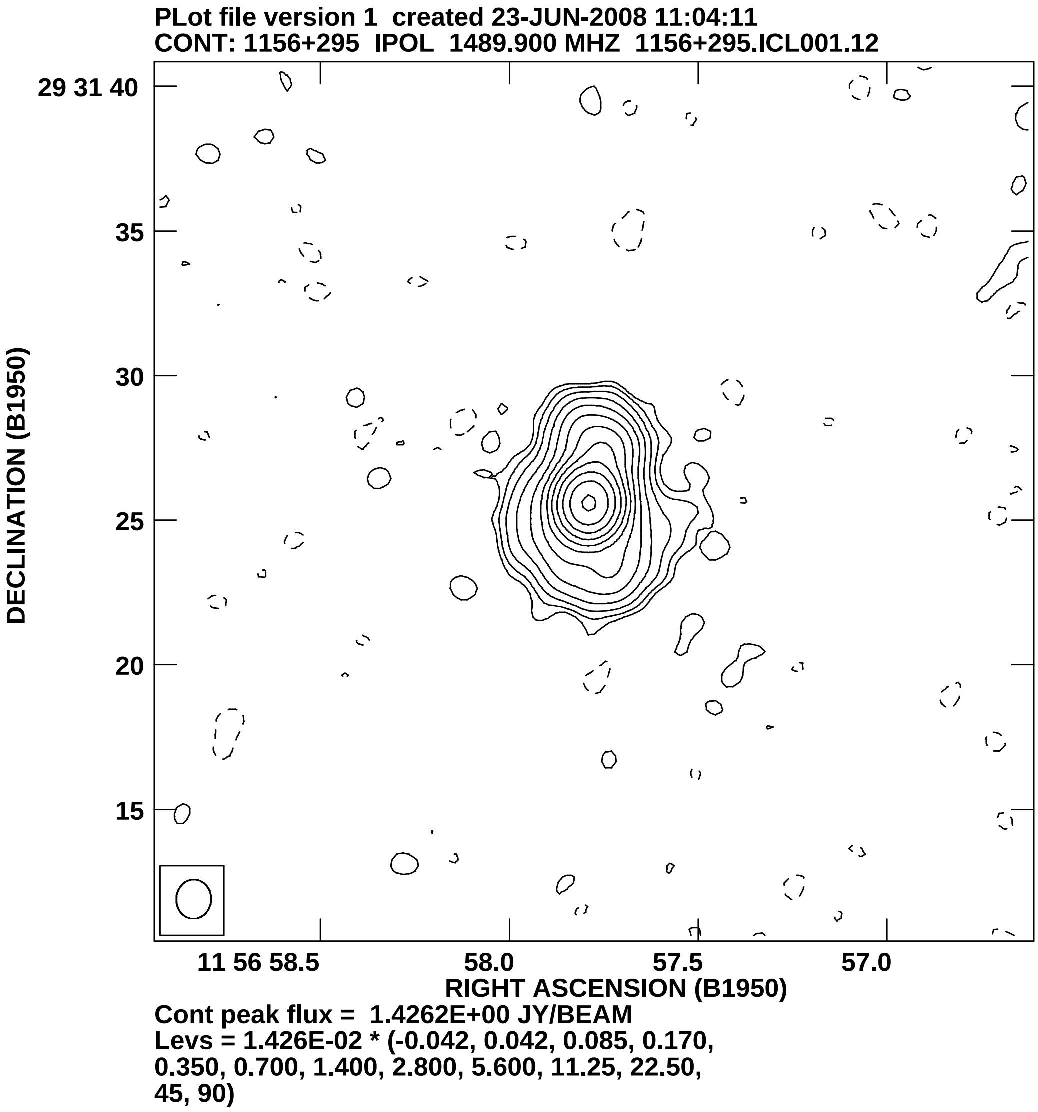

Figure 7.7. VLA L band (20 cm, 1.469 GHz) image of the HPRQ 1156+295. The presence of a 2-sided halo is confirmed. The halo to the south of the core, probably from the counterlobe, is slightly fainter and more extended.

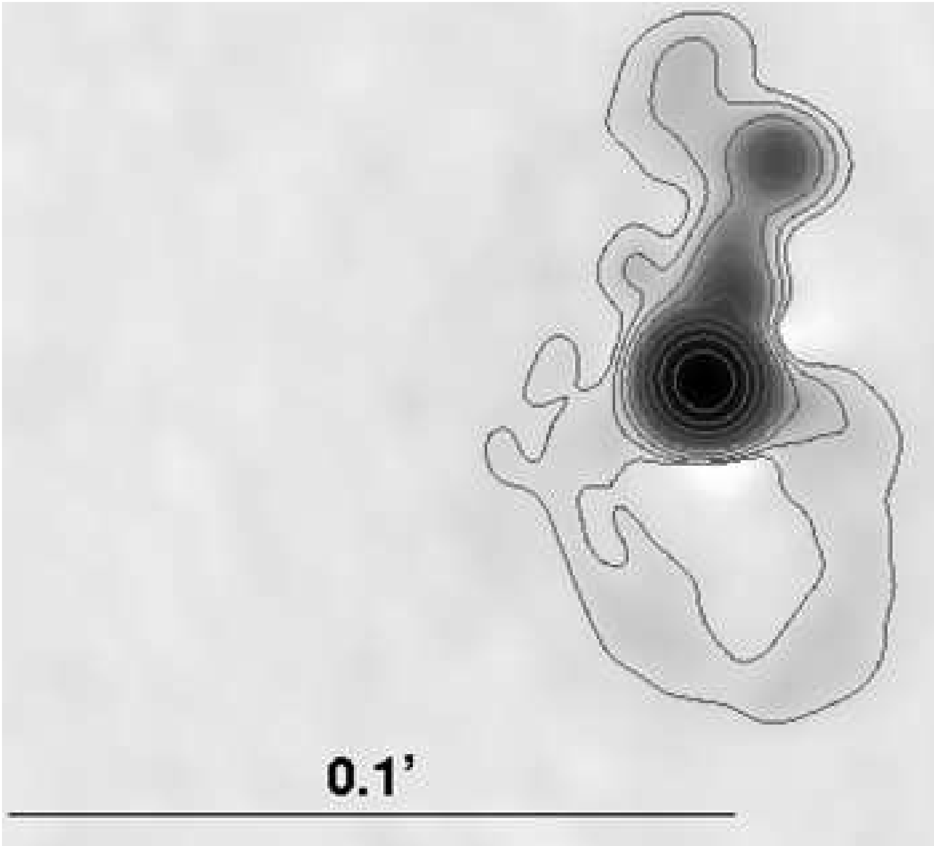

Figure 7.8. VLA C band (6 cm, 4.86 GHz) image of the high galactic latitude HPRQ 1156+295. The contour levels are: (0.042, 0.085, 0.17, 0.35, 0.7, 1.4, 2.8, 5.6, 11.25, 22.5, 45, 90)% and the maximum is 1.662 Jy/beam. A bent kpc scale jet is evident. Also evident is the presence of a faint halo in a southernly direction from the central core, which might be from the counter lobe.

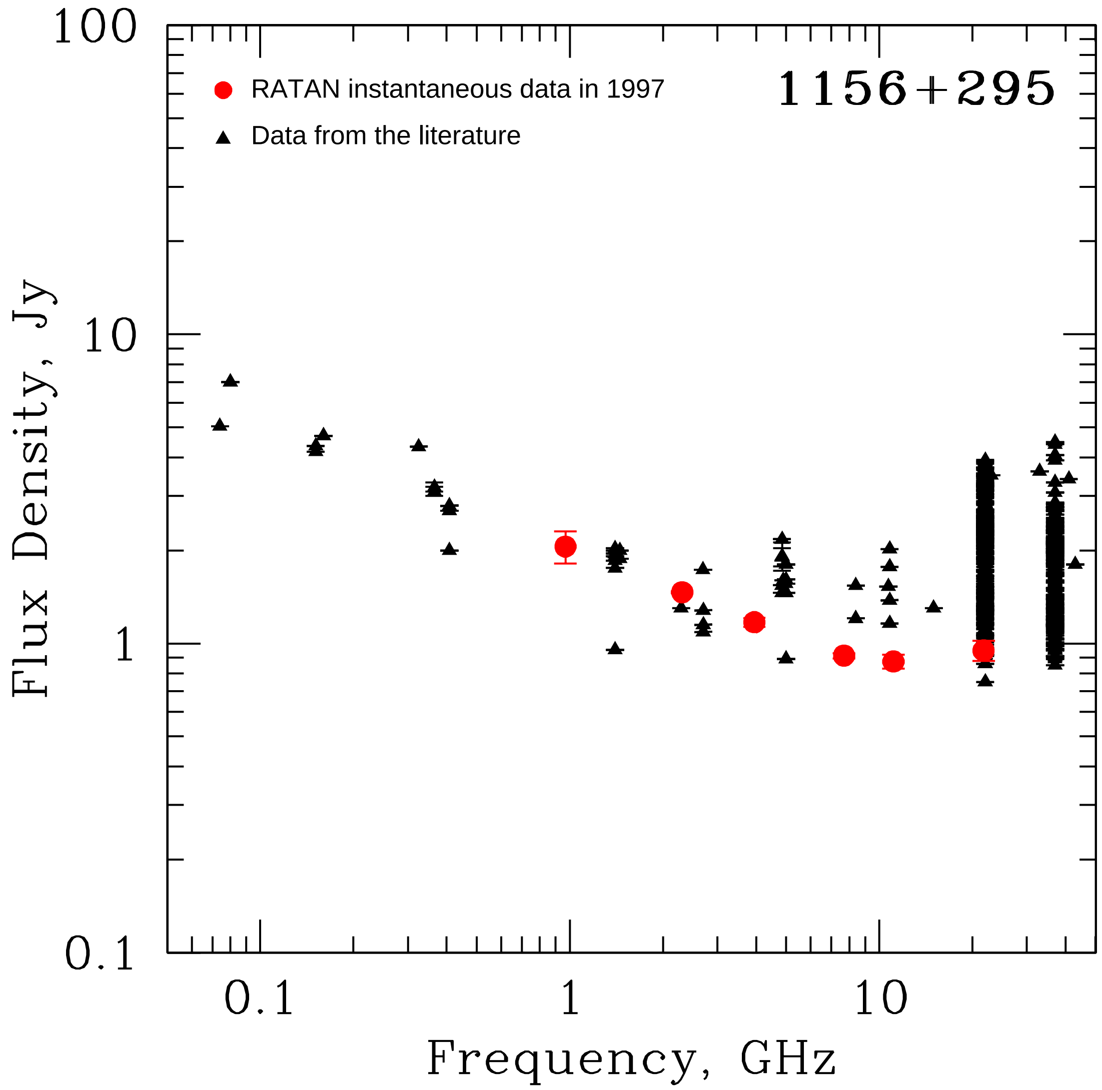

Figure 7.9. The radio spectrum of the EGRET & LAT (*Fermi*) detected HPRQ 1156+295. Large variations for $\nu > 10$ GHz are evident.

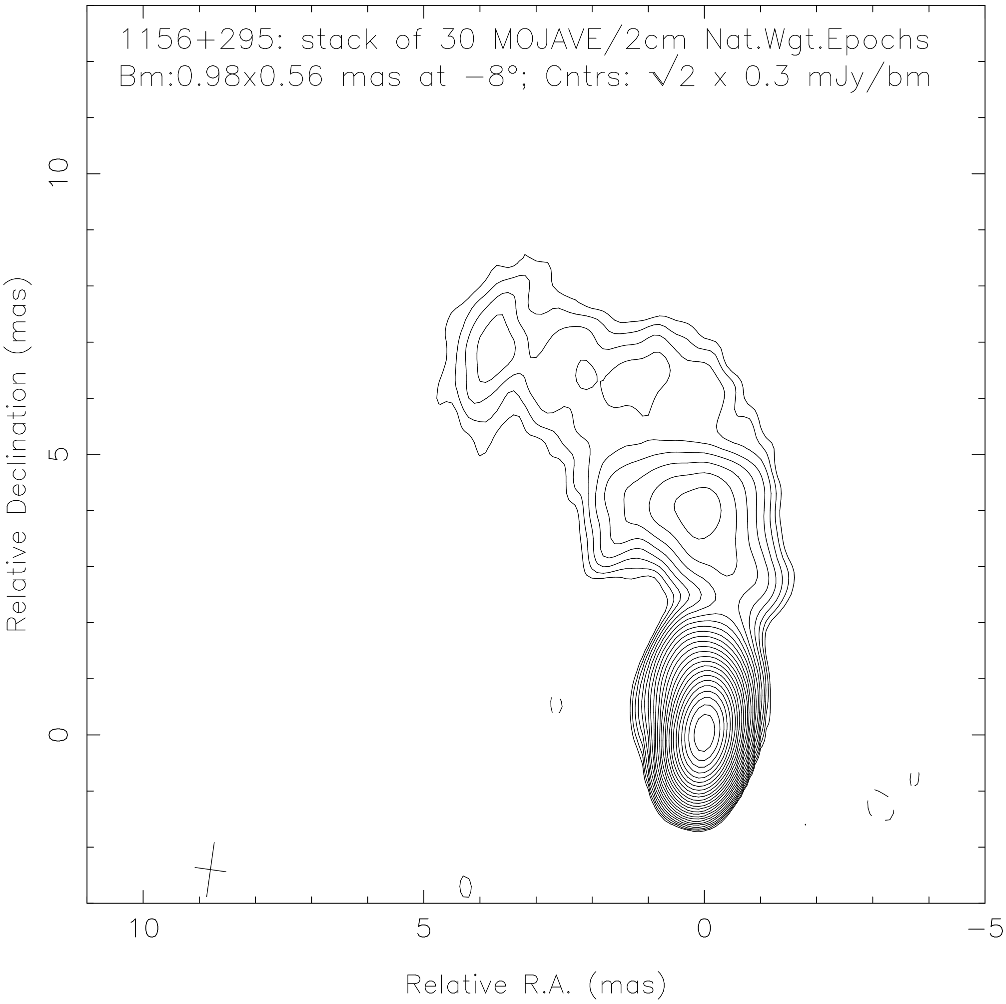

Figure 7.10. Stacked, naturally weighted, 2 cm VLBA images of 1156+295 from the *MOJAVE* project [Lister et al., 2009a]. The HPRQ 1156+295 has been observed to show intra–night variability in optical and hence classified as an Optically Violently Variable (OVV) quasar.

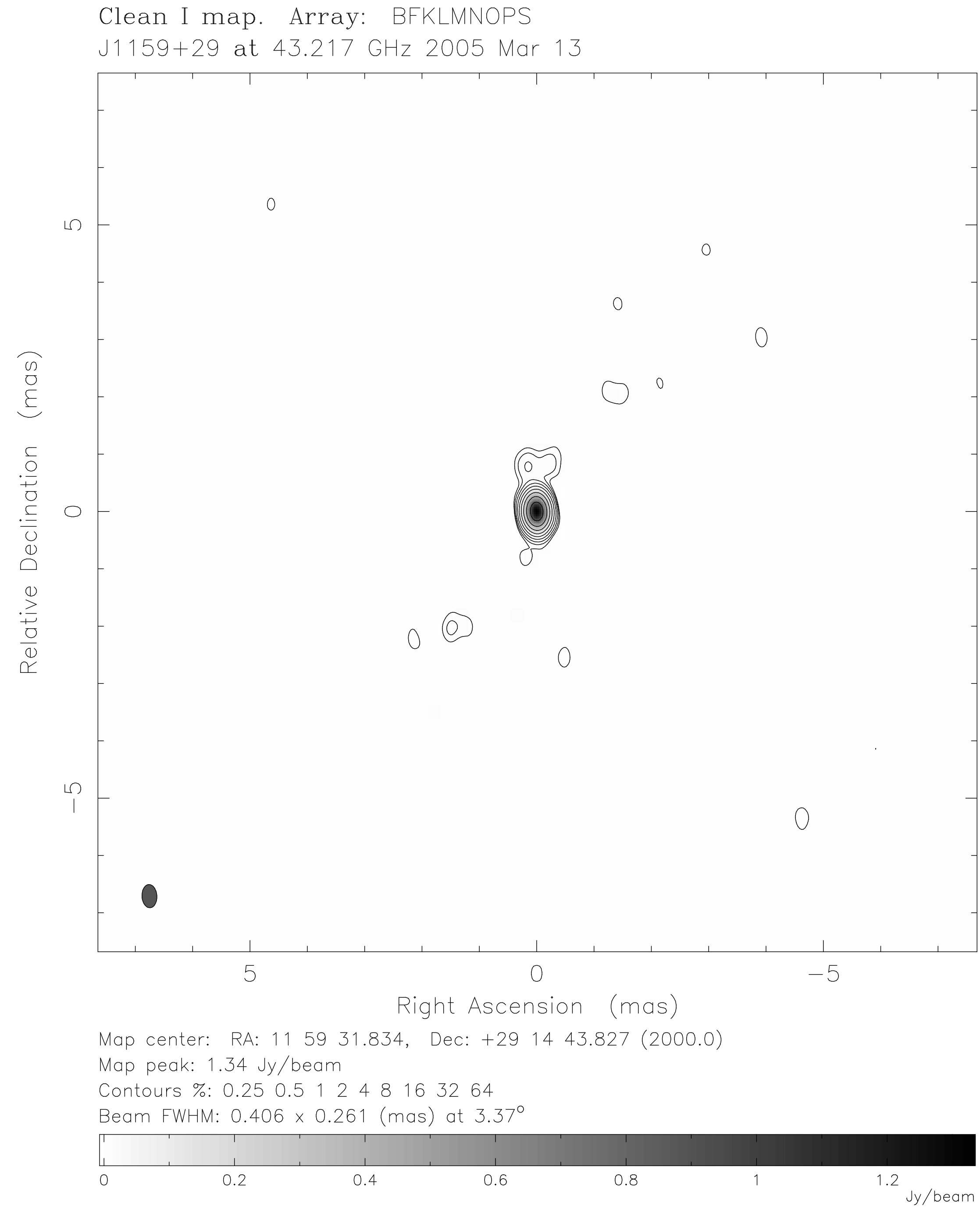

Figure 7.11. 43 GHz VLBA image of 1156+295 (4C +29.45). Mattox et al. [2001] list 1156+295 as being a 'Probable' EGRET source and has been detected by the *Fermi* LAT instrument above 10σ level [Abdo et al., 2009, 2010].

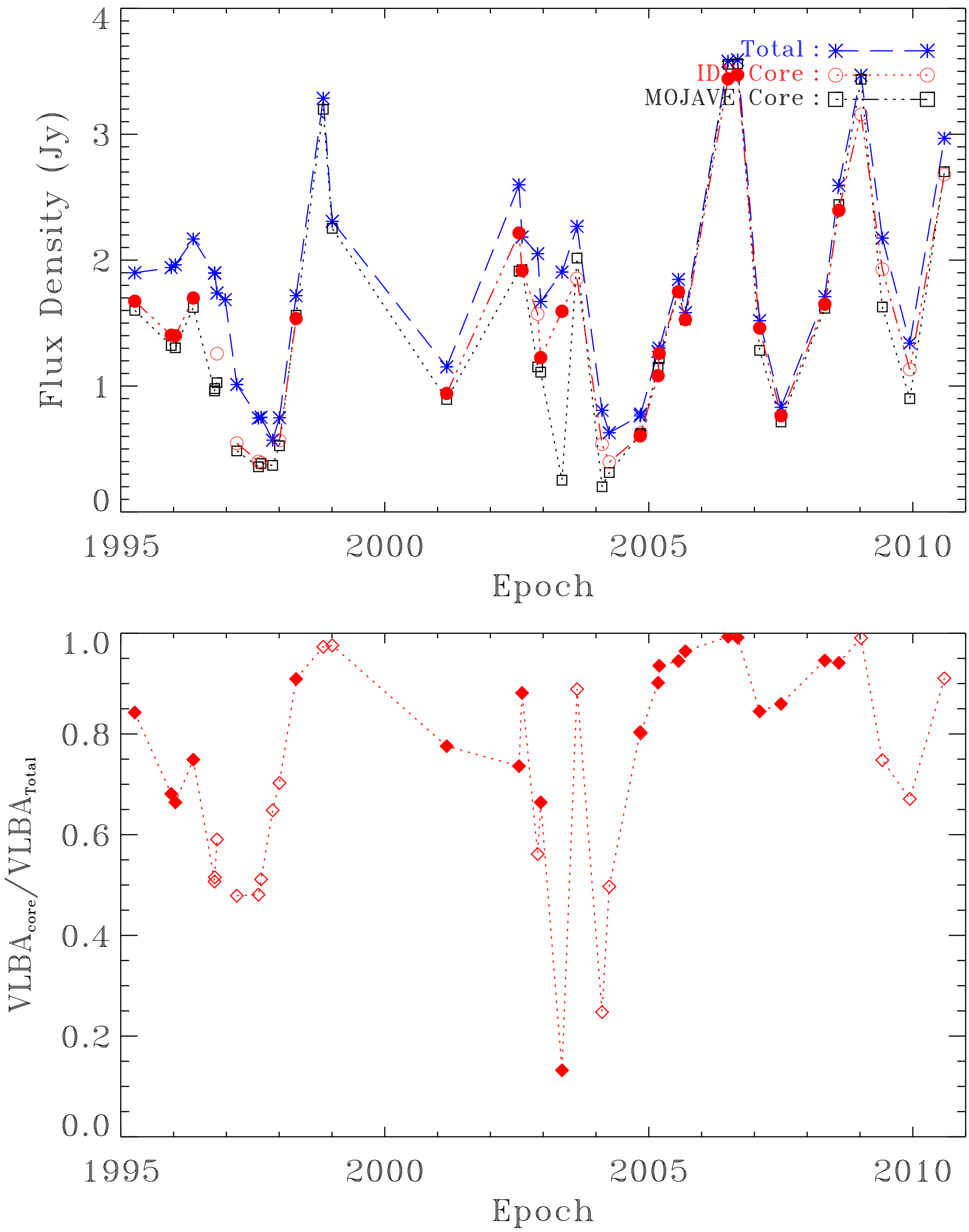

Figure 7.12. VLBA 2 cm light curves for the HPRQ 1156+295. *Top*: Shown are the total 2 cm VLBA flux density, flux density of the IDV core, as well as the flux density of the 'core' (as modelled in the kinematic analysis) for the source. *Bottom*: Plot of the 'compactness' for this source. Here 'compactness' is defined as the ratio of the VLBA 15 GHz core flux density to the VLBA total flux density. Epochs with pronounced IDV activity (e.g., Fig. 7.13) are indicated by filled symbols.

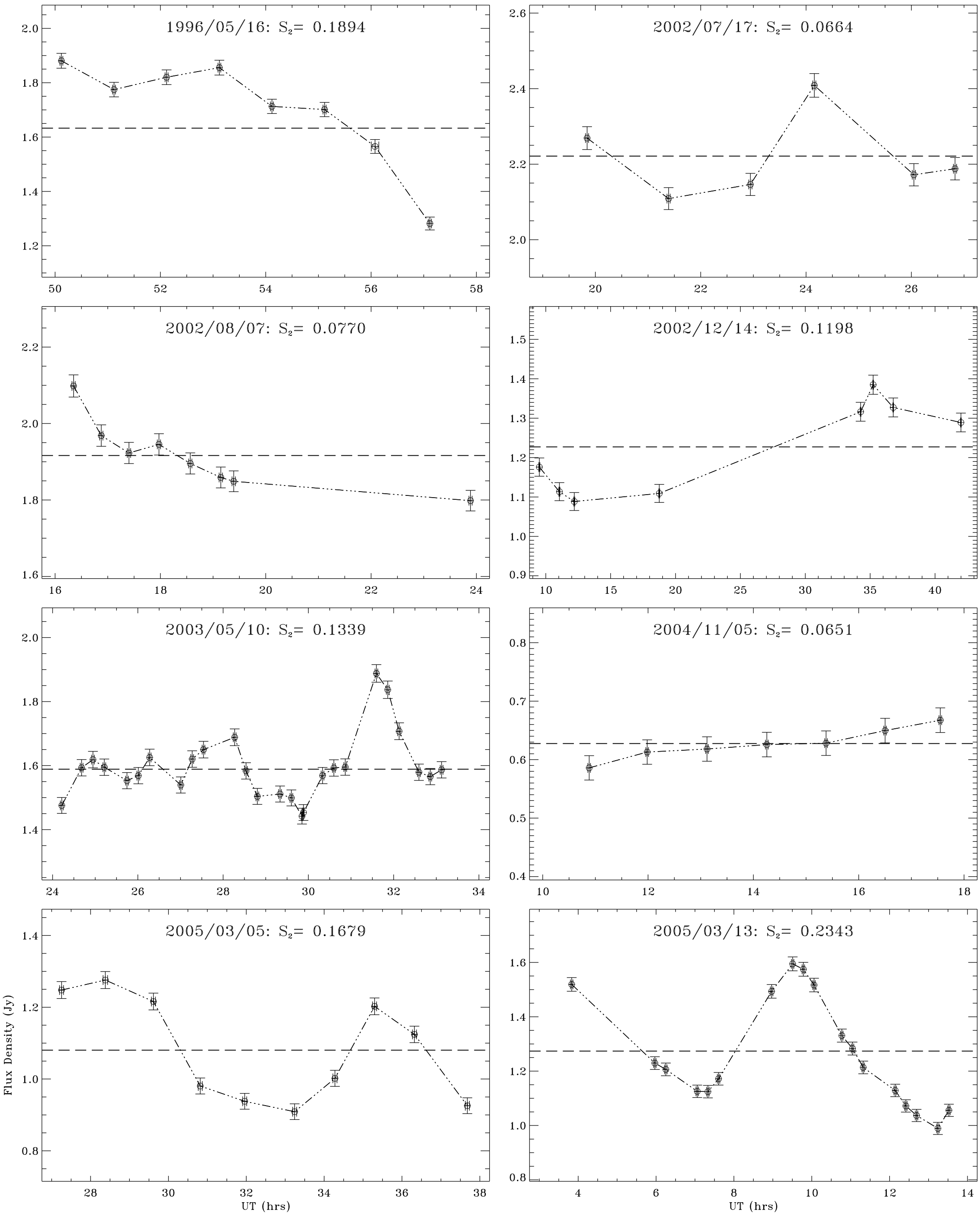
1996/05/16: S₂= 0.1894
2002/07/17: S₂= 0.0664
2002/08/07: S₂= 0.0770
2002/12/14: S₂= 0.1198
2003/05/10: S₂= 0.1339
2004/11/05: S₂= 0.0651
2005/03/05: S₂= 0.1679
2005/03/13: S₂= 0.2343
Flux Density (Jy)
UT (hrs)

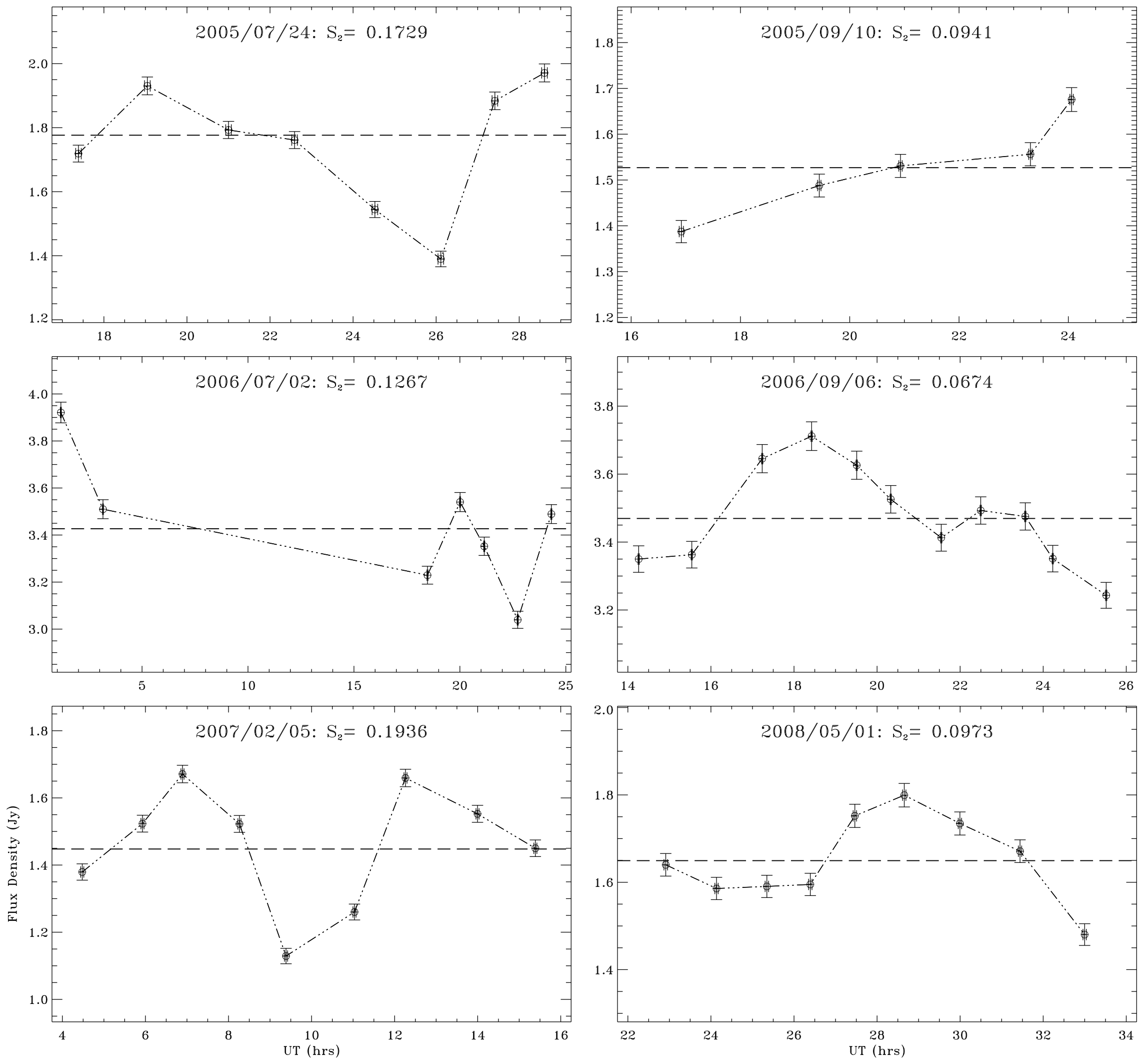

Figure 7.13. 2 cm VLBA light curves for the HPQ 1156+295, which is among the few persistent IDV sources in the current analysis, with an unambiguous IDV detection in 19 out of 38 epochs dating back to 1996. It has exhibited IDV in almost all epochs after 2002 [Savolainen & Kovalev, 2008]

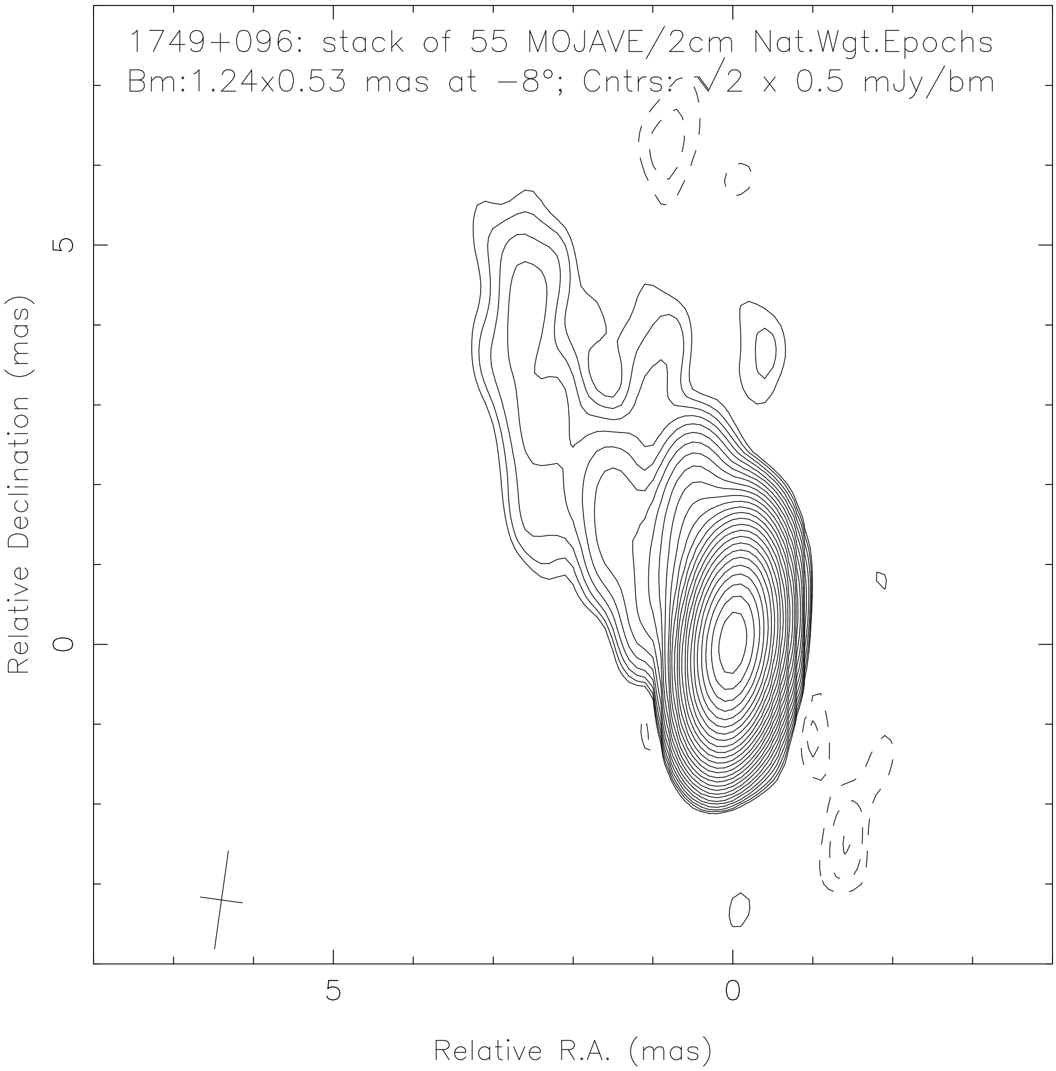

Figure 7.14. Stacked, naturally weighted, 2 cm VLBA images of 1749+096 from the *MOJAVE* project [Lister et al., 2009a]. 1749+096 has been listed by Véron-Cetty & Véron [2001] as QSO, but is an intermediate BLL/QSO.

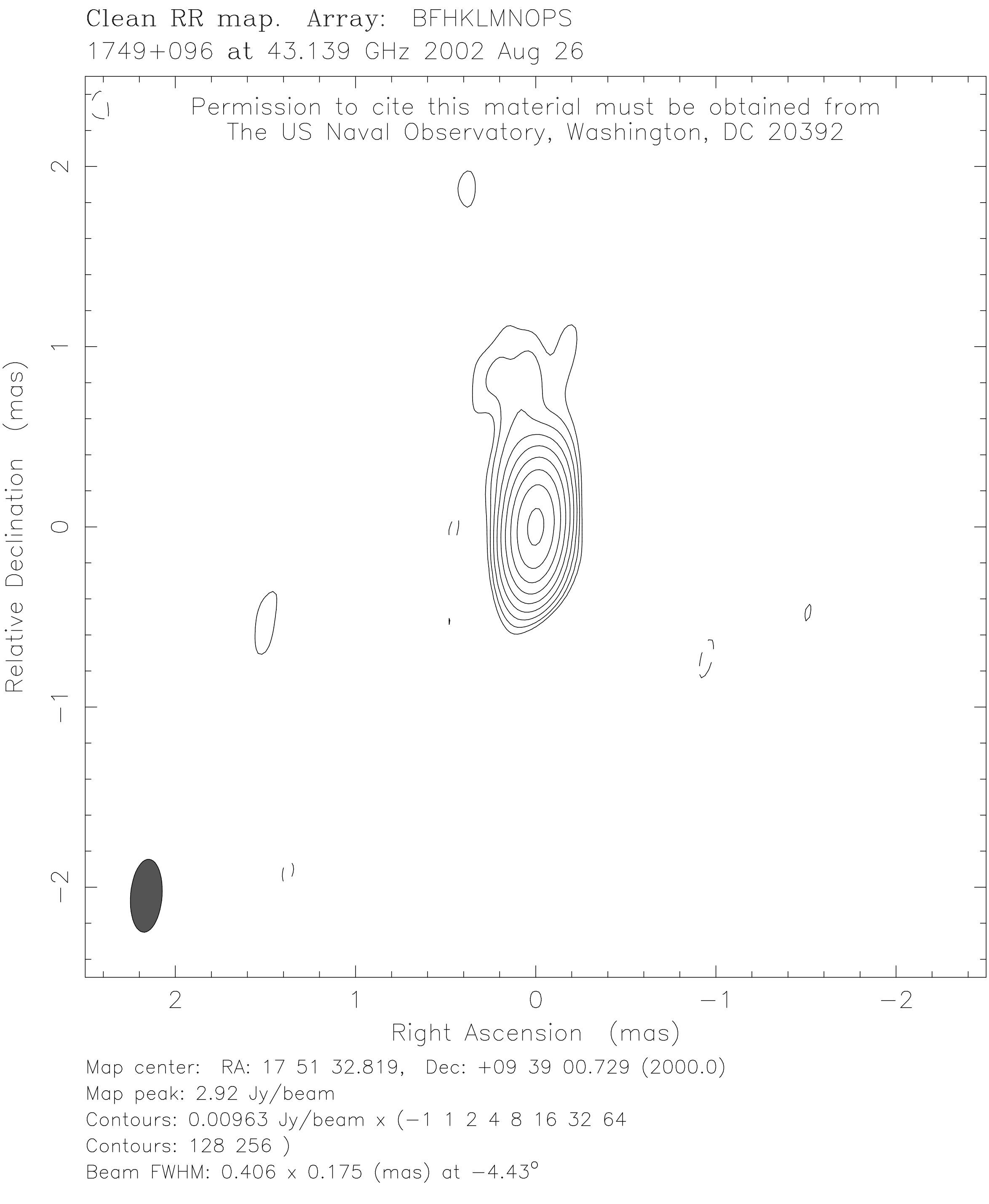

Figure 7.15. 43 GHz VLBA image of 1749+096 obtained from the USNO RRFID Survey database. 1749+096 was not detected by EGRET, but is a member of the *Fermi* LAT bright source list [sources detected by the LAT instrument above 10σ level; Abdo et al., 2009, 2010]. Remarkable similarity between this image and the 7mm image of the IDV source 1156+295 (Fig. 7.11), in that both appear to be very compact objects, may be noted.

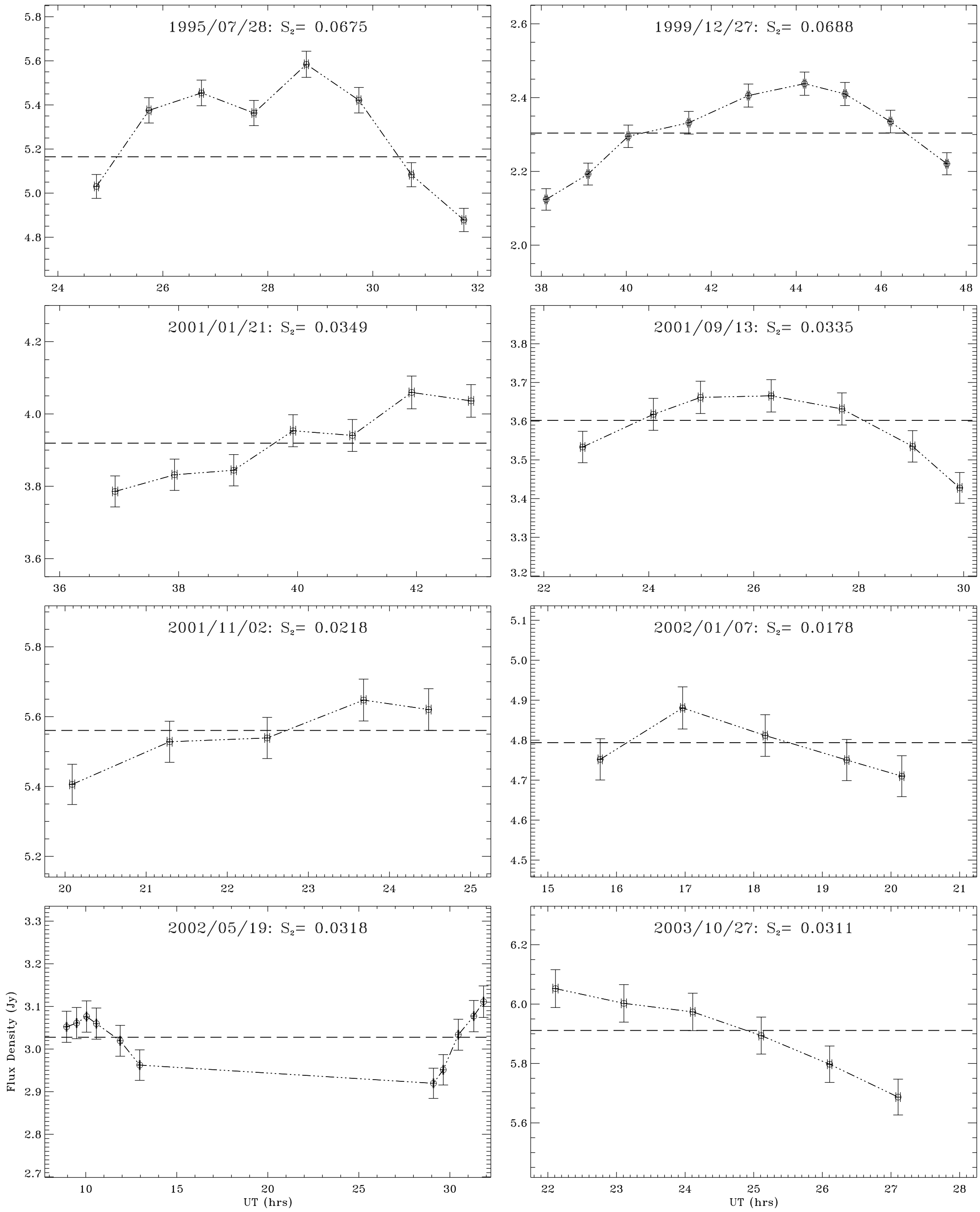

1995/07/28: S_2= 0.0675
1999/12/27: S_2= 0.0688
2001/01/21: S_2= 0.0349
2001/09/13: S_2= 0.0335
2001/11/02: S_2= 0.0218
2002/01/07: S_2= 0.0178
2002/05/19: S_2= 0.0318
2003/10/27: S_2= 0.0311
Flux Density (Jy)
UT (hrs)
UT (hrs)

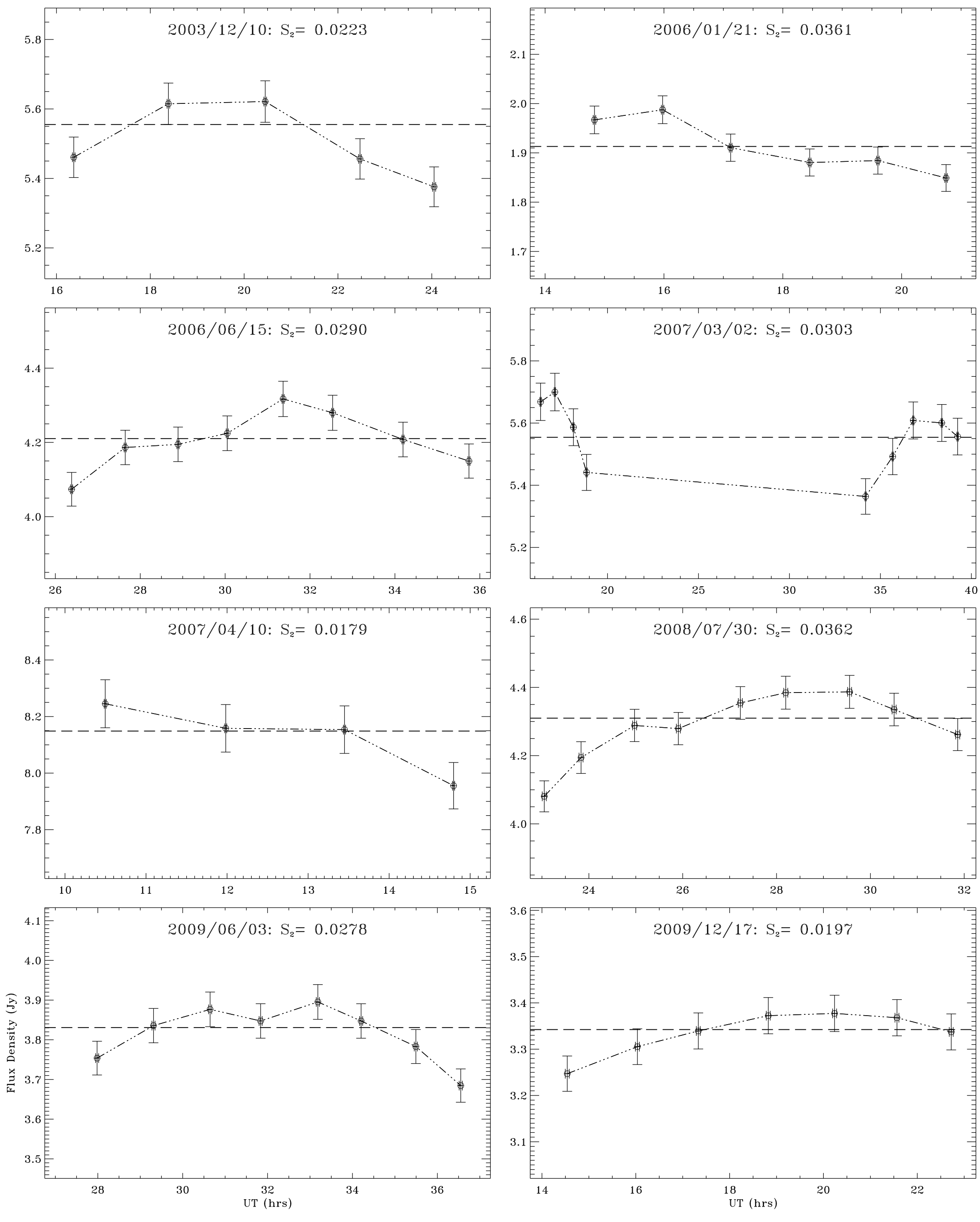

Figure 7.16. Multi-epoch VLBA 2 cm light curves for the BLL/QSO 1749+096, a source very similar in pc scale structure to the IDV source 1156+295.

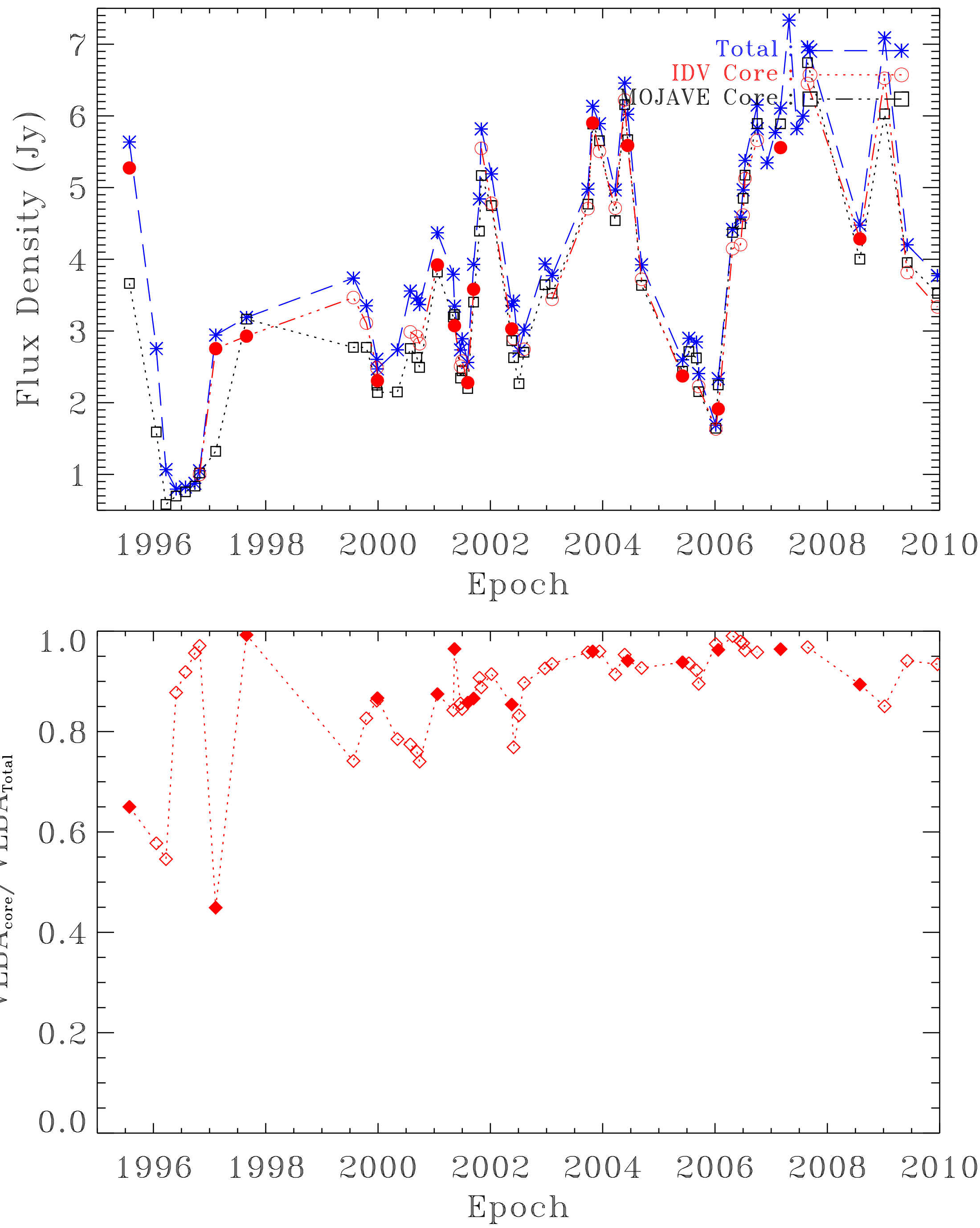

Figure 7.17. VLBA 2 cm light curves for the intermediate BL/Q object 1749+096. *Top*: Shown are the total 2 cm VLBA flux density, flux density of the IDV core, as well as the flux density of the 'core' for the source. *Bottom*: Plot of the 'compactness' for this source. Epochs with pronounced IDV activity (e.g., Fig. 7.16) are indicated by filled symbols. 1749+096, an extremely variable optical source, is one of a handful of sources in the current study that exhibited persistent IDV activity.

8. SUMMARY AND FUTURE WORK

In summary, approximately 3800 VLBA 2 cm light curves spanning 350 epochs (from 1994 – 2011), corresponding to ~ 375 sources comprising the full sample, have been analyzed for IDV for the first time, as part of the *MOJAVE* program. A novel 'Gain Transfer' methodology, developed by the *MOJAVE* team, was used for this purpose. Brightness temperatures were used to estimate the equipartition Doppler factors ($\delta_{\rm eq}$) for the *MOJAVE* sources, which were found to be in agreement with Doppler factor estimates via other techniques, reported in literature. Galaxies and BL Lacs were found to have a narrower distribution of $\delta_{\rm eq}$ factors compared to the QSOs.

IDV was detected in $\sim 28\%$ of sources and $\sim 11\%$ of epochs from the full sample, which is in agreement with dedicated IDV studies from the past [e.g., Quirrenbach et al., 1992, Lovell et al., 2008]. When only the 131 sources from the statistically complete, flux density limited *MOJAVE_1* sample were considered, IDV was detected in $\sim 62\%$ of sources and $\sim 15\%$ of epochs. Also, $\sim 67\%$ of the *MOJAVE_1* sources have a *Fermi* GeV detection. As expected, all the sources with high $\delta_{\rm eq}$ values have a *Fermi* GeV detection.

A correlation between IDV activity and the optical type of the source was noticed, with almost all the genuine BL Lacs and Galaxies turning out to be non–IDV sources. As expected, CSS/GPS sources showed no IDV, and hence were used as in determining the criteria for IDV classification. IDV activity was found to be positively correlated with beaming indicators (such as $\delta_{\rm eq}$ & $\beta_{\rm app}$), and negatively correlated with the galactic latitude position of the source. No correlation between redshift and IDV activity was noticed. A correlation between flaring, superluminal component ejection and IDV was also noticed. All these observations can qualitatively be explained by invoking a model involving scintillation of tiny, high brightness temperature components dominated by inverse Compton (IC) losses.

Persistent IDV activity was noticed in only a handful of sources. The high galactic latitude HPRQ 1156+295 was found to be a new rapid IDV source, possibly the brightest IDV source to date. Some of the common radio selected low enery peaked BL Lacs (LBLs), which in actuality are intermediate BL Lac/QSOs, as inferred from the occassional presence of lines in their optical spectra, were found to have IDV characteristics similar to those of the quasars. This is in agreement with the recent reports of similarities between the GeV SEDs of these two classes of objects. Also, the IDV activity in these intermediate BL/Q sources was found to be slower and of lesser magnitude compared to that in the HPRQs.

Some ideas for future work are as follows:

1. Continue processing future epochs of *MOJAVE* data, which continue to be gathered every three weeks on the VLBA. Besides the modulation index and the S_2 statistic, there are a few other variability indices often cited in IDV literature [e.g., Aller et al., 2003]. Although vastly different results are not expected upon using them, it is worthwhile to investigate those as-well, with a more extensive dataset.

2. In light of the probable association between IDV activity, flaring and superluminal component ejection, variability analysis of *Fermi* data should be carried out. Also, correlated data from other frequencies (like hard X-ray) should be analyzed, specifically, comparing times of flaring in multiple bands with IDV and pc scale jet activity.

3. It is expected that the polarization variability amplitudes are larger than the total flux density variability [see Fig. 8.1 & Medvedev, 2000]. Hence, an analysis similar to the one discussed in this dissertation was carried out on polarization

data (where available). However, the fact that the AGN cores in question are in general weakly polarized, and the polarized features are often contained in the pc scale jet (and hence displaced from the core) renders any direct interpretation of the results subject to error. Moreover, the observed polarized source structure could be very sensitive to the (u,v) coverage, and hence vary among the individual scans. An attempt to characterize this systematic effect should be carried out.

4. Initial analysis of the *MOJAVE* data has revealed differences among BL Lacs and quasars, with the former having magnetic fields preferentially oriented perpendicular to the jet direction while the latter have a wide range of orientations [Lister & Homan, 2005]. Data from *Fermi* instrument also has revealed a difference in the $\gamma-$ray spectral indices and SED of the two classes [Abdo et al., 2009, Ghisellini et al., 2009]. It is also known that the Mg II λ 2798 line luminosity in BL Lacs is about an order of magnitude lower than that of quasars, and also that the BL Lacs occupy the lower luminosity region of the continuum versus line luminosity plane [Sbarufatti et al., 2005, 2006]. Equipartition Doppler factors from the current analysis also indicate that despite the lower radio luminosities observed for BL Lacs, the intrinsic luminosities for the two types of objects are very similar i.e., the BL Lacs are less beamed than quasars (see Fig. 8.2). These lower $\delta_{\rm eq}$ values for BL Lacs would also explain the lack of IDV detections among them in the current study. One possible explanation for all these observations is that the BL Lacs have smaller jet opening angles. A consequence of such a scenario is that radio observations should reveal the presence of recollimation shocks among a larger fraction of BL Lacs than quasars, provided the only difference between the jets among these two classes is the jet opening angle [e.g., Nalewajko, 2009]. Indeed, a cursory examination of *MOJAVE* data has revealed that a higher fraction of BL Lacs have stationary features, often associated with recollimation shocks (see Fig. 1.11; Lister et al. in prep.). Hence, these differences need to be studied in detail.

5. *MOJAVE* data has revealed distinction in the pc scale jet properties of QSOs and the high energy peaked AGN (chiefly HBLs), especially in the component ejection and structural evolution of the jets [e.g., Lyutikov & Lister, 2010]. In light of these, and differences in the beaming properties of BL Lacs and QSOs, a prediction from the proposed qualitative model for IDV is that: In a sample of BL Lacs and QSOs, with similar galactic latitude distribution for the two source types, the decrease in the fractional number of IDV sources with increasing galactic latitude should be steeper for the BL Lacs compared to QSOs, since the former have lower $\delta_{\rm eq}$ values compared to the latter.

6. In deriving the $\delta_{\rm eq}$ factors, it was assumed that the intrinsic brightness temperature of all the objects was equal to the equipartition value of T_{eq}. On the whole, this appears to be a fair assumption. However, for a few frequently flaring sources (like 3C 279) the inferred Lorentz factors appear to be slightly large. This problem may be overcome if a higher intrinsic T_b value is assumed. One choice would be the IC T_b value of 10^{12} K. This T_b value was derived under the assumption of incoherent synchrotron emission in an isotropic magnetic field. Assumption of an anisotropic **B** field geometry can yield T_b limits up to an order of magnitude higher [e.g., Qian et al., 2002]. Though the reason for such an anisotropic geometry is unknown, it could explain the occurence of rapidly decaying flares (isotropization of the **B** field would lead to rapid cooling) and observation of episodic IDV. Hence, these various T_b limits should be explored to derive physically meaningful limits on the $\delta_{\rm eq}$ factors for various objects.

7. Besides the rapid IDV source 1156+295, the current analysis has revealed a few other intriguing sources. For example, the high redshift object 0808+019 ($z = 1.148$; $\beta_{\rm app} \sim 13$)[1] has the highest $\delta_{\rm eq}$ factor among all the BL Lacs, but only has a very marginal IDV detection (and hence its classification as a non–IDV source). One reason could be that the object has been in a faint state since

[1]See: `http://www.physics.purdue.edu/MOJAVE/sourcepages/0808+019.shtml`

the early 90s. Another intriguing source is the high redshift QSO 2005+403. Located in the Cygnus region, this source has been reported to show scattering below 8 GHz [Gabányi, 2006]. VLBA 2 cm light curves for this source are shown in Fig. 8.3. Shown are the total 2 cm VLBA flux density, flux density of the IDV core, as well as the flux density of the 'core' (as modelled in the kinematic analysis) for this source. Also plotted is the 'compactness' for 2005+403, where 'compactness' is defined as the ratio of the VLBA 15 GHz core flux density to the VLBA total flux density. As can bee seen from the aforementioned plot, there appears to be episodes of abrupt dimming of the core (indicated by a precipitous drop in compactness) followed by gradual brightening. It may be noted that, contrary to expectations, such a dimming does not precede a superluminal component ejection (Fig. 8.4), which makes this phenomenon all the more interesting. Hence, this source would make an excellent target for regular monitoring campaigns [e.g., Richards et al., 2009].

8. In the current IDV analysis, the core has been modelled as a single Gaussian component. This approach might not work for sources with extremely complicated VLBA core structure, like the HPRQ 2251+158 ($z = 0.859$; $\beta_{\rm app} \sim 14.2$)[2]. Hence, such sources have currently been excluded from the final modelling and analysis. However, 2251+158 has been reported to be a rapidly flaring GeV source (and one of the brightest GeV sources in the sky) by the *Fermi* LAT team [e.g., Pacciani et al., 2010, Striani et al., 2010]. A giant radio flare has also been recently observed in this source (see Fig. 8.5, 8.6). The source seems to become more compact during flaring as expected. There is also evidence for IDV activity, especially in polarized flux and polarization angle during these episodes of flaring. Hence, sources like this one need to be investigated further.

9. Marginal IDV has been detected in the LPRQ 1828+487, which is quite unusual, given its steep spectrum source with compact structure (and hence its classifica-

[2]See: `http://www.physics.purdue.edu/MOJAVE/sourcepages/2251+158.shtml`

tion as a CSS source). Its high $\beta_{\rm app}$ and $\delta_{\rm eq}$ values also indicate it to be a member of the growing class of 'masquerading' CSS/GPS sources, i.e., blazars with significant extended emission, giving rise to a single dish radio spectrum similar to that of CSS/GPS sources. An accurate classification of such sources would go a long way towards resolving the problem of statistical overabundance of GPS sources and enhancing the current understanding of these objects. Hence, this source warrants further study, especially imaging and spectral studies at sub-arcsecond resolutions.

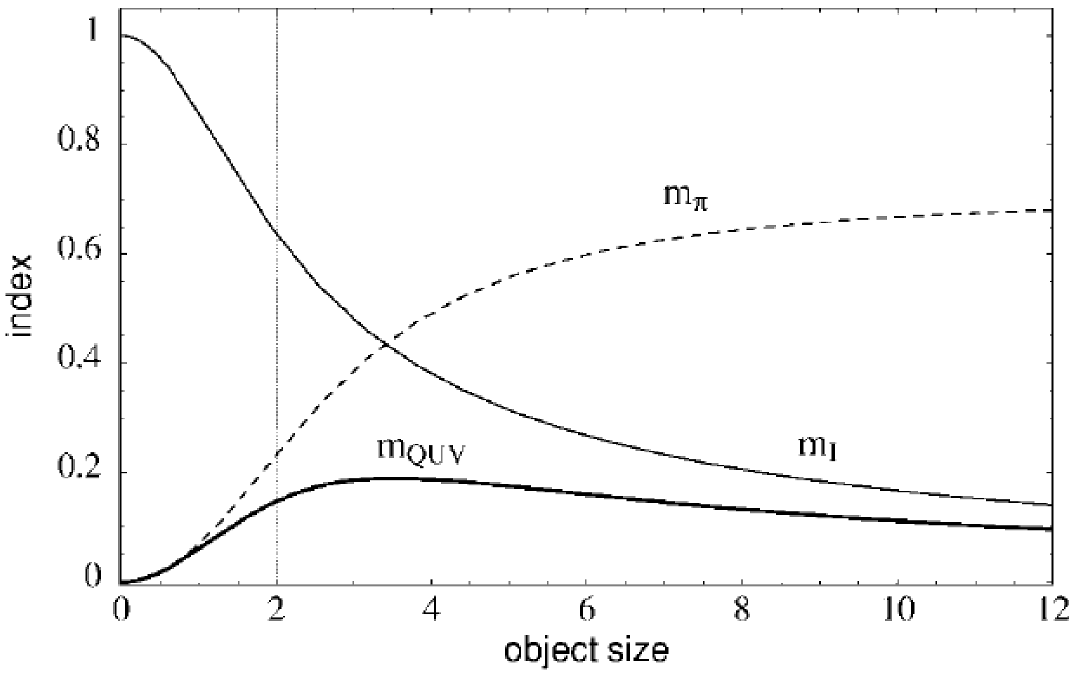

Figure 8.1. Plot of total flux and polarized flux modulation indices ($\rm m_I$, $\rm m_{QUV}$) vs. normalized angular size of the source from Medvedev [2000]. $\rm m_\pi = m_{QUV}/m_I$ denotes the 'degree' of polarization and $\theta = 2\theta_s/\theta_0$ where θ_s, θ_0 are the source size and the characteristic size for the various scattering regimes (see section 3.1.3. $\rm m_\pi$ increases with increasing source size and hence would be useful in identifying new scintillating sources.

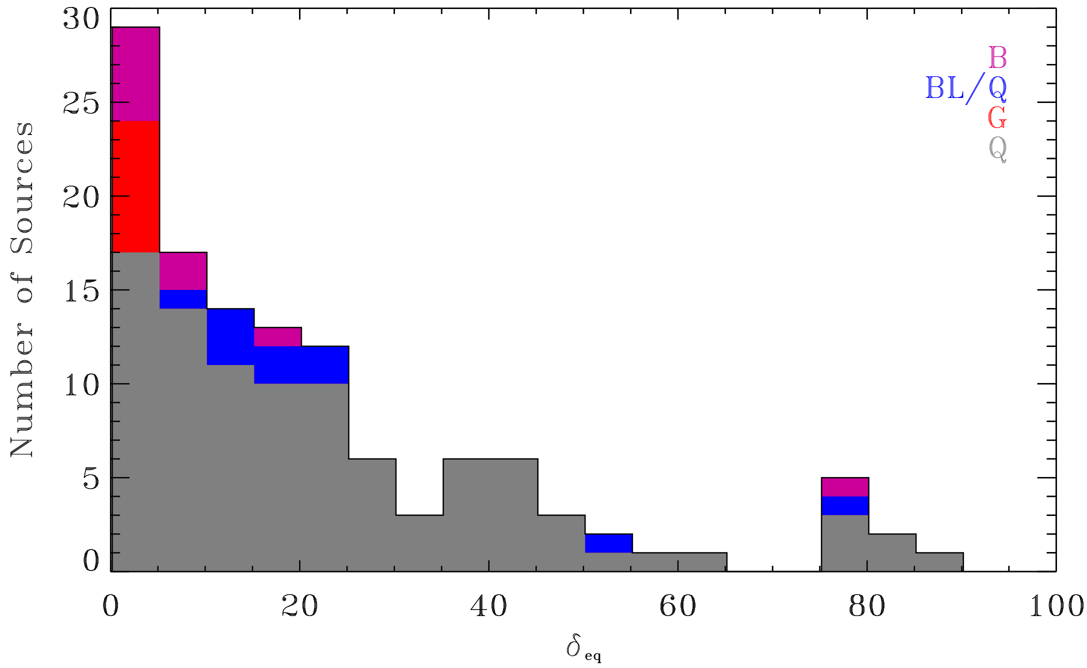

Figure 8.2. Distribution of the δ_{eq} in the *MOJAVE* sample. The δ_{eq} values of QSOs span a much wider range compared to the other types of objects. As expected galaxies have very low δ_{eq} values.

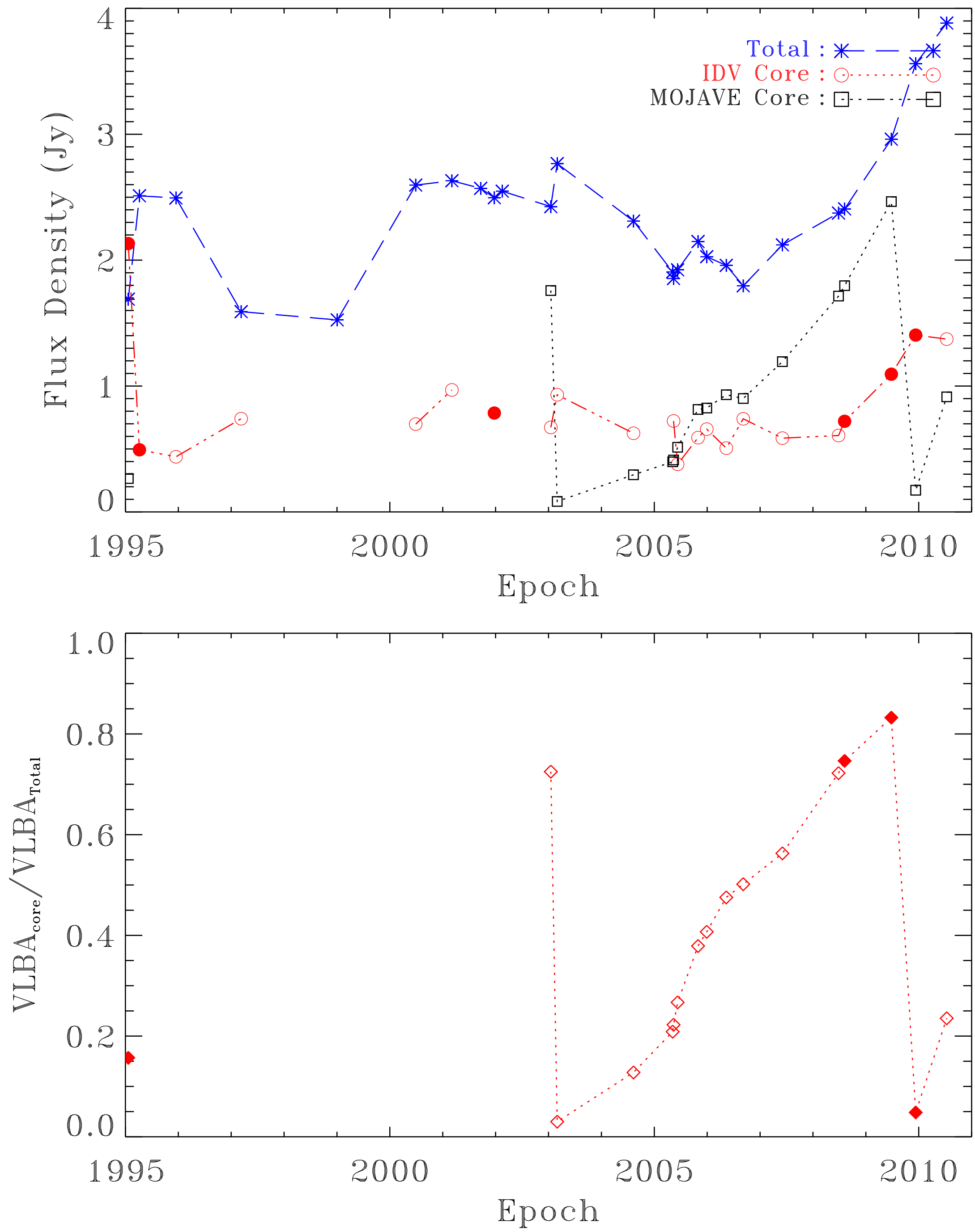

Figure 8.3. VLBA 2 cm light curves for the high redshift QSO 2005+403. *Top*: Shown are the total 2 cm VLBA flux density, flux density of the IDV core, as well as the flux density of the 'core' (as modelled in the kinematic analysis) for 2005+403. *Bottom*: Plot of the 'compactness' for this source. Here 'compactness' is defined as the ratio of the VLBA 15 GHz core flux density to the VLBA total flux density. Filled symbols indicate epochs with IDV detection.

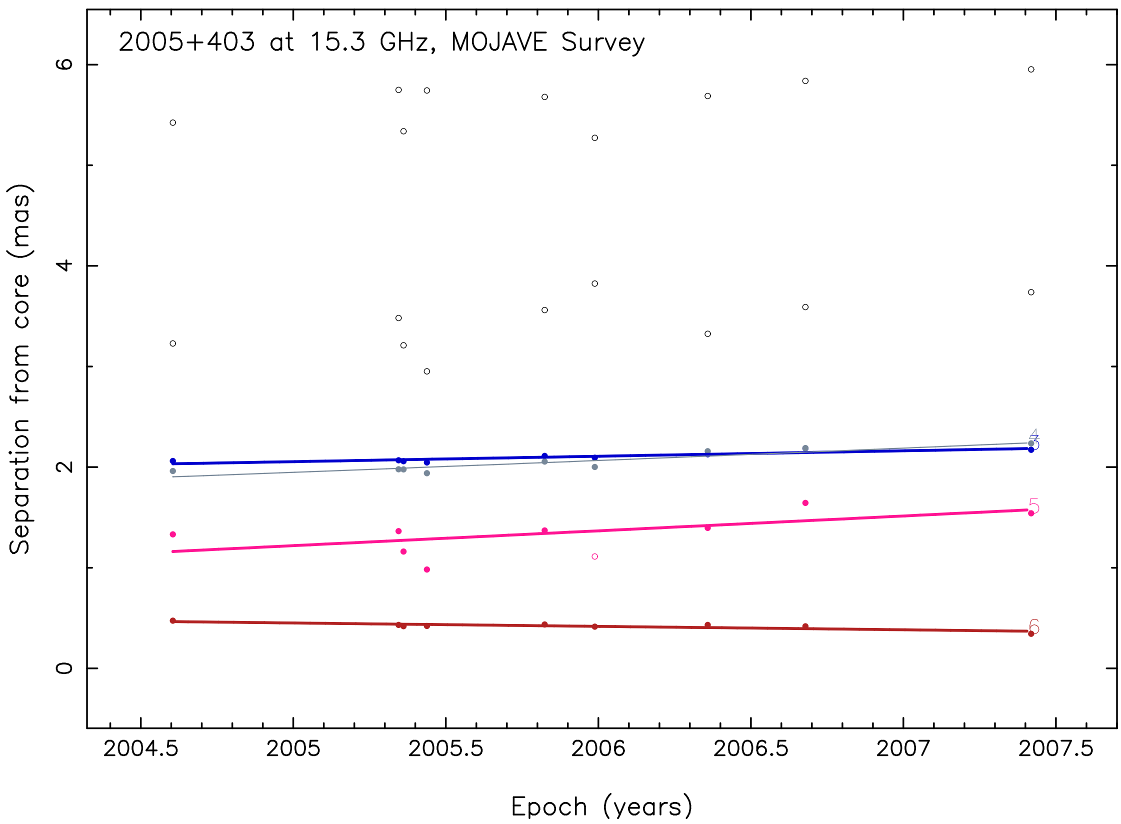

Figure 8.4. 2005+403 – component separation vs. time plot (Lister et al., in prep.).

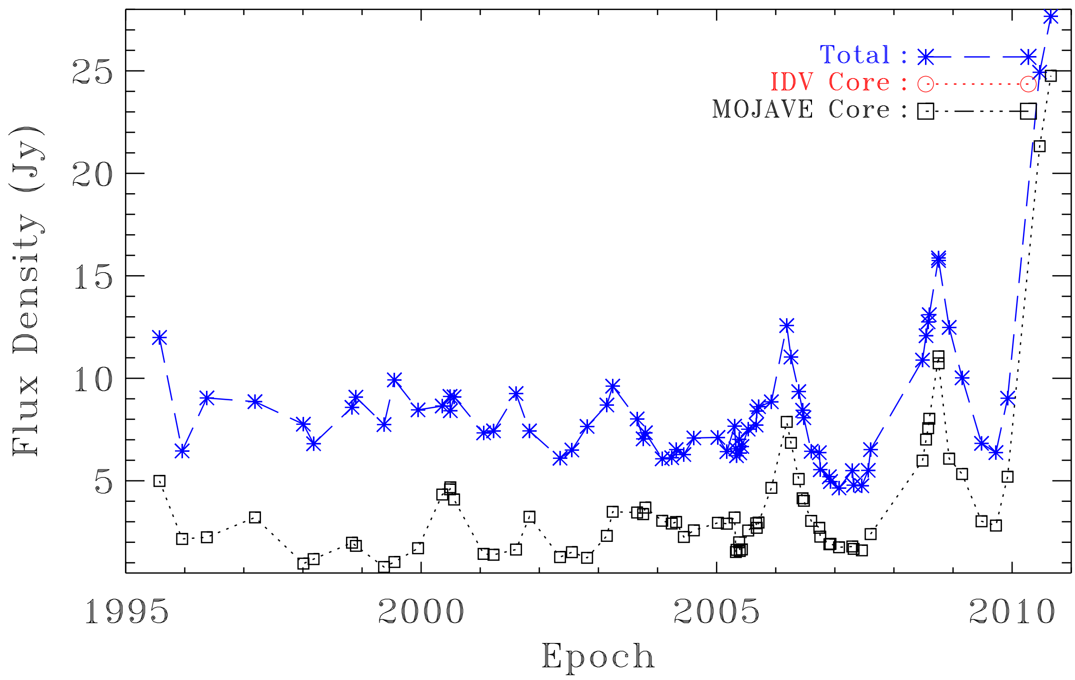

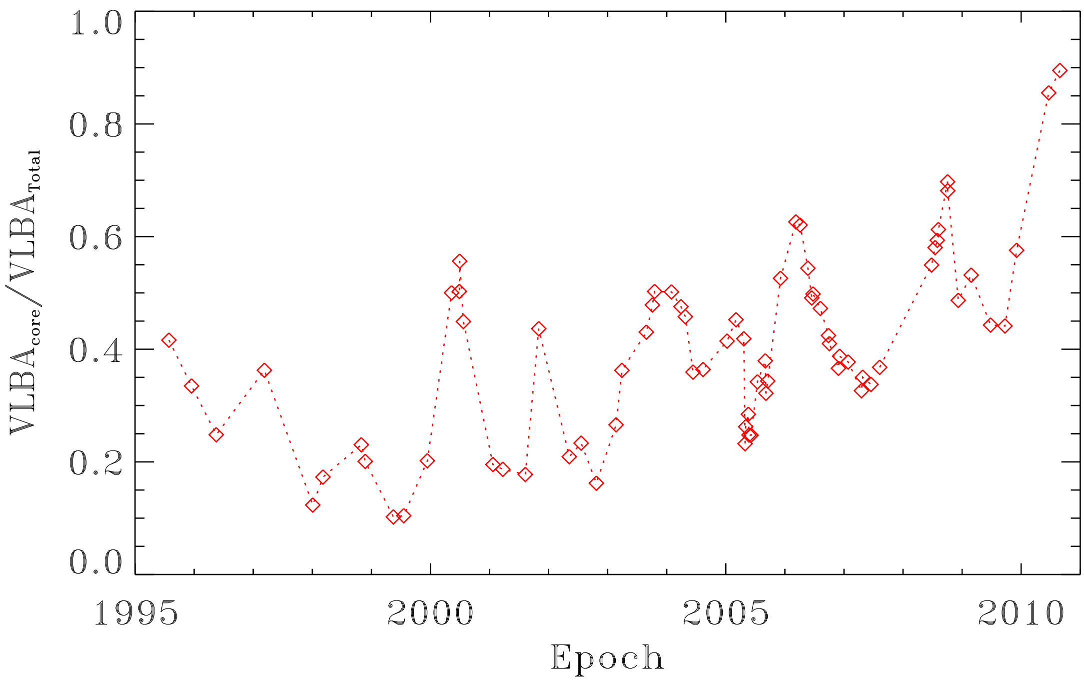

Figure 8.5. VLBA 2 cm light curves for the HPRQ 2251+158. *Top*: Shown are the total 2 cm VLBA flux density, flux density of the IDV core, as well as the flux density of the 'core' (as modelled in the kinematic analysis) for this source. *Bottom*: Plot of the 'compactness' for this source. A trend towards the source becoming compact (core dominated) with increasing flux density viz., during flaring is evident.

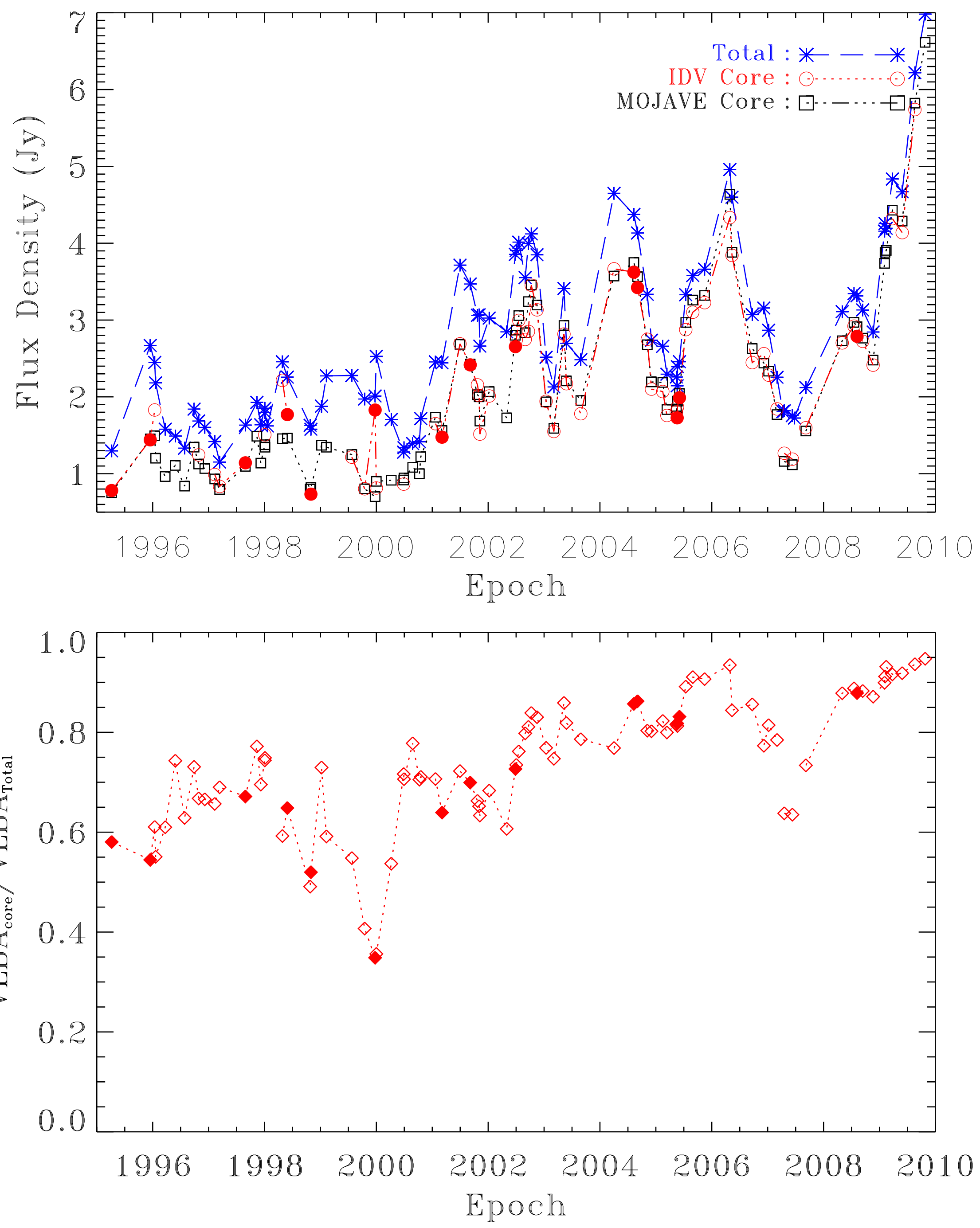

Figure 8.6. VLBA 2 cm light curves for the intermediate BL/Q object 0851+202 (OJ 287). *Top*: Shown are the total 2 cm VLBA flux density, flux density of the IDV core, as well as the flux density of the 'core' for this source. *Bottom*: Plot of the 'compactness' for this source. The core of this source is thought to be comprised of a SMBH binary and exhibits periodicity of $\sim$ 12 yrs. [e.g., Sillanpää et al., 1988, Lehto & Valtonen, 1996] in its optical light curves, along with rapid variability in optical and radio polarization [e.g., D'Arcangelo et al., 2009]. Once again, a trend towards the source becoming compact (core dominated) with increasing flux density viz., during flaring is evident.

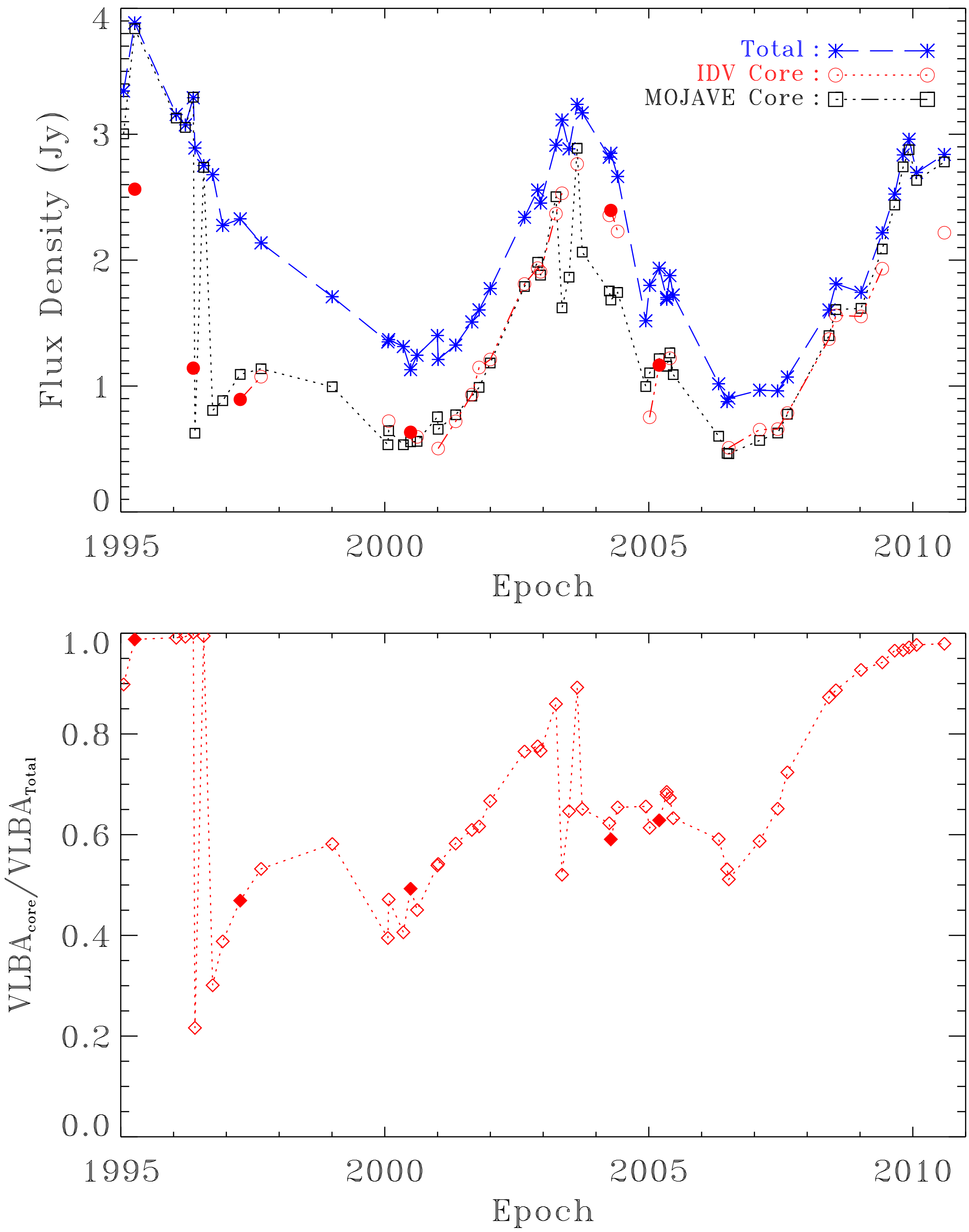

Figure 8.7. VLBA 2 cm light curves for the intermediate BL/Q object 1308+326. Shown are the total 2 cm VLBA flux density, flux density of the IDV core, as well as the flux density of the 'core' (as modelled in the kinematic analysis) for this source. Different components have been observed to be ejected at different angles in this very high $\beta_{\rm app}$ source [Lister et al., 2009c].

LIST OF REFERENCES

LIST OF REFERENCES

Abdo, A.A., et al. 2009, ApJ, 700, 597

Abdo, A.A., et al. 2010, ApJ, 716, 30

Aharonian, F., et al. 2007, ApJ, 664, 71

Albert, J., et al. 2008, Science, 320, 1752

Aller, M.F., et al. 2003, ASPC, 300, 159

Antonucci, R.R.J., & Ulvestad, J. 1985, ApJ, 294, 158

Antonucci, R.R.J., & Miller, J.S. 1985, ApJ, 297, 621

Baum, S.A., et al. 1995, ApJ, 451, 88

Begelman, M.C., et al. 1994, ApJ, 429, L57

Bicknell, G.V., et al. 1990, ApJ, 354, 98

Biggs, A.D., et al. 2001, MNRAS, 323, 995

Bignall, H.E., et al. 2003, ApJ, 585, 653

Bindu, R., et al. 2010, ApJ, 719, L153

Blandford, R.D., & Rees, M. 1974, MNRAS, 169, 395

Blandford, R.D., & Znajek, R.L. 1977, MNRAS, 179, 433

Blandford, R.D., & Königl, A. 1979, ApJ, 232, 34

Blandford, R.D., & Payne, D.G. 1982, MNRAS, 199, 883

Blundell, K.M., & Beasley, A.J. 1998, MNRAS, 299, 165

van Breugel, W., et al. 1984, AJ, 89, 5

Bridle, A.H. 1986, *Can. J. Phys.*, 64, 353

Britzen, S., et al. 2000, A&A, 360, 65

Britzen, S., et al. 2001, A&A, 374, 784

Camenzind, M. & Krockenberger, M. 1992, A&A, 255, 59

Cara, M., & Lister, M.L. 2008, ApJ, 674, 111

Carter, S.J.B., et al. arXiv:0903.5384

Cimó, G., et al. 2003, A&A, 402, 151

Cohen, M.H., et al. 1971, ApJ, 170, 207

Cohen, M.H., et al. 2007, ApJ, 658, 232

Cohen, A.S., et al. 2007a, AJ, 134, 1245

Cooper, N.J., et al. 2007, ApJS, 171, 376

Cotton, W.D., et al. 1980, ApJ, 238, 123

Cox, D.P., & Reynolds, R.J. 1987, ARA&A, 25, 303

Czerny, B., et al. 2009, ApJ, 698, 840

Daly, R.A. 2008, arXiv0811.1897

D'Arcangelo, F.D., et al. 2007, ApJ, 2, 107

D'Arcangelo, F.D., et al. 2009, ApJ, 697, 985

D'Arcangelo, F.D. 2010, *PhD Thesis* (Boston University)

Dennett-Thorpe, J., & de Bruyn, A.G. 2001, Ap&SS, 278, 100

Dennett-Thorpe, J., & de Bruyn, A.G. 2002, Nature, 415, 57

De Young, D.S. 1993, ApJ, 405, L13

Edwards, P.G., & Piner, B.G. 2002, ApJ, 579, L67

Fanaroff, B.L., & Riley, J.M. 1974, MNRAS, 167 31P

Fanti, C., et al. 1995, A&A, 302, 317

Fender, R.P. 2003, MNRAS, 340, 1353

Ferland, G.J., & Mushotzky, R.F. 1982, ApJ, 262 564

Fiedler, R., et al. 1994, ApJ, 430, 581

Francis, P., et al. 1991, ApJ, 373, 465

Fuhrmann, L., et al. 2008, A&A, 490, 1019

Gabányi, K.É. 2006, *PhD Thesis* (University of Bonn)

Gabányi, K.É., et al. 2007, A&A, 470, 83

Gabuzda, D.C., et al. 2000a, MNRAS, 313, 627

Gabuzda, D.C., et al. 2000b, MNRAS, 319, 1125

Garrington, S.T., et al. 1988, Nature, 331, 147

Ghisellini, G., et al. 1993, ApJ, 407, 65

Ghisellini, G., & Tavecchio, F. 2008, MNRAS, 386, L28

Ghisellini, G., et al. 2009, arXiv:0903.2043v1

Goodman, J. 1997, New Astron., 2, 449

Gopal-Krishna, Subramanian, K. 1991, Nature, 349, 766

Gopal-Krishna, & Wiita, P.J. 1992, A&A, 259, 109

Goyal, A., et al. 2009, MNRAS, 399, 1622

Gugliucci, N.E., et al. 2005, ApJ, 622, 136

Hartman, R.C., et al. 2001, ApJ, 558, 583

Heeschen, D.S., et al. 1987, AJ, 94, 1493

Hill, G.J., & Lilly, S.J. 1991, ApJ, 367, 1

Homan, D.C. 1999, *PhD Thesis* (Brandeis University)

Homan, D.C., & Lister, M.L. 2006, AJ, 131, 1262

Homan, D.C., et al. 2006, ApJ, 642, L115

Hovatta, T., et al. 2008, A&A, 485, 51

Hovatta, T., et al. 2009, A&A, 494, 527

Hoyle, F., et al. 1996, Nature, 209, 751

Jackson, J.D. 1999, *Classical Electrodynamics, 3rd. ed.* (New York, Wiley)

Jauncey, D.L., et al. 2003, Ap&SS, 288, 63

Jauncey, D.L., et al. 2007, A&AT, 26, 575

Jorstad, S., et al. 2001a, ASPC, 227, 69

Jorstad, S., et al. 2001b, ApJ, 556, 738

Kadler, M., et al. 2004, A&A, 426, 481

Kedziora-Chudczer, et al. 1997, ApJ, 490, L9

Kedziora-Chudczer, L. 1998, *PhD Thesis*

Kedziora-Chudczer, et al. 2001, MNRAS, 325, 1411

Keel, W.C. 1983, ApJ, 269, 466

Kellermann, K.I., & Pauliny-Toth, I.I.K. 1969, ApJ, 155, L71

Kellermann, K.I., et al. 1989, AJ, 98, 1195

Kellermann, K.I., et al. 1998, AJ, 115, 1295

Kellermann, K.I., et al. 2004, ApJ, 609, 539

Kembhavi, A. & Narlikar, J. 1999, *Quasars and Active Galactic Nuclei* (Cambridge UK, Cambridge University Press)

Kharb, P., et al. 2010, ApJ, 710, 764

Kovalev, Y.Y., et al. 2005, AJ, 130, 2473

Kovalev, Y.Y., et al. 2008a, *Memorie della Societa Astronomica Italiana*, 79, 1153

Kovalev, Y. Y., et al. 2008b, In: *The role of VLBI in the Golden Age for Radio Astronomy*, Proceedings of Science, 7

Kovalev, Y.Y., et al. 2009, ApJ, 696, 17

Kraus, A., et al. 2003, A&A, 401, 161

Krolic, J.H. 1999, *Active Galactic Nuclei From the Central Black hole to the Galactic Environment* (New Jersey, Princeton)

Kunert-Bajraszewska, M., et al. 2006, A&A, 450, 945

Lähteenmäki, A, et al. 1999, ApJ, 521, 493

Laing, R.A., & Bridle, A.H. 1987, MNRAS, 228, 557

Laing, R.A. 1988, Nature, 331, 149

Landt, H., & Bignall, H.E. 2008, MNRAS, 391, 967

Lawrence, C., et al. 1996, ApJS, 107, 541

Lazio, T.J.W., et al. 2008, ApJ, 672, 115

Leahy, J.P. 1993, *Jets in Extragalactic Radio Sources* (ed: Röser, H.J. & Meisenheimer, K., Berlin, Springer-Verlag)

Leahy, J.P. 1997, `http://www.jb.man.ac.uk/atlas/dragns.html`

Lee, Sang-Sung, et al. 2008, AJ, 136, 159

Lehto, H.J., & Valtonen, M.J. 1996, ApJ, 460, 207

Lindfors, E.J., et al. 2006, A&A, 456, 895

Lister, M.L., & Marscher, A.P. 1997, ApJ, 476, 572

Lister, M.L., & Smith, P.S. 2000, ApJ, 541, 66

Lister, M.L., et al. 2001, ApJ, 554, 964

Lister, M.L., & Homan, D.C. 2005, AJ, 130, 1389

Lister, M.L., et al. 2009a, AJ, 137, 3718

Lister, M.L., et al. 2009b, AJ, 138, 1874

Lister, M.L., et al. 2009c, ApJ, 696, 22

Lobanov, A.P. 1998, A&A, 330, 79

Lobanov, A.P., et al. 2000, A&A, 364, 391

Lobanov, A.P., & Zensus, J.A. 2001, Science, 294, 128

Longair, M.S. 1997, *High energy astrophysics vol. 1 & 2, 2nd. ed.* (Cambridge New York, Cambridge University Press)

Lovell, J.E.J., et al. 2003a, ASPC, 290, 347

Lovell, J.E.J., et al. 2003b, AJ, 126, 1699

Lovell, J.E.J., et al. 2007, ASPC, 365, 279

Lovell, J.E.J., et al. 2008, ApJ, 689, 108

Lyutikov, M., & Lister, M.L. 2010, ApJ, 722, 197

Madau, P.G., et al. 1987, MNRAS, 224, 257

Marscher, A.P. 2005, *Memorie della Societa Astronomica Italiana*, 76, 13

Marscher, A.P., et al. 2008, Nature, 452, 966

Mattox, J.R., et al. 2001, ApJ, 135, 155

McFarland, J.P. 2005, *PhD Thesis* (Georgia State University)

McHardy, I.M., et al. 1990, MNRAS, 246, 305

Medvedev, M.V. 2000, ApJ, 532, L63

Meier, D.L., et al. 2001, Science, 291, 84

Mellott, N., & Lister, M.L. 2004, AAS Meeting Abstracts, 205, Vol. 36, p.1389

Nalewajko, K. 2009, MNRAS, 395, 524

Narayan, R. 1992, *Phil. Trans. R. Soc. Lond. A*, 341, 151

Nieppola, E., et al. 2007, AJ, 133, 1947

Nieppola, E., et al. 2009, AJ, 137, 5022

O'Dea, C.P. 1998, PASP, 110, 493

Ojha, R., et al. 2004, ApJ, 614, 607

Oke, J.B. 1967, ApJ, 147, 901

Owen, F.N., & Laing R.A. 1989, MNRAS, 238, 357

Owen, F.N., et al. 1990, ApJ, 352, 44

Owen, F.N., & Ledlow, M.J. 1994, ASPC, 54, 319

Pacciani, L., et al. 2010, ApJ, 716, 170

Paltani, S., et al. 1997, A&A327, 539

Peck, A. B., & Taylor, G. B. 2000, ApJ, 534, 90

Pelletier, G., & Sol, H. 1992, MNRAS, 254, 635

Perley, R., et al. 1979, Nature, 281, 437

Peterson, B.M. 1997, *An Introduction to Active Galactic Nuclei* (Cambridge UK, Cambridge University Press)

Peterson, B.M., et al. 2004, ApJ, 613, 682

Petrov, L., et al. 2008, AJ, 136, 580

Piner, B.G., & Edwards, P.G. 2005, ApJ, 622, 168

Prestage, R.M., & Peacock, J.A. 1989, MNRAS, 230, 131

Qian, S.J., et al. 1991, A&A, 241, 15

Qian, S.J., et al. 2002, ChJAA, 2, 325

Quirrenbach, A., et al. 1992, A&A, 258, 279

Readhead, A.C.S. 1994, ApJ, 426, 51

Rees, M.J. 1966, Nature, 211, 468

Richards, J.L., et al. arXiv:0912.3780

Rickett, B.J., et al. 1995, A&A293, 479

Rickett, B.J., et al. 2001, ApJ, 550, L11

Rybicki, G., & Lightman, A. 1979, *Radiation Processes in Astrophysics* (New York, Wiley)

Sarma, K.H., & Lister, M.L. 2007, Bulletin of the AAS, Vol. 39, p.731

Sarma, K.H., & Lister, M.L. 2009, AAS Meeting Abstracts, 213, #446.04

Savolainen, T., et al. 2002, A&A, 394, 851

Savolainen, T., et al. 2006, A&A, 446, 71

Savolainen, T., & Kovalev, Y.Y. 2008, A&A, 489, L33

Savolainen, T., et al. 2010, A&Aaccepted, arXiv:0911.4924v2

Sbarufatti, B., et al. 2005, AJ, 129, 559

Sbarufatti, B., et al. 2006, AJ, 132, 1

Senkbeil, C.E., et al. 2008, ApJ, 672, 95

Shepherd, M.C. 1997, ASPC, 125, 77

Siemiginowska, A. 2009, *Astronomische Nachrichten*, 330, 264

Sillanpää, A., et al. 1988, ApJ, 325, 628

Simonetti, J.H., et al. 1985, ApJ, 296, 46

Singal, A.K., & Gopal-Krishna 1985, MNRAS, 215, 383

Sowards-Emmerd, D., et al. 2003, ApJ, 590, 109

Sowards-Emmerd, D., et al. 2004, ApJ, 609, 564

Spada, M., et al. 1999, ApJ, 511, 136

Spangler, S.R., et al. 1993, A&A, 267, 213

Stevens, J.A., et al. 1996, ApJ, 466, 158

Striani, E., et al. 2010, ApJ, 718, 455

Stickel, M., et al. 1991, ApJ, 374, 431

O'Sullivan, S.P., & Gabuzda, D.C. 2009, MNRAS, 400, 26O

Taylor, J.H., & Cordes, J.M. 1993, ApJ, 411, 674

Teräsranta, H., et al. 2005, A&A, 440, 409

Tingay, S.J., et al. 2001, ApJ, 549, 55

Torniainen, I., et al. 2005, A&A, 435, 839

Tornikoski, M., et al. 2001, AJ, 121, 1306

Tsang, O., & Kirk, J.G. 2007, A&A, 463, 145

Urry, C.M., & Padovani, P. 1995, PASP, 107, 803

Valtaoja, E., et al. 2000, ApJ, 531, 744

Véron-Cetty, M.P., & Véron, P. 2001, A&A, 374, 92

Vijayanarasimha, U., et al. 1985, MNRAS, 212, 601

Wagner, S.J., & Witzel, A. 1995, ARA&A, 33, 163

Wagner, S.J., et al. 1996, AJ, 111, 2187

Walker, M.A. 1998, MNRAS, 294, 307

Wall, J.V., & Jenkins, C. 2003, *Practical Statistics for Astronomers* (Cambridge UK, Cambridge University Press)

Weedman, D.W. 1977, ARA&A, 15, 69

Weedman, D.W. 1986, *Quasar astronomy* (Cambridge UK, Cambridge University Press)

Wehrle, A.E., et al. 2001, ApJS, 133, 297

Whitney, A.R., et al. 1971, Science, 173, 225

Wills, B.J., et al. 1992, ApJ, 398, 454

Wu, J., et al. 2008, AJ, 135, 258

Wu, J., et al. 2009, AJ, 137, 3961

Zhang, Y.H., et al. 1999, ApJ, 527, 719

APPENDICES

A. *MOJAVE* Source Properties

The following table lists some of the properties of the sources from the *MOJAVE* sample included in the current study.

Table A.1: Properties of *MOJAVE* sources

Source	Opt. Class	High Opt. Pol.	kpc morph.	Gal. Lat. b (°)	z	S (Jy)	$\beta_{\rm app}$	GeV
(1)	(2)	(3)	(4)	(5)	(6)	(7)	(8)	(9)
$0003+380$	Q	—	core	$-23.7°$	0.229	0.800	4.61	Y
$0003-066$	B	Y	1 sided	$-66.6°$	0.347	3.302	2.89	N
$0007+106$	G	—	2 sided	$-50.6°$	0.0893	1.889	0.97	N
$0010+405$	Q	—	1 sided	$-21.4°$	0.256	0.522	8.18	N
$0015-054$	Q	—	—	$-66.6°$	0.227	—	—	Y
$0016+731$	Q	N	core	$10.7°$	1.781	2.027	6.74	N
$0027+056^{\dagger}$	Q	—	1 sided	$-56.5°$	1.317	—	—	N
$0048-071$	Q	—	—	$-69.7°$	1.975	—	—	Y
$0048-097$	B	Y	2h	$-72.4°$	—	1.835	—	Y
$0055+300$	G	—	2 sided	$-32.5°$	0.0165	0.804	0.08	N
$0059+581$	Q	—	1h	$-4.4°$	0.644	3.323	11.09	Y
$0106+013$	Q	Y	2 sided	$-61.0°$	2.099	2.906	26.50	Y
$0106+612$	Q	—	—	$-1.2°$	0.783	—	—	N
$0106+678$	U	—	—	$5.3°$	0.29	—	—	Y
$0108+388$	G	—	1 sided	$-23.6°$	0.668	0.464	0.30	N
$0109+224$	B	Y	core	$-39.9°$	0.265	0.981	—	Y

(1)	(2)	(3)	(4)	(5)	(6)	(7)	(8)	(9)
$0110+318$	Q	—	1h	$-30.5°$	0.603	0.705	—	Y
$0111+021$	B	—	core	$-60.0°$	0.047	0.529	0.13	N
$0113-118$	Q	—	1 sided	$-73.4°$	0.672	1.312	—	N
$0116-219$	Q	—	—	$-81.7°$	1.161	—	—	Y
$0118-272$	B	—	—	$-83.5°$	0.559	—	—	N
$0119+115$	Q	—	1h	$-50.4°$	0.57	3.625	17.10	N
$0130-171$	Q	—	—	$-76.0°$	1.02	—	—	Y
$0133+476$	Q	Y	1 sided	$-14.3°$	0.859	5.615	12.98	Y
$0136+176^{\dagger}$	Q	—	1 sided	$-43.5°$	2.73	—	—	N
$0141+268$	U	—	—	$-34.3°$	—	—	—	N
$0142-278$	Q	—	—	$-78.1°$	1.155	—	—	N
$0149+218$	Q	—	1 sided	$-38.6°$	1.32	1.402	13.82	N
$0202+149$	Q	Y	core	$-44.0°$	0.405	2.287	6.42	Y
$0202+319$	Q	N	1 sided	$-28.1°$	1.466	2.333	8.30	Y
$0202-172$	Q	—	—	$-70.2°$	1.74	—	—	Y
$0212+735$	Q	Y	1 sided	$12.0°$	2.367	3.535	7.64	Y
$0214+083$	Q	—	—	$-48.6°$	1.4	—	—	N
$0215+015$	BL/Q	Y	2h	$-54.4°$	1.715	3.247	34.16	Y
$0219+428$	B	Y	1 sided	$-16.8°$	0.444	1.055	18.35	Y
$0224+671$	Q	—	2 sided	$6.2°$	0.523	1.888	11.64	N
$0234+285$	Q	Y	1 sided	$-28.5°$	1.207	4.787	12.27	Y
$0235+164$	BL/Q	Y	1h	$-39.1°$	0.94	2.783	—	Y
$0238-084$	G	—	2 sided	$-57.9°$	0.005037	2.446	0.32	Y
$0241+622$	Q	—	core	$2.4°$	0.045	1.719	1.11	N
$0250-225$	Q	—	—	$-62.1°$	1.427	0.666	—	Y

(1)	(2)	(3)	(4)	(5)	(6)	(7)	(8)	(9)
$0300 + 470$	B	Y	1h	$-9.9°$	—	1.249	—	Y
$0301 - 243$	B	—	—	$-59.7°$	0.26	—	—	N
$0305 + 039$	G	—	1h	$-44.5°$	0.029	0.545	0.25	Y
$0309 + 411$	G	—	2h	$-14.1°$	0.136	1.024	0.48	N
$0316 + 413$	G	N	2h	$-13.3°$	0.0176	17.933	0.31	Y
$0333 + 321$	Q	N	1 sided	$-18.8°$	1.259	2.277	12.76	Y
$0336 - 019$	Q	Y	1 sided	$-42.5°$	0.852	3.444	22.36	Y
$0346 + 800$	U	—	—	$20.1°$	—	—	—	Y
$0347 - 211$	Q	—	—	$-49.0°$	2.944	—	—	Y
$0355 + 508$	Q	—	1h	$-1.6°$	1.51	11.751	0.28	N
$0403 - 132$	Q	Y	1 sided	$-42.7°$	0.571	1.795	19.70	Y
$0414 - 189$	Q	—	1 sided	$-42.4°$	1.536	0.837	7.35	Y
$0415 + 379$	G	—	2 sided	$-8.8°$	0.0491	6.555	5.87	Y
$0420 - 014$	Q	Y	2 sided	$-33.1°$	0.914	11.605	7.35	Y
$0422 + 004$	B	Y	1 sided	$-31.8°$	—	1.739	—	Y
$0429 + 415$	G	—	ch	$-4.3°$	1.022	1.104	1.81	N
$0430 + 052$	G	N	2 sided	$-27.4°$	0.033	4.296	5.38	N
$0430 + 289$	B	—	core	$-12.6°$	—	0.331	—	Y
$0440 - 003$	Q	—	2 sided	$-28.5°$	0.844	1.433	4.83	Y
$0446 + 112$	B	—	1 sided	$-20.7°$	—	2.252	—	Y
$0451 - 282$	Q	—	—	$-37.0°$	2.559	—	—	Y
$0454 - 234$	Q	—	core	$-34.9°$	1.003	2.385	—	Y
$0458 - 020$	Q	Y	1 sided	$-25.3°$	2.286	2.398	16.52	Y
$0506 + 056$	B	—	—	$-19.6°$	—	—	—	Y
$0518 + 211$	U	—	—	$-8.7°$	—	—	—	Y

(1)	(2)	(3)	(4)	(5)	(6)	(7)	(8)	(9)
$0528+134$	Q	Y	2 sided	$-11.0°$	2.07	8.735	19.20	Y
$0529+075$	Q	—	1 sided	$-13.7°$	1.254	1.632	12.66	Y
$0529+483$	Q	—	1h	$8.2°$	1.162	1.460	19.79	Y
$0539-057$	Q	—	—	$-18.1°$	0.839	0.969	7.97	Y
$0552+398$	Q	—	core	$7.3°$	2.363	5.028	0.36	N
$0605-085$	Q	—	1 sided	$-13.5°$	0.872	2.802	19.79	Y
$0605-153$	U	—	—	$-16.4°$	—	—	—	N
$0607-157$	Q	—	core	$-16.2°$	0.324	10.565	3.94	N
$0609+413$	B	—	—	$10.9°$	—	—	—	N
$0640+090$	U	—	—	$2.3°$	—	—	—	Y
$0642+449$	Q	—	core	$17.9°$	3.396	4.305	0.76	N
$0648-165$	U	—	1 sided	$-7.7°$	—	3.772	—	Y
$0650+453$	Q	—	—	$19.4°$	0.933	—	—	Y
$0650+507$	U	—	—	$21.1°$	—	—	—	Y
$0710+196$	U	—	—	$13.6°$	0.54	—	—	Y
$0710+439$	G	—	core	$22.2°$	0.518	0.586	0.98	N
$0716+332$	B	—	core	$19.9°$	0.779	0.566	—	Y
$0716+714$	B	Y	2h	$28.0°$	0.31	2.587	10.07	Y
$0722+145$	Q	Y	—	$13.9°$	1.038	—	—	N
$0723-008$	B	—	ch	$7.2°$	0.127	2.081	0.77	Y
$0727-115$	Q	—	1 sided	$3.1°$	1.591	6.793	—	Y
$0730+504$	Q	—	1 sided	$27.1°$	0.72	1.333	14.07	N
$0735+178$	B	Y	1 sided	$18.1°$	0.424	1.636	4.76	Y
$0736+017$	Q	Y	2 sided	$11.4°$	0.191	2.670	14.44	Y
$0738+313$	Q	—	2 sided	$23.6°$	0.631	2.889	10.76	N

(1)	(2)	(3)	(4)	(5)	(6)	(7)	(8)	(9)
$0742+103$	Q	—	core	16.6°	2.624	1.494	—	N
$0743-006$	B	—	—	11.7°	0.994	—	—	N
$0745+241$	Q	Y	2h	22.7°	0.409	0.948	5.83	N
$0748+126$	Q	—	1 sided	18.8°	0.889	4.259	18.37	Y
$0754+100$	BL/Q	Y	1h	19.1°	0.266	1.809	14.41	Y
$0804+499$	Q	Y	1 sided	32.6°	1.436	1.604	1.83	N
$0805-077$	Q	—	2 sided	13.2°	1.837	1.511	50.61	Y
$0808+019$	B	Y	1 sided	18.6°	1.148	1.344	13.00	Y
$0814+425$	B	Y	1 sided	33.4°	0.245	1.431	1.71	Y
$0821+394$	Q	—	1 sided	34.2°	1.216	1.654	—	N
$0823+033$	BL/Q	Y	1 sided	22.4°	0.506	2.091	17.80	Y
$0823-223$	B	—	—	8.9°	0.91	—	—	Y
$0827+243$	Q	N	1 sided	31.9°	0.94	2.216	21.98	Y
$0829+046$	B	Y	1 sided	24.3°	0.174	1.365	10.11	Y
$0834-201$	Q	—	core	12.2°	2.752	3.279	6.57	N
$0836+710$	Q	N	1 sided	34.4°	2.218	2.197	25.39	Y
$0838+133$	Q	—	2h	30.1°	0.681	1.918	12.93	Y
$0847-120$	Q	—	core	19.5°	0.566	0.950	14.38	Y
$0850+581$	Q	N	2 sided	38.9°	1.322	0.593	9.41	N
$0851+202$	BL/Q	Y	1 sided	35.8°	0.306	4.959	15.18	Y
$0854-108$	U	—	—	21.5°	—	—	—	N
$0859-140$	Q	—	1 sided	20.7°	1.339	1.551	6.07	N
$0906+015$	Q	Y	1 sided	30.9°	1.024	2.737	20.66	Y
$0917+449$	Q	—	2 sided	44.8°	2.18	1.460	1.57	Y
$0917+624$	Q	—	1 sided	41.0°	1.446	1.374	15.57	Y

(1)	(2)	(3)	(4)	(5)	(6)	(7)	(8)	(9)
0923 + 392	Q	N	1h	46.2°	0.695	12.727	4.29	N
0945 + 408	Q	N	1 sided	50.3°	1.249	1.826	18.60	N
0946 + 006	Q	—	core	38.7°	0.585	0.437	—	Y
0953 + 254	Q	N	1 sided	51.0°	0.712	1.312	10.53	Y
0954 + 658	BL/Q	Y	1 sided	43.1°	0.367	2.556	14.35	Y
0955 + 476	Q	—	1 sided	50.7°	1.882	1.721	2.48	N
1011 + 496	B	—	—	52.7°	0.2	0.200	—	Y
1013 + 054	Q	—	—	47.0°	1.713	—	—	Y
1015 + 359	Q	—	1 sided	56.4°	1.226	0.781	8.27	Y
1030 + 611	Q	Y	—	49.1°	1.401	—	—	Y
1034 − 293	Q	—	—	24.8°	0.312	—	—	N
1036 + 054	Q	—	2 sided	51.6°	0.473	2.664	6.15	N
1038 + 064	Q	—	1 sided	52.7°	1.265	1.843	11.87	N
1045 − 188	Q	—	2 sided	34.9°	0.595	1.317	8.57	N
1055 + 018	Q	Y	2 sided	52.8°	0.89	5.880	10.99	Y
1101 + 384	B	Y	ch	65.0°	0.031	0.532	0.42	Y
1118 − 056	Q	Y	—	50.4°	1.297	0.517	8.66	Y
1124 − 186	Q	Y	1 sided	39.6°	1.048	2.834	12.44	Y
1127 − 145	Q	—	1 sided	43.6°	1.184	3.360	14.18	Y
1128 + 385	Q	—	1 sided	69.8°	1.733	1.123	1.07	N
1128 − 047	G	—	core	52.5°	0.266	0.719	2.06	N
1148 − 001	Q	—	2 sided	58.8°	1.98	0.850	5.28	N
1150 + 497	Q	—	—	65.0°	0.3334	1.037	27.94	N
1150 + 812	Q	—	1 sided	35.8°	1.25	1.796	7.09	N
1156 + 295	Q	Y	2h	78.4°	0.729	3.591	24.86	Y

(1)	(2)	(3)	(4)	(5)	(6)	(7)	(8)	(9)
$1213-172$	U	—	1 sided	44.5°	—	2.578	—	N
$1215+303$	B	—	—	82.1°	0.13	0.365	—	Y
$1219+044$	Q	Y	2 sided	66.1°	0.965	1.175	2.35	Y
$1219+285$	B	Y	1 sided	83.3°	0.102	0.573	6.44	Y
$1222+216$	Q	—	2h	81.7°	0.432	1.798	21.02	Y
$1226+023$	Q	N	1 sided	64.4°	0.158	40.022	13.44	Y
$1228+126$	G	—	2 sided	74.5°	0.00436	2.983	0.03	Y
$1236+049$	Q	—	—	67.4°	1.762	0.642	—	Y
$1243-072^{\dagger}$	Q	—	2 sided	55.3°	1.286	1.070	27.84	N
$1244-255$	Q	Y	core	37.1°	0.633	1.348	—	Y
$1250+532$	B	—	—	64.1°	—	—	—	N
$1253-055$	Q	Y	2 sided	57.1°	0.536	28.935	20.58	Y
$1302-102$	Q	N	2 sided	52.2°	0.278	0.718	7.11	N
$1308+326$	Q	Y	2h	83.3°	0.997	3.885	27.16	Y
$1310+487$	Q	—	—	68.3°	0.501	—	—	N
$1324+224$	Q	—	core	80.5°	1.4	2.184	—	Y
$1329-049$	Q	—	—	56.2°	2.15	—	—	Y
$1329-126$	U	—	—	48.7°	1.498	—	—	N
$1331+170^{\dagger}$	Q	—	core	75.8°	2.084	0.372	4.75	N
$1334-127$	Q	Y	1 sided	48.4°	0.539	8.872	10.26	Y
$1341-171$	U	—	—	43.7°	2.49	—	—	Y
$1343+451$	U	—	—	69.2°	2.534	—	—	Y
$1345+125$	G	—	2 sided	70.2°	0.121	0.769	1.59	N
$1404+286$	G	—	core	73.3°	0.077	1.191	0.18	N
$1406-076$	Q	Y	core	50.3°	1.494	1.608	24.93	Y

(1)	(2)	(3)	(4)	(5)	(6)	(7)	(8)	(9)
$1413 + 135$	B	—	core	65.9°	0.247	1.720	1.80	N
$1417 + 385^‡$	Q	—	1 sided	68.4°	1.831	1.665	15.44	N
$1418 + 546$	B	Y	1h	58.3°	0.152	1.187	7.24	Y
$1424 + 240$	B	—	—	68.2°	—	0.221	—	Y
$1435 + 638$	Q	—	—	49.7°	2.068	—	—	N
$1458 + 718$	Q	N	2 sided	42.1°	0.904	1.446	7.04	N
$1502 + 106$	Q	Y	1 sided	54.6°	1.839	1.811	14.77	Y
$1504 - 166^‡$	Q	Y	core	35.1°	0.876	2.186	4.31	N
$1508 - 055$	Q	—	core	42.9°	1.191	0.684	0.60	Y
$1509 + 054$	G	—	core	50.1°	0.084	0.646	0.14	N
$1510 - 089$	Q	Y	2 sided	40.1°	0.36	3.135	20.15	Y
$1514 + 004$	G	—	2 sided	46.0°	0.052	0.940	0.41	N
$1514 + 197$	B	—	—	55.9°	1.07	—	—	Y
$1514 - 241$	B	Y	1h	27.6°	0.0486	3.043	7.64	Y
$1519 - 273$	B	Y	core	24.4°	1.297	1.643	—	Y
$1520 + 319$	Q	—	—	57.0°	1.487	0.448	1.04	Y
$1538 + 149$	B	Y	1 sided	48.8°	0.605	1.424	8.73	N
$1546 + 027$	Q	Y	1 sided	40.9°	0.414	3.904	12.08	Y
$1548 + 056$	Q	Y	core	42.2°	1.422	3.068	11.57	Y
$1551 + 130$	Q	—	1 sided	45.2°	1.29	0.716	—	Y
$1604 + 159$	B	—	—	43.4°	0.4965	0.476	—	Y
$1606 + 106$	Q	—	1 sided	40.8°	1.226	2.306	18.91	Y
$1607 + 268$	G	—	core	46.2°	0.473	0.347	0.40	N
$1611 + 343$	Q	N	2 sided	46.4°	1.397	5.666	14.09	Y
$1617 + 229^†$	Q	—	—	43.0°	1.987	—	—	N

(1)	(2)	(3)	(4)	(5)	(6)	(7)	(8)	(9)
$1622-253$	Q	—	2 sided	16.3°	0.786	2.523	—	Y
$1622-297$	Q	—	core	13.3°	0.815	1.707	18.41	Y
$1633+382$	Q	Y	2 sided	42.3°	1.814	4.143	29.46	Y
$1637+574$	Q	N	1h	40.4°	0.751	2.298	10.61	N
$1637+826$	G	—	2 sided	31.2°	0.024	0.877	0.06	Y
$1638+398$	Q	—	2 sided	41.4°	1.666	1.660	12.28	N
$1641+399$	Q	Y	1h	40.9°	0.593	10.609	19.27	Y
$1642+690$	Q	Y	2 sided	36.6°	0.751	2.176	18.25	N
$1652+398$	B	Y	1h	38.9°	0.033	1.152	0.08	Y
$1655+077$	Q	Y	2h	28.7°	0.621	2.218	14.45	N
$1700+685$	Q	Y	—	35.2°	0.301	0.440	—	Y
$1717+178$	B	—	—	28.1°	0.137	0.637	—	Y
$1722+401$	Q	—	—	33.2°	1.049	—	—	Y
$1725+044$	Q	—	1 sided	20.5°	0.293	0.814	8.60	Y
$1726+455$	Q	—	1 sided	33.3°	0.717	2.183	1.82	Y
$1730-130$	Q	Y	2 sided	10.8°	0.902	11.909	35.70	Y
$1732+389$	B	—	—	31.0°	0.97	1.021	—	Y
$1738+499^{\dagger}$	Q	—	—	31.7°	1.545	—	—	N
$1739+522$	Q	Y	1 sided	31.7°	1.379	2.474	—	Y
$1741-038^{\dagger}$	Q	Y	core	13.1°	1.054	7.012	—	N
$1749+096$	BL/Q	Y	core	17.6°	0.322	7.336	6.84	Y
$1749+701$	B	Y	1h	30.7°	0.77	0.824	6.68	Y
$1751+288$	Q	—	1 sided	24.5°	1.118	2.014	3.08	N
$1758+388$	Q	—	core	26.0°	2.092	1.783	2.38	N
$1800+440$	Q	—	2 sided	27.1°	0.663	1.735	15.41	N

(1)	(2)	(3)	(4)	(5)	(6)	(7)	(8)	(9)
$1803+784$	BL/Q	Y	1 sided	29.1°	0.68	3.088	8.97	Y
$1807+698$	B	Y	1h	29.2°	0.051	1.600	0.10	Y
$1823+568$	BL/Q	Y	1h	26.1°	0.664	2.321	20.86	Y
$1827+062$	U	—	—	7.6°	0.75	—	—	Y
$1828+487$	Q	N	1h	23.5°	0.692	2.342	13.66	Y
$1845+797$	G	—	2 sided	27.1°	0.0555	0.474	2.48	N
$1846+322$	Q	—	—	14.7°	0.798	0.617	—	Y
$1849+670$	Q	—	2 sided	25.0°	0.657	3.046	30.63	Y
$1901+319$	Q	—	1h	11.8°	0.635	1.326	6.72	N
$1908-201$	Q	—	core	−13.2°	1.119	2.844	6.44	Y
$1914-194$	B	—	—	−14.3°	0.137	—	—	N
$1920-211$	Q	—	—	−16.3°	0.874	—	—	Y
$1921-293$	Q	Y	1 sided	−19.6°	0.352	14.393	4.19	Y
$1923+210$	U	—	1 sided	2.3°	—	3.320	—	N
$1928+738$	Q	N	2 sided	23.5°	0.302	3.834	8.43	N
$1936-155^{\ddagger}$	Q	Y	core	−17.4°	1.657	1.771	2.60	N
$1951-115$	Q	—	—	−19.1°	0.683	—	—	N
$1954+513$	Q	N	2 sided	11.8°	1.223	1.179	16.14	N
$1957+405$	G	—	2 sided	5.8°	0.0561	1.678	0.21	N
$1958-179$	Q	Y	core	−23.1°	0.65	2.842	1.90	Y
$1959+650$	B	Y	—	17.7°	0.047	0.194	—	Y
$2005+403$	Q	—	core	4.3°	1.736	2.767	12.21	N
$2007+777$	B	Y	2 sided	22.7°	0.342	1.343	0.21	Y
$2008-159$	Q	—	1 sided	−24.6°	1.18	2.382	7.99	N
$2013+370$	U	—	—	1.2°	—	4.472	—	N

(1)	(2)	(3)	(4)	(5)	(6)	(7)	(8)	(9)
$2021+317$	U	—	1h	$-3.1°$	—	2.135	—	N
$2021+614$	G	N	core	$13.8°$	0.227	3.029	0.42	N
$2022-077$	Q	—	core	$-24.4°$	1.388	0.734	19.26	Y
$2023+335$	Q	—	—	$-2.4°$	0.219	3.295	1.35	N
$2037+511$	Q	—	1 sided	$6.0°$	1.686	2.727	3.30	N
$2113+293$	Q	—	core	$-13.3°$	1.514	0.937	2.10	Y
$2121+053$	Q	Y	core	$-30.1°$	1.941	3.744	13.29	N
$2128-123$	Q	N	1 sided	$-41.0°$	0.501	3.251	6.95	N
$2131-021$	BL/Q	Y	1 sided	$-36.5°$	1.285	2.462	20.04	Y
$2134+004$	Q	N	1h	$-35.6°$	1.932	6.668	5.94	N
$2136+141$	Q	—	core	$-27.5°$	2.427	2.731	5.43	N
$2141+175$	Q	—	core	$-26.1°$	0.211	0.876	1.55	Y
$2144+092$	Q	—	2 sided	$-32.3°$	1.113	0.799	0.62	Y
$2145+067$	Q	N	1 sided	$-34.1°$	0.99	10.339	2.50	Y
$2155+312$	Q	—	—	$-18.2°$	1.486	—	—	N
$2155-152$	Q	Y	2h	$-48.0°$	0.672	2.268	18.12	Y
$2200+420$	BL/Q	Y	ch	$-10.4°$	0.0686	5.689	10.57	Y
$2201+171$	Q	—	2h	$-29.6°$	1.076	1.987	2.55	Y
$2201+315$	Q	N	2 sided	$-18.8°$	0.295	3.240	7.88	N
$2209+236$	Q	—	core	$-26.1°$	1.125	1.900	3.43	Y
$2216-038$	Q	—	1 sided	$-46.6°$	0.901	3.318	5.62	N
$2223-052$	Q	Y	2 sided	$-48.8°$	1.404	7.719	17.34	Y
$2227-088$	Q	Y	1 sided	$-51.7°$	1.56	2.158	8.14	Y
$2230+114$	Q	Y	2h	$-38.6°$	1.037	5.836	15.41	Y
$2233-148$	B	—	—	$-56.2°$	0.325	—	—	N

(1)	(2)	(3)	(4)	(5)	(6)	(7)	(8)	(9)
$2234+282$	Q	Y	1 sided	$-25.6°$	0.795	1.444	1.27	Y
$2243-123$	Q	Y	1 sided	$-57.1°$	0.632	3.500	5.49	N
$2247-283$	U	—	—	$-63.3°$	0.525	—	—	Y
$2251+158$	Q	Y	1 sided	$-38.2°$	0.859	12.750	14.19	Y
$2254+074$	B	Y	ch	$-45.5°$	0.19	0.613	0.69	N
$2255-282$	Q	—	1 sided	$-64.9°$	0.927	7.030	8.37	Y
$2308+341$	Q	—	—	$-24.0°$	1.817	—	—	Y
$2320-035$	Q	Y	core	$-58.2°$	1.411	1.369	13.38	Y
$2325+093$	Q	—	—	$-48.0°$	1.843	2.550	—	Y
$2331+073$	Q	—	1h	$-50.6°$	0.401	1.529	4.47	Y
$2342-161$	Q	—	—	$-71.0°$	0.621	—	—	Y
$2344+514$	B	N	—	$-9.9°$	0.044	0.145	0.06	Y
$2345-167$	Q	Y	1h	$-71.9°$	0.576	2.541	13.45	Y
$2351+456^{\ddagger}$	Q	—	core	$-15.8°$	1.986	1.810	18.01	N
$2356+196^{\dagger}$	Q	—	core	$-41.3°$	1.07	0.418	1.27	N

† — No LAT detection, but 'Confirmed' EGRET detection

‡ — No LAT detection, but 'Probable' EGRET detection

NOTE. — Columns are as follows: (1) IAU Name (B1950.0); (2) source type, where Q = quasar, B = BL Lac object, G = active galaxy, BL/Q = intermediate BL Lac/quasar as inferred from the presence of broad lines in their optical spectra (but usually listed as BLL), and U = optically unidentified; (3) Flag for high optical polarization, where Y = optical polarization > 3%; (4) kpc scale radio morphology as inferred from VLA observations, where c = compact core, 1 sided = 1 sided jet, 2 sided = 2 sided jet, h = halo and ch = core–halo; (5) source latitude (in degrees) with respect to the galactic plane; (6) redshift; (7) maximum 2 cm VLBA total flux density (in Jy) up to 2008; (8) Maximum apparent jet speed determined from the *MOJAVE* program; (9) GeV detection by the *Fermi* LAT instrument.

B. SAMPLE IDV PROCESSING PROCEDURE

```
userid: 660
epoch: 2010_08_27

cd /net/miranda/project/miranda/IDV/BL149CN

***In a Terminal window:
cd /net/miranda/project/miranda/IDV/BL149CN
export U=$PWD
/project/prospero/AIPS/START_AIPS NEW TV=local

run vlbautil

** Step 1
dowait true
tget fitld
intape = -1
douvcomp -1
ncount 1
clint 0.5

outcl 'EDIT'; outseq 1; outdi 1

datain 'U:0010+405/0010+405.EDIT
outnam '0010+405'; go
datain 'U:0113-118/0113-118.EDIT
```

```
outnam '0113-118'; go
datain 'U:0202+149/0202+149.EDIT
outnam '0202+149'; go
datain 'U:0219+428/0219+428.EDIT
outnam '0219+428'; go
datain 'U:0333+321/0333+321.EDIT
outnam '0333+321'; go
datain 'U:0414-189/0414-189.EDIT
outnam '0414-189'; go
datain 'U:0415+379/0415+379.EDIT
outnam '0415+379'; go
datain 'U:0430+052/0430+052.EDIT
outnam '0430+052'; go
datain 'U:0529+483/0529+483.EDIT
outnam '0529+483'; go
datain 'U:0716+714/0716+714.EDIT
outnam '0716+714'; go
datain 'U:0722+145/0722+145.EDIT
outnam '0722+145'; go
datain 'U:0808+019/0808+019.EDIT
outnam '0808+019'; go
datain 'U:0827+243/0827+243.EDIT
outnam '0827+243'; go
datain 'U:0917+449/0917+449.EDIT
outnam '0917+449'; go
datain 'U:1055+018/1055+018.EDIT
outnam '1055+018'; go
datain 'U:1329-049/1329-049.EDIT
outnam '1329-049'; go
```

```
datain 'U:1341-171/1341-171.EDIT
outnam '1341-171'; go
datain 'U:1502+106/1502+106.EDIT
outnam '1502+106'; go
datain 'U:1520+319/1520+319.EDIT
outnam '1520+319'; go
datain 'U:1519-273/1519-273.EDIT
outnam '1519-273'; go
datain 'U:1532+016/1532+016.EDIT
outnam '1532+016'; go
datain 'U:1636+473/1636+473.EDIT
outnam '1636+473'; go
datain 'U:1730-130/1730-130.EDIT
outnam '1730-130'; go
datain 'U:1732+389/1732+389.EDIT
outnam '1732+389'; go
datain 'U:1749+701/1749+701.EDIT
outnam '1749+701'; go
datain 'U:1920-211/1920-211.EDIT
outnam '1920-211'; go
datain 'U:2200+420/2200+420.EDIT
outnam '2200+420'; go
datain 'U:2201+171/2201+171.EDIT
outnam '2201+171'; go
datain 'U:2251+158/2251+158.EDIT
outnam '2251+158'; go
datain 'U:2345-167/2345-167.EDIT
outnam '2345-167'; go
```

```
outcl 'ICLN'; outseq 1; outdi 1

datain 'U:0010+405/0010+405.IMAP
outnam '0010+405'; go
datain 'U:0113-118/0113-118.IMAP
outnam '0113-118'; go
datain 'U:0202+149/0202+149.IMAP
outnam '0202+149'; go
datain 'U:0219+428/0219+428.IMAP
outnam '0219+428'; go
datain 'U:0333+321/0333+321.IMAP
outnam '0333+321'; go
datain 'U:0414-189/0414-189.IMAP
outnam '0414-189'; go
datain 'U:0415+379/0415+379.IMAP
outnam '0415+379'; go
datain 'U:0430+052/0430+052.IMAP
outnam '0430+052'; go
datain 'U:0529+483/0529+483.IMAP
outnam '0529+483'; go
datain 'U:0716+714/0716+714.IMAP
outnam '0716+714'; go
datain 'U:0722+145/0722+145.IMAP
outnam '0722+145'; go
datain 'U:0808+019/0808+019.IMAP
outnam '0808+019'; go
datain 'U:0827+243/0827+243.IMAP
outnam '0827+243'; go
datain 'U:0917+449/0917+449.IMAP
```

```
outnam '0917+449'; go
datain 'U:1055+018/1055+018.IMAP
outnam '1055+018'; go
datain 'U:1329-049/1329-049.IMAP
outnam '1329-049'; go
datain 'U:1341-171/1341-171.IMAP
outnam '1341-171'; go
datain 'U:1502+106/1502+106.IMAP
outnam '1502+106'; go
datain 'U:1520+319/1520+319.IMAP
outnam '1520+319'; go
datain 'U:1519-273/1519-273.IMAP
outnam '1519-273'; go
datain 'U:1532+016/1532+016.IMAP
outnam '1532+016'; go
datain 'U:1636+473/1636+473.IMAP
outnam '1636+473'; go
datain 'U:1730-130/1730-130.IMAP
outnam '1730-130'; go
datain 'U:1732+389/1732+389.IMAP
outnam '1732+389'; go
datain 'U:1749+701/1749+701.IMAP
outnam '1749+701'; go
datain 'U:1920-211/1920-211.IMAP
outnam '1920-211'; go
datain 'U:2200+420/2200+420.IMAP
outnam '2200+420'; go
datain 'U:2201+171/2201+171.IMAP
outnam '2201+171'; go
```

```
datain 'U:2251+158/2251+158.IMAP
outnam '2251+158'; go
datain 'U:2345-167/2345-167.IMAP
outnam '2345-167'; go

** Step 2
inext 'an'; indi 1; inver 1
for i=1 to 30; getn i; extdest; end

task 'tbin'; default; outdi 1;
intext 'U:DTERMS/FINAL.DTERMS
for i=1 to 30; geton i; go tbin; end

** Step 3
******Note the reference antenna name; Here we are using 'LA'
task 'calib'; default; outcl 'GCALIB'; indi 1; in2di 1; outdi 1;
in2cl 'ICLN'; cmeth 'dft'; refant=antnum('LA'); solint 0.5;
aparm 4,0; solmode 'p'; inver 1
for i=1 to 30; getn i; in2nam=innam; outn=innam; go calib ; end

** Step 4
task 'calib'; default; outcl 'GCALIB'; indi 1; in2di 1; outdi 1;
in2cl 'ICLN'; cmeth 'dft'; refant=antnum('LA'); solint 10;
aparm 4,0; solmode 'a&p'; inver 1
for i= 61 to 90; getn i; in2nam=innam; outn=innam; go calib ; end

** Step 5
task 'multi'; default
outcl 'gmulti'
```

```
indi 1; outdi 1; aparm 0;
for i= 61 to 90; getn i; outn=innam; outseq 1; inseq 1;
go multi; end

** Step 6
task 'indxr'; default; cparm 0; indi 1;
for i = 121 to 150; getn i; go indxr; end

** Step 7
outdi 1; indi 1; getn 61; outname=inname
outcl 'tasav'; runwait('tasav');
task 'tacop'; default; outdi 1; indi 1; geton 61; inext 'sn';
inver 1; for i= 62 to 90; getn i; go tacop; end

** Step 8
task 'clcal'; default; indi 1; getn 61; opcode 'merg';
runwait('clcal')

** Step 9
task 'tbout'; default; indi 1; getn 61; docrt 1000; inext 'sn';
inv 31; outtext 'U:sntables.txt
runwait('tbout');

** Step 10
********Exit to linux
*Run the following 4 perl scripts to get the final smoothed SN table

***#1: read the input SN table:
perl /project/miranda/IDV/scripts/InitialReadRoutine sntables.txt
```

```
BL149CN

***#2: flag the bad data:
perl /project/miranda/IDV/scripts/Flag1Routine BL149CN 5 3

**5, 3: 1st pass & 2nd pass threshold sigma respectively.
**Can change them if desired.
****Manual flagging of the output files is highly recommended.
*Consider using the perl script
"/project/miranda/IDV/scripts/AutoFlaggerRoutine"

***#3: smooth the data:
perl /project/miranda/IDV/scripts/RunningMedianRoutine
5-3Sigma_BL149CN 3

**5-3Sigma_: Prefix of the files produced by the flagging step.
**Change if different.
**3: HALF-WIDTH of the smoothing box in hrs.

***#4: write out the data to the smoothed table:
perl /project/miranda/IDV/scripts/OutRoutine sntables.txt
sntable.smoothed Runmed_5-3Sigma_BL149CN

**Runmed_5-3Sigma: Prefix of the files produced by the smoothing step.
**Change if different.

***Moving all the files (except the final smoothed table) produced
***by the above 4 perl scripts to a temp_files directory is highly
***recommended. Use these cmds:
```

```
mkdir temp_files
mv BL149CN_IF* temp_files/
mv 5-3Sigma* temp_files/
mv Runmed* temp_files/

** Step 11
*********Go back to AIPS
task 'tbin'; default; outdi 1;
intext 'U:sntable.smoothed
for i = 121 to 150; geton i; go tbin; end

** Check the SN table
task 'snplt'; default; indi 1; getn 121; inv 2; inext 'sn';
optype 'phas'; dotv 1; go snplt;

** Step 12
task 'clcal'; default; indi 1; inv 1; gainuse 2;
gainver 1; snver 1; refant=antnum('LA');
for i = 121 to 150; getn i; go clcal; end

** Step 13
task 'clcal'; default; indi 1; inv 2; gainuse 3;
gainver 1; snver 2; refant=antnum('LA');
for i = 121 to 150; getn i; go clcal; end

** Step 14
task 'clcor'; default; OPCODE='PHAS' ; stokes 'l';
CLCORPRM -5.2,-5.2,-5.2,-5.2,-5.2,-5.2,-5.2,-5.2
```

```
*** -5.2 : Must be Twice the EVPA correction.

for i = 121 to 150; getn i; geton i; gainver 2;
gainuse 4; go clcor; end

for i = 121 to 150; getn i; geton i; gainver 3;
gainuse 5; go clcor; end

** Step 15
task 'split'; default; inclass 'GMULTI'; douvcomp -1;
inseq 1; indi 1; outdi 1; outseq 1; dopol 3; docalib 2;
for i = 121 to 150; getn i; geton i; outclass 'SELFC';
gainuse 4; go split; end

** Step 16
task 'split'; default; inclass 'GMULTI'; douvcomp -1;
inseq 1; indi 1; outdi 1; outseq 1; dopol 3; docalib 2;
for i = 121 to 150; getn i; geton i; outclass 'GAINT';
gainuse 5; go split; end

** Step 17
task 'fittp'; default;

getn 152; geton 152;
dataout 'U:0010+405/0010+405.u.2010_08_27.SELFC1
go fittp
getn 153; geton 153;
dataout 'U:0113-118/0113-118.u.2010_08_27.SELFC1
go fittp
```

```
getn 154; geton 154;
dataout 'U:0202+149/0202+149.u.2010_08_27.SELFC1
go fittp
getn 155; geton 155;
dataout 'U:0219+428/0219+428.u.2010_08_27.SELFC1
go fittp
getn 156; geton 156;
dataout 'U:0333+321/0333+321.u.2010_08_27.SELFC1
go fittp
getn 157; geton 157;
dataout 'U:0414-189/0414-189.u.2010_08_27.SELFC1
go fittp
getn 158; geton 158;
dataout 'U:0415+379/0415+379.u.2010_08_27.SELFC1
go fittp
getn 159; geton 159;
dataout 'U:0430+052/0430+052.u.2010_08_27.SELFC1
go fittp
getn 160; geton 160;
dataout 'U:0529+483/0529+483.u.2010_08_27.SELFC1
go fittp
getn 161; geton 161;
dataout 'U:0716+714/0716+714.u.2010_08_27.SELFC1
go fittp
getn 162; geton 162;
dataout 'U:0722+145/0722+145.u.2010_08_27.SELFC1
go fittp
getn 163; geton 163;
dataout 'U:0808+019/0808+019.u.2010_08_27.SELFC1
```

```
go fittp
getn 164; geton 164;
dataout 'U:0827+243/0827+243.u.2010_08_27.SELFC1
go fittp
getn 165; geton 165;
dataout 'U:0917+449/0917+449.u.2010_08_27.SELFC1
go fittp
getn 166; geton 166;
dataout 'U:1055+018/1055+018.u.2010_08_27.SELFC1
go fittp
getn 167; geton 167;
dataout 'U:1329-049/1329-049.u.2010_08_27.SELFC1
go fittp
getn 168; geton 168;
dataout 'U:1341-171/1341-171.u.2010_08_27.SELFC1
go fittp
getn 169; geton 169;
dataout 'U:1502+106/1502+106.u.2010_08_27.SELFC1
go fittp
getn 170; geton 170;
dataout 'U:1520+319/1520+319.u.2010_08_27.SELFC1
go fittp
getn 171; geton 171;
dataout 'U:1519-273/1519-273.u.2010_08_27.SELFC1
go fittp
getn 172; geton 172;
dataout 'U:1532+016/1532+016.u.2010_08_27.SELFC1
go fittp
getn 173; geton 173;
```

```
dataout 'U:1636+473/1636+473.u.2010_08_27.SELFC1
go fittp
getn 174; geton 174;
dataout 'U:1730-130/1730-130.u.2010_08_27.SELFC1
go fittp
getn 175; geton 175;
dataout 'U:1732+389/1732+389.u.2010_08_27.SELFC1
go fittp
getn 176; geton 176;
dataout 'U:1749+701/1749+701.u.2010_08_27.SELFC1
go fittp
getn 177; geton 177;
dataout 'U:1920-211/1920-211.u.2010_08_27.SELFC1
go fittp
getn 178; geton 178;
dataout 'U:2200+420/2200+420.u.2010_08_27.SELFC1
go fittp
getn 179; geton 179;
dataout 'U:2201+171/2201+171.u.2010_08_27.SELFC1
go fittp
getn 180; geton 180;
dataout 'U:2251+158/2251+158.u.2010_08_27.SELFC1
go fittp
getn 181; geton 181;
dataout 'U:2345-167/2345-167.u.2010_08_27.SELFC1
go fittp

getn 182; geton 182;
dataout 'U:0010+405/0010+405.u.2010_08_27.GAINT1
```

```
go fittp
getn 183; geton 183;
dataout 'U:0113-118/0113-118.u.2010_08_27.GAINT1
go fittp
getn 184; geton 184;
dataout 'U:0202+149/0202+149.u.2010_08_27.GAINT1
go fittp
getn 185; geton 185;
dataout 'U:0219+428/0219+428.u.2010_08_27.GAINT1
go fittp
getn 186; geton 186;
dataout 'U:0333+321/0333+321.u.2010_08_27.GAINT1
go fittp
getn 187; geton 187;
dataout 'U:0414-189/0414-189.u.2010_08_27.GAINT1
go fittp
getn 188; geton 188;
dataout 'U:0415+379/0415+379.u.2010_08_27.GAINT1
go fittp
getn 189; geton 189;
dataout 'U:0430+052/0430+052.u.2010_08_27.GAINT1
go fittp
getn 190; geton 190;
dataout 'U:0529+483/0529+483.u.2010_08_27.GAINT1
go fittp
getn 191; geton 191;
dataout 'U:0716+714/0716+714.u.2010_08_27.GAINT1
go fittp
getn 192; geton 192;
```

```
dataout 'U:0722+145/0722+145.u.2010_08_27.GAINT1
go fittp
getn 193; geton 193;
dataout 'U:0808+019/0808+019.u.2010_08_27.GAINT1
go fittp
getn 194; geton 194;
dataout 'U:0827+243/0827+243.u.2010_08_27.GAINT1
go fittp
getn 195; geton 195;
dataout 'U:0917+449/0917+449.u.2010_08_27.GAINT1
go fittp
getn 196; geton 196;
dataout 'U:1055+018/1055+018.u.2010_08_27.GAINT1
go fittp
getn 197; geton 197;
dataout 'U:1329-049/1329-049.u.2010_08_27.GAINT1
go fittp
getn 198; geton 198;
dataout 'U:1341-171/1341-171.u.2010_08_27.GAINT1
go fittp
getn 199; geton 199;
dataout 'U:1502+106/1502+106.u.2010_08_27.GAINT1
go fittp
getn 200; geton 200;
dataout 'U:1520+319/1520+319.u.2010_08_27.GAINT1
go fittp
getn 201; geton 201;
dataout 'U:1519-273/1519-273.u.2010_08_27.GAINT1
go fittp
```

```
getn 202; geton 202;
dataout 'U:1532+016/1532+016.u.2010_08_27.GAINT1
go fittp
getn 203; geton 203;
dataout 'U:1636+473/1636+473.u.2010_08_27.GAINT1
go fittp
getn 204; geton 204;
dataout 'U:1730-130/1730-130.u.2010_08_27.GAINT1
go fittp
getn 205; geton 205;
dataout 'U:1732+389/1732+389.u.2010_08_27.GAINT1
go fittp
getn 206; geton 206;
dataout 'U:1749+701/1749+701.u.2010_08_27.GAINT1
go fittp
getn 207; geton 207;
dataout 'U:1920-211/1920-211.u.2010_08_27.GAINT1
go fittp
getn 208; geton 208;
dataout 'U:2200+420/2200+420.u.2010_08_27.GAINT1
go fittp
getn 209; geton 209;
dataout 'U:2201+171/2201+171.u.2010_08_27.GAINT1
go fittp
getn 210; geton 210;
dataout 'U:2251+158/2251+158.u.2010_08_27.GAINT1
go fittp
getn 211; geton 211;
dataout 'U:2345-167/2345-167.u.2010_08_27.GAINT1
```

```
go fittp

** Step 18
********Exit to linux
cd /net/miranda/project/miranda/IDV/BL149CN

cd 0010+405
mv *.SELFC1 2010_08_27/
mv *.GAINT1 2010_08_27/
cd ..
cd 0113-118
mv *.SELFC1 2010_08_27/
mv *.GAINT1 2010_08_27/
cd ..
cd 0202+149
mv *.SELFC1 2010_08_27/
mv *.GAINT1 2010_08_27/
cd ..
cd 0219+428
mv *.SELFC1 2010_08_27/
mv *.GAINT1 2010_08_27/
cd ..
cd 0333+321
mv *.SELFC1 2010_08_27/
mv *.GAINT1 2010_08_27/
cd ..
cd 0414-189
mv *.SELFC1 2010_08_27/
mv *.GAINT1 2010_08_27/
```

```
cd ..
cd 0415+379
mv *.SELFC1 2010_08_27/
mv *.GAINT1 2010_08_27/
cd ..
cd 0430+052
mv *.SELFC1 2010_08_27/
mv *.GAINT1 2010_08_27/
cd ..
cd 0529+483
mv *.SELFC1 2010_08_27/
mv *.GAINT1 2010_08_27/
cd ..
cd 0716+714
mv *.SELFC1 2010_08_27/
mv *.GAINT1 2010_08_27/
cd ..
cd 0722+145
mv *.SELFC1 2010_08_27/
mv *.GAINT1 2010_08_27/
cd ..
cd 0808+019
mv *.SELFC1 2010_08_27/
mv *.GAINT1 2010_08_27/
cd ..
cd 0827+243
mv *.SELFC1 2010_08_27/
mv *.GAINT1 2010_08_27/
cd ..
```

```
cd 0917+449
mv *.SELFC1 2010_08_27/
mv *.GAINT1 2010_08_27/
cd ..
cd 1055+018
mv *.SELFC1 2010_08_27/
mv *.GAINT1 2010_08_27/
cd ..
cd 1329-049
mv *.SELFC1 2010_08_27/
mv *.GAINT1 2010_08_27/
cd ..
cd 1341-171
mv *.SELFC1 2010_08_27/
mv *.GAINT1 2010_08_27/
cd ..
cd 1502+106
mv *.SELFC1 2010_08_27/
mv *.GAINT1 2010_08_27/
cd ..
cd 1520+319
mv *.SELFC1 2010_08_27/
mv *.GAINT1 2010_08_27/
cd ..
cd 1519-273
mv *.SELFC1 2010_08_27/
mv *.GAINT1 2010_08_27/
cd ..
cd 1532+016
```

```
mv *.SELFC1 2010_08_27/
mv *.GAINT1 2010_08_27/
cd ..
cd 1636+473
mv *.SELFC1 2010_08_27/
mv *.GAINT1 2010_08_27/
cd ..
cd 1730-130
mv *.SELFC1 2010_08_27/
mv *.GAINT1 2010_08_27/
cd ..
cd 1732+389
mv *.SELFC1 2010_08_27/
mv *.GAINT1 2010_08_27/
cd ..
cd 1749+701
mv *.SELFC1 2010_08_27/
mv *.GAINT1 2010_08_27/
cd ..
cd 1920-211
mv *.SELFC1 2010_08_27/
mv *.GAINT1 2010_08_27/
cd ..
cd 2200+420
mv *.SELFC1 2010_08_27/
mv *.GAINT1 2010_08_27/
cd ..
cd 2201+171
mv *.SELFC1 2010_08_27/
```

```
mv *.GAINT1 2010_08_27/
cd ..
cd 2251+158
mv *.SELFC1 2010_08_27/
mv *.GAINT1 2010_08_27/
cd ..
cd 2345-167
mv *.SELFC1 2010_08_27/
mv *.GAINT1 2010_08_27/
cd ..

***Run the following perl scripts to make a copy of the GAINT1
***& SELFC1 files prior to editing them in difmap

perl /project/miranda/IDV/scripts/CopyMakerRoutine GAINT1 _raw
perl /project/miranda/IDV/scripts/CopyMakerRoutine SELFC1 _raw

** Step 19
***In linux open Difmap again & execute the following scripts:

cd /net/miranda/project/miranda/IDV/BL149CN

difmap
@scripts/BL149CN_2010_08_27_fit_sources

***Flux density needs to be made the sole variable.
**Go back to linux & execute the following perl script:

cd /net/miranda/project/miranda/IDV/BL149CN
```

```
perl /project/miranda/IDV/scripts/Make_tmodRoutine
scripts/BL149CN_sources 2010_08_27 u

** Step 20
***In linux open Difmap again & execute the following scripts:

cd /net/miranda/project/miranda/IDV/BL149CN

difmap
@scripts/BL149CN_2010_08_27_ScanBreak
@scripts/BL149CN_2010_08_27_IndividualScanfit_GAINT
@scripts/BL149CN_2010_08_27_IndividualScanfit_SELFC

** Step 21
***At linux prompt use the following perl scripts to write a file
***containing the AIPS commands to plot the UV visibilities for
***each source and scan

perl /project/miranda/IDV/scripts/WriteUV 2010_08_27 212 GAINT1 u
***Run the AIPS commands contained in the file: BL149CN_UV.script
***and then run the following command:

perl /project/miranda/IDV/scripts/UVFNDscript
*===Refer to the IDV analysis text file for further steps.

*===Refer to the /project/miranda/IDV/scripts directory for useful
scripts like 'MultiEpochPlotterRoutine', 'AntennaElevationPlotter'.
```

VITA

VITA

Hutha K. Sarma has a BS degree in Mechanical Engineering, and MS degrees in Nuclear Engineering, Material Science & Engineering. His research interests span the entire gamut of high energy astrophysics in general, especially the areas of multi–wavelength observations of supernova remnants, pulsars & pulsar wind nebulae, X–Ray binaries & other compact galactic objects and AGN. His dissertation work was carried out as part of the *MOJAVE* project, involving long term radio observations of blazars.